ON THE COUPLING OF MOLECULAR DYNAMICS TO CONTINUUM COMPUTATIONAL FLUID DYNAMICS

Edward Smith

Thermofluids & Tribology group
Department of Mechanical Engineering
Imperial College London, UK

Submitted in partial fulfilment of the requirements for the degree of Doctor of Philosophy
Department of Mechanical Engineering, Imperial College London
December 2013

Declarations

Declaration of Originality

The work presented in this document builds on a wide body of literature. The discussion of this literature is appropriately referenced and paraphrased. Any direct quotes are in italics and include appropriate page numbers from the source. All other text has been written by me (with assistance from David Heyes, Daniele Dini and Tamer Zaki) and any figures have been generated by me using data generated from simulations that I have run myself (unless otherwise stated). Any published work is reproduced here with permission.

Copyright Declaration

Abstract

Molecular dynamics (MD) is a discrete modelling technique that is used to capture the nano-scale motion of molecules. MD can be used to accurately simulate a range of physical problems where the continuum assumption breaks down. Examples include surface interaction, complex molecules, local phase changes, shock waves or the contact line between fluids. However, beyond very small systems and timescales (μm and $msec$), MD is prohibitively expensive. Continuum computational fluid dynamics (CFD), on the other hand, is easily capable of simulating scales of engineering interest, (m and s). However, CFD is unable to capture micro-scale effects vital for many modern engineering fields, such as nanofluidics, tribology, nano-electronics and integrated circuit development. This work details the development of a set of techniques that combine the advantages of both continuum and molecular modelling methodologies, allowing the study of cases beyond the range of either technique alone.

The present work is split into both computational and theoretical developments. The computational aspect involves the development of a new high-performance MD code, as well as a coupler (CPL) library to link it to a continuum solver. The MD code is fully verified, has similar performance to existing MD software and allows simulation of a wide range of cases. The CPL library is a robust, flexible and language independent API and the source code has been made freely available under the GNU GPL v3 license. Both MD and CPL codes are developed to allow very large scale simulation on high performance computing (HPC) facilities.

The theoretical aspect includes the development of a rigorous mathematical framework and its application to develop novel coupling methodologies. The mathematical framework allows a discrete molecular system to be expressed in terms of the control volume (CV) formulation from continuum fluid dynamics. A discrete form of Reynolds' transport theorem is thus obtained allowing both molecular and continuum systems to be expressed in a consistent manner. This results in a number of insights into the molecular definition of stress. This CV framework allows mathematical operations to be localised to a control volume in space. It is ideally suited to apply coupling constraints to a region in space. To link the CFD and MD solvers in a rigorous and physically consistent manner, the CV framework is combined with the variational principles of classical mechanics. The result is a unification of a number of existing equations used in the coupling literature and a rigorous derivation of a new and more general coupling scheme.

Preface

The work presented in this document represents a coherent story on the development of coupling. It contains a summary of the vast majority of the work the author has been involved in during the last four year. The work in chapter 4 on the control volume formulation, Smith, Heyes, Dini & Zaki (2012), has been published in Physical Review E. The computational developments of the coupling library has also resulted in two technical papers (Anton & Smith, 2012; Smith, Trevelyan & Zaki, 2013) and an open source software project (Smith & Trevelyan, 2013).

However, not all of the work is reported here. The work on the connection between the volume average and method of planes stress, Heyes, Smith, Dini & Zaki (2011) in the Journal of Chemical Physics, is only mentioned in passing. Although this deserves a far more extensive treatment, this would have required a tangent from the development of coupling schemes, which this work is devoted to.

In addition, some work toward a project published in Journal of Chemical Physics, Heyes, Smith, Dini, Spikes & Zaki (2012) on the study of lubrication between two sliding surface is not reported herein. Much of the choice of setup and insight into Couette flow, which feature heavily in this work, stems from the work in this publication. Again, however, a detailed review of this work does not fit naturally into the story presented here.

Acknowledgements

To my supervisors, for ensuring that every week, without fail, they were available to meet. To Dr Daniele Dini for his support, both academic and otherwise and for being available to discuss and solve any problem. To Professor David Heyes for sharing his wide ranging experience, unique way of finding interesting problems and their solutions. In addition, for allowing me to be involved on a number of his publications, without which I would not have the broad insight into molecular dynamics and as strong a basis to start my career in research. To Dr Tamer Zaki for his unflinching honesty and through, insightful and detailed technical review of my work. To Lucian Anton for his work on the coupler and improvements to the MD solver. To my Viva examiners Professor Jason Reese and Dr Fernando Bresme for taking the time to read this thesis and for a number of constructive and useful suggestions.

To my girlfriend Amy Clifford for always being there and supporting me, as well as putting up with my relentless working over the last four years.

To my family, my parents Mel and Kay – without them I wouldn't be here (in every sense). To my sisters Georgina and Melanie for their support, counselling and guidance.

To the friends and colleagues I've met over the last four years, including Sandeep Saha, Nicholas Vaughan, Laura Nicolaou Fernandez, Luca Burini, Tom Jelly, Philipp Hack, Akshat Agarwal, Kevin Nolan, David Trevelyan, Jacob Page, Sang Jin Lee, Luca Biancofiore and Slava Stetsyuk.

Finally I would like to thank EPSRC and Imperial College London for funding the work presented in this thesis, through a Doctoral Training Award and beyond.

Contents

List of Figures

Symbol List

General Notation
$< .. >$ – System average which can be ensemble, spatial or temporal depending on context.
α, β, γ and ζ – Dimensional indices.
$\delta_{\alpha\beta}$ – Kronecker delta.
δ – Dirac delta function.
$\mathcal{C}$ – Used to denotes differentiability class .
i, j, k, n and m – Molecular indices.

Molecular Notation
ϵ – Strength of atomic interactions.
ℓ – Length scale of the molecular system, usually the atomic diameter.
τ – MD time unit.
k_B – Boltzmann's constant.
N – Number of molecules in whole system.
V – Volume of MD system.
ρ – MD density defined by $\rho = mN/V$.
N_I – Number of molecules in cell I.
N' – Number of molecules in flux.
$\boldsymbol{r}_i$ – Vectorial position of atom i in Cartesian coordinates where $\boldsymbol{r} = [x, y, z]^T$.
$\boldsymbol{r}_{ij}$ – Difference between position of atom i and atom j – $\boldsymbol{r}_{ij} = \boldsymbol{r}_i - \boldsymbol{r}_j$.
$\boldsymbol{r}_c$ – Molecular interaction truncation (cut-off) distance.
$\dot{\boldsymbol{r}}_i$ – Velocity of molecule i.
$\ddot{\boldsymbol{r}}_i$ – Acceleration of molecule i.
Φ – Potential field approximated using the Lennard-Jones potential for pairwise interactions.
$\boldsymbol{F}_i$ – Total force on molecule i from all interactions and external forces.
$\boldsymbol{f}_{ij}$ – Force between molecule i and j.
O_{ij} – Irving & Kirkwood (1950) operator
ϑ_i – Control volume (CV) function for molecule i (also called the $\mathcal{LCV}$ function)
ϑ_{ij} – Difference between CV for i and j, where $\vartheta_{ij} = \vartheta_i - \vartheta_j$
ϑ_s – Control volume (CV) function for point on interaction line between i and j, denoted by $\iota = \boldsymbol{r}_i + s\boldsymbol{r}_{ij}$
$d\mathbf{S}_i$ – Derivative of CV function ϑ_i for molecule i
$d\mathbf{S}_{ij}$ – Derivative of CV function ϑ_s integrated over all s
$\boldsymbol{\varsigma}_{ij}$ – Outer product of the intermolecular forces with $\boldsymbol{\varsigma}_{ij} = \boldsymbol{f}_{ij} \cdot \tilde{\mathbf{n}}$ where $\tilde{\mathbf{n}} = [111]^T$
$\mathcal{L}$ – Lagrangian
g – Constraint
$\mathcal{L}_c$ – Constrained Lagrangian $\mathcal{L}_c = \mathcal{L} + g$
$\mathcal{H}$ – Hamiltonian of the system.
$\boldsymbol{q}_i$ – Generalised coordinate of molecule i.
$\boldsymbol{p}_i$ – Laboratory momentum $\boldsymbol{p}_i = m_i\dot{\boldsymbol{r}}_i$ in chapters 1 to 4. Conjugate momentum in chapter 5.
$\overline{\boldsymbol{p}}_i$ – Peculiar (or conjugate) momentum $\overline{\boldsymbol{p}}_i = m_i\dot{\boldsymbol{r}}_i - \boldsymbol{u}$ used in chapter 1 to 4 only.
$\Delta t_{_{MD}}$ – Molecular timestep

Continuum Notation
L – Length scale of the continuum.
U – Velocity scale of the continuum.
t – Continuum time scale
ρ – Density of the continuum
μ – Coefficient of viscosity.
$\nu = \rho/\mu$ – Kinematic viscosity.
λ – Second coefficient of viscosity, also used for Lagrangian multiplier.
P – Continuum thermodynamic pressure (scalar).
$Re = UL/\nu$ – Reynolds number.
T – Kinetic temperature.
$\boldsymbol{u}$ – Continuum velocity vector.
u^t_{IJ} – Discretised continuum velocity at timestep t and located at cell I, J.
$\Delta t_{_{CFD}}$ – Continuum timestep

Pressure/Stress Notation
$\boldsymbol{\sigma}$ – Cauchy stress tensor (configurational terms)
$\mathbf{T}^{\pm}_{\alpha}$ – Traction on $\alpha = x, y$ or z surfaces, $\pm$ denotes top or bottom, given by $\mathbf{T}^{\pm}_{\alpha} = \boldsymbol{\sigma}\cdot\mathbf{n}^{\pm}_{\alpha}$.
$\boldsymbol{\kappa}$ – Kinetic pressure tensor
$\mathbf{K}^{\pm}_{\alpha}$ – Kinetic pressure analogue to traction on $\alpha = x, y$ or z surfaces with $\pm$ denoting top or bottom, given by $\mathbf{K}^{\pm}_{\alpha} = \boldsymbol{\kappa} \cdot \mathbf{n}^{\pm}_{\alpha}$.
$\boldsymbol{\Pi}$ – Total pressure tensor including kinetic pressure and stress tensor.
$\boldsymbol{p}^{\pm}_{\alpha}$ – Total traction on $\alpha = x, y$ or z surfaces with $\pm$ denoting top or bottom, given by $\boldsymbol{p}^{\pm}_{\alpha} = \boldsymbol{\Pi} \cdot \mathbf{n}^{\pm}_{\alpha}$

Chapter 1

Introduction

1.1 Motivation

The nature of reality has long been a source of philosophical debate. Around 400BC, Democritus and Leucippus postulated an indivisible unit which they called the atom (Coveney & Highfield, 1991). With no evidence for the existence of atoms and the widespread adoption of Aristotelian physics, the discrete paradigm largely fell from favour over the ensuing millennia. The first quantitative challenge to the continuous nature of reality is attributed to the alchemist Robert Boyle in 1666 (Boyle, 1666). By introducing the corpuscle, he provided a mechanism for the behaviour of gases as interacting particles. Despite this work and that of other "atomist" proponents like John Dalton *et al.* (1808), the lack of experimental evidence for atoms ensured the continuum dominated science over the next three hundred years. This view was so ingrained by the late 19th century that, despite being central to Ludwig Boltzmann's development of statistical mechanics, discrete atoms were regarded as no more than a tool. Convincing evidence for the existence of atoms was provided, in part, through Einstein's atomistic explanation for Brownian motion and the scattering experiments of Rutherford at the start of the 20th century. As a result of this dichotomy, the fields of continuum mechanics and discrete particles dynamics evolved separately, well into the age of computers. Even today, the two descriptions are often studied independently by separate communities. Philosophically, the link between the two is far from clear. Molecular analogues to even steady state continuum concepts such as pressure have proved troublesome (Zhou, 2003). Move away from the steady state and the link between the continuum and discrete is very difficult to define.

The nature of reality is no longer simply a philosophical debate. Engineering modelling is built on the continuum hypothesis. As science attempts to explore smaller scales and more extreme phenomena, the cracks begin to appear – from the apparently innocuous assumption of no-slip between a solid and a fluid to the simulation of the extreme environment of space shuttle re-entry. The failure to model the contact line between two phases of a fluid or a moving shock wave highlights the limitations of this continuous view of matter. Many modern technologies employ nano-scale components from the ubiquitous computer transistor to the various promising forms of carbon. Modelling of nano-scales for these emerging technologies requires discrete effects to be fully captured. This necessitates increased sophistication of the modelling techniques beyond continuum only models.

It is this improvement in modelling techniques that motivates the current work. By attempting to resolve the differences between the continuous and discrete formulations, it will be possible

to combine the successes of both. The next sections outline a brief history of both formulations and the progress to date in linking them.

1.2 Continuum Mechanics

The calculus developed by Newton and Leibniz in the seventeenth century motivates a view of nature that is continuous in space. This notion of an infinitely divisible substance became popular in the following two centuries underpinning the field of continuum mechanics. By ignoring the atomic nature of material, it is possible to express solvable differential equations describing the temporal and spatial evolution of a continuous field. The field of continuum mechanics includes the study of solid mechanics, thermodynamics and fluid mechanics. A key distinction between these fields is the choice of reference frame. As solids deform by small amounts, it is possible to follow a fixed collection of material as it evolves in time. This is termed the Lagrangian reference frame. For thermodynamics and fluid mechanics, the movement of the material is too great to keep track of a fixed collection and it is simpler to observe the flow past a reference volume (called a control volume). This is termed the Eulerian reference frame.

Solid mechanics attempts to model the stress and strain of a material. The solid mechanics concepts of stress were developed by Lenard Euler and the Bernoullis (James then John) with the notion of the stress tensor finally formalised by Cauchy in 1823 (Soutas-Little & Merodio, 2007). In its modern guise, continuum solid mechanics has demonstrated great success through the Finite Element Method (Zienkiewicz, 2005). However fracture mechanics, non-isotropic material and extreme loads all require modelling techniques beyond the continuum assumption.

The field of thermodynamics was developed during the industrial revolution to quantify the interplay of heat and work. It provides continuum notions of temperature, pressure and entropy. The entire formulation of thermodynamics assumes a fluid at thermodynamic equilibrium (Sandler & Woodcock, 2010). This significantly limits the applicability of thermodynamics, a restriction that is likened by Coveney & Highfield (1991) to the field of medicine focusing on the dead.

Continuum fluid dynamics models the flow of fluids away from hydrodynamic equilibrium, typically for phenomena acting at larger time and length scales than required for thermodynamic equilibrium (Gad-el Hak, 2006). It is governed by the Navier-Stokes equation. This equation was formulated independently by Claude-Louis Navier in 1822 and George Gabriel Stokes in 1845 (Gad-el Hak, 1995) and represents a continuum implementation of Newton's laws with a variety of closure assumptions. By virtue of these assumptions, the solids mechanics stress tensor is often replaced by a scalar hydrodynamic pressure, a shear viscosity and, in some cases, a bulk viscosity. Analytical solution of these non-linear partial differential equations is impossible for all but the simplest of ideal cases. Steady state solutions were obtained by Jean Louis Marie Poiseuille and Maurice Couette for the now eponymously named flows, while Joseph Fourier pioneered a time dependent solution in terms of trigonometric functions. Only with the advent of computers have general solutions been possible, the modern field of computational fluid dynamics (CFD) (Hirsch, 2007). With these numerical solutions, chaotic behaviour can result, a phenomenon known in fluid mechanics as turbulence. Turbulence is a feature of almost every case of engineering interest and a detailed understanding of this phenomenon would allow untold improvements in design and predictive capabilities. With the aid of computer simulation, great strides have been made in the categorisation, modelling and understanding of turbulence. Direct numerical simulation (DNS)

resolves the range of turbulent eddies down to the smallest dissipative scales (the Kolmogorov length scale) (Kim *et al.*, 1987). It is not known the role that smaller scale effects have on the dynamics of the turbulence. It has been suggested, however, that the microscale fluctuations play an important role in fluid instability (K. Kadau *et al.*, 2010).

Although the focus of this work is primarily the field of fluid mechanics, it also contains many elements of solid mechanics (stress) and thermodynamics, through statistical mechanics. As discussed in the next section, molecular dynamics does not respect the separation between the continuum fields of study, and can often contain features of all three in a single simulation.

Continuum mechanics is limited to simulations where the Knudsen number is much less than unity throughout the entire domain. Many simulations of real world phenomena involve some region where the length scale of interest is microscopic, for example, the liquid-solid interaction, presence of multiple phases, impulse started walls or shock waves. Whenever these '*discontinuities*' are present in the continuum field, a molecular description is required to capture the physics. In addition, the behaviour of the continuum fluid no longer conforms to Newtonian mechanics or Stokes' hypothesis (Gad-el Hak, 1995). Again, in these cases a molecular model can be used to provide the correct behaviour for the fluid.

1.3 Molecular Dynamics

As for continuous systems, Newton's laws of motion are of central importance at the molecular level. They are valid for all but the most extreme scales where relativity or quantum mechanics become important. Newton's laws are still applicable at the atomic scale, although a closed form solution to the motion of even three bodies is a long standing problem. The 'many body' problem has been solved only through the advent of computers, with the first molecular simulations by Alder and Wainwright (Alder & Wainwright, 1957, 1959). The solution of these systems reveal an apparently chaotic set of molecular trajectories, similar to the chaotic behaviour observed in the continuum. Indeed, the behaviour from large simulations of RayleighTaylor instability using MD simulation at the micro-scale show agreement with turbulent behaviour observed on the macroscale (K. Kadau *et al.*, 2010).

This is the field of molecular dynamics (MD) which simulates nature as a collection of discrete atoms. Within this framework, the full range of solid mechanics, thermodynamics or fluid mechanics behaviour can be observed. At appropriately low temperatures, the molecules cluster and form a solid lattice or boil at high temperatures and become a gas. The movement of molecules and their collisions (on average) reproduce the predictions of empirical thermodynamic laws.

Moving away from equilibrium molecular dynamics into the realm of non-equilibrium simulation, one finds a very vibrant and active research area (Evans & Morriss, 2007). It is possible to match results to the continuum analytical solution of Poiseuille and Couette as well as obtain definition of concepts such as viscosity using Green-Kubo (Green, 1954; Kubo, 1957) formulas. In the case of linear departures from equilibrium, theories exist which allow analysis of the onset of non-Newtonian behaviour.

Molecular dynamics is by its nature very computationally expensive. The largest simulations to date have been of the order 10^{12} molecules run for $10ps$ (Germann & Kadau, 2008). This may appear to be a large number, but $1m^3$ of air contains over 10^{25} molecules. Therefore, molecular dynamics is confined to the modelling of small systems at very short time scales. Predictions

from the work of Germann & Kadau (2008), based on Moore's law, suggest that 3D turbulence ($0.25mm$ for $100ns$) will be possible in 50 years while 3D engineering scales (cm for ms) will take over 100 years.

1.4 Coupling

Most cases which are of engineering interest require the resolution of molecular systems sizes far beyond foreseeable computational capabilities. However, the molecular and continuum simulations show excellent agreement away from these *discontinuities*, discussed in the continuum section 1.2. As a result, molecular simulation is only required close to the discontinuity, and a continuum description can then be used to model the remainder of the domain. This observation is key to the work presented herein, where a continuum model and molecular model are combined to simulate problems whose modelling is not achievable using either model by itself. This allows the impact of microscopic effects to be observed over scales of engineering interest. This approach, it is envisaged, will have widespread applications in nanofluidics, tribology, micro-electronics, surface chemistry, surface texture research and fundamental fluid mechanics simulations. Given future trends towards smaller scale engineering and increasing reliance on numerical modelling, the need for coupled simulation tools can only become more pronounced.

However, despite excellent progress in recent publications, there remain a number of challenges to address before continuum to molecular coupling is a reliable tool for industrial engineering. The inherent challenges to overcome, in order to develop a successful coupling, are extremely non-trivial. The coupled problem is inherently one of computational optimisation, where the continuum is employed to reduce the computing load of a large MD system. Even with coupling based improvements, problems of interest will require state of the art high performance computing techniques in order to exploit the architecture of many-core computers.

In addition, the theoretical and scientific challenges remain great. Molecular dynamics is typically applied to thermodynamic problems; systems at steady state simulated with periodic boundaries. These systems have very clear solutions in the canonical ensemble and numerical models can be easily validated. Away from equilibrium, many problems must be overcome, several of which are still active areas of research. It is no longer possible to use periodic boundaries, therefore molecular walls must be created, forces generated to drive the flow and thermostats applied to remove generated heat. Averaging to obtain properties away from equilibrium is also non-trivial, with controversial definitions of pressures and temperature and statistical noise plaguing attempts to average and retrieve continuum style properties. The problems of coupling require methods to link the systems along the open boundaries of both systems. The issues of numerical stability must be considered on the CFD side, especially in the presence of the noisy boundary conditions obtained from the molecular system. Even once these problems have been addressed, and an apparently successful coupling has been developed, it is unclear how to verify that it is physically meaningful or correct for all but the simplest of cases.

The aim of this work is to develop the methodology for linking a local molecular description to a large region simulated using a continuum description. This will include both computational and theoretical development. The computational development will focus on a general purpose, modern and robust computational tools to simulate a wide range of problems. The theoretical emphasis will be on the development of a rigorous mathematical framework based on sound physical principles. In doing this, some progress towards the goal of a unifying framework to link

and verify coupled models will be made.

The work will be split into three strands:

The first will be computational; the development of efficient simulation tools, often from the ground up, which work efficiently on modern computers and provide the flexibility to exchange information between the various models. These are designed to use state of the art optimisations (Plimpton, 1995; Rapaport, 2004) and build on modern developments in efficient parallelisation techniques for high performance computing (HPC) (Anderson *et al.*, 2008; Gropp *et al.*, 1999*a*,*b*). The result of this development is a generalised computational library for coupling on HPC platforms (Anton & Smith, 2012; Smith *et al.*, 2013; Smith & Trevelyan, 2013)

The second strand is the development of a mathematical framework in order to provide a consistent formulation for both systems. The link between descriptions in the continuous and discrete system is explored, with particular emphasis on the controversial field of the molecular stress tensor (Parker, 1954; Irving & Kirkwood, 1950; Noll, 1955; Tsai, 1978; Todd *et al.*, 1995; Han & Lee, 2004; Hardy, 1982; Lutsko, 1988; Cormier *et al.*, 2001; Zhou, 2003; Murdoch, 2007, 2010; Schofield & Henderson, 1982; Admal & Tadmor, 2010; Heyes *et al.*, 2011). The result is a discrete analogue of Reynolds' transport theorem and an operator which allows localisation of mathematical operations to a control volume (Smith *et al.*, 2012). This operator provides developments and some resolutions in the field of molecular stress.

The final strand will be the development of a method to 'stitch' the two descriptions together along their common interface. In this part of the work, tools are developed to link the continuum model to the molecular in a physically meaningful and rigorous manner. This builds on the modern and extensive literature on coupling schemes (O'Connell & Thompson, 1995; Hadjiconstantinou, 1998; Li *et al.*, 1997; Hadjiconstantinou, 1999; Flekkøy *et al.*, 2000; Wagner *et al.*, 2002; Delgado-Buscalioni & Coveney, 2003*a*; Curtin & Miller, 2003; Nie *et al.*, 2004*a*; Werder *et al.*, 2005; Ren, 2007; Borg *et al.*, 2010). The end result is a coupled framework which applies a constraint to an arbitrary volume in space.

1.5 Outline of this Work

This document is organised as follows. In chapter 2 the basic mathematical forms of the continuum and discrete systems, as well as the statistical mechanics used to link them, are presented. Careful attention is given to the various forms of classical mechanics which allow constraints to be applied. These constraints are important for the field of coupling also discussed in chapter 2, where the literature will be reviewed with emphasis on the limitations of the existing formulations. In chapter 3, the computational developments are outlined for a new molecular dynamics (MD) solver, the adaption of an existing computational fluid dynamics (CFD) solver and a new coupler (CPL) library to link them. High performance computing is an important part of modern simulation work and details of the developments and optimisation are provided. Verification tests will also be presented in support of later simulation results. Then, in chapter 4, a novel mathematical framework will be presented to express both systems in a consistent manner in terms of the Control Volume (CV) formulation. The CV mathematical framework will be verified and its utility demonstrated. The various constraint methodologies will be tested and compared. The CV formulation will then be exploited together with constrained dynamics to develop new methodologies for coupling in chapter 5. Finally, in chapter 6 the conclusions of

this work will be presented along with aims for future work.

Chapter 2

Background

2.1 Introduction

In this chapter, the governing equations of molecular dynamics and continuum fluid dynamics are introduced. The mathematical link between the two are discussed in the context of matching reference frames, spatial and temporal averaging and definition of equivalent densities, momenta and stresses between both systems. The chapter finishes with a review of the more advanced developments in the field of computational coupling schemes.

The first part of this chapter, section 2.2, introduces the governing equations of molecular dynamics (MD). In addition, a number of forms of variational principle are discussed in detail. These alternate forms of classical mechanics are essential to coupling. The statistical mechanics used to coarse grain a discrete system are also outlined.

The second part of this chapter, section 2.3, introduces the continuum formulation, starting with the control volume form and discussing the approximations required to obtain the Navier-Stokes equations. The various assumptions inherent in the Navier-Stokes equations are discussed.

The third part of this chapter, section 2.4, focuses on obtaining a mutually self-consistent mathematical description in both systems. Equivalent state properties – density, velocity and energy – are obtained by formulating both systems in the same reference frame following the work of Irving & Kirkwood (1950). The time evolution of these state properties then yield equivalent expressions for flux and the pressure in the two domains. The form of the pressure tensor is not unique, an issue which is considered by reviewing the various descriptions of the stress tensor proposed in the literature.

The fourth part of this chapter, section 2.5, investigates practical and computational aspects of linking a continuum and molecular system for a fluid mechanics simulation. This includes a review of the modern coupling literature which contains a number of methodologies, using either state or flux coupling being applied either explicitly or implicitly. The most challenging aspect of coupling is to ensure that the molecular system shares the same key state/flux variables (a non-unique problem). Particular emphasis is placed on the methods employed to solve this problem, including the use of constrained dynamics and the correct definition of localised state and flux properties. The summary of the literature underpins the strategy adopted for the remainder of this work.

This chapter finishes with a concluding summary in section 2.6.

2.2 Molecular Dynamics

This section introduces molecular dynamics, variational principles and statistical mechanics.

A molecular dynamics system consists of a number of discrete molecules (N), where each molecule i is located at a point in continuous space denoted by positional vector $\boldsymbol{r}_i$ with velocity vector $\dot{\boldsymbol{r}}_i$. Each molecule in the domain is followed and its evolution is calculated as a function of time - a Lagrangian framework for each molecule. The initial position and velocity of every molecule is the required initial state. Using Newton's second law it should (in principle) be possible to obtain any future state of the N-body system.

2.2.1 Governing Equations

In its simplest form, MD involves solving Newton's law for each molecule i of the N-molecule system,

$$m_i \ddot{\boldsymbol{r}}_i = \boldsymbol{F}_i \tag{2.1}$$

where m_i is the mass of molecules i and $\ddot{\boldsymbol{r}}_i$ its acceleration. The force $\boldsymbol{F}_i$ is calculated by adding the contribution from its interaction with the other $N-1$ molecules in the system box. The force on molecule i is given by $\boldsymbol{F}_i = -\boldsymbol{\nabla}\Phi(r)$, where the potential Φ is a function of all the relative molecular positions only. The potential Φ can be expressed as a series of interactions between atomic pairs, triplets, etc,

$$\Phi(\boldsymbol{r}_1, \boldsymbol{r}_2, \ldots, \boldsymbol{r}_N) = \sum_{i=1}^{N} \Phi(\boldsymbol{r}_i) + \sum_{i=1}^{N}\sum_{j>i}^{N} \Phi(\boldsymbol{r}_i, \boldsymbol{r}_j) + \sum_{i=1}^{N}\sum_{j>i}^{N}\sum_{k>j}^{N} \Phi(\boldsymbol{r}_i, \boldsymbol{r}_j, \boldsymbol{r}_k) + \ldots \tag{2.2}$$

where $\boldsymbol{r}_i$, $\boldsymbol{r}_j$ and $\boldsymbol{r}_k$ are the positions of molecules i, j and k respectively. The $\Phi(\boldsymbol{r}_i)$ is a body term which represents an external field, while higher order terms represent the interactions between two and higher numbers of molecules. The inclusion of pairwise and higher molecular interactions mark the departure from the theory of dilute gas. The greater the density of a fluid, the more terms required from Eq. (2.2) to model that fluid accurately. A common assumption for molecular dynamics is that the potential, Φ, is dependent on external fields and pair interactions only,

$$\Phi(\boldsymbol{r}_1, \boldsymbol{r}_2, \ldots, \boldsymbol{r}_N) \approx \sum_{i=1}^{N} \Phi(\boldsymbol{r}_i) + \sum_{i=1}^{N}\sum_{j>i}^{N} \Phi(\boldsymbol{r}_i, \boldsymbol{r}_j) \equiv \sum_{i=1}^{N} \Phi_i + \sum_{i,j}^{N} \Phi_{ij}. \tag{2.3}$$

In the interest of being concise, the double sum has been written using a single sum, where i, j denote all pairs and the molecular indices used in the potential's position dependence are expressed by subscripts so $\Phi(\boldsymbol{r}_i, \boldsymbol{r}_j) \equiv \Phi_{ij}$. The forces are then calculated from $\boldsymbol{f}_{ij} = -\partial/\partial \boldsymbol{r}_{ij}\Phi$, with $\boldsymbol{r}_{ij} = \boldsymbol{r}_i - \boldsymbol{r}_j$ and $\boldsymbol{f}_{iext} = -\partial/\partial \boldsymbol{r}_i\Phi$ so that, the resulting form of Newton's law is,

$$m_i \ddot{\boldsymbol{r}}_i = \boldsymbol{F}_i = \sum_{j\neq i}^{N} \boldsymbol{f}_{ij} + \boldsymbol{F}_{iext}. \tag{2.4}$$

In this work, the pairwise potential field is approximated using the Lennard-Jones potential (Rahman, 1964), which is commonly used to model monatomic liquid argon, but is actually a

good representation of more complex fluids,

$$\Phi(\boldsymbol{r}_{ij}) = 4\epsilon\left[\left(\frac{\ell}{\boldsymbol{r}_{ij}}\right)^{12} - \left(\frac{\ell}{\boldsymbol{r}_{ij}}\right)^{6}\right] - 4\epsilon\left[\left(\frac{\ell}{\boldsymbol{r}_c}\right)^{12} - \left(\frac{\ell}{\boldsymbol{r}_c}\right)^{6}\right], \quad |\boldsymbol{r}_{ij}| \leq |\boldsymbol{r}_c|. \tag{2.5}$$

$$\Phi(\boldsymbol{r}_{ij}) = 0 \quad , \quad |\boldsymbol{r}_{ij}| > |\boldsymbol{r}_c|, \tag{2.6}$$

Although the Lennard-Jones potential describes the interaction of pairs of molecules, it also shows very good agreement to experimental data for real systems which have two and greater molecular interactions (Allen & Tildesley, 1987). This is because Φ in Eqs. (2.5) and (2.6) is now an effective pair potential whose parameters incorporate, in a mean field sense, the three body and higher order terms which are formally absent. It therefore represents a good balance between simulation efficiency and accuracy.

In Eq. (2.5), ℓ is the length scale of the molecular system, the atomic diameter, and ϵ is a constant specifying the strength of inter-atomic interactions. The term with an exponent of 12 represent the repulsion which becomes stronger as the two atoms move together. The term with the exponent of 6 is the attraction and is greater than repulsion only when $r_{ij} > 2^{1/6}$. The effect of the potential drops off rapidly with distance. For computational reasons, the calculation is often truncated when $r_{ij} > r_c$ and shifted to be zero at $r_{ij} = r_c$, where r_c is an arbitrary cutoff distance often chosen to be $2^{1/6}$. Instead of an 'all pairs' system with all molecules interacting, the interactions are local and each molecule is only affected by its immediate neighbours. It is assumed the effects of the potential for $r_{ij} > r_c$ are insignificant.

Typically, the molecular representation is non-dimensionalised using length scale ℓ, mass m and energy ϵ (Rapaport, 2004), resulting in the equation of motion 2.7 in terms of these LJ units,

$$\ddot{\boldsymbol{r}}_i = 48\sum_{j\neq i}^{N}\left(r_{ij}^{-12} - \frac{1}{2}r_{ij}^{-6}\right)\boldsymbol{r}_{ij}. \tag{2.7}$$

Therefore, the variables in the above equation are non-dimensionalised by the molecular parameters. The method for discretising and solving this equation on a computer is deferred to chapter 3.

2.2.2 Variational Principles

The literature on coupling is introduced in detail in section 2.5, however, for the present it is sufficient to note that the fundamental techniques for coupling require the introduction of more general classical mechanics formulations than Newton's laws. The requirement is to apply constraints on the molecular system in a physically meaningful manner so that they evolve in the same way as the coupled continuum fluid. In this section, two formulations which allow constraints will be introduced: Hamilton's principle and Gauss' principle. The most commonly used is Hamilton's principle (the principle of least action). This forms the basis of much of modern physics due to its applicability to relativistic and quantum mechanics as well as its exposure of the underlying symmetries through Noether's theorem (Neuenschwander, 2011). Gauss' principle is less well known in general but is commonly used for non-equilibrium molecular dynamics (NEMD) (Hoover, 1991; Evans & Morriss, 2007).

Integral Variational Principle – Hamilton's principle

Hamilton's principle (Goldstein *et al.*, 2002) describes the evolution of the integral of a Lagrangian. For a classical N molecule system, the Lagrangian $\mathcal{L}$ is the difference between the kinetic and potential energy in the form,

$$\mathcal{L} = \sum_{i=1}^{N} \frac{1}{2} m_i \dot{q_i}^2 - \Phi(q_1, q_2, \ldots, q_N), \tag{2.8}$$

where q_i is the generalised coordinate of molecule i and $\dot{q_i}$ its velocity. The coordinates are, by construction, independent of coordinate system and frame of reference. The so called action, $\mathcal{A}$, is defined through the following integral between times t_a and t_b,

$$\mathcal{A} = \int_{t_a}^{t_b} \mathcal{L}(q_i, \dot{q_i}) dt, \tag{2.9}$$

where the endpoints of the integration are assumed to have fixed position, i.e. $q(t_a) = q_a$ and $q(t_b) = q_b$. Hamilton's principle states that the true trajectory of a dynamical system will be one in which action is an extremum,

$$\delta A = \delta \int_{t_a}^{t_b} \mathcal{L}(q_i, \dot{q_i}) dt = 0. \tag{2.10}$$

In practice, the action must be a minimum for the solution to be physically significant. Assuming the variation in action occurs smoothly, in time and space, the departure from the true trajectory q_i of molecule i can be written as,

$$q_i(t, \epsilon) = q_i(t, 0) + \epsilon \eta_i(t), \tag{2.11}$$

where ϵ is the magnitude of the departure and η_i is a $\mathcal{C}^2$ continuous function which satisfies the end points. The true trajectory of the system can then be obtained by ensuring ϵ is a minimum,

$$\delta A = \frac{\partial A}{\partial \epsilon} = \int_{t_a}^{t_b} \sum_{i=1}^{N} \left[\frac{\partial \mathcal{L}}{\partial q_i} \frac{\partial q_i}{\partial \epsilon} + \frac{\partial \mathcal{L}}{\partial \dot{q_i}} \frac{\partial \dot{q_i}}{\partial \epsilon} \right] dt = 0. \tag{2.12}$$

The second terms can be expanded using integration by parts,

$$\frac{\partial \mathcal{L}}{\partial \dot{q_i}} \frac{\partial \dot{q_i}}{\partial \epsilon} = \left[\frac{\partial \mathcal{L}}{\partial \dot{q_i}} \frac{\partial q_i}{\partial \epsilon} \right]_{t_a}^{t_b} - \int_{t_a}^{t_b} \frac{d}{dt} \left(\frac{\partial \mathcal{L}}{\partial \dot{q_i}} \right) \frac{\partial q_i}{\partial \epsilon} dt. \tag{2.13}$$

As the endpoints vanish, the first terms is zero. Taking out a common factor of $\partial q_i / \partial \epsilon = \eta_i$, the minimised action is,

$$\delta A = \int_{t_a}^{t_b} \sum_{i=1}^{N} \left[\frac{\partial \mathcal{L}}{\partial q_i} \frac{\partial q_i}{\partial \epsilon} - \frac{d}{dt} \left(\frac{\partial \mathcal{L}}{\partial \dot{q_i}} \right) \right] \eta_i dt = 0. \tag{2.14}$$

From the fundamental lemma of the calculus of variation, in general $\eta_i(t) \neq 0$, so the action is a minimum only if,

$$\frac{d}{dt}\frac{\partial \mathcal{L}}{\partial \dot{q}_i} - \frac{\partial \mathcal{L}}{\partial q_i} = 0, \tag{2.15}$$

at every point in time. This is the Euler-Lagrange equation. Eq. (2.15) can be expressed in terms of the canonical momentum conjugate,

$$\boldsymbol{p}_i \equiv \frac{\partial \mathcal{L}}{\partial \dot{q}_i} \;\; ; \quad \dot{\boldsymbol{p}}_i = \frac{\partial \mathcal{L}}{\partial q_i}, \tag{2.16}$$

The Euler-Lagrange Eq. (2.15), can be shown to yield Newton's second law by inserting the Lagrangian of Eq. (2.8), with cartesian coordinates $q_i \rightarrow r_i$,

$$m_i \ddot{\boldsymbol{r}}_i = -\frac{\partial \Phi}{\partial \boldsymbol{r}_i} = \boldsymbol{F}_i. \tag{2.17}$$

The strength of a minimisation formulation like Eq. 2.10, over Newton's law is the ability to apply arbitrary constraints to a dynamical system in the form,

$$\delta A = \delta \int_{t_a}^{t_b} \underbrace{\left[\mathcal{L}(q_i, \dot{q}_i) + \sum_{\alpha=1}^{C} \lambda_\alpha g_\alpha \right]}_{\mathcal{L}_C} dt = 0, \tag{2.18}$$

where C is the total number of constraints g_α and λ_α is a Lagrangian multiplier (Goldstein *et al.*, 2002). Constraints applied in this manner allow the dynamics of the system to evolve in a physically correct manner (minimising the action) while simultaneously satisfying a prescribed constraint condition. This is of vital importance when the molecular system must evolve in a consistent manner with the continuum system. A constraint derived in this manner should also satisfy conservation of energy for the system (Goldstein *et al.*, 2002). The constraint g_α can be one of two types – a holonomic constraint (a function of position and time only),

$$g_\alpha(q, t) = 0, \tag{2.19}$$

or a non-holonomic constraint (a function of position, velocity and time),

$$g_\alpha(q, \dot{q}, t) = 0. \tag{2.20}$$

For the case of the holonomic constraint in Eq. (2.19), Eq. (2.18) results in a modified Euler-Lagrange equation (Goldstein *et al.*, 2002),

$$\frac{d}{dt}\frac{\partial \mathcal{L}}{\partial \dot{q}_i} - \frac{\partial \mathcal{L}}{\partial q_i} = \sum_{\alpha=1}^{C} \lambda_\alpha \frac{\partial g_\alpha}{\partial q_i}. \tag{2.21}$$

For the case of the non-holonomic constraint in Eq. (2.20), Eq. (2.18) yields the following equation,

$$\frac{d}{dt}\frac{\partial \mathcal{L}}{\partial \dot{q}_i} - \frac{\partial \mathcal{L}}{\partial q_i} = \sum_{\alpha=1}^{C} \left(\dot{\mu}_\alpha \frac{\partial g_\alpha}{\partial \dot{q}_i} + \mu_\alpha \left[\frac{d}{dt}\frac{\partial g_\alpha}{\partial \dot{q}_i} - \frac{\partial g_\alpha}{\partial q_i} \right] \right). \tag{2.22}$$

where the Lagrangian multiplier is assumed to be a function of time only and is denoted by $\mu_\alpha = \mu_\alpha(t)$ to distinguish it from the holonomic case. It is known that this form of constraint does not, in general, give the correct equations of motion for non-holonomic constraints (Saletan & Cromer, 1970). This is still an active area of research and some controversy; the standard text on classical mechanics, Goldstein *et al.* (2002) 3rd edition in the errata at *http://astro.physics.sc.edu/Goldstein/* acknowledges several errors and suggests the reference by Flannery (2005). The latest paper by Flannery (2011) demonstrates that non-holonomic constraints can be applied using the following equation,

$$\frac{d}{dt}\frac{\partial \mathcal{L}}{\partial \dot{q}_i} - \frac{\partial \mathcal{L}}{\partial q_i} = \sum_{\alpha=1}^{C} \lambda_\alpha \frac{\partial g_\alpha}{\partial \dot{q}_i}. \tag{2.23}$$

The validity of this method is justified using Gauss' Principle of Least Constraint, favoured for NEMD (Evans & Morriss, 2007). This is because Gauss' Principle, as stated in Flannery (2011) p23, is *"a true minimisation principle,* [...] *with the additional and powerful advantage that it can be applied to general non-holonomic constraints"*. Gauss' Principle of Least Constraint is outlined in the next section – it is a local differential constraint and allows application of non-holonomic constraints. The price for this generality is the loss of guaranteed energy conservation ensured by Hamilton's principle.

The difference between equations 2.22 and 2.23 with $\dot{\mu}_\alpha \to \lambda_\alpha$ is the requirement that,

$$\frac{d}{dt}\frac{\partial g_\alpha}{\partial \dot{q}_i} - \frac{\partial g_\alpha}{\partial q_i} = 0. \tag{2.24}$$

This has the result that although Hamilton's principle cannot be used with non-holonomic constraints in general, the exception is a constraint of a form which satisfies equation (2.24). These are termed semi-holonomic constraints (Saletan & Cromer, 1970).

It is common in the NEMD literature to write the equations of motion in terms of the canonical momentum conjugate of Eq. (2.16),

$$\boldsymbol{p}_i = m_i \dot{\boldsymbol{q}}_i + \sum_{\alpha=1}^{C} \mu_\alpha \frac{\partial g_\alpha}{\partial \dot{q}_i} \tag{2.25a}$$

$$\dot{\boldsymbol{p}}_i = \boldsymbol{F}_i + \sum_{\alpha=1}^{C} \mu_\alpha \frac{\partial g_\alpha}{\partial q_i}. \tag{2.25b}$$

Differentiating Eq. (2.25a) and combining the result with Eq. (2.25b) results in Eq. (2.22), suggesting that these equations are valid provided the formula in Eq. (2.24) is satisfied.

Differential Variational Principle – Gauss' principle of least constraint

Gauss' principle of least constraint is a local minimisation procedure similar to the least square technique used in curve fitting. This can be compared to the global minimisation formulation of Lagrange (global integral minimised) outlined in the previous section. It is derived from a similar form to D'Alembert equations for static systems but considering the change in a system due to a virtual acceleration (Morriss & Dettman, 1998),

$$\frac{\partial}{\partial \ddot{\boldsymbol{r}}_j}\left[\frac{1}{2}\sum_{i=1}^{N} m_i\left(\boldsymbol{r}_i - \frac{\boldsymbol{F}_i}{m_i}\right)^2\right] = 0. \tag{2.26}$$

For molecules with no external forces this is equivalent to Newton's 2nd law,

$$\begin{aligned}\frac{\partial}{\partial \ddot{\boldsymbol{r}}_j}\left[\frac{1}{2}\sum_{i=1}^{N} m_i\left(\ddot{\boldsymbol{r}}_i - \frac{\boldsymbol{F}_i}{m_i}\right)^2\right] &= \sum_{i=1}^{N}\frac{m_i}{2}\frac{\partial}{\partial \ddot{\boldsymbol{r}}_j}\left(\ddot{\boldsymbol{r}}_i^2 - 2\frac{\boldsymbol{F}_i\cdot\ddot{\boldsymbol{r}}_i}{m_i} + \frac{\boldsymbol{F}_i^2}{m_i^2}\right)\\ = m_j\ddot{\boldsymbol{r}}_j - \boldsymbol{F}_j &= 0,\end{aligned} \tag{2.27a}$$

where the force is not a function of acceleration, i.e. $\partial \boldsymbol{F}_i/\partial \ddot{\boldsymbol{r}}_j = 0$, and the acceleration of molecule j is independent of the $N-1$ other molecules, i.e. $\partial/\partial \ddot{\boldsymbol{r}}_j \sum_{i=1}^{N} \ddot{\boldsymbol{r}}_i = \ddot{\boldsymbol{r}}_j$.

The strength of this formulation lies in the ability to apply non-holonomic constraints on any of the system's degrees of freedom using Lagrangian multipliers through,

$$\frac{\partial}{\partial \ddot{\boldsymbol{r}}_j}\left[\frac{1}{2}\sum_{i=1}^{N} m_i\left(\ddot{\boldsymbol{r}}_i - \frac{\boldsymbol{F}_i}{m_i}\right)^2 - \sum_{\alpha=1}^{C}\lambda_\alpha g_\alpha\right] = 0. \tag{2.28}$$

As the Lagrangian description cannot be used for non-holonomic constraints, Gauss' constraint is a more general formulation for classical systems.

Due to its generality, the validity of any derived constraint will be checked against Gauss' principle in this work.

2.2.3 Statistical Mechanics

The aim of this section is to introduce the mesoscopic framework which links the discrete microscopic and the continuum macroscopic descriptions.

A molecular system can be described in three dimensions in terms of three molecular positions $\boldsymbol{r}(t)$ and three momenta $\boldsymbol{p}(t)$ for every one of the N molecules at a time t. A convenient framework to consider this system is a $6N$ dimensional phase space in which each combination of molecule position and velocity has a unique value. Consider a probability function f which describes how likely a given point in phase space is to contain a molecule.

$$f = f(\boldsymbol{r}_1, \boldsymbol{r}_2, ..., \boldsymbol{r}_N, \boldsymbol{p}_1, \boldsymbol{p}_2, ..., \boldsymbol{p}_N, t). \tag{2.29}$$

This can be normalised to unity over the whole of phase space,

$$\int_{6N}\cdots\int f(\boldsymbol{r}_1, \boldsymbol{r}_2, ..., \boldsymbol{r}_N, \boldsymbol{p}_1, \boldsymbol{p}_2, ..., \boldsymbol{p}_N, t) d\boldsymbol{r}_1 d\boldsymbol{p}_1 ... d\boldsymbol{r}_N d\boldsymbol{p}_N = 1, \tag{2.30}$$

which, in this form, represents the canonical ensemble formulation of statistical mechanics. It is

based on the idea of an average over an arbitrary number of independent molecular systems (an ensemble). This average is used as a probability f of finding a molecule at a point in phase space. In other words, for a given $\boldsymbol{r}$ and $\boldsymbol{p}$ how likely it is to find a molecule with these properties in any of the ensemble of different systems. This is called a mesoscopic system as it is not based on the macroscopic continuum hypothesis and does not follow individual microscopic discrete molecules. The requirement is that a statistically significant number of molecules exist across the arbitrary number of systems. The evolution in time of f is governed by the Liouville equations of statistical mechanics. This is derived in an analogous way to the conservation equations of fluid mechanics but using a volume in phase space (Evans & Morriss, 2007),

$$\frac{\partial f}{\partial t} = \sum_{i=1}^{N} \left[\boldsymbol{F}_i \cdot \frac{\partial f}{\partial \boldsymbol{p}_i} - \frac{\boldsymbol{p}_i}{m_i} \cdot \frac{\partial f}{\partial \boldsymbol{r}_i} \right]. \tag{2.31}$$

The Liouville equation in the form of Eq. (2.31) contains all the complexity of the averaged MD systems, including the internal structure. The Liouville equation can be simplified to obtain the Boltzmann equation by assuming a statistical model of pair collisions (a truncation of the BBGKY hierarchy (Succi, 2001)). The key difference between the equation obtained by Boltzmann and a MD approach comes from replacing the all pairs calculation in MD with the assumption of uncorrelated collisions. This means that although both approaches model the streaming and collision of molecules (albeit statistically vs. explicitly), the Boltzmann equation does not model the microscopic structure of the fluid. For this reason, the Boltzmann equation, especially in the form of the lattice Boltzmann method, is easily applied to macroscopic flows. The Boltzmann equation can also be shown to yield the Navier-Stokes and other continuum conservation equations through low Knudsen number expansion (Chapman & Cowling, 1970). However, there has been limited success applying Boltzmann based equations to problems modelling smaller scales. The use of mean field theory where an N-molecule system is approximated as one molecule with a force applied to model the $N-1$ other molecules cannot capture the full underlying complexities of a dense fluid. The concept of a Knudsen number only applies to dilute gases, governed by kinetic theory, for dense liquids very little theoretical guidance is available (Gad-el Hak, 2006). It is for this reason that molecular dynamics is essential in capturing the effects of microscopic phenomena and, through coupling to the continuum, the effect on the macroscopic flow properties.

For a property α, the expectation value of α can be obtained by evaluating the inner product of Eq. (2.30) with the probability function defined by Eq. (2.29),

$$\Big\langle \alpha; f \Big\rangle \equiv \int_{6N} \cdots \int \alpha(\boldsymbol{r}_1, .., \boldsymbol{r}_N, \boldsymbol{p}_1, .., \boldsymbol{p}_N) f(\boldsymbol{r}_1, .., \boldsymbol{r}_N, \boldsymbol{p}_1, .., \boldsymbol{p}_N, t) d\boldsymbol{r}_1 d\boldsymbol{p}_1 .. d\boldsymbol{r}_N d\boldsymbol{p}_N, \tag{2.32}$$

where angled bracket notation $\langle \alpha; f \rangle$ is introduced to define the ensemble average. Here α is any dynamic variable expressed as a function of position and velocity (although not time explicitly). Assuming phase space is bounded, the evolution in time of the expected value of a property, α, is,

$$\frac{\partial}{\partial t} \Big\langle \alpha; f \Big\rangle = \sum_{i=1}^{N} \Big\langle \boldsymbol{F}_i \cdot \frac{\partial \alpha}{\partial \boldsymbol{p}_i} + \frac{\boldsymbol{p}_i}{m_i} \cdot \frac{\partial \alpha}{\partial \boldsymbol{r}_i}; f \Big\rangle, \tag{2.33}$$

which is obtained by Irving & Kirkwood (1950) from the Liouville Eq. (2.31). This equation is the key to deriving the evolution in time of molecular properties in section 2.4.3 as well as the new control volume formulation of chapter 4. In a molecular dynamics simulation, which is the micro-canonical ensemble, a property is found by averaging in time and space. Sufficient measurements in time and space must be taken to ensure the results are statistically significant and representative of the system. The ergodic hypothesis is used to link the canonical ensemble, based on independent systems, to the micro-canonical ensemble based on one system. That is, sufficient time must has passed for the successive measurements being averaged to become uncorrelated (Allen & Tildesley, 1987). The same result can be obtained in the micro-canonical molecular simulation using.

$$\left\langle \alpha; f \right\rangle \approx \frac{1}{\Delta t} \int_{t_0}^{t_0+\Delta t} \alpha(\boldsymbol{r}, \boldsymbol{p}) dt \approx \frac{1}{\Delta t} \sum_{t=t_0}^{t_0+\Delta t} \alpha(\boldsymbol{r}, \boldsymbol{p}), \tag{2.34}$$

where the first equality follows from the ergodic hypothesis.

In this section, the microscopic molecular dynamics equations in terms of Newton's laws were outlined, followed by the variational principles of classical mechanics. The mesoscopic statistical mechanical description was also introduced which is an intermediate between the discrete system of molecular dynamics and continuum mechanics. The next section considers the macroscopic continuum formulation of mechanics.

2.3 Continuum Fluid Dynamics

This section introduces the equations used in continuum fluid dynamics. The continuum assumption states that the material being considered is continuous in space and time, allowing calculus to be freely applied. It is widely assumed that the continuum assumption is reasonable given the length scales of the problem are much larger than the mean free path of the individual molecules, *i.e.* there are enough molecules in the smallest length scale that the material still acts like a continuum ($\mathcal{O}(10^6)$ molecules for standard deviations in statistical fluctuations to be less than 0.1% (Gad-el Hak, 2006)). This continuum assumption underpins the vast majority of engineering simulations.

2.3.1 Governing Equations

The continuum conservation of mass and momentum balance can be derived in an Eulerian frame by considering the fluxes through a Control Volume (CV). The mass continuity equation can be expressed as,

$$\frac{\partial}{\partial t} \int_V \rho dV = - \oint_S \rho \boldsymbol{u} \cdot d\mathbf{S}, \tag{2.35}$$

where ρ is the mass density and $\boldsymbol{u}$ is the fluid velocity. The rate of change of momentum is determined by the balance of forces on the CV,

$$\frac{\partial}{\partial t} \int_V \rho \boldsymbol{u} dV = - \oint_S \rho \boldsymbol{u}\boldsymbol{u} \cdot d\mathbf{S} + \mathbf{F}_{\text{surface}} + \mathbf{F}_{\text{body}}. \tag{2.36}$$

The forces are split into ones which act on the bounding surfaces, $\mathbf{F}_{\text{surface}}$, and body forces, $\mathbf{F}_{\text{body}}$. Surface forces are expressed in terms the pressure tensor, $\mathbf{\Pi}$, on the CV surfaces,

$$\mathbf{F}_{\text{surface}} = -\oint_S \mathbf{\Pi} \cdot d\mathbf{S}. \tag{2.37}$$

The rate of change of energy in a CV is expressed in terms of fluxes, the pressure tensor and a heat flux vector $\boldsymbol{Q}$,

$$\frac{\partial}{\partial t}\int_V \rho\mathcal{E} dV = -\oint_S \left[\rho\mathcal{E}\boldsymbol{u} + \mathbf{\Pi}\cdot\boldsymbol{u} + \boldsymbol{Q}\right]\cdot d\mathbf{S}, \tag{2.38}$$

which has been obtained by neglecting the term for the energy change due to body forces. In order to express the CV equations in differential form, the divergence theorem is used This relates surface fluxes to the divergence within the volume, *e.g.* for a variable A,

$$\oint_S \boldsymbol{A}\cdot d\mathbf{S} = \int_V \boldsymbol{\nabla}\cdot\boldsymbol{A} dV. \tag{2.39}$$

which in the limit of an infinitesimal control volume (Borisenko & Tarapov, 1979) defines the differential form,

$$\boldsymbol{\nabla}\cdot\boldsymbol{A} = \lim_{V\to 0}\frac{1}{V}\oint_S \boldsymbol{A}\cdot d\mathbf{S}. \tag{2.40}$$

Therefore, taking the zero volume limit of the conservation of mass through a control volume, Eq. (2.35), results in the differential continuity equation,

$$\frac{\partial\rho}{\partial t} + \nabla_\beta(\rho u_\beta) = 0. \tag{2.41}$$

Index notation has been used with the Einstein summation convention. Subscript and bold notations are used interchangeably to describe tensors throughout this work.

The differential momentum balance equation is obtained from the zero volume limits of the CV momentum balance equation Eq. (2.36),

$$\frac{\partial\rho u_\alpha}{\partial t} + \nabla_\beta\left[\rho u_\alpha u_\beta - \Pi_{\alpha\beta}\right] + F_{\alpha ext} = 0. \tag{2.42}$$

with surface forces, $\mathbf{F}_{\text{surface}}$, expressed in terms of pressure using Eq. (2.37). Effects due to external forces $F_{\alpha ext}$ (body forces, $\mathbf{F}_{\text{body}}$, at a point) are usually not considered and will be neglected in the following treatment. Finally for energy ($\mathcal{E}$) conservation at a point is derived from Eq. (2.38) as,

$$\frac{\partial}{\partial t}\rho\mathcal{E} = -\nabla_\beta\left[\rho\mathcal{E}u_\beta + \Pi_{\alpha\beta}u_\alpha + Q_\beta\right], \tag{2.43}$$

The pressure tensor, $\Pi_{\alpha\beta}$, can be further subdivided into the equilibrium pressure from kinetic theory, P, and solid mechanics concept of stress $\sigma_{\alpha\beta}$ acting on the control volume,

$$\Pi_{\alpha\beta} = -P\delta_{\alpha\beta} + \sigma_{\alpha\beta}, \tag{2.44}$$

where $\delta_{\alpha\beta}$ is the Kronecker delta. The decomposition is arbitrary and it is only the total stress

tensor $\Pi_{\alpha\beta}$ that has any physical meaning, as it satisfies the definition of an infinitesimal force acting on an infinitesimal area (Evans & Morriss, 2007). The term, $\sigma_{\alpha\beta}$, is the Cauchy stress widely measured in solid mechanics. The pressure term, P, does not typically appear in the solid mechanics formulation as the solid is assumed to be initially undeformed (gauge of zero). In a fluid, P can vary throughout the domain. The convective term is unique to liquids as it describes transport resulting from the actual movement of fluid through the control volume.

The stress tensor can be expanded as a power series in strain rate. Generally it is assumed to be a linear function of strain rate (not assuming this for gases will lead to the Burnett or super Burnett equations depending on the order of the relationship). A fourth order tensor is the simplest linear relation between stress and strain (i.e. a relation linking each of the 9 stress components linearly to each of the 9 strain components needs 81 components).

$$\sigma_{\alpha\beta} = C_{\alpha\beta\gamma\zeta}\varepsilon_{\gamma\zeta}. \tag{2.45}$$

The assumed symmetry of the stress and strain tensors ($C_{\alpha\beta\gamma\zeta} = C_{\beta\alpha\gamma\zeta}$ and $C_{\alpha\beta\gamma\zeta} = C_{\alpha\beta\zeta\gamma}$) along with the requirement that work done by deformation be zero ($C_{\alpha\beta\gamma\zeta} = C_{\gamma\zeta\alpha\beta}$) allows the 81 components to be reduced. The following relationship results between just second order tensors with only two unknown coefficients, λ and μ,

$$C_{\alpha\beta\gamma\zeta} = \lambda\delta_{\alpha\beta}\delta_{\gamma\zeta} + \mu(\delta_{\beta\gamma}\delta_{\alpha\zeta} + \delta_{\alpha\gamma}\delta_{\beta\zeta}), \tag{2.46}$$

The fluid is assumed to be physically and structurally isotropic meaning it can only deform by shear and bulk deformation. The equation linking stress and strain takes the form,

$$\sigma_{\alpha\beta} = \lambda\delta_{\alpha\beta}\varepsilon_{\gamma\gamma} + \mu(\varepsilon_{\gamma\zeta} + \varepsilon_{\zeta\gamma}). \tag{2.47}$$

Using the definition of small strains for $\varepsilon_{\alpha\beta} = \nabla_\beta u_\alpha + \nabla_\alpha u_\beta$, the equation for $\Pi_{\alpha\beta}$ can be written (in vector notation) as,

$$\boldsymbol{\Pi} = P\boldsymbol{\delta} - \mu(\boldsymbol{\nabla u} + (\boldsymbol{\nabla u})^T - \boldsymbol{\nabla}\cdot\boldsymbol{u\delta}) - \lambda\boldsymbol{\nabla}\cdot\boldsymbol{u\delta}. \tag{2.48}$$

The Stokes hypothesis relates the two co-efficients μ and λ which is exactly true for a monatomic gas but a good approximation for most gases. The coefficient μ is often called the shear viscosity coefficient and is the same form as the one in Newton's law of viscosity. The bulk viscosity coefficient is $(\lambda - \frac{2}{3}\mu\ )$ (Hoover, 1991), although some textbooks incorrectly describe λ itself as the bulk viscosity. It is the bulk or compressional viscosity which is zero under Stokes' hypothesis, i.e. $\lambda = \frac{2}{3}\mu$. A bulk viscosity of zero is an approximation not correct for fluids with internal structures (Gad-el Hak, 1995). Molecular dynamics explicitly incorporates the effect of finite bulk viscosity.

Using the assumption of incompressibility, the continuity Eq. (2.41) reduces to $\boldsymbol{\nabla}\cdot\boldsymbol{u} = 0$ and Eq. (2.42) can be simplified to

$$\frac{\partial \boldsymbol{u}}{\partial t} + (\boldsymbol{u}\cdot\boldsymbol{\nabla})\,\boldsymbol{u} = -\frac{1}{\rho}\boldsymbol{\nabla}P + \nu\nabla^2\boldsymbol{u}, \tag{2.49}$$

where $\boldsymbol{u}(\boldsymbol{x},t)$ is the fluid velocity and $P(\boldsymbol{x},t)$ pressure, at each spatial position $\boldsymbol{x}$ and time t. The fluid is assumed to have a uniform density ρ and viscosity $\nu = \rho/\mu$. Non-dimensionalising using

a length scale L, a characteristic velocity U and time of U/L with the definition of the Reynolds number $Re = UL/\nu$, Eq. (2.49) becomes,

$$\frac{\partial \boldsymbol{u}}{\partial t} + (\boldsymbol{u} \cdot \boldsymbol{\nabla})\, \boldsymbol{u} = -\boldsymbol{\nabla} P + \frac{1}{Re} \nabla^2 \boldsymbol{u}, \tag{2.50}$$

where the variables shown are non-dimensional for the continuum scale. The method for solving this equation on a computer is outlined in chapter 3.

2.4 Towards a Consistent Mathematical Framework

This section outlines the mathematical relationship between the discrete framework of molecular dynamics and the equations of continuum mechanics. First the difference in reference frame used in the Eulerian fluid mechanics and the many Lagrangian molecules is discussed. The link between these is provided by the seminal work of Irving & Kirkwood (1950) through the Dirac delta functional. Using the Dirac delta, a number of localised 'state' properties are defined including density, momentum, temperature and energy. The time derivatives of these state properties can be used to obtain the fluxes (again following Irving & Kirkwood (1950)). The fluxes include advection of momentum (convection) and the notion of the stress tensor in a molecular system. A consistent stress definition is essential to flux coupling schemes, however, the exact definition of the molecular stress is a controversial area. The various issues associated with the molecular stress tensor are discussed in this section. This section directly motivate chapter 4.

2.4.1 Lagrangian and Eulerian frameworks

Both the continuum and molecular systems are classical systems, entirely governed by Newton's law. It should therefore be possible to express the time evolution of both in an equivalent manner. This is achieved in this subsection, by considering an arbitrary and equivalent Lagrangian element in both systems. The link to the Eulerian formulation for both systems is then discussed.

Newton formulated his law based on the evolution of discrete objects, subject to impressed forces [1]. The equation resulting from Newton's second law,

$$m \frac{d^2 \boldsymbol{r}}{dt^2} = \boldsymbol{F},$$

relates a particle's mass m and second temporal derivative of its position $\boldsymbol{r}$ to the forces it experiences, $\boldsymbol{F}$. The application of Newton's law to a continuous substance requires the division of that substance into arbitrary interacting regions. These "discrete elements" are often called particles, although to avoid confusion, this term is here reserved for discrete molecules and the term element is used instead.

A Lagrangian continuum element is defined to be an arbitrary and fixed quantity of continuous media with a time evolving volume $V = V(t)$ contained inside a bounding surface S. The temporal evolution of this volume and the momentum inside is governed by the forces acting over

[1] "*An impressed force is an action exerted upon a body, in order to change its state, either of rest, or of moving uniformly forward in a right line.*" Newton (1726) from definition IV, page 3 in the translation by Motte (1729).

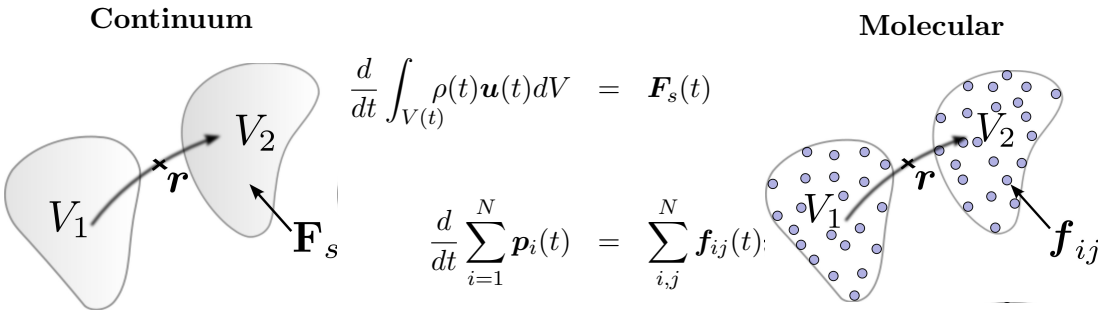

Figure 2.1: An equivalent Lagrangian element for the continuum and discrete system with corresponding forms of Newton's law. An arbitrary fixed point $\boldsymbol{r}$ on the path of evolution represents an infinitesimal Eulerian frame. The equations of motion in the Eulerian frame are given by expressing the flow through this infinitesimal control volume in the continuum or application of the Dirac delta function in the discrete system.

its bounding surface $\boldsymbol{F}_s$. Figure 2.1 shows this continuum element and the form of Newton's law which governs its evolution.

In order to link the two, a similar element can be defined in the molecular system, containing a fixed number of molecules N (*c.f.* the fixed quantity of continuous media) and surrounded by a bounding surface S. The volume $V = V(t)$ of this molecular element is given by the shape enclosing the positions of all N molecules and its evolution is governed by the sum of all intermolecular forces acting over the surface $\boldsymbol{f}_{ij}$. Note by following an 'element' of molecules, the sum over all i and j is the surface forces, as internal interactions between molecules inside the element cancel (Newton's 3rd law).

These two element in both system are equivalent; both advancing due to Newton's law, following a fixed collection of substance and evolving as a result of external forces due to interactions with substance outside the element. In this form, the equations represent the Lagrangian formulation of mechanics (see Figure 2.1), in which the evolution of a fixed quantity of substance is followed through time. However, fluid mechanics is almost always written in the Eulerian reference frame, which considers the flow past a fixed point in space. For this reason, the coupling strategies employed in the solid mechanics literature (Curtin & Miller, 2003) are generally not applicable to fluid system. The continuum can be written in an Eulerian frame using Reynolds Transport Theorem (Reynolds, 1903)

$$\frac{d}{dt}\int_V \rho\boldsymbol{u}dV = \int_V \frac{\partial\left(\rho\boldsymbol{u}\right)}{\partial t}dV + \oint_S \left(\rho\boldsymbol{u}\boldsymbol{u}\right)\cdot d\mathbf{S}.$$

The use of the Dirac delta function provides a way to write the molecular systems in an Eulerian framework. This is due to the property of the Dirac delta that,

$$h(\boldsymbol{r}) = \int_{-\infty}^{\infty} \delta(\boldsymbol{r}_i - \boldsymbol{r})h(\boldsymbol{r}_i)d\boldsymbol{r}_i, \tag{2.52}$$

here, $\boldsymbol{r}$ is a location in space (of the Eulerian reference) and $\boldsymbol{r}_i$ the location of molecule i. Consider the point $\boldsymbol{r}$ in Figure 2.1, which includes molecules only as they pass through point $\boldsymbol{r}$. As the Dirac delta is defined only at a infinitesimal position in space, the molecular system is effectively considered only at the location $\boldsymbol{r}$. Regardless of the shape or size of the element,

the Dirac delta only considers the properties as they move past $\boldsymbol{r}$. The analysis of Irving & Kirkwood (1950) provides the link between the ensemble averaged microscopic variables and the macroscopic density, momentum and energy at a fixed Eulerian point in space as discussed in the next subsection. The reader is referred to Irving & Kirkwood (1950) for a full justification of the Dirac delta function as a link between macroscopic and mesoscopic descriptions.

2.4.2 State Variable, Density Velocity and Temperature

In this subsection, an equivalent definition for state properties (density, momentum, energy and temperature) is obtained for a fixed Eulerian point in space in both the molecular and continuum system. Recall from section 2.2.3, that the expectation value of any variable $\alpha = \alpha(\boldsymbol{r}_1, ..., \boldsymbol{r}_N, \boldsymbol{p}_1, ..., \boldsymbol{p}_N, t)$ is given by the inner product with the probability density function,

$$\left\langle \alpha; f \right\rangle = \int \cdots \int_{6N} \alpha f(\boldsymbol{r}_1, ..., \boldsymbol{r}_N, \boldsymbol{p}_1, ..., \boldsymbol{p}_N, t) d\boldsymbol{r}_1 d\boldsymbol{p}_1 ... d\boldsymbol{r}_N d\boldsymbol{p}_N.$$

By letting α be the Dirac delta function, Irving & Kirkwood (1950) provided the link between the Lagrangian and Eulerian descriptions. The macroscopic density definition follows from $\alpha = \sum_{i=1}^{N} m_i \delta(\boldsymbol{r}_i - \boldsymbol{r})$, giving,

$$\rho(\boldsymbol{r}, t) \equiv \left\langle \sum_{i=1}^{N} m_i \delta(\boldsymbol{r}_i - \boldsymbol{r}); f \right\rangle. \tag{2.53}$$

This returns the possible configurations of the system in phase space which satisfy the criterion that a molecule is located at a point $\boldsymbol{r}$. This is the definition of average density of mass located at $\boldsymbol{r}$ for an ensemble of molecular systems. The momentum density at a point in space is similarly defined by,

$$\rho(\boldsymbol{r}, t)\boldsymbol{u}(\boldsymbol{r}, t) \equiv \sum_{i=1}^{N} \left\langle \boldsymbol{p}_i \delta(\boldsymbol{r}_i - \boldsymbol{r}); f \right\rangle, \tag{2.54}$$

where the momentum of molecule i is $\boldsymbol{p}_i = m_i \dot{\boldsymbol{r}}_i$. Note that $\boldsymbol{p}_i$ is the momentum in the laboratory frame, and not the peculiar value $\overline{\boldsymbol{p}}_i$, which excludes the macroscopic streaming term at the location of molecule i, $\boldsymbol{u}(\boldsymbol{r}_i)$, (Evans & Morriss, 2007). The laboratory frame and peculiar momentum are related through,

$$\overline{\boldsymbol{p}}_i \equiv m_i \left(\frac{\boldsymbol{p}_i}{m_i} - \boldsymbol{u}(\boldsymbol{r}_i) \right). \tag{2.55}$$

The energy density at a point in space is defined by

$$\rho(\boldsymbol{r}, t)\mathcal{E}(\boldsymbol{r}, t) \equiv \sum_{i=1}^{N} \left\langle e_i \delta(\boldsymbol{r}_i - \boldsymbol{r}); f \right\rangle, \tag{2.56}$$

where the energy of the i^{th} molecule is defined as the sum of the kinetic energy and the intermolecular interaction potential ϕ_{ij},

$$e_i \equiv \frac{p_i^2}{2m_i} + \frac{1}{2}\sum_{j\neq i}^{N}\phi_{ij}.$$

It is implicit in this definition that the potential energy of an interatomic interaction, ϕ_{ij}, is arbitrarily divided equally between the two interacting molecules, i and j. The factor of $1/2$ in the last term of the above equation is therefore included to avoid double counting. Related to the energy is the definition of temperature, which can be defined at a point in terms of the peculiar momentum,

$$T(\boldsymbol{r},t) = \frac{1}{3k_B(N-1)}\sum_{i=1}^{N}\left\langle \frac{\overline{p}_i^2}{m_i}\delta(\boldsymbol{r}_i-\boldsymbol{r});f\right\rangle. \tag{2.57}$$

The time evolution of these state properties provides the fluxes in the next section.

2.4.3 Momentum Fluxes and the Pressure Tensor

The fluxes are obtained by evaluating the time evolution of state properties using the Irving & Kirkwood (1950) time evolution equation (2.33). This section states only the main results of this process as a full treatment is deferred to chapter 4, where control volume forms of these equations are derived in an similar manner. The link to the equations in this section will be obtained in the limiting case of zero volume (see appendix C.2). The reader is also referred to the original work of Irving & Kirkwood (1950) for the full derivation of the equations presented in this section.

The time evolution of mass is obtained by taking the time derivative of both sides of Eq. (2.53) and applying Eq. (2.33),

$$\frac{\partial}{\partial t}\rho(\boldsymbol{r},t) = \frac{\partial}{\partial t}\sum_{i=1}^{N}\left\langle m_i\delta(\boldsymbol{r}_i-\boldsymbol{r});f\right\rangle = -\frac{\partial}{\partial \boldsymbol{r}}\cdot\sum_{i=1}^{N}\left\langle \boldsymbol{p}_i\delta(\boldsymbol{r}_i-\boldsymbol{r});f\right\rangle = -\frac{\partial}{\partial \boldsymbol{r}}\cdot\rho(\boldsymbol{r},t)\boldsymbol{u}(\boldsymbol{r},t), \tag{2.58}$$

which results in the divergence of momentum given in Eq. (2.54). This circumvents the process of defining the momentum in Eq. (2.54) and also results in a form of momentum which is not unique (the gauge can be set by adding an arbitrary constant).

The time evolution of momentum is obtained by taking the time derivative of both sides of Eq. (2.54) and applying Eq. (2.33),

$$\frac{\partial}{\partial t}\rho(\boldsymbol{r},t)\boldsymbol{u}(\boldsymbol{r},t) = \frac{\partial}{\partial t}\sum_{i=1}^{N}\left\langle \boldsymbol{p}_i\delta(\boldsymbol{r}_i-\boldsymbol{r});f\right\rangle = \frac{\partial}{\partial \boldsymbol{r}}\cdot\rho(\boldsymbol{r},t)\boldsymbol{u}(\boldsymbol{r},t)\boldsymbol{u}(\boldsymbol{r},t) + \frac{\partial}{\partial \boldsymbol{r}}\cdot\boldsymbol{\Pi}(\boldsymbol{r},t),$$

which results in the molecular flux and stress at a point in space. The resulting stress tensor, known as the IK stress tensor, is of the form,

$$\boldsymbol{\Pi} = \sum_{i=1}^{N}\left\langle m_i\left(\frac{\boldsymbol{p}_i}{m_i}-\boldsymbol{u}\right)\left(\frac{\boldsymbol{p}_i}{m_i}-\boldsymbol{u}\right)\delta(\boldsymbol{r}_i-\boldsymbol{r}) + \frac{1}{2}\sum_{j\neq i}^{N}\boldsymbol{f}_{ij}\boldsymbol{r}_{ij}O_{ij}\delta(\boldsymbol{r}_i-\boldsymbol{r});f\right\rangle. \tag{2.59}$$

The O_{ij} term is the Irving & Kirkwood (1950) operator resulting from a Taylor expansion of two Dirac delta functionals, *i.e.*

$$\delta(\boldsymbol{r}_i - \mathbf{r}) - \delta(\boldsymbol{r}_j - \boldsymbol{r}) = -\boldsymbol{r}_{ij} \cdot \frac{\partial}{\partial \boldsymbol{r}} O_{ij} \delta(\boldsymbol{r}_i - \boldsymbol{r}),$$

where the so-called IK operator is,

$$O_{ij} = \left(1 - \frac{1}{2}\boldsymbol{r}_{ij} \cdot \frac{\partial}{\partial \boldsymbol{r}_i} + \ldots + \frac{1}{n!}(-\boldsymbol{r}_{ij} \cdot \frac{\partial}{\partial \boldsymbol{r}_i})^{n-1} + \ldots\right). \tag{2.60}$$

It is instructive to compare the continuum momentum equations Eq. (2.42) (with $\boldsymbol{\Pi} = P\boldsymbol{I} - \sigma$) and the mesoscopic Eq. (2.59) obtained by Irving & Kirkwood (1950),

$$\begin{aligned} \frac{\partial}{\partial t}\rho\boldsymbol{u} + \boldsymbol{\nabla}\cdot\rho\boldsymbol{u}\boldsymbol{u} &= \boldsymbol{\nabla}\cdot \quad [\ P\boldsymbol{I} \quad - \quad \sigma \quad] \\ \sum_{i=1}^{N}\left\langle \frac{\partial}{\partial t}\boldsymbol{p}_i\delta(\boldsymbol{r}_i - \boldsymbol{r}); f\right\rangle + \boldsymbol{\nabla}\cdot\rho\boldsymbol{u}\boldsymbol{u} &= \boldsymbol{\nabla}\cdot\sum_{i=1}^{N}\left\langle \frac{\overline{\boldsymbol{p}}_i\overline{\boldsymbol{p}}_i}{m_i}\delta(\boldsymbol{r}_i - \boldsymbol{r}) + \frac{1}{2}\sum_{j\neq i}^{N}\boldsymbol{f}_{ij}\boldsymbol{r}_{ij}O_{ij}\delta(\boldsymbol{r}_i - \boldsymbol{r}); f\right\rangle. \end{aligned}$$

It is clear from this comparison that time evolution of momentum is equal to the divergence of kinetic pressure P, Cauchy stress $\boldsymbol{\sigma}$ and fluid convection $\rho\boldsymbol{u}\boldsymbol{u}$. The IK pressure of Eq. (2.59) is a formally exact definition valid at a point in space. It can be simplified to yield the kinetic theory (ideal gas) pressure as well as the virial pressure (Parker, 1954).

The kinetic pressure is obtained by assuming a homogeneous dilute gas (with $\phi_{ij}(r) = 0$) in a closed volume V (Chapman & Cowling, 1970); Eq. (2.59) simplifies to,

$$\overset{KT}{\boldsymbol{\Pi}} = \frac{1}{V}\sum_{i=1}^{N}\left\langle \frac{\boldsymbol{p}_i\boldsymbol{p}_i}{m_i}; f\right\rangle, \tag{2.61}$$

which is the ideal gas kinetic theory definition of the pressure tensor. Note that a single value is taken for the whole system and there is no local $\boldsymbol{u}$ ($\overline{\boldsymbol{p}}_i = \boldsymbol{p}_i$). With no internal interactions, the pressure tensor is entirely due to the 'stress like' movement of momentum by microscopic fluctuations. This also appears to be consistent with the common definition of P in the continuum literature (Potter & Wiggert, 2002).

The virial pressure is obtained from Eq. (2.59) in a closed volume V and taking only the first term in the IK operator of Eq. (2.60), known as the IK1 approximation, so that $\delta(\boldsymbol{r}_i - \boldsymbol{r}) = 1$ and $O_{ij}\delta(\boldsymbol{r}_i - \boldsymbol{r}) = 1$. The result is the well-known tensorial form of the virial pressure (Parker, 1954),

$$\overset{VIRIAL}{\boldsymbol{\Pi}} = \frac{1}{V}\sum_{i=1}^{N}\left\langle \frac{\boldsymbol{p}_i\boldsymbol{p}_i}{m_i} + \frac{1}{2}\sum_{i\neq j}^{N}\boldsymbol{f}_{ij}\boldsymbol{r}_{ij}; f\right\rangle.$$

The virial form of pressure is the most widely used in the molecular dynamics literature due to its simplicity. However, the virial can only be used to provide a single pressure tensor for an entire isolated system. Using the virial pressure locally is incorrect, as interactions with the surrounding fluid are not included (Tsai, 1978). This is a consequence of neglecting terms of higher order in Eq. (2.60). As a result, the effects of local inhomogeneity in the fluid are lost. Away from equilibrium a localised description is required and the full Eq. (2.60) expression must

be retained.

The IK form of pressure in Eq. (2.60) is formally exact and equal to the pointwise continuum description. The Dirac delta function is defined in the infinitely thin, infinitely large limit which is exactly the same limit in which the continuum infinitesimal is defined, as demonstrated formally in chapter 4 and appendix C.2. However, despite this equivalence, the IK pressure has a number of inherent problems, including:

a) The use of a Dirac delta functional in practice (Hardy, 1982).

b) The Taylor expansion in delta functions of Eq. (2.60), (Evans & Morriss, 2007).

c) The uncertainty in the inclusion of kinetic terms in the molecular stress (Zhou, 2003).

These issues stem from the non-uniqueness of the Irving & Kirkwood (1950) (and other molecular) symmetrical stress tensors, as discussed by Schofield & Henderson (1982). These problems have been addressed in a number of ways:

a) The Dirac delta functions have been avoided by integrating over the molecule i in phase space as in Noll (1955), replacing the delta function by defining a non-infinite function with a finite width and compact support as in Hardy (1982) and Murdoch (2007, 2010) or treating the functions in Fourier space as in Lutsko (1988) and Evans & Morriss (2007) to yield more mathematically amenable forms. These weighting function approaches have been reviewed and expressed in a unified form in the paper by Admal & Tadmor (2010). The Dirac delta functions can also be evaluated using an expansion in terms of their roots in time as done first by Todd *et al.* (1995) and extended in Daivis *et al.* (1996).

b) The Taylor expansion of the delta functions has been weakened by reformulating the stress as the integral between two molecules and integrating over a volume in Lutsko (1988) and Cormier *et al.* (2001). This leads to the so-called Volume Average (VA) stress formulation which includes the fraction of the length of the pair interaction included in a given volume in space. This has the advantage that it is equivalent to the virial when averaged over the full system,

$$\overset{VA}{\mathbf{\Pi}} = \frac{1}{\Delta V}\sum_{i=1}^{N}\left\langle \frac{\boldsymbol{p}_i\boldsymbol{p}_i}{m_i}\Lambda_i + \frac{1}{2}\sum_{i,j}^{N}\boldsymbol{f}_{ij}\boldsymbol{r}_{ij}l_{ij}\right\rangle, \tag{2.62}$$

where ΔV is the local volume; the Λ_i functions is only non-zero for a molecule inside the volume and the l_{ij} includes the fraction of the interaction inside the averaging volume. Another approach which avoids the expansion in Dirac delta functionals is to consider the interaction over a plane; introduced empirically by Tsai (1978) and derived formally from the Irving & Kirkwood (1950) form using Fourier manipulation by Todd *et al.* (1995), the Method Of Planes (MOP) treatment gives three components of the stress tensor acting across a plane. The MOP form has a number of advantages including the ability to deal with inhomogeneous stress fields (Tsai, 1978),(Todd *et al.*, 1995). The stress for a plane whose normal is aligned along the x axis,

$$\overset{MOP}{\mathbf{\Pi}}\ \Delta A_x = \sum_{i=1}^{N}\left\langle \frac{\boldsymbol{p}_i p_{ix}}{m_i}\delta(x_i - x) + \frac{1}{4}\sum_{i,j}^{N}\boldsymbol{f}_{ij}\left[sgn(x - x_j) - sgn(x - x_i)\right]\right\rangle.$$

where $sgn(x)$ is the signum function of x, where $sgn(x) = 1$, if $x > 1$ and $sgn(x) = -1$, if $x < 0$. The original MOP formulation only provides three stress components, Π_{xx}, Π_{xy} and Π_{xz}.

As the plane is infinite in y and z, this returns only a single stress vector at each x location. Han & Lee (2004) used three mutually perpendicular planes converging at a point to obtain all nine components of stress and limited the planes to a local region of interest. In a recent paper, Heyes *et al.* (2011), the MOP and VA were shown to be equivalent in the limit of zero volume of a thin slice parallel to the plane. The derivation in this paper was carried out as part of this work. As the pressure tensor is central to the link between the continuum and the discrete representation, this is an important result for coupling. However, further discussion of this point will be deferred to chapter 4 where a more general framework for coupling will be introduced. In the coupling literature it is generally the virial pressure which is used, although exceptions include the paper by Ren (2007) who uses the IK form of pressure but localised to a volume (i.e. the VA of Eq. (2.62)).

c) The inclusion of kinetic terms is largely an unresolved problem, with Zhou (2003) arguing the stress should include only force terms. This controversy is, in part, due to the differing definitions of pressure/stress tensor in the solid mechanics, thermodynamics and fluid mechanics literature (note pressure is simply negative stress). In the solid mechanics literature, the Cauchy stress tensor is defined in terms of forces at zero temperature ($i.e.$ no kinetic part). Often the temperature dependence is included using an extra term in the continuum. Consistent behaviour is demonstrated in the molecular system by Subramaniyan & Sun (2007) in a thermo-elastic study demonstrating the importance of temperature on stress. From a thermodynamics perspective, kinetic pressure is due to a dilute gas atom colliding with the walls of a container (or measured as they cross a hypothetical wall, see section 4.2). Fluid mechanics includes both the kinetic pressure and the Cauchy type stress together with a convection term. The problem of separating the pressure as in the continuum, Eq. (2.44), is one of definition. There are two mechanisms for transmitting momentum – forces and movement of molecules. The use of time averaged molecular simulations means convection can be zero but fluctuations serve to transmit a change of momentum – this acts like a force. This issue is discussed more fully in section 4.2.

In summary, the IK form of pressure in Eq. (2.60) is formally exact and equal to the pointwise continuum description. However, in practice the Dirac delta function cannot be implemented in a molecular system as no molecule will ever be exactly at point $\boldsymbol{r}$. Therefore, some relaxation of the Dirac delta is required and a number of possibilities from the literature have been discussed. This problem is more acute for the purpose of coupling, as both systems effectively exist at the same scales. Therefore, a spatial coarse grain of the MD to obtain continuum properties may not be possible. It is the solution of this problem that motivates the formulation of both systems in an equivalent manner, the control volume formulation, in chapter 4.

2.4.4 Energy Equations

The final type of flux expression is for energy, which includes the definition of the stress tensor. The molecular equivalents of various terms from the energy evolution, Eq. (2.64), can be defined

as follows,

$$\rho\mathcal{E}\boldsymbol{u} = \sum_{i=1}^{N}\left\langle e_i\boldsymbol{u}\,\delta\left(\boldsymbol{r}-\boldsymbol{r}_i\right);f\right\rangle, \tag{2.63a}$$

$$\boldsymbol{\Pi}\cdot\boldsymbol{u} = \sum_{i=1}^{N}\left\langle\left[\frac{\overline{\boldsymbol{p}}_i\,\overline{\boldsymbol{p}}_i}{m_i}-\frac{1}{2}\sum_{j\neq i}^{N}\boldsymbol{f}_{ij}\boldsymbol{r}_{ij}O_{ij}\right]\cdot\boldsymbol{u}\,\delta\left(\boldsymbol{r}-\boldsymbol{r}_i\right);f\right\rangle, \tag{2.63b}$$

$$\boldsymbol{Q} = \sum_{i=1}^{N}\left\langle\overline{e}_i\frac{\overline{\boldsymbol{p}}_i}{m_i}\delta\left(\boldsymbol{r}-\boldsymbol{r}_i\right)-\frac{1}{2}\sum_{j\neq i}^{N}\frac{\overline{\boldsymbol{p}}_i}{m_i}\cdot\boldsymbol{f}_{ij}\boldsymbol{r}_{ij}O_{ij}\delta\left(\boldsymbol{r}-\boldsymbol{r}_i\right);f\right\rangle,$$

where the peculiar momentum and energy are defined by,

$$\frac{\overline{\boldsymbol{p}}_i}{m_i}\equiv\left(\frac{\boldsymbol{p}_i}{m_i}-\boldsymbol{u}\right);\quad e_i\equiv\frac{p_i^2}{2m_i}+\frac{1}{2}\sum_{j\neq i}^{N}\phi_{ij}\quad\text{and}\quad\overline{e}_i\equiv\frac{\overline{p}_i^2}{2m_i}+\frac{1}{2}\sum_{j\neq i}^{N}\phi_{ij}.$$

The energy equation at a point in space is therefore,

$$\begin{aligned}\frac{\partial}{\partial t}\rho\mathcal{E}=-\boldsymbol{\nabla}\cdot\sum_{i=1}^{N}\Bigg\langle & e_i\boldsymbol{u}\,\delta\left(\boldsymbol{r}-\boldsymbol{r}_i\right)+\left[\frac{\overline{\boldsymbol{p}}_i\,\overline{\boldsymbol{p}}_i}{m_i}-\frac{1}{2}\sum_{j\neq i}^{N}\boldsymbol{f}_{ij}\boldsymbol{r}_{ij}O_{ij}\right]\cdot\boldsymbol{u}\,\delta\left(\boldsymbol{r}-\boldsymbol{r}_i\right)\\ & +\overline{e}_i\frac{\overline{\boldsymbol{p}}_i}{m_i}\delta\left(\boldsymbol{r}-\boldsymbol{r}_i\right)-\frac{1}{2}\sum_{j\neq i}^{N}\frac{\overline{\boldsymbol{p}}_i}{m_i}\cdot\boldsymbol{f}_{ij}\boldsymbol{r}_{ij}O_{ij}\delta\left(\boldsymbol{r}-\boldsymbol{r}_i\right);f\Bigg\rangle\Bigg),\end{aligned} \tag{2.64}$$

It is possible to take the IK1 form of the energy, with $O_{ij}\delta(\boldsymbol{r}-\boldsymbol{r}_i)=1$ from Eq. (2.60) and averaging over the Dirac delta function,

$$\rho\mathcal{E}\boldsymbol{u} = \sum_{i=1}^{N}\left\langle e_i\boldsymbol{u}\right\rangle, \tag{2.65a}$$

$$\boldsymbol{\Pi}\cdot\boldsymbol{u} = \sum_{i=1}^{N}\left\langle\left(\frac{\overline{\boldsymbol{p}}_i\,\overline{\boldsymbol{p}}_i}{m_i}-\frac{1}{2}\sum_{j\neq i}^{N}\boldsymbol{f}_{ij}\boldsymbol{r}_{ij}\right)\cdot\boldsymbol{u}\right\rangle, \tag{2.65b}$$

$$\boldsymbol{Q} = \sum_{i=1}^{N}\left\langle\overline{e}_i\frac{\overline{\boldsymbol{p}}_i}{m_i}-\frac{1}{2}\sum_{j\neq i}^{N}\frac{\overline{\boldsymbol{p}}_i}{m_i}\cdot\boldsymbol{f}_{ij}\boldsymbol{r}_{ij}\right\rangle, \tag{2.65c}$$

this is the most commonly used form of energy equation in the coupling literature due to it simplicity. Many of the issues associated with the definition of the stress tensor also apply to the energy equations and the heat flux $\boldsymbol{Q}$.

The equations presented in this section provide a direct mathematical link between state properties: mass, momentum, temperature and energy in the continuum and molecular system. The linking of the flux properties, *i.e.* convection, energy advection, pressures and heat flux have also been discussed. In the next section, the mathematical links between both descriptions form the basis of the computational implementation in the modern field of coupling. However, there are a number of problems associated with the definition of stress in the molecular system which must be resolved before flux coupling is possible using the definitions presented in this chapter. The solution of some of these problems will be presented in Chapter 4, where the control volume formulation is applied to a molecular system.

2.5 Coupling

This section describes the modern literature on continuum-to-molecular coupling, giving an outline of the state-of-the-art coupling methodologies and the shortcomings of these approaches.

This section starts with an outline of the main considerations for coupling in subsection 2.5.1. There are two branches in the coupling literature, state coupling and flux coupling. State coupling is discussed first in subsection 2.5.2, split into explicit and implicit coupling techniques. In this context, 'explicit' coupling means that equations in both the continuum and molecular domains are solved locally and directly with an exchange between them to evolve the coupled system. For 'implicit' coupling, the entire system is evolved globally solving the equations in both domains together, by iteration or matrix inversion. Variational principle algorithms subject to constraints are key to derive physically meaningful coupling schemes. Several state coupling schemes from the literature apply these methods and the derivations are outlined in detail in this section.

After state coupling, a description of the coupling of fluxes is provided in subsection 2.5.3 and the motivation, developments and associated problems are reviewed. By covering both types of coupled properties, this section will highlight the relative advantages and disadvantages of state coupling and coupling of fluxes. It will also highlight the shortcomings in the currently developed flux coupling, in particular the lack of formal derivation of a flux-coupled scheme from variational principles. This section directly motivate chapter 5.

2.5.1 Introduction to Coupling

The four key challenges which must be addressed by any coupling scheme are highlighted here.

1. **Determine the spatial relationship between the two regions.** The molecular system can be embedded in the continuum system or overlap in part and exist in a separate region. Embedding uses the molecular simulation as a local refinement of the continuum system while when using two separate systems, each covers a distinct spatial region and an overlap between the two regions allow gradual relaxation and agreement between the two different descriptions. The appropriate choice depends on the problem of interest and the assumptions inherent in each of the models.

2. **Termination of the MD domain.** A restraint mechanism is required at the boundary of the molecular region to prevent molecules escaping. This can be a generic force (O'Connell & Thompson (1995)/Nie *et al.* (2004*a*)) or one based on a previous simulation or calculated from the radial distribution function (Werder *et al.*, 2005). Alternatively, a buffer zone of molecules can be used (Hadjiconstantinou, 1998).

3. **Procedure for averaging the MD region to obtain the continuum boundary conditions.** This was discussed in the previous section 2.4, which in practice requires summing over time and space to establish averaged values in discrete locations (Allen & Tildesley, 1987) or averaging using least squares fitting to instantaneous data (Li *et al.*, 1997). The removal of statistical noise is a key issue, as is the choice of which properties are transferred (density and velocity or stresses and fluxes) as well as the averaging methods (Hadjiconstantinou *et al.*, 2003).

4. **Constraint applied to the molecular region to match properties to the continuum.** This can be performed by an applied force derived as a constraint using a variational principle formulation of mechanics (Goldstein *et al.*, 2002), a numerically favourable control style algorithm (Borg *et al.*, 2010), a selectively permeable membrane (Li *et al.*, 1997) or Maxwell's demon type approach (Hadjiconstantinou, 1998). A method of inserting and removing molecules is also required to match the mass flux from the continuum.

A typical coupled setup is show in Figure 2.2. The challenges above are addressed in this case by domain decomposition (1), an arbitrary boundary force (2), average momentum to provide the CFD boundary (3) and a constraint force applied at top of domain (4). In this section the full range of possibilities for coupling will be discussed along with the justification for focusing on the case shown in Figure 2.2 in subsequent chapters (3 and 5).

2.5.2 State Variable Coupling

The state variables, so called because they define the current state of a system are density, velocity, pressure and temperature defined in section 2.4.2. For an isothermal continuum, the stress which governs the systems temporal evolution,

$$\frac{\partial \rho \boldsymbol{u}}{\partial t} + \boldsymbol{\nabla} \cdot \rho \boldsymbol{u}\boldsymbol{u} = \boldsymbol{\nabla} \cdot \boldsymbol{\Pi} \tag{2.66}$$

can be approximated in terms of state variables,

$$\boldsymbol{\Pi} = P\boldsymbol{\delta} - \mu(\boldsymbol{\nabla}\boldsymbol{u} + (\boldsymbol{\nabla}\boldsymbol{u})^T - \boldsymbol{\nabla} \cdot \boldsymbol{u}\boldsymbol{\delta}) - \lambda \boldsymbol{\nabla} \cdot \boldsymbol{u}\boldsymbol{\delta}. \tag{2.67}$$

Consequently, knowledge of the density, velocity and scalar pressure P allows the stress to be determined from Eq. (2.66) and the evolution of the continuum system to be calculated from Eq. (2.67). Provided the viscosity is consistent, a coupling scheme should only need to ensure these state variables agree between the two systems to ensure the stresses agree. State coupling is a process which enforces one system's state, *i.e.* the density, velocity and pressure, on the other system to achieve this matching.

Explicit Coupling

O'Connell & Thompson (1995) is perhaps the first notable attempt to couple continuum fluid dynamics and molecular dynamics. The previous work on discrete/continuum coupling, discussed in O'Connell & Thompson (1995), had typically been used to model chemical reactions or obtain thermodynamic properties, by *embedding* a particle model in a continuum simulation. There have also been atomic-to-molecular coupling attempts in the solid mechanics literature dating back as far as the 1970s (Curtin & Miller, 2003). However, the work of O'Connell & Thompson (1995) attempts to address the problems unique to fluid mechanics in their implementation of coupling.

The method of O'Connell & Thompson (1995) was novel in that it was the first to use separate and distinct subdomain for both the continuum and molecular model, with an interface between them. This arrangement can be used to represent a large number of problems of both practical and engineering interest. An overlap region is introduced to allow the two descriptions to relax into each other, avoiding sharp changes at the boundary of the molecular region. The use of an

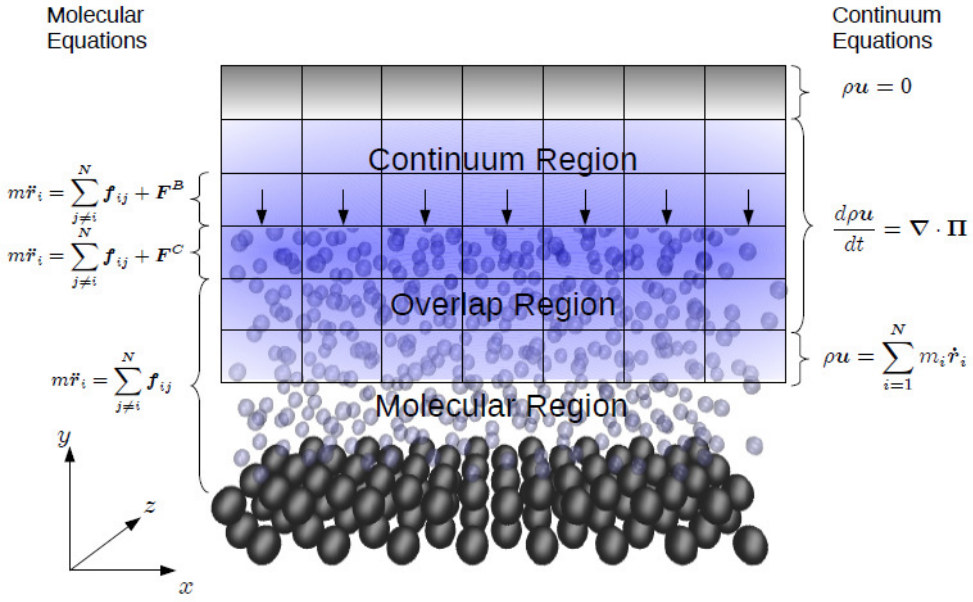

Figure 2.2: A schematic diagram illustrating the molecular and continuum regions with an overlap region. The MD has a constraint force ($\boldsymbol{F}^C$) and boundary force ($\boldsymbol{F}^B$). The CFD boundary conditions are obtained from the average of the MD velocity. This setup represents a large number of domain decomposition-based coupling schemes discussed in this section, *e.g.* O'Connell & Thompson (1995); Hadjiconstantinou (1999); Flekkøy *et al.* (2000); Nie *et al.* (2004*a*); Delgado-Buscalioni & Coveney (2003*a*).

overlap region is in fact well established in the solid coupling literature (the "transition region" (Curtin & Miller, 2003)). The interfacial region between the two solutions where the coupling is applied is often relatively small. The overlap is many times as large and extends beyond this into the continuum region to allow padding and averaging. This setup is shown in Figure 2.2.

Molecular to Continuum Exchange

For state coupling, the continuum boundary condition is determined from the average in a cell I. This reduces all the N_I degrees of freedom of the cells' molecules to a single (average) value. For example, the momentum $M_I \boldsymbol{u}_I$ is obtained from the momentum density defined in Eq. (2.54) of the previous section,

$$M_I \boldsymbol{u}_I = \frac{1}{N_I} \sum_{n=1}^{N_I} \left\langle m_n \dot{\boldsymbol{r}}_n ; f \right\rangle \approx \frac{1}{\Delta t_{CFD} N_I} \sum_{t=0}^{\Delta t_{CFD}} \sum_{n=1}^{N_I} m_n \dot{\boldsymbol{r}}_n, \tag{2.68}$$

where the Irving & Kirkwood (1950) statistical average notation is replaced by a time-averaged value. O'Connell & Thompson (1995) used Eq. (2.68) in order to obtain the boundary condition for the continuum. This kind of spatiotemporal averaging is common to most state coupling schemes in order to obtain state properties from the molecular system, *e.g.* Nie *et al.* (2004*a*); Hadjiconstantinou (1998); Werder *et al.* (2005); Yen *et al.* (2007); Sun *et al.* (2010); Wang & He (2007). In some cases, further averages over an ensemble of molecular systems are also taken (Nie *et al.*, 2004*a*). An alternative to Eq. (2.68) from the coupling literature is to use a technique such as least squares inference to generate a continuous function from the molecular region (Li *et al.*, 1997) (called the thermodynamic field estimator). The size and length of averaging affect

the noise introduced into the molecular system. The average is typically taken on the cell below the overlap region, corresponding to the cell used to set the CFD bottom boundary - see Figure 2.2.

Continuum to Molecular Exchange

For the continuum to molecular coupling, the momentum in the molecular region is adjusted to be the same as the continuum. This is done by applying a constraint force to the molecular equations of motion.

$$m_i \ddot{\boldsymbol{r}}_i = \sum_{j \neq i}^{N} \boldsymbol{f}_{ij} + \boldsymbol{F}^c,$$

where $\boldsymbol{F}^c$ is a constraint force which adjusts the molecule's average velocity to correspond with the velocity field in the continuum at the same region of space. The location at which the constraint is applied is typically at the top of the molecular domain, see Figure 2.2. A molecular system has a large number of degrees of freedom to be specified and the solution is non-unique. Ideally the constraint should be applied in a way which disturbs the dynamics as little as possible. This is implemented in the paper of O'Connell & Thompson (1995) by minimising the action (Hamilton's principle, Eq. (2.10)) subject to a constraint. The constraint is consistent with the continuum boundary condition and is of the form which minimises the difference in momentum between the two regions [2],

$$g_\alpha(\dot{r}_{\alpha n}) = M_I u_{\alpha I} - \sum_{n=1}^{N_I} m_n \dot{r}_{\alpha n} = 0. \tag{2.69}$$

The quantity M_I is the mass of a fluid region I, containing N_I molecules and $u_{\alpha I}$ $\alpha \in \{x, y, z\}$ is the component of velocity of the continuum element I. Note that the sum over N_I molecules is understood to limit the area of application of the force to only molecules located within a certain spatial region (i.e. a positional dependence to the constraint). This seemingly minor technicality motivates chapter 4 and is essential in chapter 5 where a rigorous treatment of local constraints leads to a number of important conclusions. For now, the constraint in this form is assumed to be integrable (semi-holonomic (Goldstein *et al.*, 2002)). By integrating the equation in time it can be written as a holonomic constraint,

$$f_\alpha = \int g_\alpha dt = M_I u_{\alpha I} t - \sum_{n=1}^{N_I} m_n r_{\alpha n} - \mathcal{D}_1 = 0,$$

where $\mathcal{D}_1$ is an arbitrary constant of integration Notice the continuum velocity is assumed to be constant in time. The derivation given in the thesis of O'Connell (1995) is reproduced here, starting from Eq. 2.21, the constrained Euler-Lagrangian equation for holonomic constraints ,

$$\frac{d}{dt}\frac{\partial \mathcal{L}}{\partial \dot{r}_i} - \frac{\partial \mathcal{L}}{\partial r_i} = \sum_{\alpha \in \{x,y,z\}} \lambda_\alpha \frac{\partial f_\alpha}{\partial r_{\alpha i}},$$

[2]The constraint applied in the thesis of O'Connell (1995) is $M_I u_{xI} t - \sum_{n=1}^{N_I} p_{xn} = 0$. In this work, the constraint is modified using the substitution $\boldsymbol{p}_i \to m_i \dot{\boldsymbol{r}}_i$. In order to be consistent with the use of $\boldsymbol{p}_i = m_i \dot{\boldsymbol{r}}_i$ in this chapter, the variable $\overline{\boldsymbol{p}}_i$ denotes the conjugate (or peculiar) momentum. The final form of the constraint Eq. 2.72a, is unchanged from the work of O'Connell (1995).

which yields the three components of Newton's law with added constraint,

$$m_i \ddot{r}_{\alpha i} = F_{\alpha i} + \lambda_\alpha m_i. \tag{2.70}$$

This must be solved with Eq. (2.69) in order to apply the correct constraint. To do this, Eq. 2.70 is integrated with respect to time,

$$m_i \dot{r}_{\alpha i} = \overline{p}_{\alpha i} + \lambda_\alpha m_i t + \mathcal{D}_2. \tag{2.71}$$

The α component of the momentum is denoted $\overline{p}_{\alpha n}$, where $\dot{\overline{p}}_{\alpha i} = F_{\alpha i}$ is used and $\mathcal{D}_2$ is an arbitrary constant of integration. This expression for $m_i \dot{r}_i$ is substituted into the non-holonomic form of constraint Eq. (2.69) to give,

$$\lambda_\alpha m_i t + \mathcal{D}_2 = \frac{1}{N_I}\left[M_I u_{\alpha I} - \sum_{n=1}^{N_I} \overline{p}_{\alpha n} \right],$$

which substituted into Eq. (2.71) yields the constraint equations of O'Connell (1995),

$$\dot{r}_{\alpha i} = \frac{\overline{p}_{\alpha i}}{m} + \xi \left[\frac{M_I}{m N_I} u_{\alpha I} - \frac{1}{N_I} \sum_{n=1}^{N_I} \frac{\overline{p}_{\alpha n}}{m} \right] \tag{2.72a}$$

$$\dot{\overline{p}}_{\alpha i} = -\frac{\partial \phi}{\partial r_{\alpha i}} = F_{\alpha i}, \tag{2.72b}$$

where ξ is an arbitrary relaxation parameter used to control the convergence rate to the required solution. The relaxation is added in by O'Connell & Thompson (1995) and not a result of the constraint derivation. The formula in Eq. (2.72a) can be interpreted as removing the mean velocity in a molecular region and replacing it with the target continuum value. A Langevin thermostat is applied to remove the heat added to the system by this constraint mechanism.

As the overlap consists of a number of regions, the force applied varies with location. This positional dependence is not considered explicitly in the constraint Eq. (2.69); if it is, the constraint is no longer holonomic and Hamilton's principle is no longer applicable in the same form. This important issue will be recalled in chapter 5 where the constraint is localised using a new operator developed in this work.

O'Connell & Thompson (1995) use their model to simulate the unsteady evolution of coupled wall driven flow. These results are recreated in section 3.4.1 to investigate the coupling and explore the limitations of explicit state coupling. The timestep used in the paper by O'Connell & Thompson (1995) is the same for both the molecular and continuum regimes ($\Delta t_{MD} = \Delta t_{CFD}$). A relaxation parameter $\xi = 0.01$ is introduced to the forcing term of Eq. (2.72a) to match the velocities over a number of timesteps, so as to prevents the force from cancelling intrinsic thermal fluctuations. As a result, in rapidly accelerating flows the molecular region lags behind the continuum (Nie *et al.*, 2004*a*).

This methodology is further developed in the paper by Nie *et al.* (2004*a*). The constraint equations of Nie *et al.* (2004*a*) use a non-holonomic constraint of the form,

$$g_\alpha(\dot{r}_{\alpha n}) = u_{\alpha I}(t) - \frac{1}{N_I} \sum_{n=1}^{N_I} \dot{r}_{\alpha n} = 0, \tag{2.73}$$

where the α index here represents one of the three Cartesian coordinates in which the constraint is applied (*i.e.* $C = 3$). By combining Eqs. (2.72a) and (2.72b) into a single equation, and assuming the total mass of the cell is constant, the constraint equations of Nie *et al.* (2004*a*) can be obtained (see appendix B.1). Alternatively, they can be obtained directly using Gauss' principle of least constraint. However, in line with the methodology of Nie *et al.* (2004*a*), the derivation is shown using the non-holonomic form of the constraint equation 2.23 (Flannery, 2011),

$$\frac{d}{dt}\frac{\partial \mathcal{L}}{\partial \dot{r}_i} - \frac{\partial \mathcal{L}}{\partial r_i} = \sum_{\alpha \in \{x,y,z\}} \lambda_\alpha \frac{\partial g_\alpha}{\partial \dot{r}_i}.$$

which yields the following equation of motion for the molecules in the constrained system,

$$\ddot{r}_{\alpha i} - \frac{F_{\alpha i}}{m_i} + \frac{1}{N_I}\lambda_\alpha = 0. \tag{2.74}$$

Equation (2.74) is substituted into the time derivative of the constraint given in Eq. (2.73). Assuming a constant mass for all molecules in the cell ($\forall\, i : m_i = m$), the Lagrangian multiplier can be written as,

$$\frac{1}{N_I}\lambda_\alpha = \frac{1}{mN_I}\sum_{n=1}^{N_I} F_{\alpha i} - \frac{Du_{\alpha I}}{Dt} = 0,$$

which substituted into Eq. (2.74) gives the equation of motion used by Nie *et al.* (2004*a*),

$$\ddot{\boldsymbol{r}} = \frac{\boldsymbol{F}_i}{m} - \frac{1}{mN_I}\sum_{i=1}^{N_I} \boldsymbol{F}_i + \frac{D\boldsymbol{u}_I}{Dt} \tag{2.75}$$

where the α notation has been replaced by boldface vector notation consistent with the work of Nie *et al.* (2004*a*). The relaxation factor ξ of O'Connell & Thompson (1995) is not included by Nie *et al.* (2004*a*) as they used different time step values for the molecular (Δt_{MD}) and continuum region (Δt_{CFD}) with ratio $\Delta t_{CFD} = 50\Delta t_{MD}$. The relaxation applied to the MD system therefore occurs at twice the rate of O'Connell & Thompson (1995) (equivalent to $\xi = 0.02$). The CFD is only updated every 50 MD timesteps and the constraint acts to ensure the MD agrees with the CFD gradually over the 50 steps from t to $t + 50\Delta_{MD}$. This is therefore 100 times more rigid that the concurrent evolution of O'Connell & Thompson (1995) but applied gradually over 50 times as long. In combining the equations of O'Connell & Thompson (1995), the constraint is now on the difference in time evolution of both systems (not just velocity). Nie *et al.* (2004*a*) discretised the time derivative in a way which applies a further constraint. The velocity of the cell at time t tends to the velocity of the continuum at time $t + \Delta t_{MD}$ according to,

$$\frac{D\boldsymbol{u}_I}{Dt} \approx \frac{\boldsymbol{u}_I(t + \Delta t_{MD}) - \boldsymbol{u}_I(t)}{\Delta t_{MD}} \approx \frac{1}{\Delta t_{MD}}\left[\boldsymbol{u}_I(t + \Delta t_{MD}) - \frac{1}{N_I}\sum_{i=1}^{N_I} \dot{\boldsymbol{r}}_i(t)\right]. \tag{2.76}$$

This ensures that the continuum and molecular velocity agree within the constraint region at

each MD timestep,

$$\ddot{\boldsymbol{r}} = \frac{\boldsymbol{F}_i}{m} - \frac{1}{mN_I}\sum_{i=1}^{N_I}\boldsymbol{F}_i + \frac{1}{\Delta t_{MD}}\left[\boldsymbol{u}_I(t+\Delta t_{MD}) - \frac{1}{N_I}\sum_{i=1}^{N_I}\dot{\boldsymbol{r}}_i(t)\right]. \tag{2.77}$$

Nie *et al.* (2004*a*) also introduce mass transfer using a mass flux scheme across the interface with the particle number n' defined as:

$$n' = \frac{-\rho u_y A \Delta t_{cont}}{m}, \tag{2.78}$$

where n' is related to the mass flux M' by $M' = mn'$. The mass flux is from the continuum equation, $\dot{M} = \rho u_y A$ where A is the area over which the flow occurs (the xz plane), u_y the velocity in the y direction normal to this plane and $\dot{M}$ the number of molecules leaving in a timestep $\dot{M} = M'/\Delta t_{cont}$. Driven by the mass flux in the continuum, molecules are removed or added to the molecular region at random positions.

Nie *et al.* (2004*a*) simulate impulse started Couette flow with the same setup as Figure 2.2, matching the time evolution to a continuum solution. They extend this to the more complicated cases of impulse Couette with a post on the molecular wall. The results show good agreement when compared to a full molecular simulation. The same authors also apply their scheme to singular corner flow in a second paper (Nie *et al.*, 2004*b*). This allows the molecular region to capture the discontinuity between boundary conditions present in corner flow at $Re = 50$. Only 1% of the $L = 250\ell$ domain is modelled with MD and the interface is both horizontal and vertical (so only the domain corner is modelled by the MD region). The coupled model works successfully and provides insight into the molecular behaviour at the continuum discontinuity between a stationary and moving no-slip wall.

The model of Nie *et al.* (2004*a*) has been extended to include heat transfer by the same group, (Liu *et al.*, 2007). The continuum temperature in the boundary region is obtained from the molecular system by taking Eq. (2.57) and averaging,

$$T = \frac{1}{3k_B(N_I-1)}\sum_{i=1}^{N_I} m_i(\dot{\boldsymbol{r}}_i - \boldsymbol{u}_I)^2,$$

The continuum must also apply a temperature constraint on the MD. In order to do this, a velocity rescaling is implemented in the form,

$$\dot{\boldsymbol{r}}_i = \boldsymbol{u}_I + [\dot{\boldsymbol{r}}_i - \boldsymbol{u}_I]\sqrt{\frac{T_I^{CFD}}{T_I^{MD}}},$$

where T_I^{CFD} is the set point CFD temperature and T_I^{MD} the current MD temperature. To prevent the rescaling from cancelling important thermal fluctuations, large cells are used and the rescaling is applied more than the correlation length away from the molecular domain (at the top of the overlap region). This results in a local heating to the MD domain top and a resulting heat flux downwards which acts to convey the heat flux from the continuum. The simulation construction used to test this methodology was similar to the group's previous work (Nie *et al.*, 2004*a*) with both steady state and unsteady tests performed including temperature profiles.

The Nie *et al.* (2004*a*) model has been applied to a large coupled simulation by Yen *et al.*

(2007). They simulated a $10^2 nm$ scale Couette flows with system heights of 400ℓ with simulation times of $25,000\tau$. The system domain was an order of magnitude larger than that of (Nie *et al.*, 2004*a*) with a proportionally smaller shear rate. The signal to noise ratio was less favourable consequently Yen *et al.* (2007) proposed that the sum of the force terms be averaged in Eq. (2.75) over M iterations,

$$\frac{1}{mN_I}\sum_{i=1}^{N_I}\boldsymbol{F}_i \approx \left\langle \frac{1}{mN_I}\sum_{i=1}^{N_I}\boldsymbol{F}_i \right\rangle_{M\Delta t}.$$

This is applied together with the time averaged MD velocity instead of the instantaneous values in Eq. (2.76),

$$\frac{1}{N_I}\sum_{i=1}^{N_I}\dot{\boldsymbol{r}}_i(t) \approx \left\langle \frac{1}{N_I}\sum_{i=1}^{N_I}\dot{\boldsymbol{r}}_i(t) \right\rangle_{M\Delta t}.$$

A further extension of this averaged force model was deployed by Sun *et al.* (2010) who applied the same force on all molecules in the overlap region. This could potentially have caused problems if the continuum profile varied sufficiently rapidly in the overlap region as this behaviour would not be captured. Borrowing the Quadratic Upstream Interpolation for Convective Kinetics (QUICK (Hirsch, 2007)) scheme from the continuum literature, the force applied was varied linearly across the overlap region to provide the required velocity profile. Similarly the temperature was controlled using a series of Langevin thermostat with set points based on the QUICK scheme (Sun *et al.*, 2010). They apply this model to Poiseuille flow with energy exchange (Sun *et al.*, 2010) and later to a wall of equally spaced posts (Sun *et al.*, 2012).

In a similar vein, Wang & He (2007) re-introduced the scaling parameter, $\xi(t)$, of O'Connell & Thompson (1995) to the formula of (Nie *et al.*, 2004*a*). The ξ parameter was derived as a function of time by rearranging the constrained equation of motion and the constraint was applied gradually over many MD timesteps.

Despite the superior performance for noisy simulation reported by Yen *et al.* (2007); Sun *et al.* (2010) and Wang & He (2007) when using averaged or scaled form of the Nie *et al.* (2004*a*) constraint, these changes represent a further departure from the equation obtained from Gauss' principle. As will be shown in chapter 5, the instantaneous force is important as, together with advection, these terms can be interpreted as isolating the molecular cell from the rest of the system at each timestep. This isolation is shown to be essential to ensure the correct momentum addition to the molecular system in a manner that ensures energy conservation.

This section has so far highlighted the explicit constraint of state properties to match continuum values. These constraints are obtained from the principle of least action which are based on well-established theory. A number of other coupling schemes have been proposed in the literature:

- Liu *et al.* (2008) introduce a control style algorithm which minimise the disturbance to a system and avoids applying any forces. This is motivated by the observation that any applied forces can have undesirable consequences; they add energy, have magnitudes 10^{12} times that of gravity and assume a constant pressure difference (Liu *et al.*, 2008). To avoid applying forces, Liu *et al.* (2008) use a selectively permeable membrane to bias flow in a certain direction. This membrane was of the form of Maxwell's demon, effectively reflecting certain molecules and allowing others through in a manner which ensure the required flow

profile.

- Hadjiconstantinou (1998) apply the transfer from the continuum-to-molecular by selecting velocities from a Maxwell Boltzmann distribution,

$$f(\dot{\boldsymbol{r}}) = \left(\frac{m}{2\pi k_B T}\right)^{\frac{3}{2}} exp\left(-\frac{m(\dot{\boldsymbol{r}}-\boldsymbol{u})^2}{2k_B T}\right), \tag{2.79}$$

  for molecules located near the boundary of the domain. Here k_B is Boltzmann's constant, $\boldsymbol{u}$ the continuum velocity and T the continuum temperature. The molecular domain of interest is surrounded by a molecular reservoir. The molecule velocities are completely re-defined in line with the velocities of the overlapping continuum region. A Taylor series expansion to first order is used to establish the velocities and temperatures to be specified in the Maxwell Boltzmann distribution, Eq. (2.79). The velocity $\boldsymbol{u}$, temperature T, velocity gradient $\partial\boldsymbol{u}/\partial\boldsymbol{r}$ and temperature gradient $\partial T/\partial\boldsymbol{r}$ in the continuum are all used. The surrounding reservoir ensures that a supply of molecules is available at the edge which removes the need for a force to keep molecules in the domain. The reservoir region is delimited by a periodic boundary. Although apparently crude, the effects on the dynamics of this 'Maxwell's Demon' approach are localised near the simulation boundary and the performance is said to compare favourably to constrained dynamics approaches (Hadjiconstantinou, 1998). The application of the Maxwell Boltzmann distribution were later found to result in slip Hadjiconstantinou (2005). In order to reduce this slip, the Maxwell Boltzmann distribution function is replaced by a non-equilibrium distribution generated by a Chapman Enskog expansion or previous MD simulations (Hadjiconstantinou, 2005).

- In other work, Borg *et al.* (2010) used proportional feedback control to apply the difference in velocity as a control force,

$$\ddot{\boldsymbol{r}}_i = \frac{\boldsymbol{F}_i}{m} - \frac{\xi}{\Delta t_{MD}}\left[\boldsymbol{u}_I(t+\Delta t_{MD}) - \frac{1}{N_I}\sum_{i=1}^{N_I}\dot{\boldsymbol{r}}_i(t)\right]$$

  where ξ is a tuneable parameter and this equation is written for a single MD step. This equation can be seen to be similar to the constraint of Eq. (2.77) without the sum of forces. This connection will be revisited in section 5.2.2.

These three coupling methodologies are well suited to certain problems and may perform in a superior manner to algorithms based on constrained dynamics in some cases. The problem with the Liu *et al.* (2008) and Hadjiconstantinou (1998) based schemes is that they cannot be analysed using linear response theory. A similar problem is well known in the NEMD literature, where SLLOD was introduced instead of Lees Edwards boundary driven flows (Evans & Morriss, 2007) for this reason. The control algorithm of Borg *et al.* (2010) is simple and robust making it ideal for coupling schemes on non-uniform grids and parallel computers. However, the aim of this work is to develop a coupling scheme based on minimisation principles in order to reduce unphysical artefacts in the molecular system as far as possible. For this reason, the variational principle approaches of (O'Connell & Thompson, 1995; Nie *et al.*, 2004*a*) discussed in this section are preferred.

Boundary Forces

In addition to the constrained dynamics force, a second force is applied to the molecules in the overlap region to prevent the molecules from leaving the top of the molecular domain. This is termed the 'boundary force' ($\boldsymbol{F}^B$) in this work and is shown on Figure 2.2 acting at the top of the molecular domain. The boundary force of O'Connell & Thompson (1995) is chosen to maintain a prescribed density in the interface regions,

$$F^B = -\alpha P_0 \rho^{-\frac{2}{3}} y_T \tag{2.80}$$

where F^B denotes this boundary force, P_0 is the pressure in the domain, ρ the prescribed density in the interface region, α a scaling constant and y_T specifies the distance from the top of the MD domain. This boundary force is common to the majority of coupling schemes as the molecules need to be prevented from leaving the molecular domain.

The boundary force term of Nie *et al.* (2004*a*) used to prevent molecules escaping is similar to O'Connell & Thompson (1995),

$$F^B = -\alpha P_0 \frac{(y - y_2)}{1 - (y - y_2)/(y_3 - y_2)} = -\alpha P_0 \Delta y \left[1 - \frac{\Delta y}{y_T}\right] \text{ for } 0 \leq y_T \leq \Delta y, \tag{2.81}$$

where y_2 and y_3 denote the range of the top cell of the overlap region, P_0 is the pressure in the molecular region and y is the distance from the origin. Using $y_3 = y_2 + \Delta y$ and $y_T = y_3 - y$ this is re-written in terms of distance from the domain top y_T and depth of application Δy. The applied force at the top means that there is always space for new molecules to be added by Eq. (2.78). The paper by Werder *et al.* (2005) suggests that the boundary force of Eq. (2.81) can be infinitely large and proposes a modified form which is defined to be zero outside a certain range (although this was due to a misunderstanding of the applied force, see Liu *et al.* (2007)).

This paper by Werder *et al.* (2005) also proposes an improved form of the molecule trapping force which approximates the structure of the missing fluid. This is achieved using the radial distribution function (RDF) which is calculated from the structure of the fluid. The RDF is discussed in section 3.2.5. The boundary force is,

$$F^B = -2\pi\rho \int_{z=r_w}^{r_c} \int_{x=0}^{(r_c^2 - z^2)^{\frac{1}{2}}} g(r) \frac{\partial \Phi(r)}{\partial r} \frac{z}{r} x dx dz. \tag{2.82}$$

This equation is in radial co-ordinates with z being the axial component, x the radial and using the definition that $r = (x^2 + z^2)^{\frac{1}{2}}$. The density ρ is the average for the molecular region. The sketch in Figure 2.3 outlines the principle. The force applied is based on the average molecular interaction expected if there were molecules outside the domain.

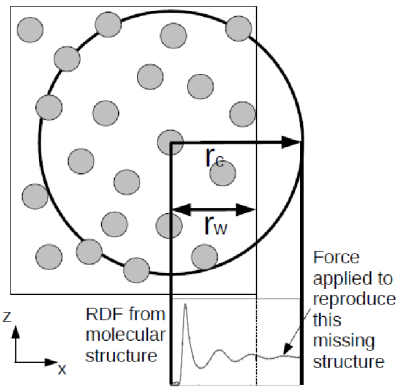

Figure 2.3: Graphical explanation of force used to terminate domain in paper by Werder *et al.* (2005)

This form is based on a pre-calculated Radial Distribution Function $g(r)$ for the system at equilibrium (for equivalent molecular system). For this reason it does not necessarily consider the effects of the flow which may distort the RDF from its spherically symmetric form. In addition,

this boundary force does not prevent molecules leaving completely and a re-insertion mechanism based on the USHER algorithm (Delgado-Buscalioni & Coveney, 2003*b*) is implemented in the paper by Werder *et al.* (2005). This is combined with moving simulation boundaries based on the mean flow in an effort to minimise fluctuations in systems when a mean flow passes through the boundary.

Werder *et al.* (2005) show good results for a case at high temperatures and low density ($T = 1.8$ and $\rho = 0.6$ in LJ units) but in a later work, the same group reported problems extending the work to liquid densities and temperatures (*e.g.* $\rho = 0.8$ and $T = 1.0$) (Kotsalis *et al.*, 2007). To correct the density fluctuations, Kotsalis *et al.* (2007) introduce a further control on the density using a feedback loop and filtering of spurious noise.

The three types of boundary force applied here all have an impact on the molecular system, with the RDF approach of Werder *et al.* (2005) minimising this as far as possible. The approach proposed in section 2.5.3 for flux coupling incorporates the boundary force as part of the constraint. The advantage of this is that an extra artificial force is removed from the coupling and only the effect of the constraint need be considered. The disadvantage is that a force of this type is not designed exclusively to prevent molecular escape, and results in the need for a mechanism to handle molecular escape and re-insertion.

So far, the simultaneous evolution of both domains has been considered explicitly – both systems evolve together and exchange data at regular intervals. The boundary conditions at the interface between the domains are specified by the other domain. This is not the only way to couple continuum to molecular dynamics. The next section looks at an implicit coupling, where the two systems evolve iteratively until the description at the boundaries agree.

Implicit Coupling

The previous methods couple the two regions explicitly by applying forces and boundary conditions to enforce agreement between the continuum and molecular system, which evolve together in time. This has a major disadvantage that the time scales of the molecular and continuum must be comparable. An alternative is to repeatedly re-run multiple realisations of both regions until certain properties agree in the overlap between the domains. The assumption is that coupled simulations are steady or can be modelled as a number of 'pseudo-steady' states. That is, the molecular simulation converges to a constant value over a short run and this is used to represent the much longer timestep of the continuum. This has the advantage that the time scale can be taken to be that of the continuum.

For steady state problems the use of implicit coupling can allow large length ($L = 10^6\ell$) and timescales ($10^{-14}s$) to be spanned by running each scale to steady state before course graining. The work of Nie *et al.* (2004*b*) modelling corner driven cavity flow was extended to domain sizes of $L = 10^6\ell$ ($Re = 6400$) using implicit coupling (Nie *et al.*, 2006). The continuum region was modelled by a hierarchy of domains, each with 64×64 cells. The next domain in the hierarchy was located in the top quarter of the larger domain and coupled along the interface. Moving down through the scales, eventually a molecular scale model was employed, coupled at the interface using the methodology of Nie *et al.* (2004*a*). A globally steady solution was obtained by iterating from the coarsest to the finest scales and back until global convergence was obtained.

The mathematical technique for ensuring agreement at the interface between scales is formalised in the work of Hadjiconstantinou (1998) using the Schwarz alternating method. The

Schwarz alternating method is an iterative method used to split a domain into connected sub-domains and solve each separately. The solution of each sub-domain provides the boundary condition for adjacent sub-domains. This method is often used for solving partial differential equations in parallel as it allows sub-division of the domain between different processes. However, Hadjiconstantinou (1998) applied this method in the context of molecular to continuum coupling. For the purpose of coupling, the molecular and continuum regions are treated as separate sub-domains and in the overlap region, the boundary conditions are iterated between the two regions until there is good agreement. The Schwarz method is for steady state solutions or pseudo-steady processes (where local equilibrium can be obtained). The iterative nature of this coupling means that direct effects of molecules are not important and only an averaged ensemble coupling is achieved. The advantage of this, as demonstrated by Nie *et al.* (2006), is that the time scale of the molecular simulation and the continuum are decoupled allowing an average of several short molecular simulations to represent a simulation run for a continuum timescale.

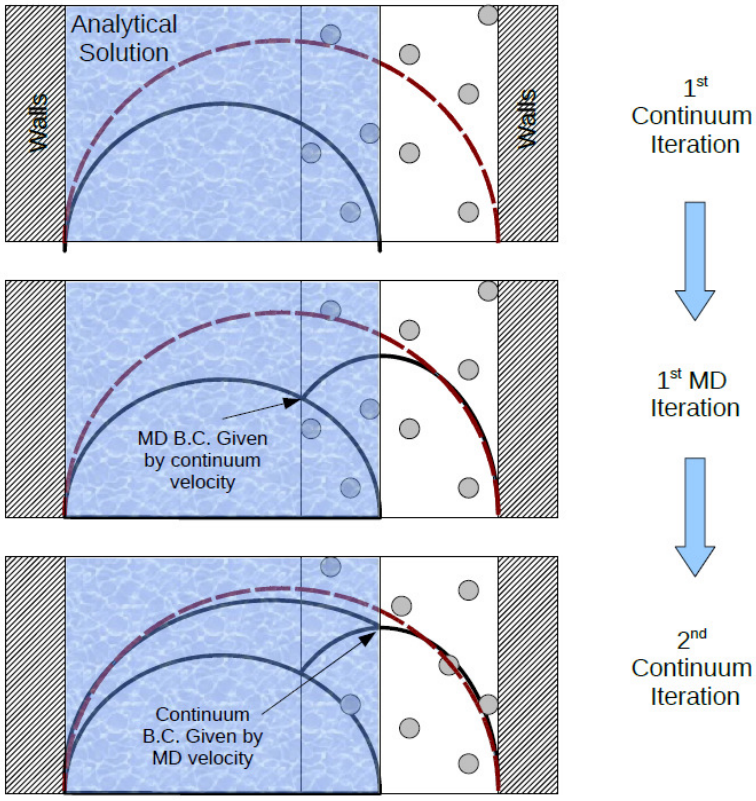

Figure 2.4: Graphical explanation of the Schwarz alternating method, based on figures 3-1 to 3-3 from Hadjiconstantinou (1998).

The coupling is implicit and iterative which means using the Schwarz decomposition to obtain the state properties of density and momentum which are then used as boundary conditions for the other domain. This is shown graphically in Figure 2.4. This is then said to couple fluxes in the overlap region. This is because between boundaries the continuum velocity and temperature are matched at two points so their gradients are also matched. The iterative scheme ensures close agreement at the boundaries and this is assumed to be possible only if the fluxes match in the domain. Stress comparisons in Hadjiconstantinou (1998) show good agreement in fluxes

between the two domains. Hadjiconstantinou (1999) used this model to investigate the moving contact line problem.

Werder *et al.* (2005) combined their RDF based boundary condition, described in the previous section, together with the implicit Schwarz based algorithm. Their method uses O'Connell & Thompson (1995) style coupling to apply velocity and a particle insertion picked from a Rayleigh distribution for direct velocities and a Maxwell Boltzmann distribution for indirect velocities. Werder *et al.* (2005) applied it to simulate flow past a carbon nanotube and observed the analytically predicted wake at low Reynolds numbers.

Recent work by Borg *et al.* (2013*b*) employ a number of representative MD simulations connected by large regions solved using CFD. The combined solution is solved implicitly, with the MD and CFD iterated until the mass flux agrees between the separate regions and solvers. In a later paper, Borg *et al.* (2013*a*), the CFD solver was replaced by mass flow and pressure-difference requirements which are used to guide the iteration of multiple coupled MD domains. Borg *et al.* (2013*b*,*a*) apply these implicit coupling scheme to the steady state simulation of a converging-diverging channel and several component of a micro-network (step contraction/expansion, long channels and wall defects). Good agreement is observed to an all MD solution.

Implicit scheme have the advantage that they allow decoupling of time scales, so molecular simulations can be run at the continuum timescale. However, they are limited to steady state cases or multiple pseudo-steady steps in an unsteady simulation. As implicit coupling iterates to steady state convergence, it does not required correct matching of the temporal evolution between the two systems. Explicit coupling is therefore more onerous, as its requires the continued matching of the time evolution of both systems. A successful explicit coupling algorithm should be applicable to implicit coupling (indeed Werder *et al.* (2005) use O'Connell & Thompson (1995) style coupling iteratively). For a given problem, it is necessary to establish whether direct time coupling (explicit coupling) is required or the pseudo-steady assumption is sufficient (implicit coupling). Ideally this could be determined a-priori using switching criteria, similar to Lockerby *et al.* (2009) for dilute gases, to identify thermodynamic non-equilibrium. However, the extention to dense fluid is far from trivial (Gad-el Hak, 2006) and prior MD simulations may be essential.

In this section, the successful matching between state properties has been achieved using variational principles. In the next section, the limitations of state coupling are discussed and the requirements for flux based schemes outlined. It is suggested that flux-based schemes result in a more general coupling; however, no rigorous derivation of flux based coupling has been provided using variational principles, an issue addressed in chapter 5 of this work. The next section outlines the flux schemes already present in the literature.

2.5.3 Flux Coupling

Consider again the time evolution of an isothermal continuum system,

$$\frac{\partial \rho \boldsymbol{u}}{\partial t} + \boldsymbol{\nabla} \cdot \rho \boldsymbol{u}\boldsymbol{u} = \boldsymbol{\nabla} \cdot \boldsymbol{\Pi}$$

In the previous section, the pressure tensor was approximated in terms of state variables which are exchanged during coupling. However, if the fluxes, $\rho \boldsymbol{u}\boldsymbol{u}$, and pressure tensor, $\boldsymbol{\Pi}$, are exchanged, there is no need to approximate pressure in terms of state properties as in Eq. (2.48). The notion of pressure is well defined in the continuum system and a form of stress can be obtained as outlined in section 2.4.3 for a molecular system. The development of a more consistent stress

description is a novel contribution of this work, detailed in chapter 4.

State coupling and flux coupling will be equivalent, provided the transport properties agree between both systems and the assumptions used to decompose the stress are valid (*e.g.* linear stress strain relation and Stokes' hypothesis outlined in section 2.3.1). A key advantage of flux coupling is it bypasses the need to define a linear stress-strain relation and links both system directly.

As a result, state coupling requires that the two regions have the same transport properties, with the consequent need for calibration simulations. For this reason, flux coupling is more general, remaining valid when the transport properties in the continuum and molecular regions differ and linearity breaks down. Delgado-Buscalioni & Coveney (2004) observed that a coupling scheme fails if transport co-efficients in the two domains differ by more than 15%. Additionally, only coupling through flux terms ensure positive entropy production of the model. They claimed that it is not sufficient to control states at the boundary but that fluxes at the surface of the cells should be included for unsteady flows to prevent numerical errors.

Statistical Errors

The paper by Werder *et al.* (2005), using the error analysis of Hadjiconstantinou *et al.* (2003), suggests that the cost of averaging to obtain fluxes is 6 orders of magnitude larger than for momentum density. This would make flux coupling schemes prohibitively expensive. Before a review of the flux coupling literature is undertaken, this important point is reviewed in this subsection.

The definition of error in the work of Hadjiconstantinou *et al.* (2003) is based on the relative standard error E,

$$E = \frac{s}{\mu\sqrt{M}}, \tag{2.83}$$

where M is the number of statistically independent samples, μ is the mean and s is the standard deviation, obtained for mass, velocity and pressure from the standard statistical mechanics formulas given in Landau & Lifshitz (1980),

$$E_\rho = \frac{1}{A_c\sqrt{N}}\frac{1}{\sqrt{M_\rho}}\ ; \quad E_u = \frac{1}{A_c\mathcal{M}_a\sqrt{\gamma N}}\frac{1}{\sqrt{M_u}}\ ; \quad E_P = \frac{k_BTAc\sqrt{\gamma N}}{PV}\frac{1}{\sqrt{M_P}}, \tag{2.84}$$

where a is the speed of sound used in the Mach number, $\mathcal{M}_a = u/a$ and the acoustic number, $Ac = a/\sqrt{\gamma k_BT/m}$, with $\gamma = c_p/c_v$ being the ratio of specific heat capacities. Substituting the Mach and acoustic numbers in Eq. (2.84) gives,

$$E_\rho = \frac{1}{a}\sqrt{\frac{\gamma k_BT}{mN}}\frac{1}{\sqrt{M_\rho}}\ ; \quad E_u = \frac{1}{u}\sqrt{\frac{k_BT}{mN}}\frac{1}{\sqrt{M_u}}\ ; \quad E_P = \frac{a\sqrt{k_BTmN}}{PV}\frac{1}{\sqrt{M_P}}. \tag{2.85}$$

The error in shear stress was derived for a dilute gas in Hadjiconstantinou *et al.* (2003) and is not included here. The error for density and velocity only are tested by Hadjiconstantinou *et al.* (2003) using molecular dynamics simulation (i.e. dense fluids) showing good agreement. The pressure and shear stress errors are not compared by Hadjiconstantinou *et al.* (2003) or Werder *et al.* (2005) to molecular dynamics and it is unclear if this error analysis applies away from the dilute gas limit (*i.e.* in dense molecular simulations). Despite this, it was claimed in a later

review paper by Hadjiconstantinou (2005) that flux coupling is prohibitively expensive owing to these errors. They reference the thesis of Werder (2005) as an application of the error analysis to dense fluids, using the following forms given in the appendix of the thesis of Werder (2005),

$$M_\rho = \frac{\kappa_T k_B T}{V E_\rho^2} \; ; \qquad M_u = \frac{k_B T}{u^2} \frac{1}{\rho V E_u^2} \; ; \qquad M_P = \frac{\gamma k_B T}{P^2 \kappa_T} \frac{1}{V E_P^2}, \tag{2.86}$$

where the speed of sound, $a = \sqrt{\gamma / \rho \kappa_T}$ is used to re-write Eq. 2.85 in terms of the isothermal compressibility. However, the thesis of Werder (2005) does not state that this form explicitly applies to dense fluids and the calculations are based on reasonably small volumes of size $1nm$ at a reduced density of 0.6 and temperature 1.8 (which is well into the gas phase for molecular dynamics (Baidakov *et al.*, 2008)). Werder (2005) showed very good agreement between the velocity error from Eq. (2.86) and molecular dynamics averages from Eq. (2.83) for a single value. The error estimates for pressure and shear stress measurements were not compared to the corresponding molecular dynamics quantities. A study of error in pressure is provided in appendix E, where the magnitudes are not found to be prohibitive for coupling.

Another important result in the Hadjiconstantinou *et al.* (2003) paper, of particular relevance to chapter 4, is the calculation of fluxes across a reference surface (*i.e.* over a plane). It can be shown that statistical errors in the samples are of the same order as the volume based statistics – only the ratio of volume to surface measurement being important.

Having considered the importance of greater statistics for flux coupling, the next section reviews the literature on flux coupling. Typical flux coupling models do not report major problems with the larger numbers of samples required. This issue is considered in more detail in appendix E.

Explicit Coupling

The paper by Flekkøy *et al.* (2000) is the first paper which uses direct flux exchange. The flux in each of the different domains is calculated and applied as a boundary to the other with an overlap used to prevent the two regions from coinciding, as in Figure 2.2. The algorithm uses different time steps for the molecular Δt_{mol} and continuum region Δt_{cont} with $\Delta t_{cont} = 100 \Delta t_{mol}$.

Molecular to Continuum Exchange

The continuum boundary condition can be applied in the form of a state quantity (Dirichlet) or its derivative (Neumann). The flux from the molecular region is a Neumann boundary condition, obtained from a time average over the 100 MD timesteps of the mass and momentum flux density. This is written as,

$$\rho \boldsymbol{u} \cdot \boldsymbol{n} \rightarrow \sum_{i=1}^{N_I} m \langle \dot{\boldsymbol{r}}_i \rangle \cdot \boldsymbol{n}. \tag{2.87}$$

for momentum flux. Here $\boldsymbol{n}$ is the normal vector to the coupled interface. The arrow in the above equation is the notation used in Flekkøy *et al.* (2000) denoting the algorithm to obtain

continuum-to-molecular boundary condition. The stress is given by,

$$\boldsymbol{\Pi}\cdot\boldsymbol{n} \rightarrow \frac{1}{V}\sum_{i=1}^{N_I}\left(m\langle\dot{\boldsymbol{r}}_i\dot{\boldsymbol{r}}_i\rangle + \frac{1}{2}\sum_{i\neq j}\langle\boldsymbol{f}_{ij}\boldsymbol{r}_{ij}\rangle\right)\cdot\boldsymbol{n}, \tag{2.88}$$

and is calculated by the virial expression, Eq. (2.61),which is correct only for a homogeneous system (recall the discussion in section 2.4.3). The localisation of the stress is an important point discussed in chapter 4, and can have a significant impact on coupling scheme as demonstrated in chapter 5. The stress Π in the continuum region is given by

$$\boldsymbol{\Pi} = \rho\boldsymbol{u}\boldsymbol{u} + P - \mu(\boldsymbol{\nabla}\boldsymbol{u} + (\boldsymbol{\nabla}\boldsymbol{u})^T - \boldsymbol{\nabla}\cdot\boldsymbol{u}) - \lambda\boldsymbol{\nabla}\cdot\boldsymbol{u}. \tag{2.89}$$

Decomposing the stress leads to the Navier-Stokes equation in the continuum system, which can be solved using standard CFD techniques (Hirsch, 2007).

Continuum to Molecular Exchange

In Flekkøy *et al.* (2000) continuum to molecular flux boundary conditions involve introducing molecules at a rate of $\dot{N} = dN/dt$ into the molecular domain. The method used to insert particles by Flekkøy *et al.* (2000) is not clear, however later papers based on the same flux coupling (Delgado-Buscalioni & Coveney, 2003*a*) use an algorithm (USHER) developed to insert molecule at a location which gives the required flux and energy (Delgado-Buscalioni & Coveney, 2003*b*).

The mass and momentum algorithms ensure momentum conservation by giving the inserted particle a time averaged velocity equal to the continuum velocity $\boldsymbol{U}_I = \langle\dot{\boldsymbol{r}}\rangle$ and making the applied force F_i proportional to the force due to the stress $\boldsymbol{\sigma} = \boldsymbol{\Pi} - \rho\boldsymbol{u}\boldsymbol{u}$. The applied momentum flux due to added molecules is,

$$m\dot{N}\langle\dot{\boldsymbol{r}}'\rangle + \sum_i \boldsymbol{F}_i = A\boldsymbol{\Pi}\cdot\boldsymbol{n}, \tag{2.90}$$

where the velocities $\dot{\boldsymbol{r}}'$ are chosen randomly from a Maxwell Boltzmann distribution continuum velocity $\boldsymbol{u}$. The flux applied to the molecular region is implemented using a constraint force of the form,

$$\boldsymbol{F}_i = \frac{g(x_i)}{\sum_i g(x_i)}A\boldsymbol{\sigma}\cdot\boldsymbol{n}, \tag{2.91}$$

where $g(\boldsymbol{x}_i)$ is a weighting function which determines the distribution of total force between different molecules. Flekkøy *et al.* (2000) used a function of the form,

$$g(x) = 2\left[\frac{1}{L-2x} - \frac{1}{L} - \frac{2x}{L^2}\right] \quad \text{where} \quad 0 \leq x \leq \frac{L}{2}, \tag{2.92}$$

which Flekkøy *et al.* (2000) states is arbitrary. This flux coupling applies not only a constraint force but also opposes molecules leaving the domain with a magnitude equal to the continuum pressure. As the constraint is normalised by the sum of all weighting functions, it does not entirely prevent escape of molecules - a problem that must be addressed by some form of molecular insertion/removal mechanisms. The flux coupling of Flekkøy *et al.* (2000) was tested to simulate

steady state Couette flow using a molecular regions at the top and bottom of the domain and a continuum region between them. In addition, steady state Poiseuille flow was simulated with a molecular region simulating the length of the channel (including both walls) in the streamwise direction. This flux exchange method was extended to include conservation of energy, (Wagner *et al.*, 2002). This was implemented by rescaling of the velocities of the molecules in the overlap region. A thermostat was also introduced to remove the added energy created by the force applied to conserve momentum.

Delgado-Buscalioni & Coveney (2003a) extended this model by introducing an energy-based flux for the purpose of simulating unsteady flow with a finite volume continuum simulation. The weighting function $g(\boldsymbol{x}_i) = 1$ was set so that the applied force was the same for all molecules to allow conservation of energy,

$$\boldsymbol{F}_i^C = \boldsymbol{F}^C = \frac{A}{N_I}\boldsymbol{\sigma}\cdot\boldsymbol{n}. \tag{2.93}$$

This results in a simplified energy equation which ensures uniform energy generation, as the continuum energy change should equal the applied energy from the molecular region, $A\boldsymbol{\sigma}^C\cdot\boldsymbol{n}\cdot\boldsymbol{u} = \sum_{i=1}^{N_I}\langle\boldsymbol{F}^C\cdot\dot{\boldsymbol{r}}_i\rangle$. The energy written with the unweighted force proposed by Delgado-Buscalioni & Coveney (2003a) yields,

$$\sum_{i=1}^{N_I}\left\langle\boldsymbol{F}^C\cdot\dot{\boldsymbol{r}}_i\right\rangle = \boldsymbol{F}^C\cdot\left\langle\sum_{i=1}^{N_I}\dot{\boldsymbol{r}}_i\right\rangle = N_I\boldsymbol{F}^C\cdot\boldsymbol{u} = A\boldsymbol{\sigma}^C\cdot\boldsymbol{u}\cdot\boldsymbol{n},$$

where the last equality uses Eq. 2.93. The correct energy flux is ensured by inserting molecules with the appropriate kinetic energy from the Maxwell Boltzmann distribution and at a location which matches the required potential energy. Delgado-Buscalioni & Coveney (2003a) use a steepest descent algorithm (USHER) to insert molecules with the required potential energy. The conduction (as a temperature gradient) is matched to the continuum using a series of thermostats.

Delgado-Buscalioni & Coveney (2003a) simulate an oscillating wall (Stokes 2nd problem). This appears to be one of the only examples of coupled code used for unsteady simulations. It is worth noting that the work of Nie *et al.* (2004a), developed after Flekkøy *et al.* (2000) was motivated by their testing of the flux coupling of Flekkøy *et al.* (2000). During these tests, Nie *et al.* (2004a) concluded that the flux coupling of Flekkøy *et al.* (2000) is unstable for complicated geometries such as the case of channel flow past a rough wall.

In later work, together with Flekkøy, Delgado-Buscalioni and Coveney (Flekkøy *et al.*, 2005) improve the energy application model by splitting the force into a constant part and a fluctuating part.

$$\boldsymbol{F}_i^C = \boldsymbol{F}^C + \boldsymbol{F}^{C\prime}. \tag{2.94}$$

The constant part, $\boldsymbol{F}^C$, is identical to Eq. (2.93) (with $g(r) = 1$), ensuring the momentum constraint is applied correctly. The fluctuating part adds no momentum, instead providing only energy. The fluctuating force is obtained by assuming that the applied constraint must be reversible (not adiabatic as energy is added by molecular insertion). The proposed force ensures $f^{eq} = exp(-k_B\mathcal{H}/T)/Z$ is preserved at every timestep, where Z is the partition function. The

resulting force is,

$$\boldsymbol{F}^{C\prime} = \frac{A\overline{\dot{\boldsymbol{r}}_i}}{\sum_{i=1}^{N_I} \overline{\dot{\boldsymbol{r}}_i}^2} \left[\tilde{\mathcal{E}} - \boldsymbol{\sigma} \cdot \langle \sum_{n=1}^{N_I} \dot{\boldsymbol{r}}_n \rangle \right],$$

where $\tilde{\mathcal{E}}$ is the energy flux and $\overline{\dot{\boldsymbol{r}}_i} = \dot{\boldsymbol{r}}_i - \sum_{n=1}^{N_I} v_n$. The energy flux is not explicitly defined in Flekkøy *et al.* (2005), but it is required to satisfy the relation,

$$\tilde{\mathcal{E}} A dt = \sum_i \boldsymbol{F}_i \cdot \dot{\boldsymbol{r}}_i dt + \sum_{i'} \Delta\epsilon_i',$$

where the i' denotes summing over only the inserted or removed molecules and $\Delta\epsilon_i'$ is the energy change due to these inserted/removed molecules.

Later work by the same group, (Fabritiis *et al.*, 2007; Delgado-Buscalioni & Fabritiis, 2007) replaced the continuum solver with the equation of fluctuating hydrodynamics (Landau & Lifshitz, 1969). These stochastic equations are simply the continuum equations with an extra noise term to model the effects of small scale fluctuations. The noise term is generated using a Weiner process and was tuned to satisfy the fluctuation-dissipation theorem. The reason Fabritiis *et al.* (2007) claim this is essential is to include molecular fluctuations in the continuum part of the solver. More recent developments for coupling to fluctuating hydrodynamics are covered in a review by Delgado-Buscalioni (2012). When these extra fluctuating terms are important and in what circumstances is still an active area of research. In many cases, their inclusion depends on the amount of spatial and temporal averaging performed on the molecular region and the modelled phenomenon of interest.

A work by Ren (2007) compares flux and state coupling. The modelling uses Lees Edwards boundaries to apply shear (Evans & Morriss, 2007); Irving Kirkwood-based stress tensors and a molecular region embedded in the continuum. Ren (2007) finds that coupling states in both directions is stable. Fluxes applied from the continuum to molecular are stable only if states are coupled the other way. Coupling fluxes both ways is shown to be unstable, possibly due to fluctuations introduced by insufficient statistical averaging. This is supported by discussion of the statistical problems associated with coupling fluxes in later work by Hadjiconstantinou *et al.* (2003).

As a final note, this literature review has focused on the coupling of dense fluid mechanics using a continuum based Navier-Stokes solver and molecular dynamics. There is also a considerable literature on other coupling schemes involving Lattice Boltzmann or Dissipative Particle Dynamics (Mohamed & Mohamad, 2009), which is outside the scope of the current work.

2.6 Overview

In this chapter, the governing equations of molecular dynamics and continuum fluid dynamics were introduced, together with the methods for linking them. This included a full review of the literature for both non-equilibrium molecular dynamics and the recent field of continuum to molecular coupling strategies. The challenges in the literature are highlighted and this motivates the work in the remainder of this document.

The molecular dynamics equation, Newton's law for the N body system, were introduced

first (section 2.2) with details of assumptions for molecular simulation. Next, a number of alternative formulations of mechanics were introduced, expressed in terms of the variational principles (Goldstein *et al.*, 2002). These formulations are essential to coupling and form the basis of the work in chapter 5 developing a general and rigorous coupling scheme. The statistical mechanical (mesoscopic) framework was then introduced to provide the bridge between the microscopic molecular and the macroscopic continuum descriptions.

Next, the continuum equations were introduced (section 2.3) in control volume form with the extension to MD being the subject of chapter 4. The control volume form in the infinitesimal limiting cases yielded the continuous differential form and the assumption required to obtain the Navier-Stokes equation from this form were discussed.

The purely formal mathematical link between the continuum differential form and a molecular system was then discussed (section 2.4). The link between the Lagrangian molecular system and Eulerian continuum system was obtained from the work of Irving & Kirkwood (1950). Equivalent properties were defined in both systems and a number of issues were highlighted in the definition of stress. The most important observation is that in moving away from the Irving & Kirkwood (1950) pointwise stress, there is no unique definition of the stress tensor. Addressing this problem motivates the definition of molecular control volume equations in chapter 4. This is of major importance to flux coupling, where an accurate definition of stress is essential to ensure correct properties are exchanged between the continuum and molecular systems.

For the remainder of the chapter (section 2.5), the practical implementation of coupling was reviewed with an overview of the recent literature. This included a discussion of most of the available literature on the subject of molecular-continuum fluid mechanics coupling. State coupling (both implicit and explicit) as well as flux coupling were discussed with advantages and limitations of both highlighted. Four main challenges for coupling were identified and current solutions discussed through reference to the literature. These challenges are; *1*) determining the spatial relationship between the two regions; *2*) enforcing a method of termination of the MD domain; *3*) determining a procedure for averaging the MD region to obtain the continuum boundary conditions and *4*) designing a control which, when applied to the molecular region, matches properties to the continuum.

The first challenge *1*) is implementation specific. Possibilities discussed include embedding MD in the continuum or alternatively, coupling using domain decomposition with both regions occupying different parts of the overall domain. Both have been discussed in this chapter, although domain decomposition is the focus of the rest of this work. The reason for this focus is the intention to simulate the more complicated case of a coupled simulation, where both regions evolve together concurrently. This allows coupling to extend the range of molecular dynamics simulation, possibly to turbulent flows. In addition, as domain decomposition requires greater consistency between the two domains, the techniques developed for this case will be applicable to embedded simulations. The second challenge *2*) can be solved by a separate and arbitrary boundary force or incorporated as part of the constraint force required by point *4*) above. Both were discussed with reference to the various existing schemes in the literature and the latter approach is favoured in this work.

It is on the solution of the third and fourth challenge that the remainder of this work will focus. The solution of challenge *3*) requires correct averaging of either the state or flux formulation as discussed in section 2.4. The various state and flux coupling schemes were introduced in this chapter, as well as a number of other methodologies for exchanging properties between the

systems. The Schwartz alternating method of Hadjiconstantinou (1999) was discussed, which is limited to steady state and will not be considered further. It was found that none of the existing flux scheme correctly localise the stress. The correct manner in which to do this is not obvious for co-existing continuum and molecular system at the same scale. The control volume formulation, introduced as part of this work in chapter 4, provides a way to address this challenge.

The solution of the fourth challenge requires the implementation of some form of control on the molecular system to ensure it agrees with the continuum. The choice of constraint is entirely arbitrary, although the variational principles introduced in section 2.2 are argued to provides the most physically meaningful solution (Evans & Morriss, 2007). The work of O'Connell & Thompson (1995), Nie *et al.* (2004*a*) and Werder *et al.* (2005) apply constraints based on variational principles and have demonstrated good success. However, the flux coupling schemes, (Flekkøy *et al.*, 2000; Delgado-Buscalioni & Coveney, 2003*a*; Flekkøy *et al.*, 2005) are not based on constrained dynamics, with constraints often being applied as arbitrary forces or using statistical arguments. Arbitrary forces do not ensure the molecule's dynamics are changed in a physically meaningful manner and add spurious energy to the system. The novel contribution of chapter 5 is an extension of the variational principle to include fluxes. In addition, chapter 5 provides a common framework for many of the existing coupling schemes by explicitly localising the constraint and linking the work of O'Connell & Thompson (1995), Nie *et al.* (2004*a*), Flekkøy *et al.* (2000) and Delgado-Buscalioni & Coveney (2003*a*).

The next chapter, 3, is an introduction to the computational developments of this project. The MD and CFD codes are introduced first followed by a computational implementation of the coupling itself. Three of the coupling schemes introduced in this section (O'Connell & Thompson, 1995; Nie *et al.*, 2004*a*; Flekkøy *et al.*, 2000) are implemented as part of the verification of the MD/CFD codes and their coupling. Many of the important features from the literature including calculation of stresses, boundary forces, application of constraints and averaging methods are addressed in the next chapter. The computational developments culminate in a generalised coupling library to exchange data between *any* MD and CFD simulation. However, it is clear from the results presented in the next chapter 3, together with the literature review in this chapter, that the implementation of a general-purpose coupling requires further theoretical developments. This therefore leads on to chapter 4 and 5, which focus on the development of a theoretical framework and a well-grounded understanding of coupling strategies building on the excellent literature summarised in this chapter.

Chapter 3

Computational Development

3.1 Introduction

This section outlines the development, verification, profiling and functionality of the molecular dynamics (MD), continuum computational fluid dynamics (CFD) and coupler codes (CPL) developed or utilised during this project. The main purpose of this section is to support the results obtained in later sections by verifying the accuracy of the code against peer-reviewed publications, experiments and analytical solutions. This section also aims to serve as an introduction to each of the codes for future users as well as a series of tests which the user can recreate to verify new developments. The CPL library, developed in section 3.4 of this chapter, is a novel contribution of this work. It should be a useful tool for researchers allowing them to coupled their own high performance CFD and MD schemes and retain the scaling of both.

This chapter is organised as follows, the first section 3.2, contains an introduction to the new molecular dynamics solver developed as part of this project. A major component of the work completed has been the development of a new high-fidelity MD solver, written using state-of-the-art optimisation techniques and developed to run in parallel using the Message Passing Interface (MPI) paradigm. The reason for developing a new MD solver is so that it can be tailored to solve fluid mechanical problems. It is therefore optimised for the simulation of large molecular systems both individually and as part of a coupled simulation with a continuum solver. A description of the numerical scheme is presented in subsection 3.2.1, the force optimisations in subsection 3.2.2 and code features are outlined in subsection 3.2.3. The optimisations, parallelisation, and profiling are discussed in subsection 3.2.4. Finally, a full range of verification tests are presented in section 3.2.5.

In section 3.3, the Continuum Fluid Dynamics (CFD) solvers used during this project are discussed. The first subsection 3.3.1 introduces a new simple finite volume CFD solver developed for the purpose of testing the coupling schemes. The code's features and its verification are briefly described. For more advanced cases, the highly optimised Direct Numerical Simulation (DNS) code, $\mathcal{T}ransFlow$, was employed (Zaki & Durbin, 2005). A brief description of the features of this code and the important changes required for coupling are outlined in subsection 3.3.2.

The final part of this chapter, section 3.4 outlines the key features of the coupler library (CPL). The verification and implementation of this code is also included. The CPL library is a novel contribution, and is available as open source software (Smith & Trevelyan, 2013).

3.2 Molecular Dynamics Solver

3.2.1 Numerical Scheme

Molecular dynamics requires the solution of Newton's laws for an N-body system. Under the assumption of classical, non-relativistic system, the evolution of the molecules is described exactly by Newton's laws,

$$m_i \ddot{r}_{i\gamma}(t) = F_{i\gamma}(t) \tag{3.1}$$

where γ is index notation denoting the three cartesian spatial dimensions. The forces $F_{i\gamma}$ on a molecule i depends entirely on its relative positions to every other molecule in the system. The next section details the process for obtaining this force $F_{\gamma i}$ in a molecular simulation. For now, it is assumed that the force on molecule i is known and the procedure by which the spatial position is derived from this force is discussed. This requires a numerical discretisation of Newton's law. The Verlet leap frog algorithm is chosen here. The time derivative of position can be written as a Taylor expansion half a step forward and half a step backward in time,

$$\dot{r}_{i\gamma}(t + 1/2\Delta t) = \dot{r}_{i\gamma}(t) + \frac{\Delta t}{2}\ddot{r}_{i\gamma}(t) + \frac{\Delta t^2}{6}\dddot{r}_{i\gamma}(t) + O(\Delta t^3) \tag{3.2}$$

$$\dot{r}_{i\gamma}(t - 1/2\Delta t) = \dot{r}_{i\gamma}(t) - \frac{\Delta t}{2}\ddot{r}_{i\gamma}(t) + \frac{\Delta t^2}{6}\dddot{r}_{i\gamma}(t) + O(\Delta t^3). \tag{3.3}$$

Taking the difference between these two equations gives an expression for the acceleration at t in terms of the velocity at $t \pm 1/2\Delta t$,

$$\ddot{r}_{i\gamma}(t)\,\Delta t = \dot{r}_{i\gamma}(t + 1/2\Delta t) - \dot{r}_{i\gamma}(t - 1/2\Delta t). \tag{3.4}$$

Substituting Eq. (3.4) into Eq. (3.1) yields,

$$m_i \dot{r}_{i\gamma}(t + 1/2\Delta t) = m_i \dot{r}_{i\gamma}(t - 1/2\Delta t) + \Delta t F_{i\gamma}(t). \tag{3.5}$$

The inter-molecular force $F_{i\gamma}(t)$ and the velocity at $t - 1/2\Delta t$ allows the velocity at $t + 1/2\Delta t$ to be obtained. A similar process is applied to obtain the position at the next time step $t + \Delta t$,

$$\dot{r}_{i\alpha}(t + 1/2\Delta t) = \frac{1}{\Delta_t}\left[r_{i\alpha}(t + \Delta t) - r_{i\alpha}(t)\right] \tag{3.6}$$

So the half timestep velocity is used to evolve the molecular position from t to $t + \Delta t$,

$$r_{i\alpha}(t + \Delta t) = r_{i\alpha}(t) + \dot{r}_{i\alpha}(t + 1/2\Delta t)\,\Delta_t \tag{3.7}$$

Any numerical approximation of an integral is normally judged for its truncation error - how well it represents the integral. The Verlet leap frog algorithm is a central difference formulation and the truncation error is of order four $\mathcal{O}(4)$ due to the cancelling of the third order terms. In addition to this good order of accuracy, it can be shown that the Verlet algorithm is symplectic (phase space conserving). As a result, it displays excellent total energy (Hamiltonian) conservation (Rapaport, 2004). This is due to the central nature of the numerical scheme where any error is damped rather than allowed to build up over time.

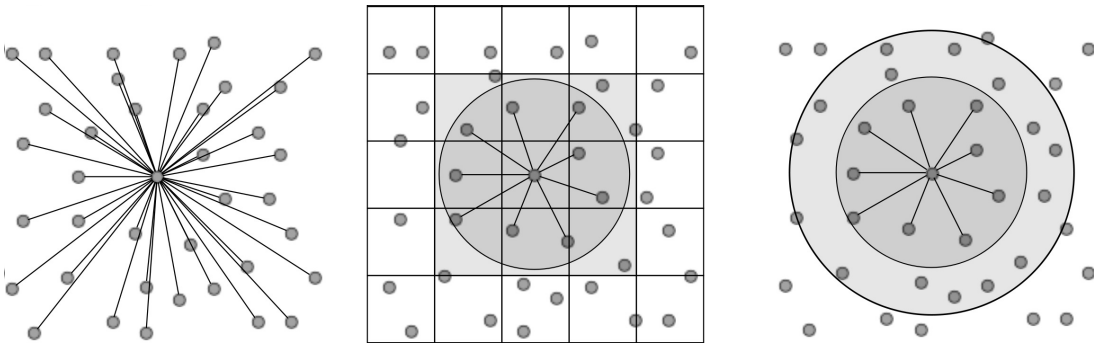

Figure 3.1: Schematic diagram of the successive optimisations of the molecular code – (a) All pairs with N^2 interactions, (b) Cell list optimisation, (c) Neighbour list optimisation

It is also possible to use an iterative scheme to integrate the equations of motion, the velocity Verlet, which has also been developed as part of the project.

3.2.2 Force calculation

The interaction potential between the molecules is the only approximation in the process and, for the work in this section, it is described by the Lennard-Jones potential,

$$\Phi(|\boldsymbol{r}_{ij}|) = 4\epsilon\left[\left(\frac{\ell}{\boldsymbol{r}_{ij}}\right)^{12} - \left(\frac{\ell}{\boldsymbol{r}_{ij}}\right)^{6}\right] - 4\epsilon\left[\left(\frac{\ell}{\boldsymbol{r}_{c}}\right)^{12} - \left(\frac{\ell}{\boldsymbol{r}_{c}}\right)^{6}\right], \quad |\boldsymbol{r}_{ij}| \leq |\boldsymbol{r}_{c}|, \tag{3.8}$$

where $\boldsymbol{r}_{ij}$ is the difference between the vectorial postion of atom i located at $\boldsymbol{r}_i$ and atom j located at $\boldsymbol{r}_j$, *i.e.* $\boldsymbol{r}_{ij} = \boldsymbol{r}_i - \boldsymbol{r}_j$, ℓ is the length scale of the molecular system, usually the atomic diameter and ϵ is a constant specifying the strength of the atomic interaction.

In its simplest form, computation of pairwise molecular interactions requires N^2 calculations for a system of N molecules. The required N interaction calculations for a given molecule are shown in Figure (3.1a). As the Lennard-Jones potential drops off rapidly with distance, the majority of the N^2 calculations are negligible. Enforcing a cutoff distance, $\boldsymbol{r}_c$, over which the potential is not evaluated allows the calculation to be significantly accelerated, as only local interactions need to be computed. A commonly used cutoff length is $|\boldsymbol{r}_c| = 2^{1/6}$, known as the Week-Chandler-Andersen (WCA) potential (Rapaport, 2004). This sets the cutoff length to the minimum of the potential well, removing the attractive tail. This has the advantage that the cutoff is short, resulting in far fewer interaction calculations and significantly faster simulations. This potential is useful for representative simulation, however a cutoff of $|\boldsymbol{r}_c| > 2.5$ is typically required to correctly model many physical process. The use of a cutoff $\boldsymbol{r}_c$ allows the N^2 inter-molecular calculations to be reduced to order N. This is achieved by splitting the domain into a series of cutoff length sized cells and considering only the interactions between molecules in neighbouring cells – a cell list (also know as the linked cell list (Allen & Tildesley, 1987)). This reduces the task of checking all pairs of interactions to just a local check over the molecules in the current and adjacent cells. The list of molecules per cell can be built efficiently using integer division. The division into cells is shown in Figure (3.1b) where the grey circle represents molecules within cut off radius r_c and the current and adjacent cells can be seen to form a cube that contains all interacting molecules.

Further improvements are obtained by keeping a list of *only* the interacting neighbours to a given molecule – a neighbour list (also know as the Verlet list (Allen & Tildesley, 1987)). This ensures calculation of the forces on a molecule requires only the checking of molecules in the surrounding sphere instead of the surrounding cube of adjacent cells. Building the neighbour list, however, is more expensive than the cell list as it requires conditional checking based on a sphere local to each molecule. To optimise this, the cell list is used to construct the neighbour list, but with larger cells. The resulting sphere containing neighbour molecules has a radius larger than $|\boldsymbol{r}_c|$, as shown in Figure (3.1c), so that rebuilding is not required at every timestep. This extra distance can then be tuned for each case (using parameter studies) to optimise the checking sphere size (*e.g.* $r_c + 0.3$) and rebuild frequency (*e.g.* 15). Further improvement in efficiency is made using Newton's third law to halve the number of interactions calculated. For further details of these methods see for example Rapaport (2004).

The improvement in simulation efficiency for the molecular dynamics solver has been tested up to a system size of one million molecules, shown in Figure 3.2. The time taken for a given simulation case, t_{case}, is divided by the time for the all pairs case, t_{ap}, in order to obtain a speedup metric. These improvements result in a simulation which now scales as N.

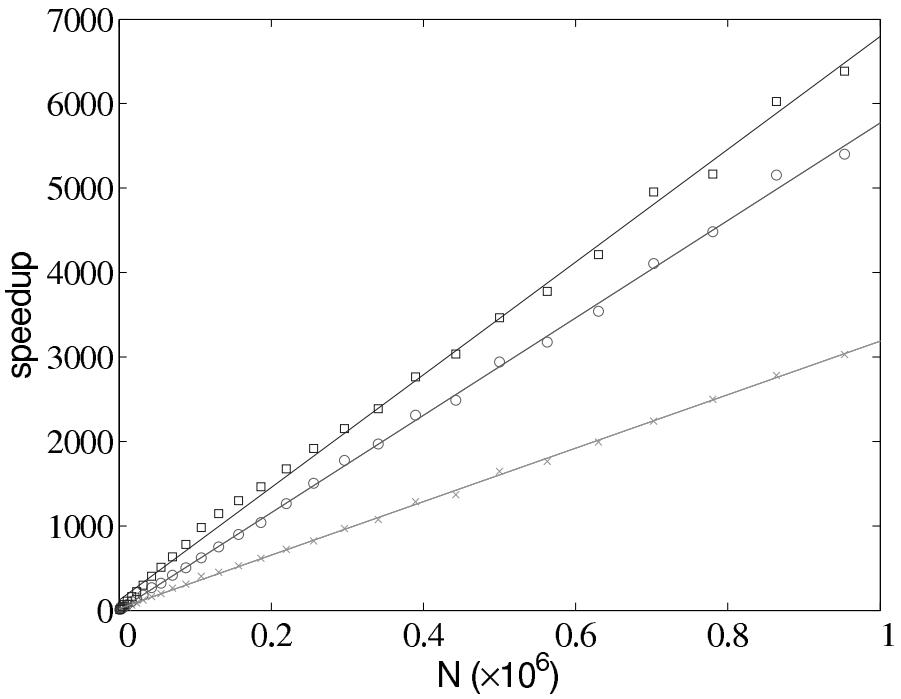

Figure 3.2: Relative speedup compared to an all pairs calculation (t_{case}/t_{ap}) – using the cell list (x), neighbour list (o) and neighbour list with half interaction (□) optimisations.

As the size of the cell/neighbour lists are not known in advance, an arbitrary array would need to be allocated to contain all possible interactions. This array would grow or develop gaps as the essential interactions change and molecules move in and out of range. To avoid this problem, a linked lists system is used. Linked lists are a chain of FORTRAN data types connected by pointers (see Figure 3.3). Each data type has an integer with the interacting molecule number n and the pointer to the next (and previous) data type in the list. The molecular number n identifies the location in memory of the molecule. This can be used to load the molecules

position r_i, velocity $\dot{r}_i$, acceleration a_i, etc. The top and the bottom item in a list point to the null pointer which identifies the end of the linked list. Each linked list is associated with a given cell (or molecule in the neighbour list case). An array of head types contains the number of items in each list and a pointer to the head element.

All cell or neighbour list operations are performed by a library of subroutines developed to build, manipulate and destroy linked lists. This function library includes linklist print, search, pop and push routines which prevent the user from having to deal with the list pointers directly. These routines have been fully tested for memory leaks with Valgrind (Nethercote, 2004) and 'soak tested' for a wide range of different cases.

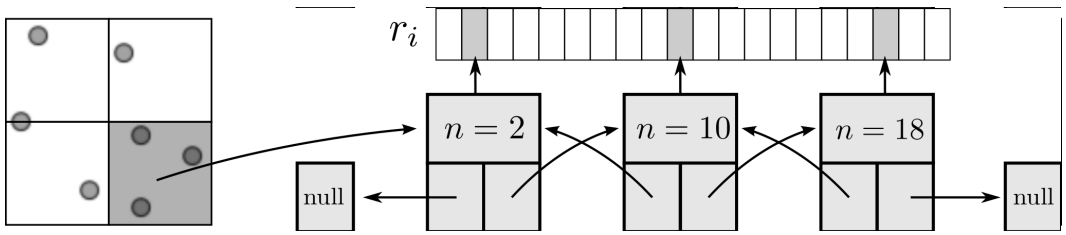

Figure 3.3: Schematic of the structure of a linked list and its reference to memory.

3.2.3 Code details

This subsection contains details of the code structure, philosophy and key features.

Code Structure

The code is structured in a modular way. The source code files are grouped into four types: setup files (`setup*`), simulation files(`simulation*`), finalisation files (`finish*`) and general library files (e.g. `modules.f90, linklist.f90, messenger.f90`). Each group performs the following tasks:

- Setup - Routines to initialise a new simulation or read in an old restart file; parameters are set by the free form keyword based `input` file; arrays are allocated, the messenger processor topology is initialised and output files are opened.
- Simulation - Routines which advances the code by calculating molecular interactive forces and advancing the molecular trajectories. A spatial decomposition is used for parallelism and message passing is used to exchange halos between the processes. Outputs are written at user specified intervals.
- Finish - Save final state files, finish and close outputs and deallocate all arrays
- General library files - Routines used throughout the setup, simulation and final parts of the code. All MPI routines are called through a messenger file which has a parallel and serial version. Linklists manipulation and other general library routines are included in this category

Compilation is performed using a makefile in the code directory. The code has been tested on a number of compilers (Intel FORTRAN, gfortran, cray, gnu, pgi) and architectures (HECToR, Imperial's CX1/2, Linux Red Hat/Ubuntu, Apple Mac OS and Windows). The makefile uses compiler information from a range of verified cases on various architectures built up during the

code's development and is designed to be easily supplemented when porting to new platforms. The serial code is self-contained with no links to external libraries and the parallel code requires only access to the MPI modules. There are a range of build options including serial and parallel versions along with a number of debug, profiling and optimisation options.

The code reads a freeform keyword based input file which entirely specifies the simulation parameters and required outputs and analysis. Most keywords are optional and a default value is used if the keyword is missing. There is also a restart facility which reads in the parameters, molecular positions and velocities from a previous simulation. The restart file is written in the same format in serial or parallel using the MPI2 I/O libraries. The spatial position of a molecule and its storage location in memory are not always consistent. As a result, restarts on different processor topologies require re-ordering. This is performed on start-up for small systems ($procs < 3^3$). For large system, parallel re-ordering is an inefficient use of time on a supercomputer – therefore a separate serial code to reorder is provided.

Features Overview

Some of the features developed for the molecular dynamics code include,

Flow control	**Molecular Properties**	**Output**
Gaussian Thermostat (Evans & Morriss, 2007)	Fixed atoms (Rapaport, 2004)	Momentum/Energy/ Temperature/Pressure
Nosè-Hoover Thermostat (Hoover, 1991)	Tethered Atoms (Petravic & Harrowell, 2006)	VMD visualisation (Humphrey *et al.*, 1996)
Constrained Dynamics ((O'Connell & Thompson, 1995; Nie *et al.*, 2004*a*; Flekkøy *et al.*, 2000))	Solid/Liquid Potentials (Allen & Tildesley, 1987)	Stress Tensor (Virial (Allen & Tildesley, 1987), MOP (Evans & Morriss, 2007), Volume Averaged (Lutsko, 1988)) Control Volume (Smith *et al.*, 2012)
SLLOD algorithm (Evans & Morriss, 2007)	Sliding/moving walls	Radial Distribution Function Velocity Distribution Function Boltzmann's H function (Rapaport, 2004)

Version Control and collaborative code development

A fully verified and working code is hosted on a subversion server to allow simultaneous development by multiple users. To prevent corruption of the codes core functionality, a number of bash and python scripts are used to check serial/parallel restarts along with other benchmarks. These are run periodically to help in pinpointing errors introduced by code developments. The MD code has been extended by other users (mainly David Trevelyan) to include more thermostats, integration algorithms, Lees Edwards sliding boundaries and the suite of tools needed to simulate a range of polymers.

3.2.4 Computational Developments

This subsection contains a description of the serial and parallel developments, optimisations and benchmarking results for the MD solver.

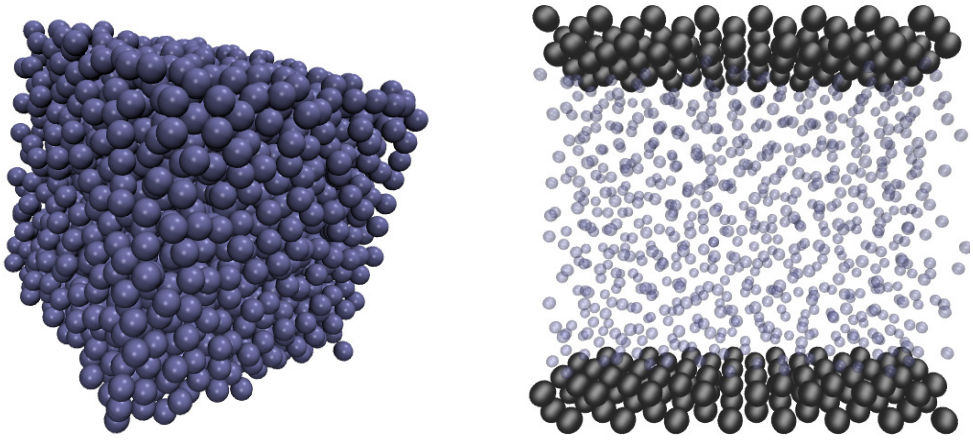

(a) Molecular domain **(b)** Molecular channel

Figure 3.4: VMD output from molecular simulation

Profiling and optimising the serial code

The interaction lists detailed in section 3.2.2 are the single biggest improvement to the computational speedup of the MD solver. However, a number of other improvements are possible as outlined in this section. The code is compiled with full optimisation flags and profiled using `gprof` (and later Tau) to obtain a detailed breakdown of time spent on various operations. This profiling data is compared to established MD codes (DL_POLY and LAMMPS). This process is used to identify routines which take longer than established codes – these then become the focus for optimisation. All profiling for the MD solver, DL_POLY and LAMMPS is performed on one core of the same quad core desktop (Intel® Core ™ 2 Quad CPU Q9300 @ 2.50GHz with 4GB of RAM).

Optimisation is separated into two types: limiting required operations and memory access optimisations.

- Operations limiting improvements include limiting branching statements inside loops, re-using calculated data by defining intermediate variables, moving operations out of loops (as far as possible) and forcing function in-lining using compiler directives.

- Memory access optimisations include minimising memory allocations, avoiding superfluous temporary array creations and maximising cache efficiency. As moving through linked list results in non-contiguous data access and reduced cache efficiency, the code is checked using Valgrind's cachegrind. The cache misses are minimised by changing nested loop order and sorting data in memory. In order to sort the data to maximise cache hits, the positions of the molecules in memory are reordered based on spatial locality. A recursive function to generate 3D Hilbert curves provides the ordering in memory of the molecules. This is thought to provide the best mapping of the 3D spatial locality of molecular positions to 1D memory (Anderson *et al.*, 2008). There is a substantial reduction in cache misses after re-ordering and a noticeable increase in speed of simulation for large system sizes and longer simulations.

In addition, profile-guided optimisation is used to tune the compilation of the executable based

on profiling data gathered from representative simulations. The results of these successive optimisations are summarised by chart 3.5 together with a comparison to LAMMPS (svn revision 8808) and DL_POLY (version 4.03). The required operations for a molecular dynamics simulation can be divided into five main areas; force calculation (`forces`), cell/neighbour list building and manipulation (`lists`), movement of the molecules (`move`), exchange of boundary information using halos (`boundary`) and other operations (`other`) including collecting statistics, re-ordering data and compiler internal operations such as memory manipulations (e.g. `__intel_new_memset` is often in the top five most expensive routines).

The force routine is the most expensive part of the calculation and the successive improvement attempts focus on this. Moving from all pairs to cell lists represents the biggest change with over an order of magnitude improvement. The cell to neighbour list improvements, detailed in section 3.2.2, have the disadvantage of requiring greater list building time – although this is offset by the improvements in force computation. The next three optimisations include using Newton's 3rd law to halve the number of interactions calculated (`neighbour list half int`), using aggressive compiler based optimisation flags with other optimising operations outlined above (`Neighbour list optimised`), and finally memory based optimisation and sorting (`Neighbour list reordered`). The sorting can be seen to improve the speed of the `forces`,`lists`, `move` and `boundary` routines by more than the increased time taken to sort (included in `other`).

DL_POLY is a FORTRAN based code while LAMMPS is written in C++. The performance of LAMMPS can be seen to be significantly better than DL_POLY and so it is taken as the benchmark. In total, LAMMPS can be seen to be faster than the MD solver by a factor of 1.3. Profiling data indicates that the force calculation take a similar amount of time in LAMMPS and the MD solver with re-ordering (which LAMMPS also employs). Manipulation of the interaction list, including neighbour and cell list building is slower in the MD solver. This may be, in part, a consequence of using linked lists in FORTRAN – these dynamic data structures are not native to FORTRAN and require significant manipulation to build and search. They would also likely be missed by FORTRAN compiler optimisation heuristics. The movement of molecules is faster in the MD solver as the leap frog algorithm is used (instead of the velocity Verlet used by LAMMPS, requiring twice the number of calculations per timestep).

The performance gap of 1.3 between LAMMPS and the in-house written MD code is deemed acceptable. LAMMPS has existed since the mid-1990s and has been the subject of extensive optimisation and development by Sandia labs, Lawrence Livermore National labs, at least three companies and many researchers and computer scientists. The performance difference may be a result of the comparisons between C++ and FORTRAN codes, especially using `gprof`, which was developed for C++. This is supported by a disproportionate amount of the time spent in routines which appear to be internal to the compiler (`other`). In addition, the performance of the MD solver relative to the FORTRAN code DL_POLY is extremely favourable.

Parallel computation of MD simulation using the Message Passing Interface (MPI)(Gropp *et al.*, 1999*a*)

Three different methods have been employed to parallelise molecular dynamics simulations on distributed computing hardware. The first is based on atomic decomposition in order to distribute the molecules evenly between processors. The second is to divide the most computationally intensive step, the force calculation, over the different processors with each taking a section of

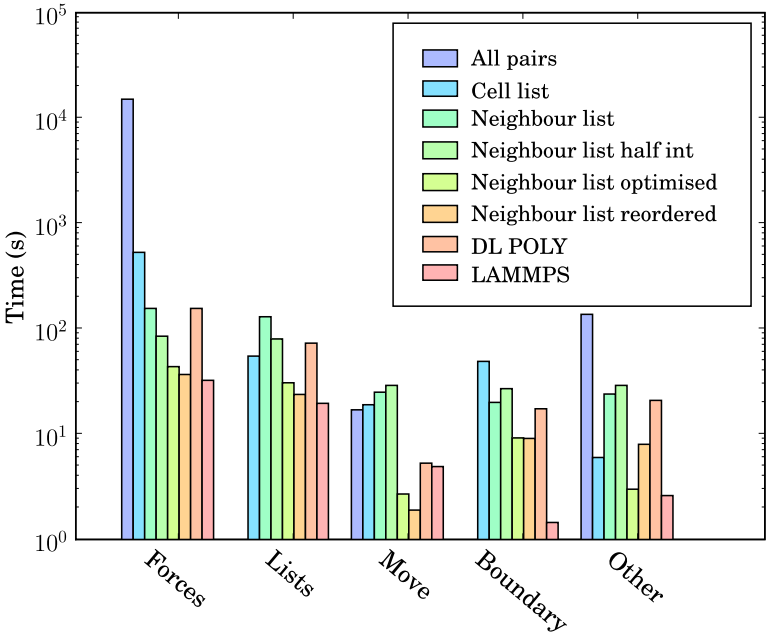

Figure 3.5: Profiling breakdown of time spent in various routines for successive code optimisations – including a comparison to DL_POLY and LAMMPS. Case is 2048 molecules, interacting with a WCA ($|\boldsymbol{r}_c| = 2^{1/6}$) potential run for $10,000$ timesteps.

the calculation. The final decomposition method subdivides the domain into individual regions, with each processor responsible for the integration of atomic trajectories in an assigned region.

Each of these methods has advantages under certain conditions. For example, an atomic decomposition provides natural load balancing, but requires large amounts of data passing for all but the smallest system. Plimpton's (Plimpton, 1995) analysis of the different methods concludes that, for short range systems with large numbers of molecules, a spatial decomposition scheme provides the best performance. Most commonly used parallel MD codes make use of spatial decomposition, including GROMACS (Spoel *et al.*, 2005), DL_POLY and LAMMPS (Plimpton *et al.*, 2003), as well as the algorithm used in this work. This approach also matches the parallel model employed for the continuum solver, which is beneficial for the purpose of algorithmic interfacing.

Verification of the parallel algorithm is performed by comparing the results for the same case in serial and parallel: a simulation started in serial saves an initial state, which is then read by the serial and parallel versions of the program (where the atoms are distributed to processor by their location in parallel). This ensures identical starting configurations.

The intermolecular force calculation in parallel requires each processor to exchange information with adjacent processors at each timestep (halo-exchange). Molecules must also be passed between processors when they leave the processor domain, a process which only occurs every rebuild time for neighbour-list calculations. The process of gathering statistics requires accumulation of data on a single root processor, as well as MPI operations that govern data writing by individual processors to a shared file, using the MPI2 standard (Gropp *et al.*, 1999*b*).

The details of a typical communication run are addressed in the next section through profiling data which is used to optimise parallel performance of the code.

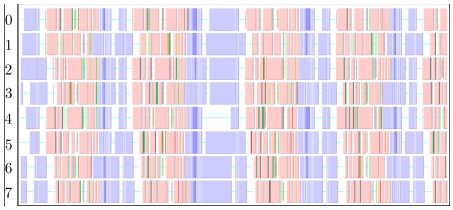

(a) Overview of a rebuild interval, in this case approximately five timesteps

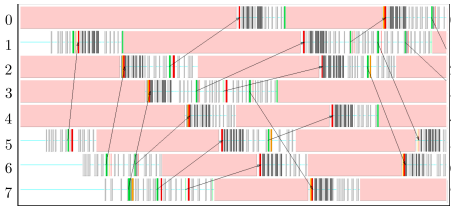

(b) Detailed view of halo data exchange for part of a single step

Figure 3.6: MultiProcessing Environment logging data showing data exchange between eight processes as a function of time. Light red – probe; grey – pack(light)/unpack(dark); red – receive; green – send (non-blocking); orange – wait; lightblue – all reduce; dark blue – all gather and black line – links send to receive;

Profiling and optimising the parallel code

The parallel code is profiled using MultiProcessing Environment (mpe) libraries which trace the communication patterns during an MD simulation. An example of this logging data is included in Figure 3.6, giving an insight into the parallel MD solver. The simulation is performed using eight processors ($2 \times 2 \times 2$) solving a periodic WCA fluid using the neighbour lists. MPI communications on the eight processors are shown on the vertical axis against time on the horizontal. Figure 3.6a shows an overview of approximately five simulation timesteps, split into alternating sections of blue and red/yellow/green blocks. The blue blocks are global (blocking between all processors) and take far more time than the many local exchanges represented by the collection of red/yellow/green blocks. Figure 3.6b shows further details of these local exchanges.

The communication process starts by packing the data into buffers to send (light grey blocks). As the number of molecules a processor will receive is not known *a-priori*, the receiving processors use `MPI_probe` (light red blocks) to establish how much data they expect to receive before allocating appropriate memory. The `MPI_send` command (green) is posted on a given processor where the black arrows on Figure 3.6b trace the movement of a message to the corresponding `MPI_receive` (dark red) command on another processor. The receives are non-blocking, so a `MPI_wait` command (orange) is placed before the received data is required. The new molecular data is unpacked using `MPI_unpack` (dark grey blocks). The neighbour-list must be rebuilt when a molecule has moved sufficient distance. As a local rebuild necessitates a global rebuild, rebuild checks must be broadcast to ensure the neighbour-list is up to date. The blue blocks in Figure 3.6a are global communications (gather/scatter) to check for this rebuild (together with exchange of other information required for rebuilding).

The profiling above is useful as it identifies areas to improve performance. MPI_probe is clearly inefficient and should be replaced by the sending of arbitrary sized buffers followed by a check for overflow. In addition, gather/reduce operations should be limited, for example by disabling the global rebuild check (usually satisfied every 15 steps) for an initial periods of time (*e.g.* first ten steps) .

A parallel performance logging tool, Tau (Shende & Malony, 2006), was also employed. This allows the user to compare time spent in computationally intensive routines, like the force calculation, to waiting times for MPI communications. As a result, optimisation can focus on expensive parallel routines and establishing the optimum particles-per-processor to balance computation and communication. Use of profiling tools periodically during developments and

before submission of long jobs help to optimise the utilisation of supercomputing resources.

Benchmark of Parallel scalability

Having verified the parallel code, it can be benchmarked for parallel scalability. This is done using up to 1024 cores on HECToR. The profile shown in Figure 3.2.4 is for 5000 iterations of a Lennard-Jones system with $3,317,760$ molecules. The number of processors is increased for a fixed system size (weak scaling) and the parallel efficiency is defined as the simulation time taken by a single core (t_{p1}) divided by the time for n cores (t_{pn}) times n – *e.g.* $\mathcal{E} = t_{p1}/(nt_{pn})$.

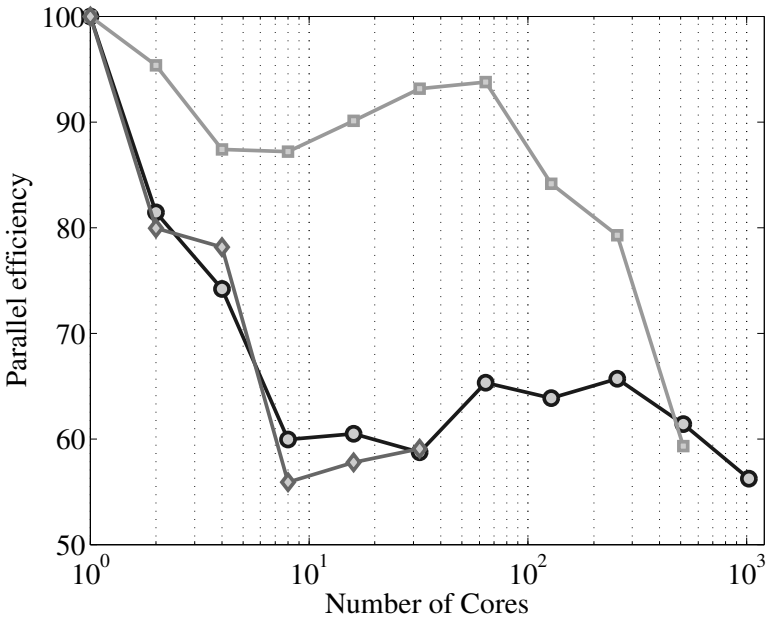

Figure 3.7: Strong scaling of the MD solver on Imperial's supercomputers CX1 (–□–) , CX2 (–◊–) and HECToR (**-o-**). The data for this plot was obtained from runs on HECToR as part of the work detailed in Anton & Smith (2012).

The initial performance drop in using one, two, four then eight cores is attributed to the increased complexity of passing data in one, two and three dimensions respectively. In serial, the molecular data is simply copied internally. With two cores, only two faces must be passed, in two dimensions, four edges and four faces must be passed. For the eight core cases, twelve edges, six faces and eight corners must be passed separately. If scaling is instead defined *vs* the eight core speed, the code can be shown to be 94% efficient on 1024 processors.

A note on Graphical processing units (GPU)

The use of GPU acceleration was investigated as part of the development of the molecular dynamics code. General purpose GPUs have been shown to give massive increases in computational speeds. Current state of the art molecular dynamics application suggest a 30 times speed up over the same code run on a CPU (Anderson *et al.*, 2008). NVIDIA Compute Unified Device Architecture is used as the programming model (the standard Open CL is under developed while

NVIDIA have invested heavily in CUDA) (NVIDIA, 2010). CUDA is a C based set of libraries, with some C++ extensions, allowing calculations to be performed on the GPU. As the majority of the code is FORTRAN, C based wrappers are used to allow variables to be passed from FORTRAN to C++ and then to CUDA C.

The first attempt to optimise the MD solver delegated only the force calculation to the GPU. The positions of all interacting pairs of molecules were passed to the GPU and the forces passed back. The performance improvement was found to be negligible as the time to copy the large numbers of interacting pairs negated any computational speed up.

The next attempt at optimisation involved copying a single set of molecular positions into GPU global memory and calculating the interaction forces. Although this showed some speed up, the improvements were still very limited. The exchange of data still greatly reduces any benefit in speed up. This is a similar discovery to the work Brown *et al.* (2011), where without neighbour list builds on the GPU, the force calculation on a GPU was actually found to be slower (0.7 speedup). In order to gain the 30 times speed up, the entire code (forces, movement, list building and averaging) would need to be ported to the GPU with data exchange only for i/o (Anderson *et al.*, 2008). For a serial GPU this represents an entire redesign of the MD solver for the GPU architecture, with all future developments written to maintain this structure.

The aim of this project is to model very large coupled runs, often simulating more molecules than a single GPU could store. This would require multiple CPUs (connected by MPI) linking together the multiple GPUs (ideally with clever use of page locked memory) (NVIDIA, 2010). Load balancing would also be required in order to ensure the available resources are efficiently utilised (Brown *et al.*, 2011). Even with load balancing and multiple CPUs linked to multiple GPUs, speed up of only 2.5 are reported when the force calculations ($r_c = 2.5$) alone performed on the GPUs (Brown *et al.*, 2011). Due to the complexity of implementation, the inflexibility of development and the added complication of required coupling to CFD codes, it was decided to postpone the GPU development until CUDA libraries are sufficiently improved or perhaps consider a solution using OpenCL.

3.2.5 Verification

As a new molecular dynamics code has been developed, full verification is essential before use as a research tool. This section outlines a range of verification cases against standard benchmarks and experimental results. The tests include energy conservation and trajectories, radial distribution functions (RDF), phase diagrams and non-equilibrium molecular dynamics (NEMD) simulations of canonical fluid mechanical flows.

Energy Conservation

The first and most important tests of a molecular dynamics algorithm are those related to conservation of momentum and energy. Total energy conservation is actually a highly sensitive test of the correctness of a program (Allen & Tildesley, 1987). This is the first verification test after each successive algorithm change. The interchange between kinetic and potential energy as well as the total energy is shown in Figure 3.8 for the $\mathcal{NVE}$ ensemble (constant number of molecules $\mathcal{N}$, $\mathcal{V}$olume and $\mathcal{E}$nergy). This simulation used a WCA potential with a truncation distance $r_c = 2^{1/6}$ and 2048 molecules initialised in an $8 \times 8 \times 8$ FCC lattice with reduced density of 0.8 and temperature of 1.0. As a result, molecules start outside of interaction range and the

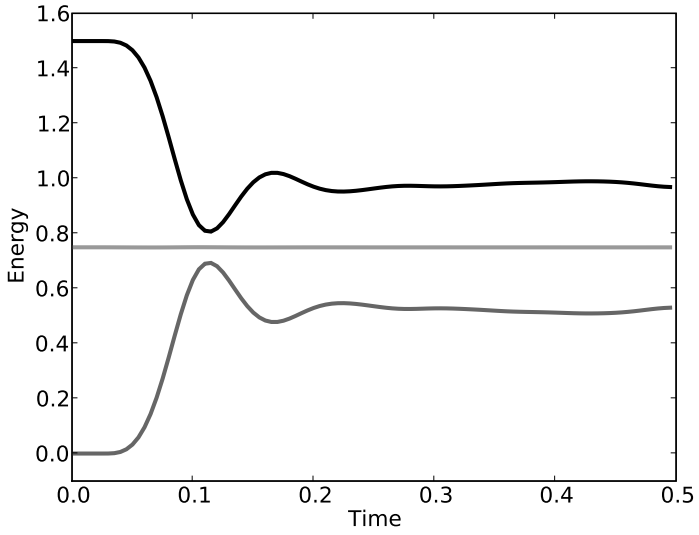

Figure 3.8: System kinetic (▬), potential (▬) and total (▬) energy evolution against time for a molecular simulation with periodic boundaries. Note – total energy is shown as half actual value to emphasise symmetry in kinetic and potential energies.

initial potential energy is zero. Periodic boundaries are used in all three directions. All quantities are given in terms of the length ℓ, atomic interaction strength ϵ and mass m of the particle so the LJ potential equation 3.8 with $\ell = \epsilon = m = 1$ is,

$$\Phi(\boldsymbol{r}_{ij}) = 4\left[\boldsymbol{r}_{ij}^{-12} - \boldsymbol{r}_{ij}^{-6}\right] - 4\left[\boldsymbol{r}_{c}^{-12} - \boldsymbol{r}_{c}^{-6}\right]. \tag{3.9}$$

The total energy remains (almost) constant, while the kinetic and potential interchange can be seen by the mirrored peaks and troughs. The use of the leapfrog algorithm to discretise the equation of motion is known to give good long time energy conservation properties (with timesteps from 0.001 up to 0.01, Rapaport (2004)). However, it can be seen that for very long simulations some energy drift occurs. Quantitative verification is performed by matching various parameter to the book by Rapaport (2004) such as evolution of total energy.

Note that the total energy in both systems is the same from the start of the simulation and stays constant throughout the time history of the simulation. The kinetic energies however, fluctuate in different ways in the two systems as they evolve through phase space along completely different trajectories.

The different evolutions of kinetic energy in table 3.1 represents a very important phenomenon in molecular simulation, which is the chaotic behaviour. This is an inevitable consequence of employing a finite precision computer in the solution of the equations of motion. Chaotic behaviour has wide ranging implications for molecular simulation, the most immediate of which is that matching the evolution of energy, or indeed any property between two molecular systems, is impossible beyond a certain number of timesteps. To demonstrate this, two identical simulations (same input data, operations and computer architecture/compiler) were run on a single processor and then split between two processors. The comparison of these two systems (serial-parallel) is shown in Figure 3.9. The divergence of trajectories, although initially at the limit of precision for a single molecule, eventually grows to 0.01% after 200 reduced time units and plateaus. This is

Table 3.1

	Rapaport Table 2.1			This Work's Simulation		
step	KE	Total Energy	Pressure	KE	Total Energy	Pressure
100	0.6592	0.9952	4.5371	0.6472	0.9951	4.6392
200	0.6490	0.9951	4.5829	0.6442	0.9950	4.6686
300	0.6397	0.9951	4.6454	0.6643	0.9951	4.3660
400	0.6477	0.9951	4.5675	0.6325	0.9951	4.6938
500	0.6596	0.9951	4.4702	0.6349	0.9951	4.6563
1000	0.6480	0.9950	4.5496	0.6391	0.9950	4.7037
2000	0.6497	0.9951	4.5371	0.6257	0.9951	4.7560
3000	0.6539	0.9952	4.5184	0.6582	0.9952	4.4758
7000	0.6370	0.9952	4.6203	0.6684	0.9952	4.3523

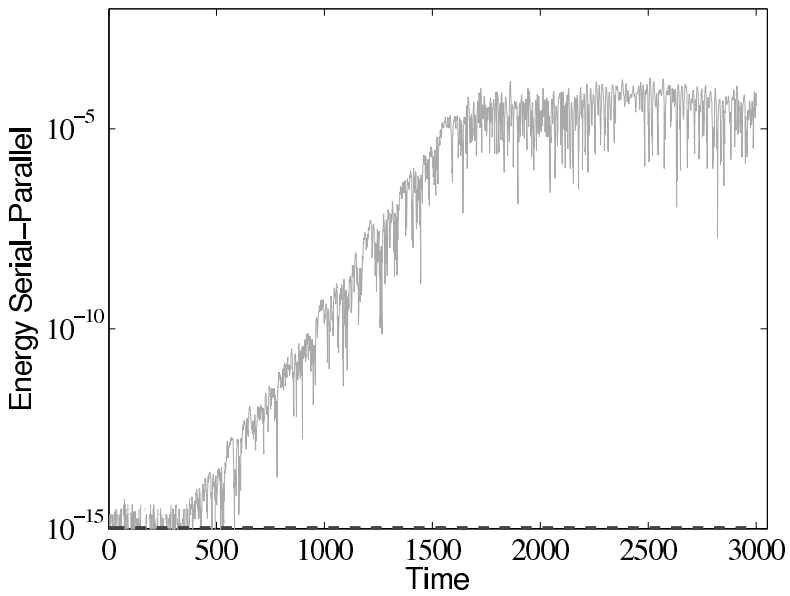

Figure 3.9: The discrepancy in energy measured for the parallel (—) or serial (**- -**) code compared to the serial code as reference for trajectory divergence. The discrepancy is defined as the total energy $\mathcal{E}_{parallel}$ from the parallel solution minus the serial solution $\mathcal{E}_{serial}$ divided by the serial solution: $[\mathcal{E}_{parallel} - \mathcal{E}_{serial}]/\mathcal{E}_{serial}$.

Table 3.2

Density	Rapaport Table 2.2			This Work's Simulation		
	Total Energy	KE	Pressure	Total Energy	KE	Pressure
0.8	0.650	0.995	4.537	0.650	0.997	4.554
0.6	0.823	0.994	1.954	0.823	0.995	1.964
0.4	0.915	0.994	0.815	0.915	0.995	0.818

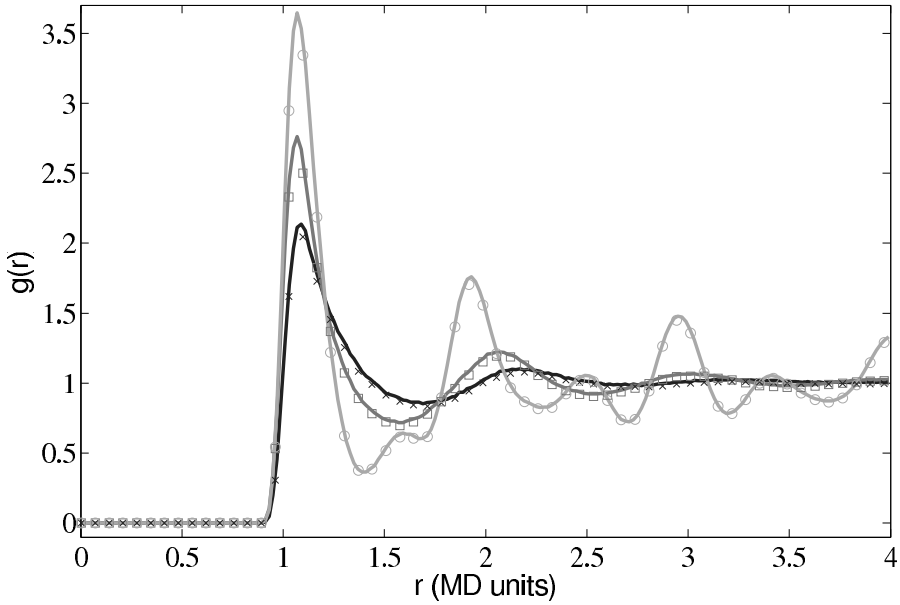

Figure 3.10: Molecular dynamics simulation RDF at densities $\rho = 0.6$ (×), $\rho = 0.8$ (□) and $\rho = 1.0$ (○), matched to results from Rapaport's `C++` program at the same densities (shown by lines with matching colours).

because the system's total energy is the same (to within 0.01% flucatations) and only the initial trajectories differ. This behaviour is observed for any changes to order of operations (during code development) or comparisons between restarted calculations. For this reason, initial agreement and trajectory divergence must be taken into account during the verification of changes made to parallel/serial codes. Any verification of new code developments therefore consist of checking agreement for the initial period of time (up to the divergence at ~ 1500 time units) and agreement of long time statistical properties.

The next table 3.2 compares the variation in energy at different densities to the values reported in Rapaport (2004). Very good agreement can be seen between the obtained results and those of Rapaport (2004).

Radial Distribution Functions

Further tests of the three dimensional code included comparing the radial distribution function (RDF), $g(r)$ as shown in Fig. 3.10.

The RDF is a normalised measure of the local particle number density as a function of

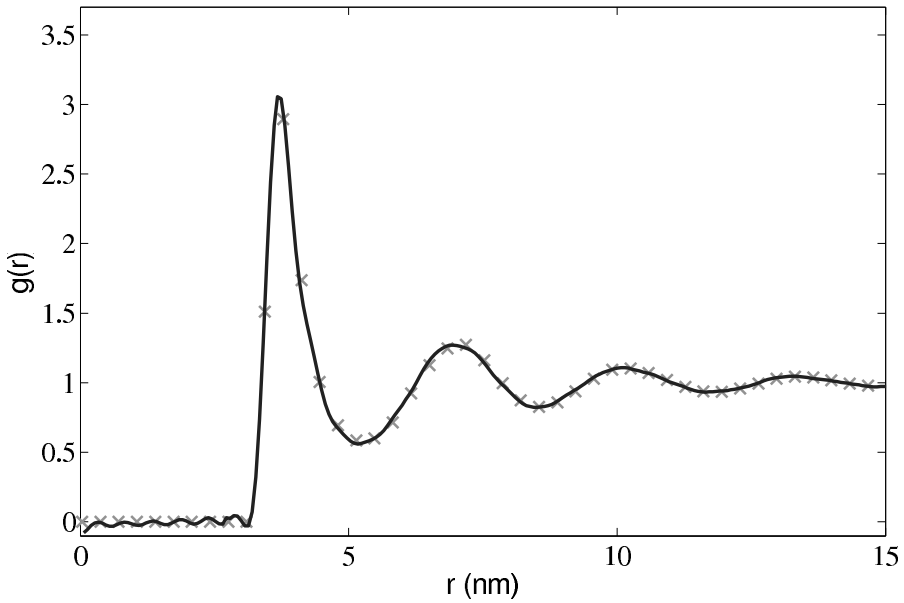

Figure 3.11: MD Radial Distribution Function (x) matched to experimental results (–) from Yamell *et al.* (1973) at $T = 85K$ and $\rho = 0.02125\text{Å}^{-3}$.

distance r from the centre of an arbitrary particle. Peaks and troughs indicate the presence of coordination shells and inter-shell regions, respectively. The RDF shows a key difference from models based on a dilute gas and a molecular dynamics simulation. It is for this reason that a full molecular simulation is required when small length scale effects become important.

The radial distribution function is an important quantity as it can also be obtained from experiments. For liquid Argon, experimental data from Yamell *et al.* (1973) with $T = 85K$ and $\rho = 0.02125\text{Å}^{-3}$ is shown in Figure 3.11. In LJ units this is $T^* = 0.708$ and $\rho^* = 0.8352$; simulation results for the corresponding case are shown on the same Figure 3.11.

Density, Temperature and Pressure Relationships

Density, Temperature and Pressure relationships are a thorough test of a molecular model over a range of different conditions. By adjusting the density and temperature the model is tested over a range of operating conditions – from solid to gas. Density, Temperature and Pressure relationships also allow verification of features such as the Nosé-Hoover thermostats and pressure calculations. The change of phase from a liquid to a solid can be observed for the lower temperature/density cases.

In comparing the results from the present MD code to those of Rapaport (2004), the LJ energy has been corrected using the standard long range correction factors (Allen & Tildesley, 1987) while the pressure results are not corrected. It is not clear from the text in Rapaport (2004) if this correction is applied to the energy or pressure. Rapaport (2004) suggests applying the correction to energy and not pressure as the magnitude is negligible in the latter case.

The density-pressure relationships are also compared to experimental data for liquid Argon at a temperature of $90.1K$ ($T^* = 0.75$), Itterbeek & Verbeke (1960). The experimental data is only available for a small density range, so the reference data for the LJ potential calculated using grand-canonical transition-matrix Monte Carlo (TMMC) with $r_c = 3.0$ (NIST, 2013), is

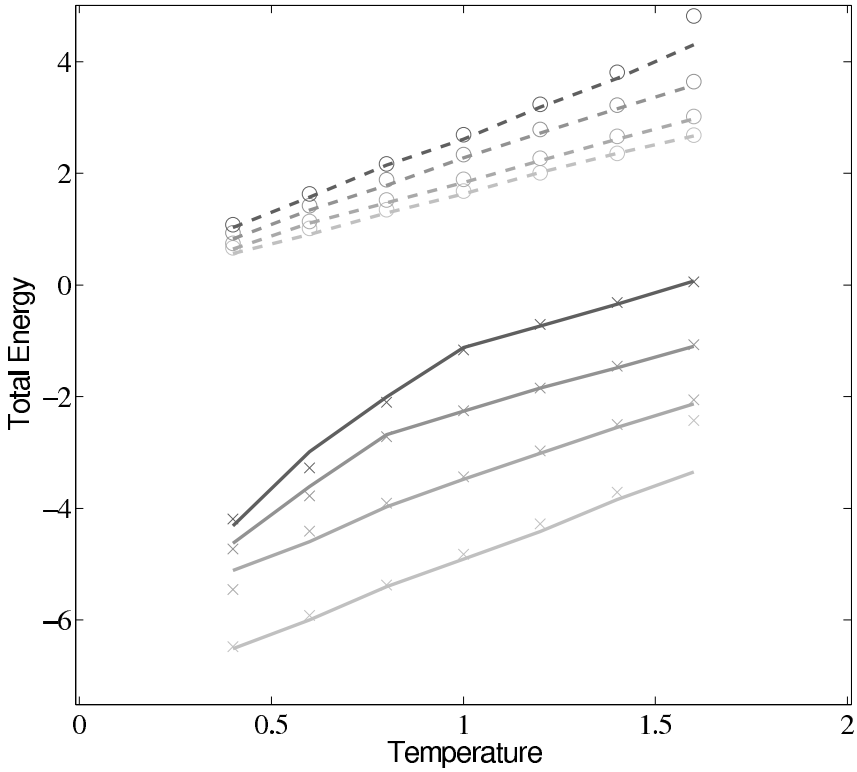

(a) Total energy vs temperature from MD code compared with Rapaport (2004)

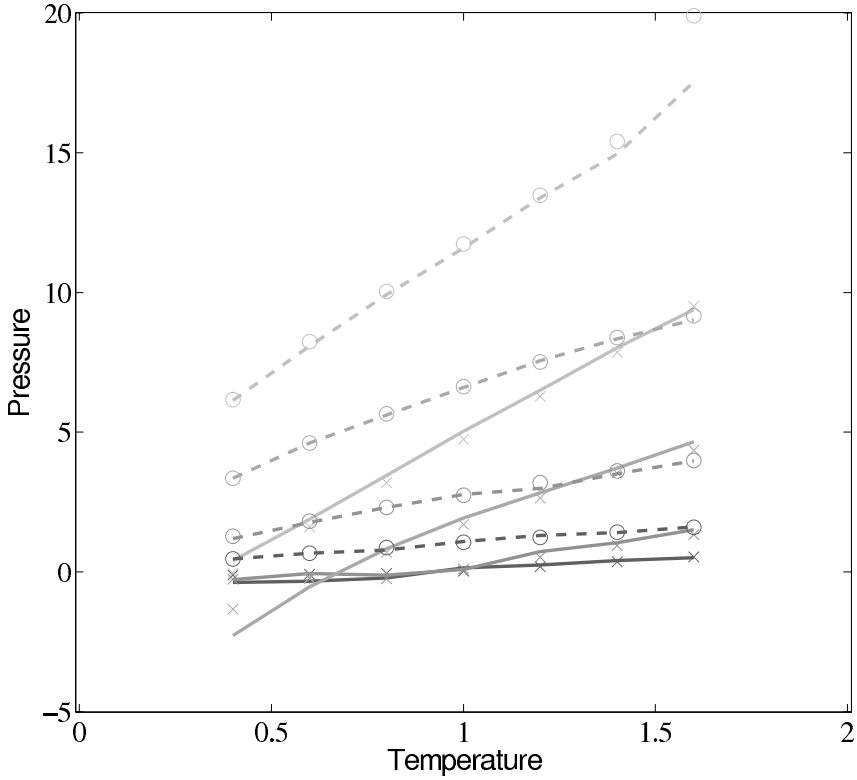

(b) Pressure vs temperature from MD code compared with Rapaport (2004)

Figure 3.12: (−) Rapaport Lennard-Jones ($r_c = 2.5$); (−−) Rapaport Weaks-Chandler-Andersen (WCA) ($r_c = 2^{\frac{1}{6}}$); (×) MD code Lennard-Jones ($r_c = 2.5$) (○) MD code WCA; (■) $\rho = 0.4$; (■) $\rho = 0.6$; (■) $\rho = 0.8$; (■) $\rho = 1.0$

also included. The TMMC reference data for the whole range is shown on the insert. In order to match the pressure, the standard long range correction must be applied. Two cutoff lengths are compared in the MD simulation, $r_c = 2.5$ and $r_c = 4.0$. The cutoff of 2.5 is chosen as a value commonly used in the literature, representing a good compromise between efficiency and accuracy (Rapaport, 2004). The cutoff value of $r_c = 4.0$ should be greater than required to capture all important interactions and match to experimental data. Reasonable agreement is observed between the MD, TMMC methods and experimental data, although the results for $r_c = 2.5$ appear to significantly underpredict the pressure. The longer MD cutoff, $r_c = 4.0$, provides closer agreement to both TMMC and experiments.

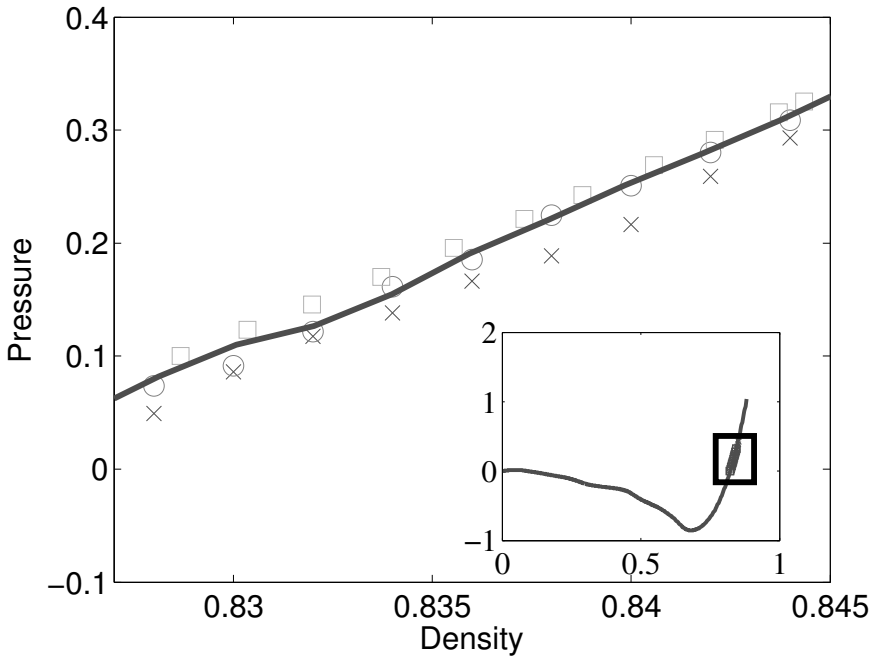

Figure 3.13: MD code Lennard-Jones for $r_c = 2.5$ (×) and $r_c = 4.0$ (◯), experimental results for liquid Argon (□) and benchmark data from the results for Lennard-Jones fluid using grand-canonical transition-matrix Monte Carlo with $r_c = 3.0$ (—) from the National Institute of Standards and Technology (NIST, 2013).

Non-equilibrium molecular dynamics simulations

Continuum fluid flow problems for which there exist analytical solutions to the Navier-Stokes provide a convenient test for non-equilibrium molecular dynamics (NEMD) algorithms. The case of Couette flow is considered here, using the time evolving analytical solution derived in appendix A,

$$u(y,t) = \sum_{n=1}^{M} -\frac{2U_0}{n\pi}\left(1 - e^{-\frac{(n\pi)^2 t}{H^2 Re}}\right) sin\frac{n\pi y}{H} + U_0\varphi\left(\frac{y}{L}\right), \tag{3.10}$$

where H is the domain height and U_0 is the wall velocity and Re is the Reynold number. This function was plotted over $M = 10,000$ modes.

Couette Flow

In this study, Couette flow was simulated by entraining a model liquid between two solid walls. The top wall was set in translational motion parallel to the bottom (stationary) wall and the evolution of the velocity profile towards the steady-state Couette flow limit was followed. All dimensions are given in LJ units.

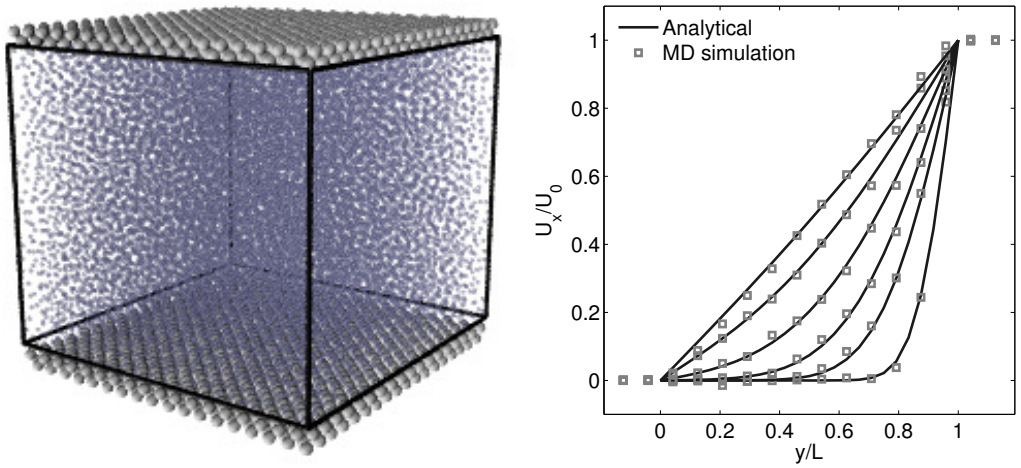

(a) Schematic of the MD Couette flow channel **(b)** Results from Couette Flow

Figure 3.14: The $y-$ dependence of the streaming velocity profile at times $t = 2^n$ for $n = 0, 2, 3, 4, 5, 6$ from right to left. The squares are the NEMD CV data values and the analytical solution Eq. (3.10) are the black lines.

The velocity profile is compared with the analytical solution of the unsteady diffusion equation. Four layers of tethered molecules were used to model each wall, with the top wall given a sliding velocity of, $U_0 = 1.0$ at the start of the simulation, time $t = 0$. The temperature of both walls was controlled by applying the Nosé-Hoover (NH) thermostat to the wall atoms (Hoover, 1991). The two walls were thermostatted separately, and the equations of motion of the wall atoms were,

$$\dot{\boldsymbol{r}}_i = \frac{\overline{\boldsymbol{p}}_i}{m_i} + U_0 \mathbf{n}_x^+, \tag{3.11a}$$

$$\dot{\overline{\boldsymbol{p}}}_i = \boldsymbol{F}_i + \boldsymbol{f}_{i_{\text{ext}}} - \xi \overline{\boldsymbol{p}}_i, \tag{3.11b}$$

$$\boldsymbol{f}_{i_{\text{ext}}} = \boldsymbol{r}_{i_0} \left(4k_4 r_{i_0}^2 + 6k_6 r_{i_0}^4 \right), \tag{3.11c}$$

$$\dot{\xi} = \frac{1}{Q_\xi} \left[\sum_{n=1}^{N} \frac{\overline{\boldsymbol{p}}_n \cdot \overline{\boldsymbol{p}}_n}{m_n} - 3T_0 \right], \tag{3.11d}$$

where $\mathbf{n}_x^+$ is a unit vector in the $x-$ direction (only non-zero for the top wall), $m_i \equiv m$, and $\boldsymbol{f}_{i_{\text{ext}}}$ is the tethered atom force, obtained using the formula of Petravic & Harrowell (2006) ($k_4 = 5 \times 10^3$ and $k_6 = 5 \times 10^6$). The vector, $\boldsymbol{r}_{i_0} = \boldsymbol{r}_i - \boldsymbol{r}_0$, is the displacement of the tethered atom, i, from its lattice site coordinate, $\boldsymbol{r}_0$. The Nosé-Hoover thermostat dynamical variable is denoted by ξ, $T_0 = 1.0$ is the target temperature of the wall, and the effective time constant or damping coefficient, in Eq. (3.11d) was given the value, $Q_\xi = N\Delta t$. The simulation was

carried out for a cubic domain of sidelength 27.40, of which the fluid region extent was 20.52 in the $y-$direction (see Figure 3.14a). Periodic boundaries were used in the streamwise (x) and spanwise (z) directions. The results presented in Figure 3.14b are the average of eight simulation trajectories starting with a different set of initial atom velocities. The lattice contained $16,384$ molecules and was at a density of $\rho = 0.8$. The molecular simulation domain was sub-divided into 16 averaging slices of height 1.72 and the velocity was determined in each of them. The results show good agreement in both space and time, although some discrepancy is observed near the molecular walls. This is due to molecular layering and stick-slip behaviour near the walls in the molecular system which is not captured in the no-slip boundary assumed in the continuum solution.

The case of Couette flow is revisited repeatedly in this work, using the CFD code and in coupled simulations. This case is chosen because it is simple enough to afford an analytical solution and has been widely studied in the MD, CFD and coupling literature. The Couette flow case for a wide range of pressures has been studied fully, as part of a side project to the work presented herein (Heyes *et al.*, 2012). The setup parameters used in this work are based on this published work Heyes *et al.* (2012), as are many of the insights into the behaviour of MD and coupled simulations.

3.3 Continuum code

3.3.1 Simple Finite Volume Solver

A two dimensional finite volume code which simulates the diffusive terms of the Navier Stokes equation has been developed to test the initial coupling. The unsteady diffusive equations are obtained by simplifying the 3 dimensional Navier Stokes Eq. (2.50) under the assumptions of developed laminar flow, a wide channel in the spanwise direction, negligible pressure gradient and no gravitational effects.

$$\frac{\partial u}{\partial t} = \frac{1}{Re}\frac{\partial^2 u}{\partial y^2}. \tag{3.12}$$

This equation is discretised in space using a central finite volume scheme on a uniform grid (Hirsch, 2007). The subscripts I and J denote cell indices in the x and y direction respectively. The equation was discretised in time using a simple forward Euler scheme

$$u_{IJ}^{t+1} = u_{ij}^{t} + \frac{\Delta t}{Re}\frac{u_{I+1,J} + u_{I-1,J} + u_{I,J+1} + u_{I,J-1}}{4(\Delta y)^2}, \tag{3.13}$$

with the corners cells calculated using an average of the three adjacent cells. A halo cell system was used to specify boundary conditions with a no-slip boundary on the top, moving wall on the bottom and periodic boundaries at both ends. The halo velocity was set to ensure the boundary condition on the surface of a finite volume cell. The analytical solution Eq. (3.10) is compared to a numerical simulation with 100 cells in Figure 3.15a. The analytical solution in Figure 3.15a appears to agree exactly at all points (N.B. outer cell values appear larger/smaller as boundary value is enforced at cell surface). In order to study this agreement, the L_2 norm is plotted in Figure 3.15b. In order to obtain the L_2 norm, the square of the discrepancy between analytical and numerical solutions at every point in the domain is obtained. The square root of the sum of

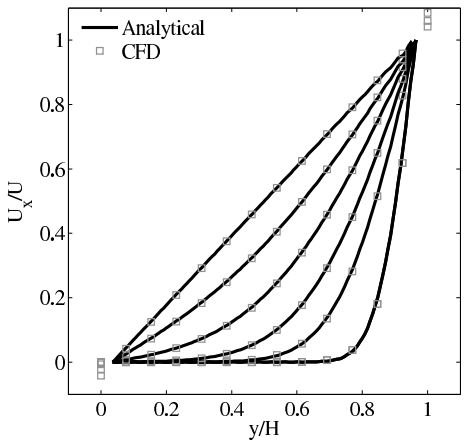

(a) Plot of analytical solution and numerical solution at times ($t = 0.1 \times 2^n, n = 1, 2, .., 14$).

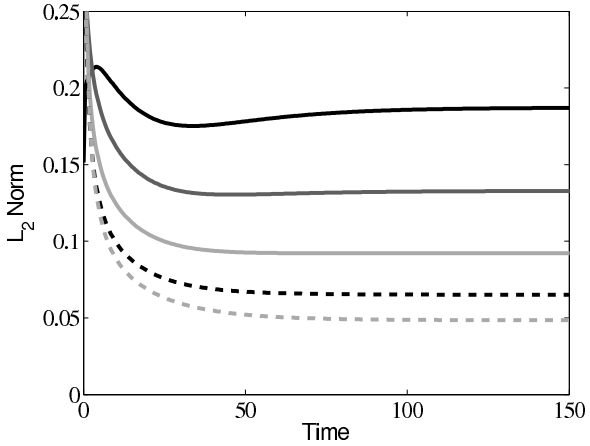

(b) Plot of L_2 error between analytical and numerical solutions against time

Figure 3.15: Plot of CFD Couette flow against the analytical solution (left) and the L_2 norm error against time (right) for 6 (—),12 (—),24 (—),48 (- -) and 96 (- -) cells. Reynolds number $Re = 10$, height $L = 10$ and wall velocity is $U_0 = 1$.

these squared discrepancies is the L_2 norm. The L_2 norm error can be seen to decrease as the solution tends to the steady state and as the number of cells used (resolution) increases in figure 3.15b. The initial error is attributed to the use of an impulse started plate which the analytical solution would not be able to accurately re-create. The agreement between solutions appears to be good, verifying the CFD code outlined in this section and to be used in coupled Couette flow simulation.

The in-group Direct Numerical Simulation code, $\mathcal{T}ransFlow$, is discussed in the next section. Coupling to $\mathcal{T}ransFlow$ is essential in order to facilitate simulation of more complicated cases than Couette flow.

3.3.2 The continuum DNS algorithm: $\mathcal{T}ransFlow$

The $\mathcal{T}ransFlow$ code is designed to preform direct numerical simulation (DNS) of the Navier-Stokes, Eq. (2.50). Simulations are performed using a staggered grid algorithm with a local volume flux formulation in general (curvilinear) coordinates (Rosenfeld *et al.*, 1991; Wu & Durbin, 2001). The time advancement of the convection terms is solved by a second order Adams-Bashforth scheme and the diffusive terms by Crank-Nicholson scheme (Hirsch, 2007). The solution to the Poisson equation for pressure $P(\mathbf{x}, t)$ is obtained by the fractional step method devised by Chorin (1967). Provided the streamwise and spanwise directions are periodic and homogeneous, Fourier transforms are employed to accelerate the solution of the possion equation. The $\mathcal{T}ransFlow$ algorithm has been verified in prior investigations of shear flow stability (Zaki & Durbin, 2005, 2006).

$\mathcal{T}ransFlow$ is parallelised using the Message Passing Interface (MPI). Performance testing was carried out using a curvilinear mesh, for turbulent flow around a compressor blade. The flow was simulated using $370,000$ grid points per MPI-task, on an SGI Altix 4700, Intel Itanium 2 (HLRB, Super-Computing Centre, Germany). During these parallel performance tests, the equations were advanced 1000 time steps, and each time-step required 19 seconds of wall-clock

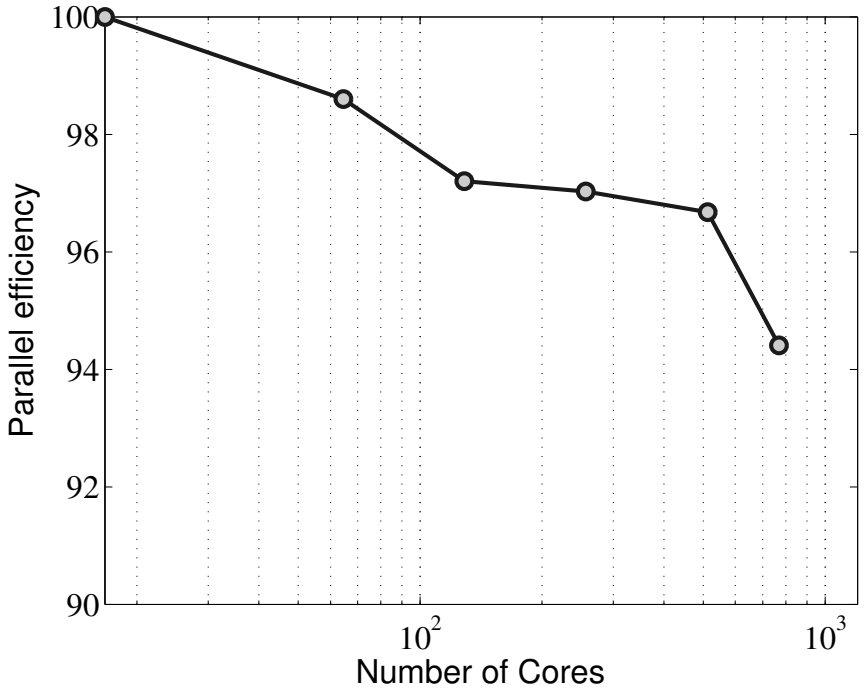

Figure 3.16: Parallel performance of TransFlow.

time. The weak scaling performance results are shown in Figure 3.16. Weak scaling means as the number of cores is increased, the number of cells per core is held fixed. Parallel efficiency is defined with respect to the performance on 16 cores and at 768 cores, the algorithm performed at 94.4% parallel efficiency.

Both the molecular and continuum algorithms have been constructed as a collection of FORTRAN 90 modules, which allows for efficient interfacing to other multi-physics algorithms. The coupling is described in the next section.

3.4 Coupling of the DNS and MD algorithms

This section outlines the coupler library. This has been developed with the intention of making the source code available to the research community. As a result, it is written using modern FORTRAN (2008) with a completely modular structure and a clear functional interface to each routine to facilitate interoperability with other languages. Thorough documentation has been included in the source codes, formatted to allow generation of HTML based documentation using f90doc (Available online; accessed 07/13 *http://erikdemaine.org/software/f90doc/doc.html*). As of May 2013, the code is freely available under a GNU GPL v3 license (Smith & Trevelyan, 2013). The development of the code has been documented in two technical reports, Anton & Smith (2012) and Smith *et al.* (2013).

Combining the capabilities of the DNS and MD codes requires interfacing and synchronising several elements of the two simulations. Each code models part of the physical problem, and is therefore responsible for a region of the computational domain. An overlap exists between those

two domains; MD and continuum information must be "communicated" between the two codes in this region, in order to dynamically couple the two simulations.

The most significant challenge is to carry out efficient and scalable (thousands of processors) computations of large continuum-molecular coupled systems. To do this, a framework must be developed to allow large scale coupling between the two parallel codes.

The proposed framework with separated coupler module and halo exchange is general enough to allow implementation of many of the existing coupling strategies (O'Connell & Thompson, 1995; Nie *et al.*, 2004*a*; Flekkøy *et al.*, 2000; Hadjiconstantinou, 1998; Werder *et al.*, 2005; Delgado-Buscalioni & Coveney, 2003*a*). This generality ensures that the code development will continue to be useful as the field develops.

3.4.1 Coupler Outline

The coupler (CPL) consists of a series of function calls which are loosely based on the MPI framework in terms of both functionality and scope. They have been developed in FORTRAN 2008 with sufficient generality that they can be used as a language independent API through `External` functional interfaces. These routines are compiled into a library module which is linked to both the MD and CFD codes. Both codes are then run using the MPI multiple program multiple data paradigm (MPMD) with a call of the form,

```
mpiexec -n 128 ./md.exe :  -n 8 ./cfd.exe.
```

The codes have entirely separate scopes and can only communicate through the coupler routines. The use of the MPMD framework enforces this separation and prevents conflicts between matching nomenclature in both the MD and CFD codes. It also pre-empts the use of dynamic processor allocation under MPI2, (`MPI_spawn`), providing a framework to support dynamic load balancing during a simulation.

The coupler consists of three classes of functions – setup, exchange and enquiry. Details of the structure and routines are included below:

- **Setup** The setup process is run once per simulation and entirely establishes the relationships between the two codes. The coupler setup routines and all coupler parameters are contained in a FORTRAN 2003 module with the `protected` attribute. This ensures *only* the three setup routines located inside this module can changes parameters internal to the coupler library. This prevents side-effects resulting from the interface with the CFD/MD codes as well as functions inside the coupler. The coupler setup functions have extensive error checking to ensure the inputs are of the correct form and the setup is completed correctly. A key part of the philosophy of the coupler is that both codes have copies of an identical set of read-only parameters including the complete knowledge of the processor topology of both regions. This ensures inter-communication between the codes is kept to a minimum.
  - `CPL_create_comm` – Setup MD/CFD `INTRA_COMM` and `INTER_COMM` between them. This should be called after both codes have initialised MPI. It defines a global communicator `CPL_WORLD_COMM`, local intra-communicators `MD_COMM`/`CFD_COMM` and an inter-communicator `CPL_INTER_COMM` between them to allow information exchange between the two domains Gropp *et al.* (1999*b*). The COUPLER.in input file is read to define relative processor topologies. The coupler input also includes parameters which are not specified from either of the coupled domains, such as the location and size of the

overlap regions, the ratio of timestep between the two codes, as well as the facility to redefine variables in both codes in line with the coupled setup.

- `CPL_CFD/MD_init` – Input CFD/MD parameters required to setup coupler parameters. Using a minimal set of parameters from both the CFD and MD code, together with the coupler input file, the entire coupling relationship between both domains is setup. The parameters are a minimal set of required and an extended range of optional arguments passed to the `CPL_CFD/MD_init` function. A hierarchy of communicators are established as part of the mapping process, including communicators containing only topologically overlapping processors `CPL_OLAP_COMM` and an optimised communicator based on the network topology of the overlapping processors `CPL_GRAPH_COMM` derived from the `MPI_graph` function. The details of the communicators are largely hidden from the user as described in the next section.

- **Exchange** The exchange routines are the core part of the coupler library. They include the following subroutines:

  - `CPL_gather` – CFD processors gather required data from overlapping MD processors.
  - `CPL_scatter` – CFD processors scatter required data to overlapping MD processors.
  - `CPL_send` – Send from current realm to overlapping processors on other realm.
  - `CPL_recv` – Receive on current realm to overlapping processors on other realm.

  All routines require two inputs; an array containing data for *all* the cells on the calling processor and the global cell numbers specifying the location and range (global extents) of the subset of these cells that the user wants to exchange. The use of global extents prevents the user from requiring any knowledge of the processor's local numbering system, communicators or the mapping between domains. The global cell number conventions used in exchanges are identical on all processors, so the same input is used on the corresponding exchange routine in the other realm. Only processors with cells in the specified region send and receive the data between the domains. The data array can be of arbitrary size, allowing any number of properties to be exchanged (*e.g.* density (1), velocity (3) or stresses (9)). As an example, consider sending the MD velocity to be used as the CFD boundary condition for the setup discussed in chapter 2 (Specifically Figure 2.2). Each MD processor averages the velocity and passes its local array of 3 averaged velocity components per cell to `CPL_send`. The extents are specified to include all global CFD cells in xz plane at the CFD minimum cell location in y. Every CFD processor posts a corresponding `CPL_recv` with the same global extents. Every CFD processor on the bottom of the domain then receives an array containing the required boundary cells per processor.

- **Enquiry** A library of functions to retrieve parameters defined in the other realm or internal to the coupler. The use of intent out on all enquiry routines forces the user to make local copies of the returned variables. This is a further safeguard against corruption of data in the coupler and the associated side effects.

  - `CPL_get` – Returns any parameter considered `protected public` in the coupler library.
  - `CPL_Cart_coords` – Returns processor cartesian topology for any processor on either realm.
  - `CPL_COMM_rank` – Returns processor rank in any of the communicators
  - `CPL_extents` – Various extent routines to return cells on the current processor, in

the overlap region or for arbitrary `INPUT=limits` subject to the limits of the current processor and overlap region.
As the coupled topology is set-up at the beginning, all processors have a copy of all processor information in both regions. As a results, the enquiry routines require no communication.

As data from the MD and CFD codes must be manipulated before being passed to the CPL, it is recommended that coupler calls be done in socket routines which contain code written specifically for a given CFD or MD implementation. Calls to the coupler routines in either code can be removed by the use of pre-processing flags or dummy socket routines to allow each code to continue to function separately.

The following flowchart in Figure 3.4.1 shows the conceptual operation of a typical coupled setup.

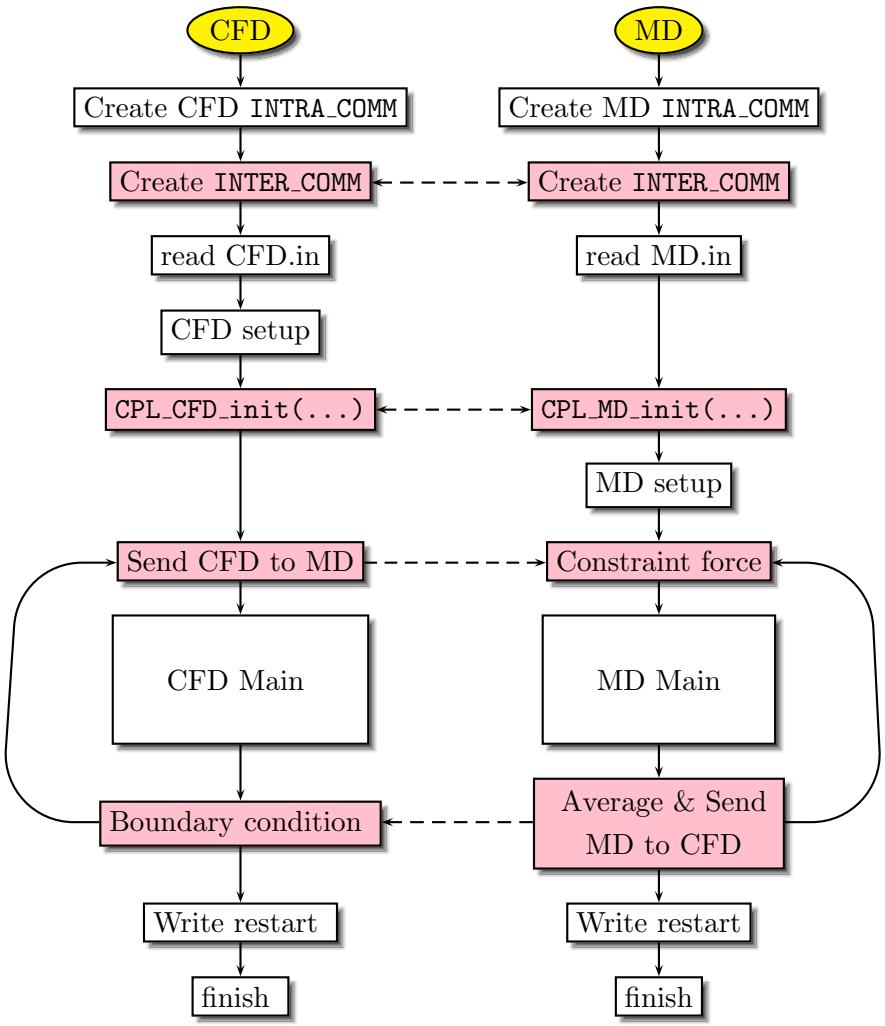

Figure 3.17: Flowchart outlining a coupled simulation using the CPL-library. The pink boxes are coupled operations, while the white boxes are internal CFD (left) and MD (right) operations.

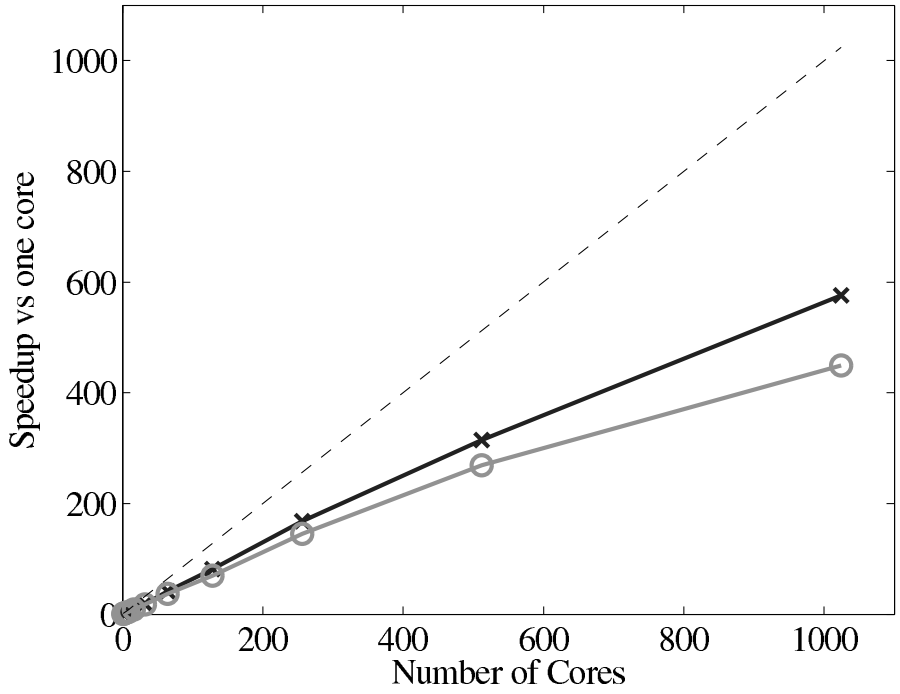

(a) Parallel speedup of the MD solver only (×), coupled code (∘) against the ideal speedup (−−)

Figure 3.18: Scalability of the coupled application. The data for this plot was obtained from runs on HECToR as part of the work detailed in Anton & Smith (2012).

3.4.2 Benchmarking and scalability of the coupled algorithm

As the coupling module is expected to load balance between both simulations and interface them efficiently, it is reasonable to expect that the coupled code will scale as well as the individual codes. The coupling region is local and can be decomposed spatially for parallel computations in the same manner as both of the codes it couples. As there is no greater requirement for communication in the coupling region, the observed scaling should be similar.

For the case of laminar Couette flow, the computational requirements of the continuum solver are almost negligible, and the continuum solver is run on a single processor with 64 cells in x and 7 in y. The speedup of the coupled code therefore depends almost entirely on the scaling of the MD solver and the coupler. If the coupler is performing efficiently, this combined speedup can be expected to be similar to the scaling of the MD solver alone. The scaling of the coupler is compared to
StreamMDin Figure 3.18a, up to 1024 processes. The system size ($N = 3,317,760$) is the same as used in the previous all MD scaling tests, section 3.2.4. The coupled timestep ratio is 50.

Figure 3.18a demonstrates that the couplers performance only slightly deteriorates speedup. It is therefore not a severe bottleneck of performance of the coupled codes.

3.4.3 Verification of the Coupler

A part of the development of the coupler library, simple functions (*e.g.* sinusoidal profiles) are used to verify the passing is implemented correctly. A testing suite was written to 'soak test' the various coupler routines for a wide range of processor topologies in both the CFD and MD

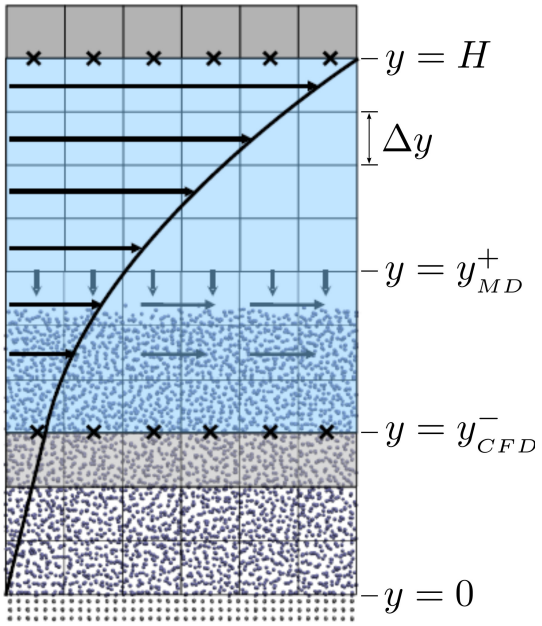

Figure 3.19: Coupled schematic showing a typical setup used in a coupling scheme, including arrows to denote the velocities in the continuum and the applied forces in the molecular (constraint and boundary forces). The crosses denote the locations at which the boundary conditions are specified in the CFD code by setting the values of the halo cells (grey). The key dimensions required to entirely define the coupled simulation are included and defined in the text for the various cases described in this section.

domains.

In this subsection, the coupler will be verified using three different types of coupling scheme from the literature. These include the state coupling of O'Connell & Thompson (1995) and Nie *et al.* (2004*a*) both discussed in section 2.5.2 as well as the flux coupling scheme of Flekkøy *et al.* (2000) discussed in section 2.5.3. These three coupling schemes will be revisited in chapter 5 where several interesting feature will be highlighted. A general schematic for the cases in this section is shown in Figure 3.19.

O'Connell & Thompson (1995)

The paper by O'Connell & Thompson (1995) presented an investigation of a sliding bottom wall in the molecular dynamics region with a fixed top wall in the continuum region. The bottom wall accelerates from stationary with a decaying exponential velocity of the form $u_w(t) = U(1-e^{-t/t_0})$ where $U = 1$ and $t_0 = 160$ in LJ units. The results of O'Connell & Thompson (1995) are recreated in Figure 3.20 as part of the coupler verification. These results are compared to the time evolving analytical solution provided in the thesis of O'Connell (1995). The essential parameters of the setup are identical and the reader is referred to O'Connell & Thompson (1995) for full details. Only the main parameters and differences are summarised here. The molecular domain had dimensions $11.9 \times 18.7 \times 8.5$ at $\rho = 0.81$ resulting in $N = 1330$ molecules. The cutoff length was $r_c = 2.2$ and the temperature $T = 1.1$. A bottom wall of thickness 2.34 was kept in place using the Petravic & Harrowell (2006) tethering potential introduced in section 3.2.5. The same density was used for the solid walls and the wall/fluid interaction potential $\epsilon = 1.0$ was chosen

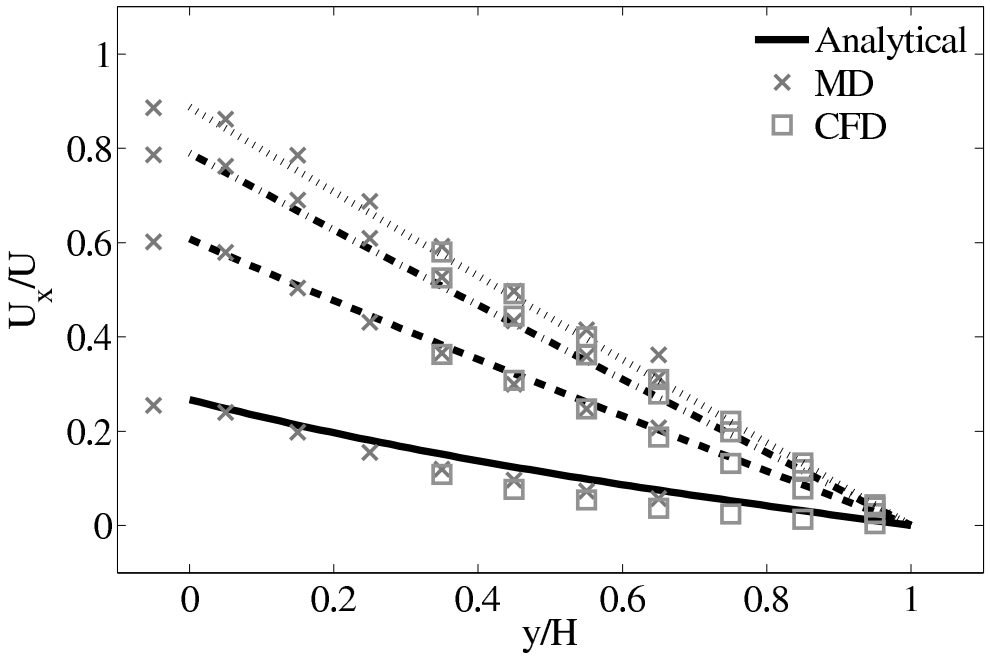

Figure 3.20: Coupled MD-CFD start-up plate simulation using the O'Connell & Thompson (1995) coupling scheme. The results are plotted at the same times as the work of O'Connell & Thompson (1995), $t = 100, 200, 300, 400$. Note the (bottom) MD wall slides and the (top) continuum is fixed.

instead of the 0.6 used by O'Connell & Thompson (1995). The domain was terminated by the O'Connell & Thompson (1995) boundary force (Eq. (2.80)) applied at the top to prevent molecules escaping. Application of this boundary force results in a compression of the MD system causing the propagation of a shock wave. To prevent this effect, a number of molecules are removed to ensure the density remains at the intended $\rho = 0.81$ in the presence of the boundary force. A Nosè-Hoover thermostat was applied instead of the Langevin thermostat used in O'Connell & Thompson (1995). A number of thermostatting strategies were tested including z-component only, profile unbiased thermostat (PUT) and wall only thermostatting. No discernible difference was found in the behaviour of the profile when compared to the analytical solution.

The setup of the coupled case was specified by the various parameters in Figure 3.19, including molecular domain top, $y^+_{MD} = 18.7$, CFD domain bottom $y^-_{CFD} = 9.34$, total coupled domain height $H = 25.68$ and cell size $\Delta y = 2.34$. The overlap region consists of four overlap cells. The arbitrary coupling strength coefficient is set to $\xi = 0.01$, as in O'Connell & Thompson (1995).

Molecules in the top MD cell experience the boundary force (Eq. (2.80)) to prevent them escaping the domain. In addition, the top cell, together with the cell below, experiences a constrained force (Eq. (2.72a)/ Eq. (2.72b)) to force the average molecular velocity inside to match the continuum. The halo cell for the CFD was obtained by averaging the momentum, Eq. (2.68), in the pure MD region at the location covered by the bottom grey cell in Figure 3.19.

The coupling was verified first using the 2D simple finite volume CFD solver outlined in section 3.3.1 with fixed top boundary condition and bottom boundary passed from the MD region. The CFD solver used a viscosity of $\mu = 2.14$ (or equivalent Reynolds number of $Re = 0.378$) which was matched to the MD value obtained from Green-Kubo (Green, 1954; Kubo, 1957) calibration calculations.

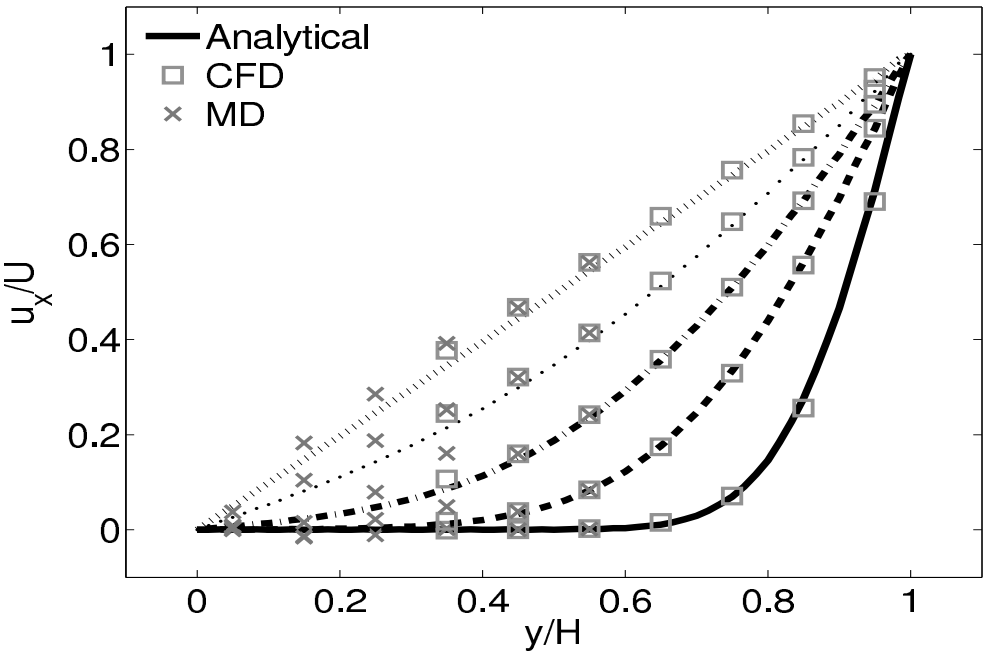

Figure 3.21: Coupled MD-CFD impulse started plate simulation using the Nie *et al.* (2004*a*) coupling scheme. The results are plotted at the same times as in the work of Nie *et al.* (2004*a*), $t = 10, 40, 75, 150, 1500$, denoted by the varying analytical lines.

Good agreement was observed to the analytical solution for an accelerating plate. The setup of this problem applies the moving boundary condition in the molecular region, which in turn drives the continuum due to the coupling between them.

This model implements no mass flux and the scaling parameters ξ is said to cause lagging behind the continuum solution in time evolving flows by Nie *et al.* (2004*a*). The coupling method presented in the work of Nie *et al.* (2004*a*) is claimed to ameliorate this problem. The implementation of this method using the CPL library is presented in the next section.

Nie *et al.* (2004*a*)

This section implements the coupled simulation of Nie *et al.* (2004*a*). The setup of the coupled simulation in this section aims to be similar to that of the previous section while matching the essential parameters of Nie *et al.* (2004*a*). As before, the reader is referred to the original work (Nie *et al.*, 2004*a*) for full details of the setup used. The simulation is impulse started Couette flow, where the top wall in the CFD domain was moved at a velocity of $u_w(t) = 1$ and the bottom wall in the molecular region was stationary.

The MD domain size was $34.06 \times 34.06 \times 34.06$ with a density of $\rho = 0.81$ giving $N = 27,200$ molecules. The molecular domain was simulated on 4 processes with topology $2 \times 2 \times 1$. The bigger domain size provides better statistics and each cell was twice the size (in each direction) of those used by O'Connell & Thompson (1995). Nie *et al.* (2004*a*) use the average of 10 MD ensembles, each of width 4.82, to provide boundary conditions for a single CFD instance. The implementation here instead uses a wider domain in z and a single MD simulation. A bottom wall of thickness 2.62 was kept in place using the Petravic & Harrowell (2006) tethering potential introduced in the NEMD section 3.2.5. The same density was used for the solid walls and fluid

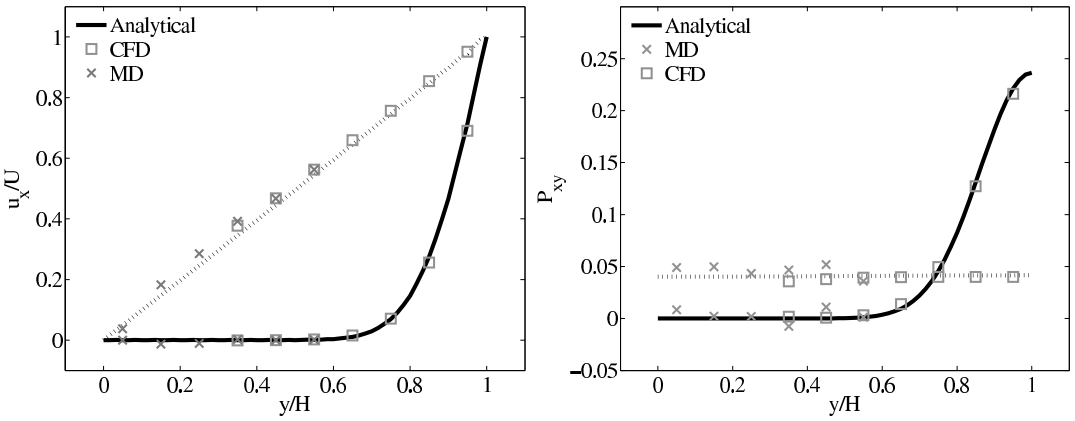

(a) Velocity **(b)** Stresses

Figure 3.22: Velocity (left) and stress (right) plotted at times $t = 10$ and at steady state $t \to \infty$ using the Nie *et al.* (2004*a*) type constraint.

regions and for simplicity the wall/fluid interaction potential is set to $\epsilon = 1.0$, instead of the 0.6 used by Nie *et al.* (2004*a*). The cutoff length was $r_c = 2.2$ and the temperature $T = 1.1$. A Nosè-Hoover thermostat was applied instead of the Langevin. Again application of the thermostat in z only, in a profile unbiased manner or simply thermostatting the wall results in similar agreement to the Couette flow time-evolving analytical solution shown in Figure 3.21.

The setup of the coupled case was specified by molecular domain top, $y^+_{MD} = 31.3$, CFD domain bottom $y^-_{CFD} = 15.6$, total coupled domain height $H = 52.1$ and cell size $\Delta y = 5.12$. The overlap was of size 15.6, split into four overlap cells. Molecules in the top MD cell are subjected to the boundary forces (Eq. (2.81)) to prevent them from escaping. In addition, the top cell, together with the cell below, experiences a constrained force (Eq. (2.75)) to ensure average molecular velocities are matched to the continuum. The halo for the CFD was obtained by averaging the pure MD region below the overlap region. The ratio of timesteps between the MD and CFD simulations was 50.

The coupling was verified using the 2D simple finite volume CFD solver and full 3D DNS code $\mathcal{T}rans\mathcal{F}low$ (run on a single processor). Both CFD solvers used a viscosity of $\mu = 2.14$ (or equivalent Reynolds number).

The velocity against time shows good agreement to the analytical solution in Figure 3.22a.

The stress in both the CFD and MD simulation can also be evaluated for the coupled case and the agreement compared to the analytical solution for stress (see appendix A Eq. (A.12)). In the MD region, the stress was obtained from the volume average (VA) localisation of the virial stress (Cormier *et al.*, 2001) discussed in section 2.62. In the CFD region, the stress can be calculated using the hydrodynamic pressure, the gradient of velocity and the shear viscosity via Eq. (2.48). The stress in both simulations and across the coupled region can be seen to match the analytical solution as shown in Figure 3.22b. The constraint on velocity can be seen to ensure the stress is also matched between both domain. In the next section, the stress itself is constrained, using the flux coupling schemes of Flekkøy *et al.* (2000).

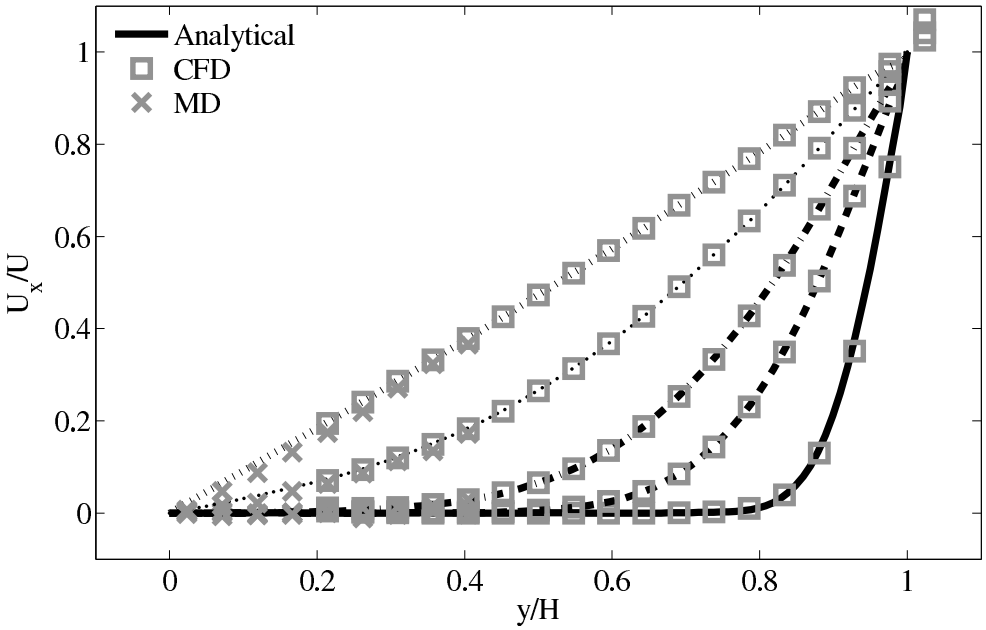

Figure 3.23: Coupled MD-continuum impulse started plate simulation using the Flekkøy *et al.* (2000) coupling scheme at $t = 100, 400, 750, 1500, 15000$, denoted by the varying analytical lines.

Flekkøy *et al.* (2000)

The final verification case is based on the flux coupling work of Flekkøy *et al.* (2000), who model Couette flow using an MD domain between two CFD regions. The results presented are only for steady state Couette flow. This section extends these results to verify the time evolution of a coupled Couette flow with flux coupling. A much larger molecular domain was used to test the coupler for large system sizes. This also addresses the higher averaging requirement of flux coupling outlined in section 2.5.3. The MD domain size was $164.2 \times 51.3 \times 41.0$ at density $\rho = 0.8$, resulting in $N = 276,480$ molecules. The molecular domain was simulated on 32 processes with topology $8 \times 2 \times 2$. The bottom wall was tethered with a thickness of 5.13 and a Nosé-Hoover thermostat was applied to only the wall molecules with a temperature setpoint of $T = 1.0$. The WCA potential was used ($r_c = 2^{\frac{1}{6}}$) for computational efficiency.

The paper by Flekkøy *et al.* (2000) is unclear of exact domain sizes but states that cells of size 7.6 are employed with 10 cells shown in the MD domain on their *Fig. 2* (*i.e.* an MD domain of 76.0). This MD region is sandwiched between two CFD domains in Flekkøy *et al.* (2000) with a coupling region on each side of width 22.8. Only one sided coupling was used here, again based on the setup shown in Figure 3.19. A domain of similar height without the bottom coupling region was used, $y^+_{MD} = 46.17$. The cells were chosen to be slightly smaller than Flekkøy *et al.* (2000) and consistent with Nie *et al.* (2004*a*) at $\Delta y = 5.13$. The continuum domain bottom was located at $y^-_{CFD} = 25.65$ and the total domain was twice the size of Nie *et al.* (2004*a*) with a height of $H = 107.8$

The constraint force of Flekkøy *et al.* (2000) given in Eq. (2.91) with weighting function Eq. (2.92) applies both the appropriate direct pressure and shear pressure to the MD domain. As the pressure applied is not designed to prevent molecules from escaping, only to match the continuum pressure, specular walls are also employed. These reflect molecules back with identical x and z velocities and exactly opposite y components of velocity. Specular walls are chosen as

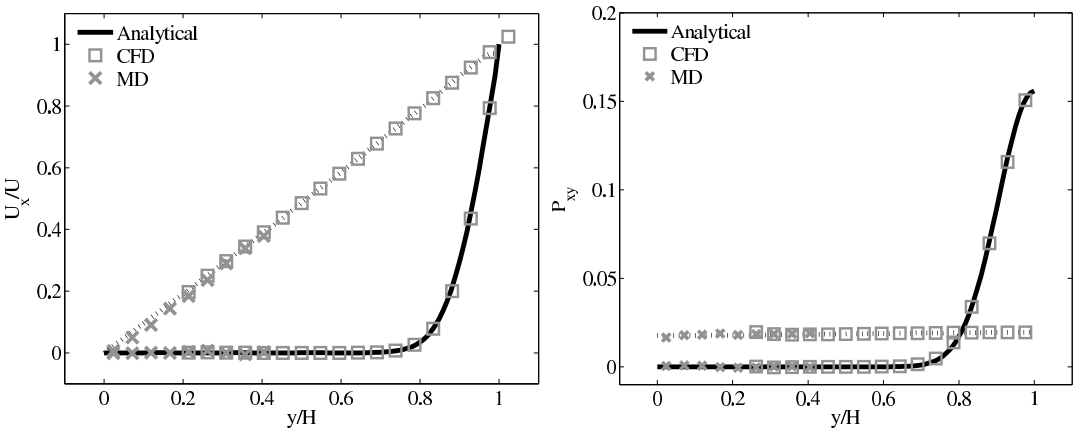

(a) Velocity **(b)** Stresses

Figure 3.24: Velocity (left) and stress (right) plotted at times $t = 100$ and at steady state $t \to \infty$ using the Flekkøy *et al.* (2000) constraint.

the continuum solver was incompressible and does not expect a mass flow into the bottom of the continuum domain, therefore restricting mass flux is consistent. Moving these walls with a mean velocity, as in the work of (Werder *et al.*, 2005), was unnecessary as the mean flow rate in the wall normal direction is, on average, zero for this case.

The viscosities are also matched in this simulation with continuum viscosity set to $\mu = 1.6$ (again from Green-Kubo autocorrelation functions). The coupling was between the MD and the full 3D DNS code $\mathcal{T}rans\mathcal{F}low$ with Reynolds number $Re = 0.5$. The parallel nature of the DNS code was employed with the $32 \times 16 \times 8$ CFD cells split between $4 \times 2 \times 1$ processes.

The coupled solution for velocity is compared to the analytical solution in Figure 3.23. Good agreement is observed at equivalent times to those shown for Nie *et al.* (2004*a*) in the previous section. As the domain is over 3 times the size of the previous Nie *et al.* (2004*a*) case, the time scales are proportional to the square of the domain height and are scaled accordingly. Note the greater number of symbols due to the much greater numbers of cells in both domains.

As the stress in both regions was matched by the coupler, this is seen to match in Figure 3.24b. The velocity can also be seen to agrees in Figure 3.24a as a result of this stress matching scheme. The near wall agreement in Figure 3.24a appears to be superior to the Nie *et al.* (2004*a*) coupling shown in Figure 3.22a. This is a consequence of the larger system size which reduces the effect of near wall molecular behaviour and improves velocity averages.

The halo for the CFD (bottom grey cells in Figure 3.19) was obtained by averaging the momentum in the pure MD domain below the overlap region in line with Eq. (2.68). This is a departure from the work of Flekkøy *et al.* (2000) who average the stresses from the MD region in line with Eqs. (2.87) and (2.88). The manner in which to obtain the stress tensor from the MD is not clear (as discussed in section 2.4.3), so the averaging of stress will be deferred until the CV form is developed in chapter 4. This mixed coupling is based on the work of Ren (2007), where flux-state coupling is found to be stable, while flux-flux coupling was found to be unstable. There are also concerns about the sample requirements, which are said to be prohibitive for flux schemes in Hadjiconstantinou *et al.* (2003). However, a parameter study of error in appendix E of this work demonstrate these averages requirements for flux shemes, while often large, are not prohibitive for all cases. Despite this, the mixed flux-state exchange was deemed to be a simpler

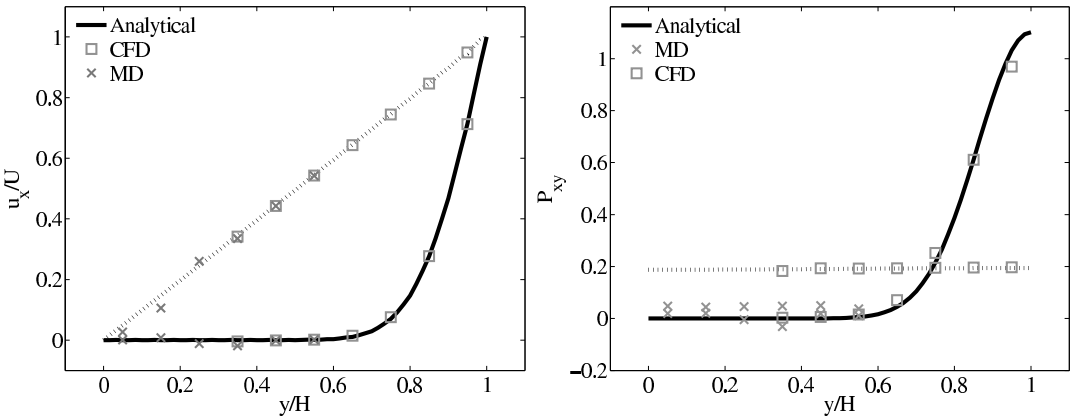

(a) Viscosity $\mu_{CFD} = 10.0$, $\mu_{MD} = 2.14$ **(b)** Viscosity $\mu_{CFD} = 10.0$, $\mu_{MD} = 2.14$

Figure 3.25: Velocity and stress evolution at similar couette profile development times to Fig 3.22 using the Nie *et al.* (2004*a*) type constraint. Note the scale on the axis is four times that used in Figure 3.22.

and more robust way to test the coupling software.

Having verified the coupler gives identical results using both flux and state coupling, the impact of specifying the wrong viscosity is evaluated in the next section. The validity of state based coupling schemes is shown to be contingent on a consistent viscosity being specified in both domains. The impact of this finding is then discussed.

3.4.4 Mismatched Viscosity in Couette Flow

The case of coupled Couette flow with a mismatch of viscosity between the continuum and molecular systems is considered in this subsection.

When coupling the continuum and molecular systems, the scaling between the two regions must be consistent. As discussed in sections 2.2 and 2.3 the continuum and molecular domains are scaled based on different parameters. The molecular region is based on length scale ℓ, mass m and energy ϵ, while the continuum is dependent on the Reynolds number $Re = \rho UL/\mu$. The two regions are matched by ensuring the length scales ℓ vs. L and densities ρ_{CFD} vs. $\rho_{MD} = \rho_{MD}(m, \ell)$ are consistent. The velocity or stress matching is then ensured by the coupling mechanism. Viscosity is a tuneable parameter in the continuum but it is a measureable quantity in a molecular simulation, not an input parameter. Nie *et al.* (2004*a*) use a viscosity of $\mu = 2.14$ based on previous simulations. As shown in the previous subsection, using this pre-matching of viscosity, good agreement is observed for both the velocity and stress between both systems, Figure 3.22. For the case where the viscosities are not the same in both regions, the velocity profiles can be seen to match but the stresses do not, Figure 3.25. Consider next the flux couping of Flekkøy *et al.* (2000). The use of the same viscosity in both domain ($\mu = 1.6$) obtained by prior simulation, Figure 3.24 in the previous subsection showed good agreement for both velocity and stresses. The use of different viscosity in both regions results in disagreement in the velocity but good agreement in the stresses, Figure 3.26.

The results for a mismatched stress in figure 3.26 are consistent with the simulation of two phase fluids with different viscosities. Molecular fluid will typically experience different viscosity measurements in the vicinity of the walls or at high shear rates (shear thinning). By using state

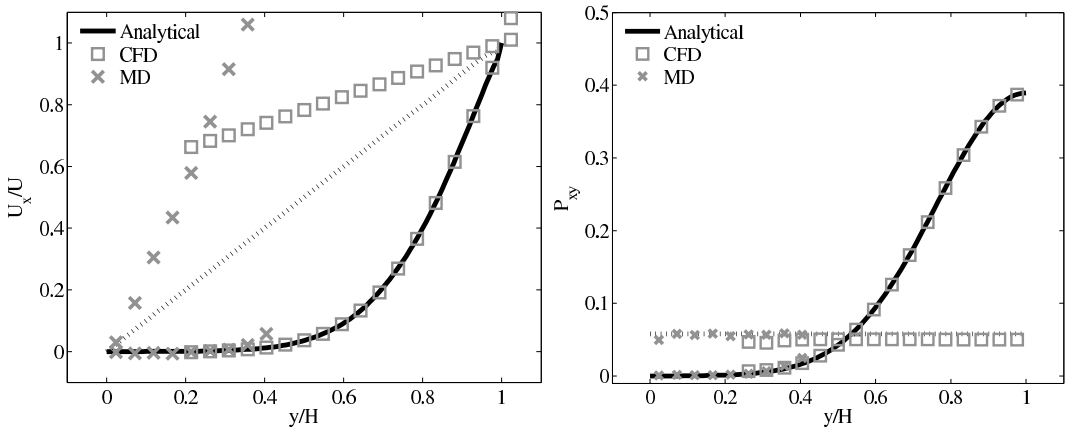

(a) Viscosity $\mu_{CFD} = 10.0$, $\mu_{MD} = 2.14$ **(b)** Viscosity $\mu_{CFD} = 10.0$, $\mu_{MD} = 1.6$

Figure 3.26: Velocity and stress evolution at similar couette profile development times to Fig 3.24 using the Flekkøy *et al.* (2000) constraint.

coupling, this behaviour would not be correctly transmitted to the CFD realm as a constant viscosity is implicitly assumed throughout the MD. In addition, it is possible to unknowingly simulate cases with viscosity difference and still obtain apparently correct velocity profiles. The conclusion is that the flux coupling scheme are more general, require no assumption of the viscosity in the MD region and simply apply a force consistent with the current state of stress in the CFD.

The results from this study of mismatched viscosity suggest that a more stringent set of tests are required in order to establish the consistency between the two realms of a coupled simulation, a problem that motivates the next chapter with the development of a consistent control volume framework for both systems. In addition, flux coupling scheme are more general and should be preferred in the computational implementation of a general purpose coupling simulation tool, which was the aim of this chapter. As they are not currently derived from a constrained dynamics approach, some theoretical development is required and this motivates the work in chapter 5.

This section has introduced a coupling library for simulation of large scale cases on many processors. The intention was to couple simulations which approach scales of engineering interest, including the modelling of turbulent phenomenon. However, there are a number of problems to overcome before a generalised coupling scheme can be implemented. The overview of this chapter is given in the next section.

3.5 Overview

This chapter includes the details of the software developments and verifications in the development of a coupled continuum-molecular solver. In order to couple molecular dynamics (MD) to continuum computational fluid mechanics (CFD), a new MD code was developed, a CFD code was adapted and a coupling library designed to manage the data exchange between them.

In section 3.2, the details of the development and testing of a new MD code were presented. The MD code was designed to use cell/neighbour lists, Hilbert curve re-ordering and other optimisations to obtain similar serial speeds to LAMMPS. The code is then parallelised using MPI to allow running on high performance computing platforms. The parallel performance is

tested and shows 94% efficiency when scaling from 8 processors to 1024. The MD code was verified by checking the energy conservation, trajectory agreement (and divergence), radial distribution function, phase diagrams and simulation of Couette flow. The optimised MD code is therefore ready for large-scale simulation of molecular dynamics and coupling problems, and is applied in the next two chapters.

Section, 3.3, outlined the development and verification of a simple CFD code. This was used as part of the development of the coupling library and for simple CFD test cases. For more complicated cases, the $\mathcal{T}ransFlow$ DNS code was used. Scaling properties of $\mathcal{T}ransFlow$ are provided demonstrating the code is 94.4% efficient when scaling from 16 cores to 768.

The final part of this chapter, section 3.4, outlined the development of a robust and minimal coupling (CPL) library. This was designed as a language independent APIs using FORTRAN 2008, which implements the data exchange between the CFD and MD codes. Implementation of coupling should be as simple as initialising the CPL module by passing the key simulation parameters from both MD/CFD codes. The data can be exchanged by `CPL_send`/`CPL_recv` calls which ensure all data is passed correctly. The library was soak tested and verified for range of cases and topologies from the literature (O'Connell & Thompson, 1995; Nie *et al.*, 2004*a*; Flekkøy *et al.*, 2000). In order to test the scaling of the coupler, performance of a CPL simulation was compared to an uncoupled case. The difference in speedup on 1024 processor was found to be 575 for the full MD and 449 for a coupled case, compared to the ideal 1024. The coupler is therefore seen to have minimal impact on the scaling of the two codes.

The conclusion of this chapter is that all three codes are ready for large-scale simulations. However, the conceptual and mathematical framework for a general-purpose simulation of turbulent flow is not yet developed. Therefore, the next two chapters are dedicated to the development of this framework. The CPL library is ready for the time when coupled simulation is possible on a large scale.

Chapter 4

The Control-Volume Representation of Molecular Dynamics

4.1 Introduction

It is advantageous to cast the fluid dynamics equations in a consistent form for both the molecular, mesoscale and continuum approaches. This objective is achieved using a Control Volume (CV) formulation applied to a molecular system. This is one of the main innovations of this work, as the construction enables a formally rigorous link between the continuum and discrete formulations. The resulting CV operator is instrumental in the derivation of rigorous localised constraint equations for use in coupled simulations in the next chapter. The work in this chapter is a slightly more thorough version of a manuscript published in Physical Review E (Smith *et al.*, 2012). It is expected that the methodology developed in this chapter will be applicable to a wide range of non-equilibrium molecular dynamics problems.

The Control Volume approach is widely adopted in continuum fluid mechanics, where Reynolds Transport Theorem (Reynolds, 1903) relates Newton's laws of motion for macroscopic fluid parcels to fluxes through a CV. In this form, fluid mechanics has had great success in simulating both fundamental (Zaki & Durbin, 2005, 2006) and practical (Hirsch, 2007; Rosenfeld *et al.*, 1991; Zaki *et al.*, 2010) flows. However, when the continuum assumption fails, or when macroscopic constitutive equations are lacking, a molecular-scale description is required. Examples include nano-flows, moving contact lines, solid-liquid boundaries, non-equilibrium fluids, and evaluation of transport properties such as viscosity and heat conductivity (Evans & Morriss, 2007).

Molecular Dynamics (MD) involves solving Newton's equations of motion for an assembly of interacting discrete molecules. Averaging is required in order to compute properties of interest, e.g. temperature, density, pressure and stress, which can vary on a local scale especially out of equilibrium (Evans & Morriss, 2007). As discussed in section 2.4, a rigorous link between mesoscopic and continuum properties was established in the seminal work of Irving & Kirkwood (1950), who related the mesoscopic Liouville equation to the differential form of continuum fluid mechanics. However, the resulting equations at a point were expressed in terms of the Dirac δ function [1] — a form which is difficult to manipulate and cannot be applied directly in a molecular simulation. Furthermore, a Taylor series expansion of the Dirac δ functions was

[1] Strictly a generalised function.

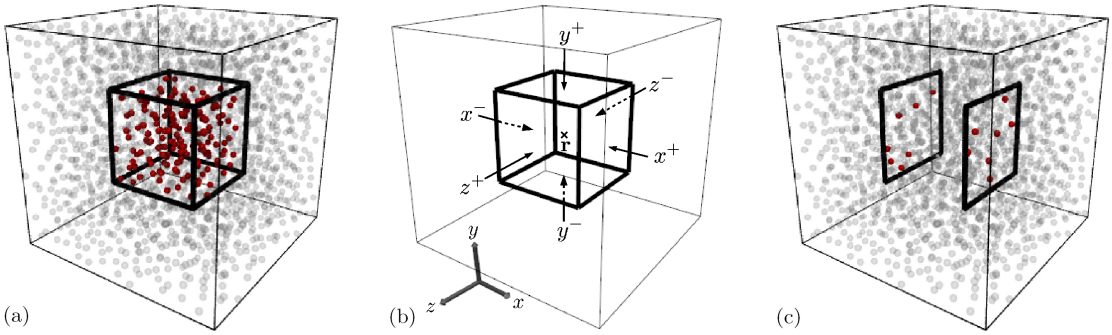

Figure 4.1: The CV function and its derivative applied to a system of molecules. The figures were generated using the VMD visualisation package, (Humphrey *et al.*, 1996). From left to right, (a) Schematic of ϑ_i which selects only the molecules within a cube, (b) Location of cube centre $\boldsymbol{r}$ and labels for cube surfaces, (c) Schematic of $\partial\vartheta_i/\partial x$ which selects only molecules crossing the x^+ and x^- surface planes.

required to express the pressure tensor. The final expression for pressure tensor is neither easy to interpret nor to compute (Zhou, 2003). As a result, there have been numerous attempts to develop an expression for the pressure tensor for use in MD simulation, as discussed in section 2.4.3 (Parker, 1954; Noll, 1955; Tsai, 1978; Todd *et al.*, 1995; Han & Lee, 2004; Hardy, 1982; Lutsko, 1988; Cormier *et al.*, 2001; Zhou, 2003; Murdoch, 2007, 2010; Schofield & Henderson, 1982; Admal & Tadmor, 2010). Some of these expressions have been shown to be equivalent in the appropriate limit. For example, Heyes *et al.* (2011)) demonstrated the equivalence between the Method of Planes (MOP Todd *et al.* (1995)) and Volume Average (VA Lutsko (1988)) in the limiting case of a zero thickness volume.

In order to avoid use of the Dirac δ function, the current work adopts a Control Volume representation of the MD system, written in terms of fluxes and surface stresses. This approach is in part motivated by the success of the control volume formulation in continuum fluid mechanics. At a molecular scale, control volume analyses of NEMD simulations can facilitate the evaluation of local fluid properties. Furthermore, the CV method also lends itself to coupling schemes between the continuum and molecular descriptions, as discussed in section 2.5 (O'Connell & Thompson, 1995; Hadjiconstantinou, 1998; Li *et al.*, 1997; Hadjiconstantinou, 1999; Flekkøy *et al.*, 2000; Wagner *et al.*, 2002; Delgado-Buscalioni & Coveney, 2003*a*; Curtin & Miller, 2003; Nie *et al.*, 2004*a*; Werder *et al.*, 2005; Ren, 2007; Borg *et al.*, 2010).

In section 4.2, a Lagrangian to Control Volume ($\mathcal{LCV}$) conversion function is used to express the mesoscopic equations for mass and momentum fluxes. Section 4.2.3 focuses on the stress tensor, and relates the current formulation to established definitions within the literature (Lutsko, 1988; Cormier *et al.*, 2001; Todd *et al.*, 1995). In Section 4.3, the CV equations are derived for a single microscopic system, and subsequently integrated in time in order to obtain a form which can be applied in MD simulations. The conservation properties of the CV formulation are demonstrated in NEMD simulations of Couette flow in Section 4.4. Finally, the key equations of this chapter are summarised and the main results outlined in the concluding section 4.5.

4.2 The Control Volume Formulation

In order to cast the governing equations for a discrete system in CV form, a 'selection function' ϑ_i is introduced, which isolates those molecules within the region of interest. This function is obtained by integrating the Dirac δ function, $\delta(\boldsymbol{r}_i - \boldsymbol{r})$, over a cuboid in space, centred at $\boldsymbol{r}$ and of side length $\Delta\boldsymbol{r}$ as illustrated in figure 4.1a [2]. Using $\delta(\boldsymbol{r}_i - \boldsymbol{r}) = \delta(x_i - x)\delta(y_i - y)\delta(z_i - z)$, the resulting triple integral is,

$$\begin{aligned}
\vartheta_i &\equiv \int_{x^-}^{x^+}\int_{y^-}^{y^+}\int_{z^-}^{z^+} \delta(x_i - x)\delta(y_i - y)\delta(z_i - z)dxdydz \\
&= \Big[\Big[\Big[H(x_i - x)H(y_i - y)H(z_i - z)\Big]_{x^-}^{x^+}\Big]_{y^-}^{y^+}\Big]_{z^-}^{z^+} \\
&\quad = \left[H(x^+ - x_i) - H(x^- - x_i)\right] \\
&\quad \times \left[H(y^+ - y_i) - H(y^- - y_i)\right] \\
&\quad \times \left[H(z^+ - z_i) - H(z^- - z_i)\right], \qquad (4.1)
\end{aligned}$$

where H is the Heaviside function, and the limits of integration are defined as, $\boldsymbol{r}^- \equiv \boldsymbol{r} - \frac{\Delta\boldsymbol{r}}{2}$ and $\boldsymbol{r}^+ \equiv \boldsymbol{r} + \frac{\Delta\boldsymbol{r}}{2}$, for each direction (see Fig. 4.1b). Note that ϑ_i can be interpreted as a Lagrangian-to-Control-Volume conversion function ($\mathcal{LCV}$) for molecule i. It is unity when molecule i is inside the cuboid, and equal to zero otherwise, as illustrated in Fig. 4.1a. Using L'Hôpital's rule and defining, $\Delta V \equiv \Delta x\Delta y\Delta z$, the $\mathcal{LCV}$ function for molecule i reduces to the Dirac δ function in the limit of zero volume,

$$\delta(\boldsymbol{r} - \boldsymbol{r}_i) = \lim_{\Delta V \to 0} \frac{\vartheta_i}{\Delta V}.$$

The spatial derivative in the x direction of the $\mathcal{LCV}$ function for molecule i is,

$$\frac{\partial \vartheta_i}{\partial x} = -\frac{\partial \vartheta_i}{\partial x_i} = \left[\delta(x^+ - x_i) - \delta(x^- - x_i)\right] S_{xi}, \qquad (4.2)$$

where S_{xi} is

$$\begin{aligned}
S_{xi} \equiv &\left[H(y^+ - y_i) - H(y^- - y_i)\right] \\
&\left[H(z^+ - z_i) - H(z^- - z_i)\right]. \qquad (4.3)
\end{aligned}$$

Eq. (4.2) isolates molecules on a 2D rectangular patch in the yz plane. The derivative $\partial\vartheta_i/\partial x$ is only non-zero when molecule i is crossing the surfaces marked in Fig. 4.1c, normal to the x direction. The contribution of the i^{th} molecule to the net rate of mass flux through the control surface is expressed in the form, $\boldsymbol{p}_i \cdot d\mathbf{S}_i$. Defining for the right x surface,

$$dS_{xi}^{+} \equiv \delta(x^+ - x_i)S_{xi}, \qquad (4.4)$$

[2] The cuboid is chosen as the most commonly used shape in continuum mechanic simulations on structured grids, although the process could be applied to any arbitrary shape

and similarly for the left surface, dS^-_{xi}, the total flux Eq. (4.2) in any direction $\boldsymbol{r}$ is then,

$$\frac{\partial \vartheta_i}{\partial \boldsymbol{r}} = d\mathbf{S}_i^+ - d\mathbf{S}_i^- \equiv d\mathbf{S}_i. \tag{4.5}$$

The $\mathcal{LCV}$ function is key to the derivation of a molecular-level equivalent of the continuum CV equations, and it will be used extensively in the following sections. The approach in sections 4.2.1, 4.2.2 and 4.2.8 shares some similarities with the work of Serrano & Español (2001) which considers the time evolution of Voronoi characteristic functions. However the $\mathcal{LCV}$ function has precisely defined extents which allows the development of conservation equations for a microscopic system. In the following treatment, the CV is fixed in space (i.e., $\boldsymbol{r}$ is not a function of time). The extension of this treatment to an advecting CV is made in Appendix C.1.

4.2.1 Mass Conservation for a Molecular CV

In this section, a mesoscopic expression for the mass in a cuboidal CV is derived. The time evolution of mass within a CV is shown to be equal to the net mass flux of molecules across its surfaces.

The mass inside an arbitrary CV at the molecular scale can be expressed in terms of the $\mathcal{LCV}$ as follows,

$$\int_V \rho(\boldsymbol{r},t)dV = \int_V \sum_{i=1}^{N} \Big\langle m_i \delta(\boldsymbol{r}_i - \boldsymbol{r}); f \Big\rangle dV \;\; = \sum_{i=1}^{N} \int_{x^-}^{x^+}\int_{y^-}^{y^+}\int_{z^-}^{z^+} \Big\langle m_i \delta(\boldsymbol{r}_i - \boldsymbol{r}); f \Big\rangle dxdydz = \sum_{i=1}^{N} \Big\langle m_i \vartheta_i; f \Big\rangle. \tag{4.6}$$

Taking the time derivative of Eq. (4.6) and using Eq. (2.33),

$$\frac{\partial}{\partial t}\int_V \rho(\boldsymbol{r},t)dV = \frac{\partial}{\partial t}\sum_{i=1}^{N}\Big\langle m_i\vartheta_i; f\Big\rangle = \sum_{i=1}^{N}\Big\langle \frac{\boldsymbol{p}_i}{m_i}\cdot\frac{\partial}{\partial \boldsymbol{r}_i} m_i\vartheta_i + \boldsymbol{F}_i\cdot\frac{\partial}{\partial \boldsymbol{p}_i} m_i\vartheta_i; f\Big\rangle. \tag{4.7}$$

The term $\partial m_i\vartheta_i/\partial \boldsymbol{p}_i = 0$, as ϑ_i is not a function of $\boldsymbol{p}_i$. Therefore,

$$\frac{\partial}{\partial t}\int_V \rho dV = -\sum_{i=1}^{N}\Big\langle \boldsymbol{p}_i\cdot\frac{\partial \vartheta_i}{\partial \boldsymbol{r}}; f\Big\rangle, \tag{4.8}$$

where the equality, $\partial\vartheta_i/\partial\boldsymbol{r}_i = -\partial\vartheta_i/\partial\boldsymbol{r}$ has been used. From the continuum mass conservation given in Eq. (2.35), the macroscopic and mesoscopic fluxes over the surfaces can be equated,

$$\sum_{faces}^{6}\int_{S_f}\rho\boldsymbol{u}\cdot d\mathbf{S}_f = \sum_{i=1}^{N}\Big\langle \boldsymbol{p}_i\cdot d\mathbf{S}_i; f\Big\rangle. \tag{4.9}$$

The mesoscopic equation for evolution of mass in a control volume is given by,

$$\frac{\partial}{\partial t}\sum_{i=1}^{N}\Big\langle m_i\vartheta_i; f\Big\rangle = -\sum_{i=1}^{N}\Big\langle \boldsymbol{p}_i\cdot d\mathbf{S}_i; f\Big\rangle. \tag{4.10}$$

Appendix C.2 shows that the surface mass flux yields the Irving & Kirkwood (1950) expression for divergence as the CV tends to a point (i.e. $V \to 0$), in analogy to Eq. (2.40).

4.2.2 Momentum Balance for a Molecular CV

In this section, a mesoscopic expression for time evolution of momentum within a CV is derived. The starting point is to integrate the momentum at a point, given in Eq. (2.54), over the CV,

$$\int_V \rho(\boldsymbol{r},t)\boldsymbol{u}(\boldsymbol{r},t)dV = \sum_{i=1}^{N}\left\langle \boldsymbol{p}_i\vartheta_i; f\right\rangle. \tag{4.11}$$

Following a similar procedure to that in section 4.2.1, Eq. (2.33) is used to obtain the time evolution of the momentum within the CV,

$$\frac{\partial}{\partial t}\int_V \rho(\boldsymbol{r},t)\boldsymbol{u}(\boldsymbol{r},t)dV = \frac{\partial}{\partial t}\sum_{i=1}^{N}\left\langle \boldsymbol{p}_i\vartheta_i; f\right\rangle = \sum_{i=1}^{N}\Big\langle \underbrace{\frac{\boldsymbol{p}_i}{m_i}\cdot\frac{\partial}{\partial \boldsymbol{r}_i}\boldsymbol{p}_i\vartheta_i}_{\mathcal{K}_\mathcal{T}} + \underbrace{\boldsymbol{F}_i\cdot\frac{\partial}{\partial \boldsymbol{p}_i}\boldsymbol{p}_i\vartheta_i}_{\mathcal{C}_\mathcal{T}}; f\Big\rangle, \tag{4.12}$$

where the terms $\mathcal{K}_\mathcal{T}$ and $\mathcal{C}_\mathcal{T}$ are the kinetic and configurational components, respectively. The kinetic part is,

$$\mathcal{K}_\mathcal{T} = \sum_{i=1}^{N}\left\langle \frac{\boldsymbol{p}_i}{m_i}\cdot\frac{\partial}{\partial \boldsymbol{r}_i}\boldsymbol{p}_i\vartheta_i; f\right\rangle = \sum_{i=1}^{N}\left\langle \frac{\boldsymbol{p}_i\boldsymbol{p}_i}{m_i}\cdot\frac{\partial \vartheta_i}{\partial \boldsymbol{r}_i}; f\right\rangle, \tag{4.13}$$

where $\boldsymbol{p}_i\boldsymbol{p}_i$ is the dyadic product. For any surface of the CV, here x^+, the molecular flux can be equated to the continuum convection and pressure on that surface,

$$\int_{S_x^+}\rho(x^+,y,z,t)\boldsymbol{u}(x^+,y,z,t)u_x(x^+,y,z,t)dydz + \int_{S_x^+}\mathbf{K}_x^+dydz = \sum_{i=1}^{N}\left\langle \frac{\boldsymbol{p}_i p_{ix}}{m_i}dS_{xi}^+; f\right\rangle,$$

where $\mathbf{K}_x^+$ is the kinetic part of the pressure tensor due to molecular transgressions across the x^+ CV surface. The average molecular flux across the surface is then,

$$\{\rho\boldsymbol{u}u_x\}^+ + \mathbf{K}_x^+ = \frac{1}{\Delta A_x^+}\sum_{i=1}^{N}\left\langle \frac{\boldsymbol{p}_i p_{ix}}{m_i}dS_{xi}^+; f\right\rangle, \tag{4.14}$$

where the continuum expression $\{\rho\boldsymbol{u}u_x\}^+$ is the average flux through a flat region in space with area $\Delta A_x^+ = \Delta y\Delta z$. This kinetic component of the pressure tensor is discussed further in Section 4.2.3.

The configurational term of Eq. (4.12) is,

$$\mathcal{C}_\mathcal{T} = \sum_{i=1}^{N}\left\langle \boldsymbol{F}_i\cdot\frac{\partial}{\partial \boldsymbol{p}_i}\boldsymbol{p}_i\vartheta_i; f\right\rangle = \sum_{i=1}^{N}\left\langle \boldsymbol{F}_i\vartheta_i; f\right\rangle, \tag{4.15}$$

where the total force $\boldsymbol{F}_i$ on particle i is the sum of pairwise-additive interactions with potential ϕ_{ij}, and from an external potential ψ_i.

$$\vartheta_i\boldsymbol{F}_i = -\vartheta_i\frac{\partial}{\partial \boldsymbol{r}_i}\left(\sum_{j\neq i}^{N}\phi_{ij} + \psi_i\right).$$

It is commonly assumed that the potential energy of an interatomic interaction, ϕ_{ij}, can be

divided equally between the two interacting molecules, i and j, such that,

$$\sum_{i,j}^{N} \vartheta_i \frac{\partial \phi_{ij}}{\partial \boldsymbol{r}_i} = \frac{1}{2} \sum_{i,j}^{N} \left[\vartheta_i \frac{\partial \phi_{ij}}{\partial \boldsymbol{r}_i} + \vartheta_j \frac{\partial \phi_{ji}}{\partial \boldsymbol{r}_j} \right], \tag{4.16}$$

where the notation $\sum_{i,j}^{N} = \sum_{i=1}^{N} \sum_{j \neq i}^{N}$ has been introduced for conciseness. Therefore, the configurational term can be expressed as,

$$\mathcal{C}_{\mathcal{T}} = \frac{1}{2} \sum_{i,j}^{N} \left\langle \boldsymbol{f}_{ij} \vartheta_{ij}; f \right\rangle + \sum_{i=1}^{N} \left\langle \boldsymbol{f}_{i_{\text{ext}}} \vartheta_i; f \right\rangle, \tag{4.17}$$

where $f_{ij} = -\partial \phi_{ij} / \partial \boldsymbol{r}_i = \partial \phi_{ji} / \partial \boldsymbol{r}_j$ and $\boldsymbol{f}_{i_{\text{ext}}} = -\partial \psi_i / \partial \boldsymbol{r}_i$. The notation, $\vartheta_{ij} \equiv \vartheta_i - \vartheta_j$, is introduced, which is non-zero only when the force acts over the surface of the CV, as illustrated in Fig. 4.2.

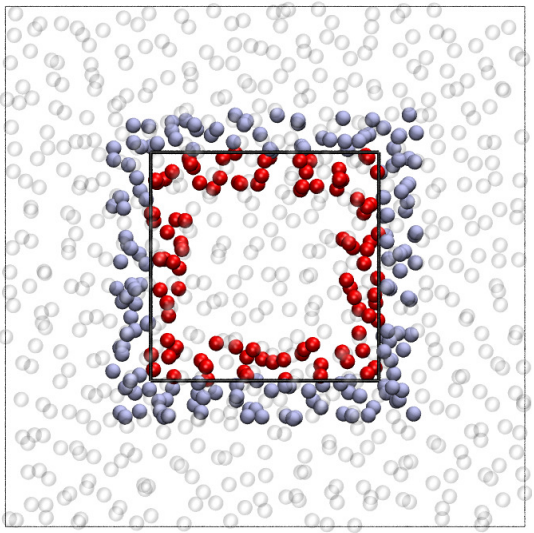

Figure 4.2: A section through the CV to illustrate the role of ϑ_{ij} in selecting only the i and j interactions that cross the bounding surface of the control volume. Due to the limited range of interactions, only the forces between the internal (red) molecules i and external (blue) molecules j near the surfaces are included.

Substituting the kinetic (K_T) and configurational (C_T) terms, from Eqs. (4.13) and (4.17) into Eq. (4.12), the time evolution of momentum within the CV at the mesoscopic scale is,

$$\frac{\partial}{\partial t} \sum_{i=1}^{N} \left\langle \boldsymbol{p}_i \vartheta_i; f \right\rangle = - \sum_{i=1}^{N} \left\langle \frac{\boldsymbol{p}_i \boldsymbol{p}_i}{m_i} \cdot d\mathbf{S}_i; f \right\rangle + \frac{1}{2} \sum_{i,j}^{N} \left\langle \boldsymbol{f}_{ij} \vartheta_{ij}; f \right\rangle + \sum_{i=1}^{N} \left\langle \boldsymbol{f}_{i_{\text{ext}}} \vartheta_i; f \right\rangle. \tag{4.18}$$

Equations (4.10) and (4.18) describe the evolution of mass and momentum respectively within a CV averaged over an ensemble of representative molecular systems. As proposed by Evans & Morriss (2007), it is possible to develop microscopic evolution equations that do not require ensemble averaging. Hence, the equivalents of Eqs. (4.10) and (4.18) are derived for a single trajectory through phase space in section 4.3.1, integrated in time in section 4.3.2 and tested

numerically using molecular dynamics simulation in section 4.4.

The link between the macroscopic and mesoscopic treatments is given by equating their respective momentum Eqs. (2.36) and (4.18),

$$-\oint_S \rho \boldsymbol{u}\boldsymbol{u}\cdot d\mathbf{S} + \boldsymbol{F}_{\text{surface}} + \boldsymbol{F}_{\text{body}} = -\sum_{i=1}^{N}\left\langle \frac{\boldsymbol{p}_i\boldsymbol{p}_i}{m_i}\cdot d\mathbf{S}_i; f\right\rangle + \frac{1}{2}\sum_{i,j}^{N}\left\langle \boldsymbol{f}_{ij}\vartheta_{ij}; f\right\rangle + \sum_{i=1}^{N}\left\langle \boldsymbol{f}_{i_{\text{ext}}}\vartheta_i; f\right\rangle. \tag{4.19}$$

As can be seen, each term in the continuum evolution of momentum has an equivalent term in the mesoscopic formulation.

The continuum momentum Eq. (2.36) can be expressed in terms of the divergence of the pressure tensor, $\boldsymbol{\Pi}$, in the control volume from,

$$\frac{\partial}{\partial t}\int_V \rho\boldsymbol{u}dV = -\oint_S \left[\rho\boldsymbol{u}\boldsymbol{u} + \boldsymbol{\Pi}\right]\cdot d\mathbf{S} + \boldsymbol{F}_{\text{body}} \tag{4.20a}$$

$$= -\int_V \frac{\partial}{\partial \boldsymbol{r}}\cdot\left[\rho\boldsymbol{u}\boldsymbol{u} + \boldsymbol{\Pi}\right]dV + \boldsymbol{F}_{\text{body}}. \tag{4.20b}$$

In the following subsection, the right hand side of Eq. (4.19) is recast first in divergence form as in Eq. (4.20b), and then in terms of surface pressures as in Eq. (4.20a).

4.2.3 The Pressure Tensor

The average molecular pressure tensor ascribed to a control volume is conveniently expressed in terms of the $\mathcal{LCV}$ function. This is shown *inter alia* to lead to a number of literature definitions of the local stress tensor. In the first part of this section, the techniques of Irving & Kirkwood (1950) are used to express the divergence of the stress (as with the right hand side of Eq. (4.20b)) in terms of intermolecular force. Secondly, the CV pressure tensor is related to the Volume Average (VA) formula ((Lutsko, 1988; Cormier *et al.*, 2001)) and, by consideration of the interactions across the surfaces, to the Method Of Planes (MOP) (Todd *et al.*, 1995; Han & Lee, 2004). Finally, the molecular CV Eq. (4.18) is written in analogous form to the macroscopic Eq. (4.20a).

The pressure tensor, $\boldsymbol{\Pi}$, can be decomposed into a kinetic $\boldsymbol{\kappa}$ term, and a configurational stress $\boldsymbol{\sigma}$. In keeping with the engineering literature, the stress and pressure tensors have opposite signs,

$$\boldsymbol{\Pi} = \boldsymbol{\kappa} - \boldsymbol{\sigma}. \tag{4.21}$$

The separation into kinetic and configurational parts is made to accommodate contention that the kinetic term should not be included in the definition of the molecular stress tensor (Zhou, 2003; Subramaniyan & Sun, 2007; Hoover *et al.*, 2009).

In order to avoid confusion, the stress, $\boldsymbol{\sigma}$, is herein defined to be due to the forces only (surface tractions). This, combined with the kinetic pressure term $\boldsymbol{\kappa}$, yields the total pressure tensor $\boldsymbol{\Pi}$ first introduced in Eq. (2.37).

4.2.4 Irving Kirkwood Pressure Tensor

As discussed in section 2.4.3, the virial expression for the stress cannot be applied locally as it is only valid for a homogeneous system, (Tsai, 1978). The Irving & Kirkwood (1950) technique for

evaluating the non-equilibrium, locally-defined stress resolves this issue, and is herein extended to a CV. To obtain the stress, σ, the intermolecular force term of Eq. (4.19) is defined to be equal to the divergence of stress,

$$\int_V \frac{\partial}{\partial \boldsymbol{r}} \cdot \boldsymbol{\sigma} dV \equiv \frac{1}{2} \sum_{i,j}^{N} \left\langle \boldsymbol{f}_{ij} \vartheta_{ij}; f \right\rangle = \frac{1}{2} \sum_{i,j}^{N} \int_V \left\langle \boldsymbol{f}_{ij} \left[\delta(\boldsymbol{r}_i - \boldsymbol{r}) - \delta(\boldsymbol{r}_j - \boldsymbol{r}) \right]; f \right\rangle dV. \tag{4.22}$$

Irving & Kirkwood (1950) used a Taylor expansion of the Dirac δ functions in $\boldsymbol{r}_{ij}$ to express the pair force contribution in the form of a divergence,

$$\begin{aligned} \boldsymbol{f}_{ij} \left[\delta(\boldsymbol{r}_i - \boldsymbol{r}) - \delta(\boldsymbol{r}_j - \boldsymbol{r}) \right] &= \boldsymbol{f}_{ij} \left[\delta(\boldsymbol{r}_i - \boldsymbol{r}) - \delta(\boldsymbol{r}_i - \boldsymbol{r} - \boldsymbol{r}_{ij}) \right] \\ = \boldsymbol{f}_{ij} \left[\boldsymbol{r}_{ij} \cdot \frac{\partial}{\partial \boldsymbol{r}_i} \delta(\boldsymbol{r}_i - \boldsymbol{r}) + \frac{1}{2} \boldsymbol{r}_{ij}^2 \cdot \frac{\partial^2}{\partial \boldsymbol{r}_i^2} \delta(\boldsymbol{r}_i - \boldsymbol{r}) + \frac{1}{3!} \boldsymbol{r}_{ij}^3 \cdot \frac{\partial^3}{\partial \boldsymbol{r}_i^3} \delta(\boldsymbol{r}_i - \boldsymbol{r}) + \ldots \right] \\ = \boldsymbol{f}_{ij} \boldsymbol{r}_{ij} \cdot \frac{\partial}{\partial \boldsymbol{r}_i} \left[1 + \frac{1}{2} \boldsymbol{r}_{ij} \cdot \frac{\partial}{\partial \boldsymbol{r}_i} + \frac{1}{6} \boldsymbol{r}_{ij}^2 \cdot \frac{\partial^2}{\partial \boldsymbol{r}_i^2} + \ldots \right] \delta(\boldsymbol{r}_i - \boldsymbol{r}) = -\frac{\partial}{\partial \boldsymbol{r}} \cdot \boldsymbol{f}_{ij} \boldsymbol{r}_{ij} O_{ij} \delta(\boldsymbol{r}_i - \boldsymbol{r}), \end{aligned}$$

where $\boldsymbol{r}_{ij} = \boldsymbol{r}_i - \boldsymbol{r}_j$ and using $\partial/\partial \boldsymbol{r}_i \delta(\boldsymbol{r}_i - \boldsymbol{r}) = -\partial/\partial \boldsymbol{r} \delta(\boldsymbol{r}_i - \boldsymbol{r})$ gives O_{ij}, the so-called 'IK' operator which acts on the Dirac δ function,

$$O_{ij} \equiv \left(1 - \frac{1}{2} \boldsymbol{r}_{ij} \cdot \frac{\partial}{\partial \boldsymbol{r}} + \ldots - \frac{1}{n!} \left(\boldsymbol{r}_{ij} \cdot \frac{\partial}{\partial \boldsymbol{r}} \right)^{n-1} + \ldots \right). \tag{4.23}$$

Equation (4.22) can therefore be rewritten,

$$\int_V \frac{\partial}{\partial \boldsymbol{r}} \cdot \boldsymbol{\sigma} dV = -\frac{1}{2} \sum_{i,j}^{N} \int_V \left\langle \frac{\partial}{\partial \boldsymbol{r}} \cdot \boldsymbol{f}_{ij} \boldsymbol{r}_{ij} O_{ij} \delta(\boldsymbol{r}_i - \boldsymbol{r}); f \right\rangle dV. \tag{4.24}$$

The Taylor expansion in Dirac δ functions is not straightforward to evaluate. This operation can be bypassed by integrating the position of the molecule i over phase space (Noll, 1955), or by replacing the Dirac δ with a similar but finite-valued function of compact support (Hardy, 1982; Murdoch, 2007, 2010; Admal & Tadmor, 2010). In the current treatment, the $\mathcal{LCV}$ function, ϑ, is used, which is advantageous because it explicitly defines both the extent of the CV and its surface fluxes. The pressure tensor can be written in terms of the $\mathcal{LCV}$ function by exploiting the following identities (based on the Appendix of Ref. (Irving & Kirkwood, 1950)),

$$O_{ij} \delta(\boldsymbol{r}_i - \boldsymbol{r}) = \int_0^1 \delta(\boldsymbol{r} - \boldsymbol{r}_i + s \boldsymbol{r}_{ij}) ds, \tag{4.25}$$

which can be verified from the Taylor expansion of the right hand side of Eq. (4.25),

$$\begin{aligned} \int_0^1 \delta(\boldsymbol{r} - \boldsymbol{r}_i + s \boldsymbol{r}_{ij}) ds &= \int_0^1 \left[1 + s \boldsymbol{r}_{ij} \cdot \frac{\partial}{\partial \boldsymbol{r}_i} + \frac{s^2}{2} \boldsymbol{r}_{ij} \cdot \frac{\partial^2}{\partial \boldsymbol{r}_i^2} + \ldots \right] \delta(\boldsymbol{r}_i - \boldsymbol{r}) ds \\ &= \left[1 + \frac{1}{2} \boldsymbol{r}_{ij} \cdot \frac{\partial}{\partial \boldsymbol{r}_i} + \frac{1}{6} \boldsymbol{r}_{ij} \cdot \frac{\partial^2}{\partial \boldsymbol{r}_i^2} + \ldots \right] \delta(\boldsymbol{r}_i - \boldsymbol{r}) = O_{ij} \delta(\boldsymbol{r}_i - \boldsymbol{r}), \end{aligned} \tag{4.26}$$

Equation (4.24) can therefore be written as,

$$\int_V \frac{\partial}{\partial \boldsymbol{r}} \cdot \boldsymbol{\sigma} dV = -\int_V \frac{1}{2} \sum_{i,j}^{N} \left\langle \frac{\partial}{\partial \boldsymbol{r}} \cdot \boldsymbol{f}_{ij} \boldsymbol{r}_{ij} \int_0^1 \delta(\boldsymbol{r} - \boldsymbol{r}_i + s\boldsymbol{r}_{ij}) ds; f \right\rangle dV. \tag{4.27}$$

Equation (4.27) leads to the VA and MOP definitions of the pressure tensor.

4.2.5 VA Pressure Tensor

The VA definition of the stress tensor of Lutsko (1988) and Cormier *et al.* (2001) can be obtained by rewriting Eq. (4.27) using the fundamental theorem of the calculus,

$$\frac{\partial}{\partial \boldsymbol{r}} \cdot \int_V \boldsymbol{\sigma} dV = -\frac{\partial}{\partial \boldsymbol{r}} \cdot \int_V \frac{1}{2} \sum_{i,j}^{N} \left\langle \boldsymbol{f}_{ij} \boldsymbol{r}_{ij} \int_0^1 \delta(\boldsymbol{r} - \boldsymbol{r}_i + s\boldsymbol{r}_{ij}) ds; f \right\rangle dV. \tag{4.28}$$

Equating the expressions inside the divergence on both sides of Eq. (4.28)[3] and assuming the stress is constant within an arbitrary local volume, ΔV, gives an expression for the VA stress,

$$\overset{\text{VA}}{\boldsymbol{\sigma}} = -\frac{1}{2\Delta V} \int_V \sum_{i,j}^{N} \left\langle \boldsymbol{f}_{ij} \boldsymbol{r}_{ij} \int_0^1 \delta(\boldsymbol{r} - \boldsymbol{r}_i + s\boldsymbol{r}_{ij}) ds; f \right\rangle dV. \tag{4.29}$$

Swapping the order of integration and evaluating the integral of the Dirac δ function over ΔV gives a different form of the $\mathcal{LCV}$ function, ϑ_s,

$$\begin{aligned} \vartheta_s \equiv \int_V \delta(\boldsymbol{r} - \boldsymbol{r}_i + s\boldsymbol{r}_{ij}) dV = \quad & \left[H(x^+ - x_i + sx_{ij}) - H(x^- - x_i + sx_{ij})\right] \\ & \times \left[H(y^+ - y_i + sy_{ij}) - H(y^- - y_i + sy_{ij})\right] \\ & \times \left[H(z^+ - z_i + sz_{ij}) - H(z^- - z_i + sz_{ij})\right], \end{aligned} \tag{4.30}$$

which is non-zero if a point on the line between the two molecules, $\boldsymbol{r}_i - s\boldsymbol{r}_{ij}$, is inside the cubic region (c.f. $\boldsymbol{r}_i$ with ϑ_i). Substituting the definition, ϑ_s (Eq. 4.30), into Eq. (4.29) gives,

$$\overset{\text{VA}}{\boldsymbol{\sigma}} = -\frac{1}{2\Delta V} \sum_{i,j}^{N} \left\langle \boldsymbol{f}_{ij} \boldsymbol{r}_{ij} l_{ij}; f \right\rangle, \tag{4.31}$$

where l_{ij} is the integral from $\boldsymbol{r}_i$ ($s = 0$) to $\boldsymbol{r}_j$ ($s = 1$) of the ϑ_s function,

$$l_{ij} \equiv \int_0^1 \vartheta_s ds.$$

Therefore, l_{ij} is the fraction of interaction length between i and j which lies within the CV, as illustrated in Fig. 4.3. The definition of the configurational stress in Eq. (4.31) is the same as in the work of Lutsko (1988) and Cormier *et al.* (2001). The microscopic divergence theorem given in Appendix C.1 can be applied to obtain the volume averaged kinetic component of the pressure

[3]The resulting equality satisfies Eq. (4.28) and both sides are equal to within an arbitrary constant (related to choosing the gauge).

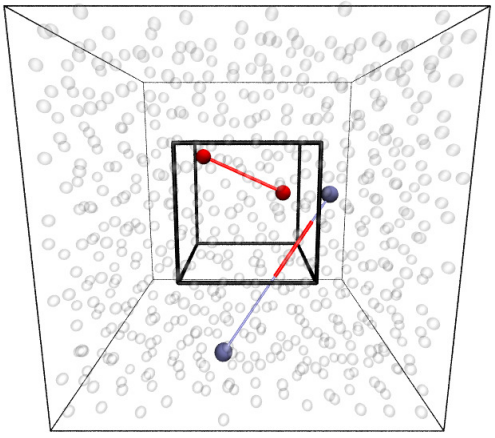

Figure 4.3: A plot of the interaction length given by the integral of the selecting function ϑ_s defined in Eq. (4.30) along the line $\boldsymbol{r}_{ij}$ between $\boldsymbol{r}_i$ and $\boldsymbol{r}_j$. The cases shown are for two molecules which are *a)* both inside the volume ($l_{ij} = 1$) and *b)* both outside the volume with an interaction crossing the volume, where l_{ij} is the fraction of the total length between i and j inside the volume. The line is thin (blue) outside and thicker (red) inside the volume.

tensor, $\mathcal{K}_\mathcal{T}$, in Eq. (4.13),

$$\sum_{i=1}^{N} \left\langle \frac{\boldsymbol{p}_i \boldsymbol{p}_i}{m_i} \cdot d\mathbf{S}_i ; f \right\rangle = \frac{\partial}{\partial \boldsymbol{r}} \cdot \sum_{i=1}^{N} \overbrace{\left\langle \frac{\boldsymbol{p}_i \boldsymbol{p}_i}{m_i} \vartheta_i ; f \right\rangle}^{\overset{VA}{\{\boldsymbol{\rho uu}\}} + \overset{VA}{\boldsymbol{\kappa}}}.$$

Note that the expression inside the divergence includes both the advection, $\overset{VA}{\{\boldsymbol{\rho uu}\}}$, and kinetic (peculiar velocity) components of the pressure tensor. The VA form (Cormier *et al.*, 2001) is obtained by combining the above expression with the configurational stress $\overset{\text{VA}}{\boldsymbol{\sigma}}$,

$$\overset{VA}{\{\boldsymbol{\rho uu}\}} + \overset{VA}{\boldsymbol{\kappa}} - \overset{\text{VA}}{\boldsymbol{\sigma}} = \overset{VA}{\{\boldsymbol{\rho uu}\}} + \overset{VA}{\mathbf{\Pi}} = \frac{1}{\Delta V} \sum_{i=1}^{N} \left\langle \frac{\boldsymbol{p}_i \boldsymbol{p}_i}{m_i} \vartheta_i + \frac{1}{2} \sum_{i,j}^{N} \boldsymbol{f}_{ij} \boldsymbol{r}_{ij} l_{ij} ; f \right\rangle. \tag{4.32}$$

In contrast to the work of Cormier *et al.* (2001), the advection term in the above expression is explicitly included, in order for this definition of the stress tensor to be compatible with the right hand side of Eq. (4.20b) and definition of the pressure tensor, $\mathbf{\Pi}$.

4.2.6 MOP Pressure Tensor

The stress in the CV can also be related to the tractions over each surface. The continuum concept of a traction is the force acting over each surface of an infinitesimal element shown in Figure 4.4. In analogy to the prior use of the molecular $\mathcal{LCV}$ function, ϑ_i, to evaluate the flux, the stress $\mathcal{LCV}$ function, ϑ_s, can be differentiated to give the tractions over each surface. These surface tractions are the ones used in the formal definition of the continuum Cauchy stress tensor. The surface traction (i.e., force per unit area) and the kinetic pressure on a surface combined

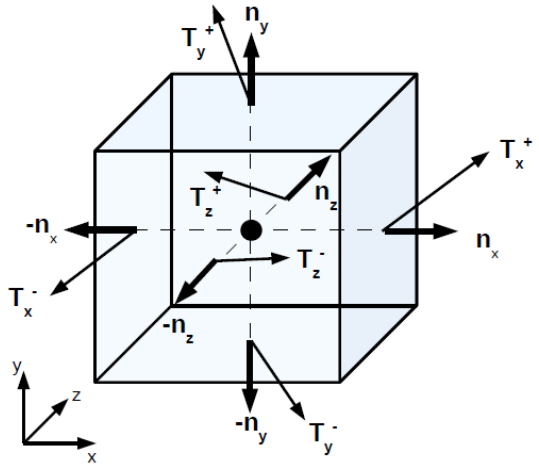

Figure 4.4: A schematic showing the tractions acting on the six surfaces of a infinitesimal element, together with the surface normals.

give the MOP expression for the pressure tensor (Todd *et al.*, 1995).

In the context of the CV, the forces and fluxes on the six bounding surfaces are required to obtain the pressure inside the CV. It is herein shown that each face takes the form of the Han & Lee (2004) localisation of the MOP pressure components. The divergence theorem is used to express the left hand side of Eq. (4.27) in terms of stress across the six faces of the cube. The mesoscopic right hand side of Eq. (4.27) can also be expressed as surface stresses by starting with the $\mathcal{LCV}$ function ϑ_s,

$$\sum_{faces}^{6} \int_{S_f} \boldsymbol{\sigma} \cdot d\mathbf{S}_f = -\frac{1}{2} \sum_{i,j}^{N} \left\langle \boldsymbol{f}_{ij} \boldsymbol{r}_{ij} \cdot \int_0^1 \frac{\partial \vartheta_s}{\partial \boldsymbol{r}} ds; f \right\rangle.$$

The procedure for taking the derivative of ϑ_s with respect to $\boldsymbol{r}$ and integrating over the volume is given in Appendix C.3. The result is an expression for the force on the CV rewritten as the force over each surface of the CV. For the x^+ face, for example, this is,

$$\int_{S_x^+} \boldsymbol{\sigma} \cdot d\mathbf{S}_{S_x^+} = -\frac{1}{4} \sum_{i,j}^{N} \left\langle \boldsymbol{f}_{ij} \left[\, sgn(x^+ - x_j) - sgn(x^+ - x_i) \right] S_{xij}^+; f \right\rangle.$$

The combination of the signum functions and the S_{xij}^+ term specifies when the point of intersection of the line between i and j is located on the x^+ surface of the cube (see Appendix C.3). Corresponding expressions for the y and z faces are defined by $S_{\alpha ij}^{\pm}$ when $\alpha = \{y, z\}$ respectively.

The full expression for the MOP pressure tensor, which includes the kinetic part given by Eq. (4.14), is obtained by assuming a uniform pressure over the x^+ surface,

$$\int_{S_x^+} \boldsymbol{\Pi} \cdot d\mathbf{S}_x^+ = [\boldsymbol{\kappa} - \boldsymbol{\sigma}] \cdot \mathbf{n}_x^+ \Delta A_x^+ \equiv \left[\mathbf{K}_x^+ - \mathbf{T}_x^+ \right] \Delta A_x^+ = \boldsymbol{p}_x^+ \Delta A_x^+, \tag{4.33}$$

where $\mathbf{n}_x^+$ is a unit vector aligned along the x coordinate axis, $\mathbf{n}_x^+ = [+1, 0, 0]$; $\boldsymbol{T}_x^+$ is the configurational stress (traction) and $\boldsymbol{p}_x^+$ the total pressure tensor acting on a plane. Hence,

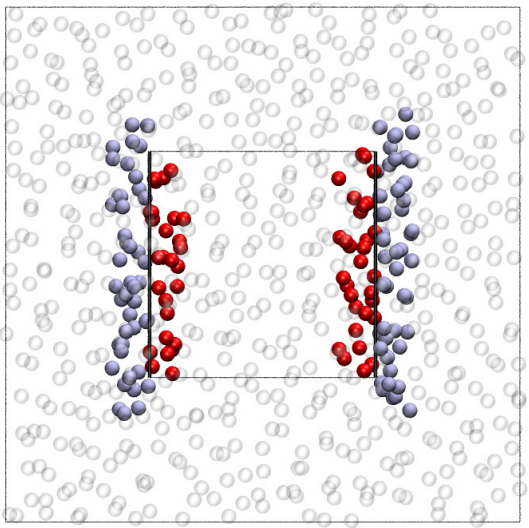

Figure 4.5: Representation of those molecules selected through dS_{xij} in Eq. (4.35) with molecules i on the side of the surface inside the CV (red) and molecules j on the outside (blue). The CV is the inner square on the figure.

$$\boldsymbol{p}_x^+ = \frac{1}{\Delta A_x^+}\sum_{i=1}^{N}\left\langle \frac{\overline{\boldsymbol{p}}_i\overline{p}_{ix}}{m_i}\delta(x_i - x^+)S_{xi}^+; f\right\rangle + \frac{1}{4\Delta A_x^+}\sum_{i,j}^{N}\left\langle \boldsymbol{f}_{ij}\left[sgn(x^+ - x_j) - sgn(x^+ - x_i)\right]S_{xij}^+; f\right\rangle, \tag{4.34}$$

where the peculiar momentum, $\overline{\boldsymbol{p}}_i$ has been used as in Todd *et al.* (1995). If the x^+ surface area covers the entire domain ($S_{xij}^+ = 1$ in Eq. (4.34)), the MOP formulation of the pressure is recovered (Todd *et al.*, 1995).

The extent of the surface is defined through S_{xij}^+, in Eq. (4.34) which is the localised form of the pressure tensor considered by Han & Lee (2004) applied to the six cubic faces. For a cube in space, each face has three components of stress, which results in 18 independent components over the total control surface. The quantity,

$$dS_{\alpha ij} \equiv \frac{1}{2}\left[sgn(r_\alpha^+ - r_{\alpha j}) - sgn(r_\alpha^+ - r_{\alpha i})\right]S_{\alpha ij}^+ \; - \frac{1}{2}\left[sgn(r_\alpha^- - r_{\alpha j}) - sgn(r_\alpha^- - r_{\alpha i})\right]S_{\alpha ij}^-,$$

selects the force contributions across the two opposite faces; similar notation to the surface molecular flux, $d\mathbf{S}_{ij} = d\mathbf{S}_{ij}^+ - d\mathbf{S}_{ij}^-$ (c.f. Eq. (4.5)), is used. The case of the two x planes located on opposite sides of the cube is illustrated in Fig. 4.5.

Taking all surfaces of the cube into account yields the final form,

$$\sum_{faces}^{6}\int_{S_f}\boldsymbol{\sigma}\cdot d\mathbf{S}_f = -\frac{1}{2}\sum_{i,j}^{N}\left\langle \boldsymbol{f}_{ij}\sum_{\alpha=1}^{3}dS_{\alpha ij}; f\right\rangle = -\frac{1}{2}\sum_{i,j}^{N}\left\langle \boldsymbol{f}_{ij}\tilde{\mathbf{n}}\cdot d\mathbf{S}_{ij}; f\right\rangle = \frac{1}{2}\sum_{i,j}^{N}\left\langle \boldsymbol{\varsigma}_{ij}\cdot d\mathbf{S}_{ij}; f\right\rangle. \tag{4.35}$$

The vector $\tilde{\mathbf{n}}$, obtained in Appendix C.3, is unity in each direction. The tensor $\boldsymbol{\varsigma}_{ij}$ is defined, for

notational convenience, to be the outer product of the intermolecular forces with $\tilde{\mathbf{n}}$,

$$\boldsymbol{\varsigma}_{ij} \equiv -\boldsymbol{f}_{ij}\tilde{\mathbf{n}} = -\boldsymbol{f}_{ij}\begin{bmatrix}1 & 1 & 1\end{bmatrix} = -\begin{bmatrix}f_{xij} & f_{xij} & f_{xij}\\ f_{yij} & f_{yij} & f_{yij}\\ f_{zij} & f_{zij} & f_{zij}\end{bmatrix}.$$

In this form, the ϑ_{ij} function for all interactions over the cube's surface is expressed as the sum of six selection functions for each of the six faces, i.e. $\vartheta_{ij} = -\sum_{\alpha=1}^{3} dS_{\alpha ij}$.

4.2.7 Relationship to the continuum

The forces per unit area, or 'tractions', acting over each face of the CV, are used in the definition of the Cauchy stress tensor at the continuum level. For the x^+ surface, the traction vector is the sum of all forces acting over the surface,

$$\mathbf{T}_x^+ = -\frac{1}{4\Delta A_x^+}\sum_{i,j}^{N}\left\langle \boldsymbol{f}_{ij}\left[sgn(x^+ - x_j) - sgn(x^+ - x_i)\right]S_{xij}^+; f\right\rangle, \tag{4.36}$$

which satisfies the definition,

$$\mathbf{T}_x^{\pm} = \boldsymbol{\sigma}\cdot\mathbf{n}_x^{\pm},$$

of the Cauchy traction (Nemat-Nasser, 2004). A similar relationship can be written for both the kinetic pressure and total pressure,

$$\boldsymbol{K}_x^{\pm} = \boldsymbol{\kappa}\cdot\mathbf{n}_x^{\pm},$$
$$\boldsymbol{p}_x^{\pm} = \boldsymbol{\Pi}\cdot\mathbf{n}_x^{\pm},$$

where $\mathbf{n}_x^{\pm}$ is a unit vector, $\mathbf{n}_x^{\pm} = [\pm 1\ \ 0\ \ 0]^T$.

The time evolution of the molecular momentum within a CV (Eq. (4.18)), can be expressed in a similar form to the Navier-Stokes equations of continuum fluid mechanics. Dividing both sides of Eq. (4.18) by the volume, the following form can be obtained; note that this step requires Eqs. (4.14), (4.34) and (4.36):

$$\frac{1}{\Delta V}\frac{\partial}{\partial t}\sum_{i=1}^{N}\left\langle p_{\alpha i}\vartheta_i; f\right\rangle + \frac{\{\rho u_\alpha u_\beta\}^+ - \{\rho u_\alpha u_\beta\}^-}{\Delta r_\beta}$$
$$= -\frac{K_{\alpha\beta}^+ - K_{\alpha\beta}^-}{\Delta r_\beta} + \frac{T_{\alpha\beta}^+ - T_{\alpha\beta}^-}{\Delta r_\beta} + \frac{1}{\Delta V}\sum_{i=1}^{N}\left\langle f_{\alpha i_{\text{ext}}}\vartheta_i; f\right\rangle, \tag{4.38}$$

where index notation has been used (e.g. $\mathbf{T}_x^{\pm} = T_{\alpha x}^{\pm}$) with the Einstein summation convention.

In the limit of zero volume, each expression would be similar to a term in the differential continuum equations (although the pressure term would be the divergence of a tensor and not the gradient of a scalar field as is common in fluid mechanics). The Cauchy stress tensor, $\boldsymbol{\sigma}$, is defined in the limit that the cube's volume tends to zero, so that $\mathbf{T}^+$ and $\mathbf{T}^-$ are related by an infinitesimal difference. This is used in continuum mechanics to define the unique nine component Cauchy stress tensor, $d\boldsymbol{\sigma}/dx \equiv \lim_{\Delta x\to 0}[\mathbf{T}^+ + \mathbf{T}^-]/\Delta x$. This limit is shown in Appendix C.2 to yield the Irving & Kirkwood (1950) stress in terms of the Taylor expansion in Dirac δ functions.

Rather than defining the stress at a point, the tractions can be compared to their continuum counterparts in a fluid mechanics control volume or a solid mechanics Finite Elements (FE) method. Computational Fluid Dynamics (CFD) is commonly formulated using CV and in discrete simulations, Finite Volume (Hirsch, 2007). Surface forces are ideal for coupling schemes between MD and CFD. Building on the pioneering work of O'Connell & Thompson (1995), there are many MD to CFD coupling schemes discussed in chapter 2. Finite volume algorithms have been used extensively in coupling methods (Nie *et al.*, 2004*a*; Werder *et al.*, 2005; Delgado-Buscalioni & Coveney, 2004; Fabritiis *et al.*, 2006; Delgado-Buscalioni & Fabritiis, 2007) together with equivalent control volumes defined in the molecular region. An advantage of the herein proposed molecular CV approach is that it ensures conservation laws are satisfied when exchanging fluxes over cell surfaces — an important requirement for accurate unsteady coupled simulations as outlined in the finite volume coupling of Delgado-Buscalioni & Coveney (2004). For solid coupling schemes, (Curtin & Miller, 2003), the principle of virtual work can be used with tractions on the element corners (the MD CV) to give the state of stress in the element (Zienkiewicz, 2005),

$$\int_V \boldsymbol{\sigma} \cdot \boldsymbol{\nabla} N_a dV = \oint_S N_a \mathbf{T} dS, \tag{4.39}$$

where N_a is a linear shape function which allows stress to be defined as a continuous function of position. It will be demonstrated numerically in the next section, 4.3, that the CV formulation is exactly conservative: the surface tractions and fluxes entirely define the stress within the volume. The tractions and stress in Eq. (4.39) are connected by the weak formulation and the form of the stress tensor results from the choice of shape function N_a.

4.2.8 Energy Balance for a Molecular CV

In this section, a mesoscopic expression for time evolution of energy within a CV is derived. As for mass and momentum, the starting point is to integrate the energy at a point, given in Eq. (2.56), over the CV,

$$\int_V \rho(\boldsymbol{r},t)\mathcal{E}(\boldsymbol{r},t)dV \equiv \int_V \sum_{i=1}^{N} \Big\langle e_i \delta(\boldsymbol{r}_i - \boldsymbol{r}); f \Big\rangle dV = \sum_{i=1}^{N} \Big\langle e_i \vartheta_i; f \Big\rangle, \tag{4.40}$$

where the energy of the i^{th} molecule is $e_i = \frac{p_i^2}{2m_i} + \frac{1}{2}\sum_{j\neq i}^{N} \phi_{ij}$. The aim is to compare the time evolution of both sides of Eq. 4.40. The time evolution of energy in a continuum CV is known to be,

$$\begin{aligned} \frac{\partial}{\partial t}\int_V \rho(\boldsymbol{r},t)\mathcal{E}(\boldsymbol{r},t)dV + \oint_S \rho(\boldsymbol{r},t)\mathcal{E}(\boldsymbol{r},t)\boldsymbol{u}(\boldsymbol{r},t)\cdot d\mathbf{S} \\ = -\oint_S \boldsymbol{Q}(\boldsymbol{r},t)\cdot d\mathbf{S} - \oint_S \boldsymbol{\Pi}(\boldsymbol{r},t)\cdot \boldsymbol{u}(\boldsymbol{r},t)\cdot d\mathbf{S}. \end{aligned} \tag{4.41}$$

Obtaining a similar time evolution of the microscopic energy in a CV is the aim of this subsection. Taking the time derivative of the energy in the molecular control volume using the (Irving &

Kirkwood, 1950) Louiville equation, Eq. (2.33),

$$\frac{\partial}{\partial t}\sum_{i=1}^{N}\left\langle e_i\vartheta_i;f\right\rangle=\sum_{i=1}^{N}\left\langle \frac{\boldsymbol{p}_i}{m_i}\cdot\frac{\partial}{\partial \boldsymbol{r}_i}e_i\vartheta_i+\boldsymbol{F}_i\cdot\frac{\partial}{\partial \boldsymbol{p}_i}e_i\vartheta_i;f\right\rangle. \tag{4.42}$$

Evaluating the derivatives of the energy and CV function results in,

$$\frac{\partial}{\partial t}\sum_{i=1}^{N}\left\langle e_i\vartheta_i;f\right\rangle=-\frac{1}{2}\sum_{i,j}^{N}\left\langle \left[\frac{\boldsymbol{p}_i}{m_i}\cdot\boldsymbol{f}_{ij}+\frac{\boldsymbol{p}_j}{m_j}\cdot\boldsymbol{f}_{ji}\right]\vartheta_i;f\right\rangle-\sum_{i=1}^{N}\left\langle e_i\frac{\boldsymbol{p}_i}{m_i}\cdot d\mathbf{S}_i-\boldsymbol{F}_i\cdot\frac{\boldsymbol{p}_i}{m_i}\vartheta_i;f\right\rangle.$$

which can be manipulated as follows,

$$\begin{aligned}\frac{\partial}{\partial t}\sum_{i=1}^{N}\left\langle e_i\vartheta_i;f\right\rangle+\sum_{i=1}^{N}\left\langle e_i\frac{\boldsymbol{p}_i}{m_i}\cdot d\mathbf{S}_i;f\right\rangle&=\sum_{i=1}^{N}\left\langle\left\{\frac{\boldsymbol{F}_i\cdot\boldsymbol{p}_i}{m_i}-\frac{1}{2}\sum_{j\neq i}^{N}\left[\boldsymbol{f}_{ij}\cdot\frac{\boldsymbol{p}_i}{m_i}+\boldsymbol{f}_{ji}\cdot\frac{\boldsymbol{p}_j}{m_j}\right]\right\}\vartheta_i;f\right\rangle\\&=\sum_{i,j}^{N}\left\langle\left[\boldsymbol{f}_{ij}\cdot\frac{\boldsymbol{p}_i}{m_i}-\left(\boldsymbol{f}_{ij}\cdot\frac{\boldsymbol{p}_i}{2m_i}+\boldsymbol{f}_{ji}\cdot\frac{\boldsymbol{p}_j}{2m_j}\right)\right]\vartheta_i;f\right\rangle=\sum_{i,j}^{N}\left\langle\boldsymbol{f}_{ij}\cdot\left(\frac{\boldsymbol{p}_i}{2m_i}+\frac{\boldsymbol{p}_j}{2m_j}\right)\vartheta_i;f\right\rangle\\&=\sum_{i,j}^{N}\left\langle\boldsymbol{f}_{ij}\cdot\frac{\boldsymbol{p}_i}{2m_i}\left(\vartheta_i-\vartheta_j\right);f\right\rangle=\sum_{i,j}^{N}\left\langle\boldsymbol{f}_{ij}\vartheta_{ij}\cdot\frac{\boldsymbol{p}_i}{2m_i};f\right\rangle\end{aligned} \tag{4.43}$$

where external forces $\boldsymbol{f}_{ext}$ are neglected and $\boldsymbol{f}_{ij}=-\boldsymbol{f}_{ji}$ has been used with indices re-labelled. The CV energy equation, Eq. (4.42), therefore becomes,

$$\frac{\partial}{\partial t}\sum_{i=1}^{N}\left\langle e_i\vartheta_i;f\right\rangle=\frac{1}{2}\sum_{i,j}^{N}\left\langle\frac{\boldsymbol{p}_i}{m_i}\cdot\boldsymbol{f}_{ij}\vartheta_{ij};f\right\rangle-\sum_{i=1}^{N}\left\langle e_i\frac{\boldsymbol{p}_i}{m_i}\cdot d\mathbf{S}_i;f\right\rangle. \tag{4.44}$$

Comparing the microscopic CV energy, Eq. (4.42), to the continuum counterpart, Eq. (4.41) yields,

$$\begin{aligned}&\overbrace{-\oint_S\rho\mathcal{E}\boldsymbol{u}\cdot d\mathbf{S}}^{\text{energy flux}}-\overbrace{\oint_S\boldsymbol{Q}\cdot d\mathbf{S}}^{\text{heat flux}}-\overbrace{\oint_S\boldsymbol{\Pi}\cdot\boldsymbol{u}\cdot d\mathbf{S}}^{\text{pressure heating}}=\\&-\sum_{i=1}^{N}\left\langle e_i\frac{\boldsymbol{p}_i}{m_i}\cdot d\mathbf{S}_i;f\right\rangle+\frac{1}{2}\sum_{i,j}^{N}\left\langle\frac{\boldsymbol{p}_i}{m_i}\cdot\boldsymbol{f}_{ij}\vartheta_{ij};f\right\rangle.\end{aligned} \tag{4.45}$$

In its current form, the microscopic equation does not delineate the contribution due to energy flux, heat flux and pressure heating. To achieve this division, the notion of the peculiar momentum at the molecular location $\boldsymbol{r}_i$ must be invoked. The peculiar velocity is written as $\boldsymbol{p}_i/m_i=\overline{\boldsymbol{p}_i}/m_i+\boldsymbol{u}(\boldsymbol{r}_i)$. Expressing the first term on the right of Eq. 4.45, in terms of peculiar

velocity leads to an expression for the energy flux,

$$\sum_{i=1}^{N}\left\langle e_i\frac{\boldsymbol{p}_i}{m_i}\cdot d\mathbf{S}_i;f\right\rangle=\sum_{i=1}^{N}\left\langle e_i\frac{\overline{\boldsymbol{p}_i}}{m_i}\cdot d\mathbf{S};f\right\rangle+\sum_{i=1}^{N}\left\langle e_i\boldsymbol{u}(\boldsymbol{r}_i)\cdot d\mathbf{S}_i;f\right\rangle$$
$$=\sum_{i=1}^{N}\left\langle e_i\frac{\overline{\boldsymbol{p}_i}}{m_i}\cdot d\mathbf{S};f\right\rangle+\oint_S\rho(\boldsymbol{r},t)\mathcal{E}(\boldsymbol{r},t)\boldsymbol{u}(\boldsymbol{r},t)\cdot d\mathbf{S}. \tag{4.46}$$

The second equality results from the continuum surface energy flux being equated to the energy carried by the microscopic streaming velocity. This is justified by the use of the $d\mathbf{S}_i$ term which is zero everywhere except the CV surface, so that $\boldsymbol{u}(\boldsymbol{r}_i)d\mathbf{S}_i=\boldsymbol{u}(\boldsymbol{r}^{\pm})d\mathbf{S}_i$. Including the expression for energy flux (Eq. 4.46) in the energy equation 4.45 yields,

$$-\oint_S\boldsymbol{Q}\cdot d\mathbf{S}-\oint_S\boldsymbol{\Pi}\cdot\boldsymbol{u}\cdot d\mathbf{S}=\frac{1}{2}\sum_{i,j}^{N}\left\langle\frac{\boldsymbol{p}_i}{m_i}\cdot\boldsymbol{f}_{ij}\vartheta_{ij};f\right\rangle-\sum_{i=1}^{N}\left\langle e_i\frac{\overline{\boldsymbol{p}_i}}{m_i}\cdot d\mathbf{S}_i;f\right\rangle. \tag{4.47}$$

To obtain the division between stress heating and heat flux the peculiar momentum is used again. The two terms on the right of Eq. 4.47 are expressed as,

$$\frac{1}{2}\sum_{i,j}^{N}\left\langle\frac{\boldsymbol{p}_i}{m_i}\cdot\boldsymbol{f}_{ij}\vartheta_{ij};f\right\rangle=\frac{1}{2}\sum_{i,j}^{N}\left\langle\frac{\overline{\boldsymbol{p}_i}}{m_i}\cdot\boldsymbol{f}_{ij}\vartheta_{ij}+\boldsymbol{u}\cdot\boldsymbol{f}_{ij}\vartheta_{ij};f\right\rangle. \tag{4.48}$$

and,

$$\sum_{i=1}^{N}\left\langle e_i\frac{\overline{\boldsymbol{p}_i}}{m_i}\cdot d\mathbf{S}_i;f\right\rangle=\sum_{i=1}^{N}\left\langle\left[\frac{\boldsymbol{p}_i\cdot\boldsymbol{p}_i}{2m_i}+\frac{1}{2}\sum_{j\neq i}^{N}\phi_{ij}\right]\frac{\overline{\boldsymbol{p}_i}}{m_i}\cdot d\mathbf{S}_i;f\right\rangle$$
$$=\sum_{i=1}^{N}\left\langle\frac{\overline{\boldsymbol{p}_i}\,\overline{\boldsymbol{p}_i}}{m_i}\cdot\boldsymbol{u};f\right\rangle+\sum_{i=1}^{N}\left\langle\left[\frac{\overline{p_i}^2}{2m_i}+\frac{u^2}{2}+\sum_{j\neq i}^{N}\phi_{ij}\right]\overline{\boldsymbol{p}_i}\cdot d\mathbf{S}_i;f\right\rangle. \tag{4.49}$$

Equation (4.47) can now be written entirely in terms of peculiar momenta,

$$\oint_S\boldsymbol{Q}(\boldsymbol{r},t)\cdot d\mathbf{S}+\oint_S\boldsymbol{\Pi}(\boldsymbol{r},t)\cdot\boldsymbol{u}(\boldsymbol{r},t)\cdot d\mathbf{S}=-\sum_{i=1}^{N}\left\langle\frac{\overline{\boldsymbol{p}_i}\,\overline{\boldsymbol{p}_i}}{m_i}\cdot\boldsymbol{u}(\boldsymbol{r}_i)\cdot d\mathbf{S}_i;f\right\rangle+\frac{1}{2}\sum_{i,j}^{N}\left\langle\boldsymbol{f}_{ij}\cdot\boldsymbol{u}(\boldsymbol{r}_i)\vartheta_{ij};f\right\rangle$$
$$+\frac{1}{2}\sum_{i,j}^{N}\left\langle\frac{\overline{\boldsymbol{p}_i}}{m_i}\cdot\boldsymbol{f}_{ij}\vartheta_{ij};f\right\rangle-\sum_{i=1}^{N}\left\langle\frac{u^2}{2}\frac{\overline{\boldsymbol{p}_i}}{m_i}\cdot d\mathbf{S}_i;f\right\rangle-\sum_{i=1}^{N}\left\langle\frac{\overline{p_i}^2}{2m_i}\frac{\overline{\boldsymbol{p}_i}}{m_i}\cdot d\mathbf{S}_i;f\right\rangle-\sum_{i,j}^{N}\left\langle\phi_{ij}\frac{\overline{\boldsymbol{p}_i}}{m_i}\cdot d\mathbf{S}_i;f\right\rangle, \tag{4.50}$$

where the terms with dependence on macroscopic velocity $\boldsymbol{u}$ have been collected. Using the definition of stress at the CV surface Eq. (4.35), dotted with the macroscopic velocity $\boldsymbol{u}(\boldsymbol{r})$,

$$\oint_S\boldsymbol{\Pi}(\boldsymbol{r},t)\cdot\boldsymbol{u}(\boldsymbol{r})\cdot d\mathbf{S}\equiv\sum_{i=1}^{N}\left\langle\frac{\overline{\boldsymbol{p}_i}\,\overline{\boldsymbol{p}_i}}{m_i}\cdot\boldsymbol{u}(\boldsymbol{r})\cdot d\mathbf{S}_i-\frac{1}{2}\sum_{i,j}^{N}\boldsymbol{\varsigma}_{ij}\cdot\boldsymbol{u}(\boldsymbol{r})\cdot d\mathbf{S}_{ij};f\right\rangle, \tag{4.51}$$

As with the energy flux, the $d\mathbf{S}_i$ function ensures the microscopic $\boldsymbol{u}(\boldsymbol{r}_i)$ is at the same surface as the macroscopic velocities $\boldsymbol{u}(\boldsymbol{r}^{\pm})$. However, the macroscopic (configurational) stress at a surface is related to the microscopic stress by the $d\mathbf{S}_{ij}$ function. This includes all interactions crossing

the CV surface with stress from molecules which are not, in general, located on the surface. Taking this expression for stress heating from the energy equation, 4.47, yields an expression for the heat flux vector,

$$\oint_S \boldsymbol{Q}(\boldsymbol{r},t)\cdot d\mathbf{S} = \frac{1}{2}\sum_{i,j}^{N}\left\langle \boldsymbol{\varsigma}_{ij}\cdot\left(\frac{\overline{\boldsymbol{p}_i}}{m_i}+\boldsymbol{u}(\boldsymbol{r}_i)-\boldsymbol{u}(\boldsymbol{r})\right)\cdot d\mathbf{S}_{ij};f\right\rangle + \sum_{i=1}^{N}\left\langle \overline{e}_i\frac{\overline{\boldsymbol{p}_i}}{m_i}\cdot d\mathbf{S}_i+\frac{u^2(\boldsymbol{r}_i)}{2}\frac{\overline{\boldsymbol{p}_i}}{m_i}\cdot d\mathbf{S}_i;f\right\rangle, \tag{4.52}$$

where internal energy $\overline{e}_i$ has been introduced as,

$$\overline{e}_i \equiv \left\langle \frac{\overline{p_i}^2}{2m_i}+\sum_{j\neq i}^{N}\phi_{ij};f\right\rangle. \tag{4.53}$$

In CV form, the heat flux vector provides a useful insight not possible with the pointwise Dirac delta form of Irving & Kirkwood (1950). This concerns the first line of Eq. (4.52) for the interaction between i and j crossing a surface selected by $d\mathbf{S}_{ij}$. It can be seen that $\oint_S \boldsymbol{Q}\cdot d\mathbf{S}$ result, in part, from a difference in the streaming velocity $\boldsymbol{u}$ at the point $\boldsymbol{r}$ and the streaming velocity at the location of the molecule $\boldsymbol{r}_i$.

In the next section, the CV equations derived in this section will be implemented.

4.3 Implementation

In this section, the CV equation for mass, momentum and energy balance, Eqs. (4.10), (4.18) and (4.44), will be proved to apply and demonstrated numerically for a microscopic system undergoing a single trajectory through phase space.

4.3.1 The Microscopic System

Consider a single trajectory of a set of molecules through phase space, defined in terms of their time dependent coordinates $\boldsymbol{r}_i$ and momenta $\boldsymbol{p}_i$. The $\mathcal{LCV}$ function depends on molecular coordinates, the location of the centre of the cube, $\boldsymbol{r}$, and its side length, $\Delta\boldsymbol{r}$, *i.e.,* $\vartheta_i \equiv \vartheta_i(\boldsymbol{r}_i(t),\boldsymbol{r},\Delta\boldsymbol{r})$. The time evolution of the mass within the molecular control volume is given by,

$$\frac{d}{dt}\sum_{i=1}^{N} m_i\vartheta_i(\boldsymbol{r}_i(t),\boldsymbol{r},\Delta\boldsymbol{r}) = \sum_{i=1}^{N} m_i\frac{\partial\vartheta_i}{\partial t} = \sum_{i=1}^{N} m_i\frac{d\boldsymbol{r}_i}{dt}\cdot\frac{\partial\vartheta_i}{\partial\boldsymbol{r}_i} = -\sum_{i=1}^{N}\boldsymbol{p}_i\cdot d\mathbf{S}_i, \tag{4.54}$$

using, $\boldsymbol{p}_i = m_i d\boldsymbol{r}_i/dt$. The time evolution of momentum in the molecular control volume is,

$$\frac{\partial}{\partial t}\sum_{i=1}^{N}\boldsymbol{p}_i(t)\vartheta_i(\boldsymbol{r}_i(t),\boldsymbol{r},\Delta\boldsymbol{r}) = \sum_{i=1}^{N}\left[\boldsymbol{p}_i\frac{\partial\vartheta_i}{\partial t}+\frac{d\boldsymbol{p}_i}{dt}\vartheta_i\right] = \sum_{i=1}^{N}\left[\boldsymbol{p}_i\frac{d\boldsymbol{r}_i}{dt}\cdot\frac{\partial\vartheta_i}{\partial\boldsymbol{r}_i}+\frac{d\boldsymbol{p}_i}{dt}\vartheta_i\right].$$

As, $d\boldsymbol{p}_i/dt = \boldsymbol{F}_i$, then,

$$\frac{\partial}{\partial t}\sum_{i=1}^{N}\boldsymbol{p}_i\vartheta_i = \sum_{i=1}^{N}\left[-\frac{\boldsymbol{p}_i\boldsymbol{p}_i}{m_i}\cdot d\mathbf{S}_i+\boldsymbol{F}_i\vartheta_i\right] = -\sum_{i=1}^{N}\frac{\boldsymbol{p}_i\boldsymbol{p}_i}{m_i}\cdot d\mathbf{S}_i+\frac{1}{2}\sum_{i,j}^{N}\boldsymbol{f}_{ij}\vartheta_{ij}+\sum_{i=1}^{N}\boldsymbol{f}_{i_{\text{ext}}}\vartheta_i, \tag{4.55}$$

where the total force on molecule i has been decomposed into surface and 'external' or body terms. The time evolution of energy in a molecular control volume is obtained by evaluating,

$$\frac{\partial}{\partial t}\sum_{i=1}^{N} e_i\vartheta_i = \sum_{i=1}^{N}\left[e_i\frac{\partial\vartheta_i}{\partial t} + \frac{\partial e_i}{\partial t}\vartheta_i\right] = -\sum_{i=1}^{N} e_i\frac{\boldsymbol{p}_i}{m_i}\cdot d\mathbf{S}_i + \sum_{i=1}^{N}\frac{\dot{\boldsymbol{p}}_i\cdot\boldsymbol{p}_i}{m_i}\vartheta_i - \frac{1}{2}\sum_{i,j}^{N}\left[\frac{\boldsymbol{p}_i}{m_i}\cdot\boldsymbol{f}_{ij} + \frac{\boldsymbol{p}_j}{m_j}\cdot\boldsymbol{f}_{ji}\right]\vartheta_i$$

using, $d\boldsymbol{p}_i/dt = \boldsymbol{F}_i$ and the decomposition of forces. The manipulation proceeds as in the mesoscopic system to yield,

$$\frac{\partial}{\partial t}\sum_{i=1}^{N} e_i\vartheta_i = -\sum_{i=1}^{N} e_i\frac{\boldsymbol{p}_i}{m_i}\cdot d\mathbf{S}_i + \frac{1}{2}\sum_{i,j}^{N}\frac{\boldsymbol{p}_i}{m_i}\cdot\boldsymbol{f}_{ij}\vartheta_{ij} + \sum_{i=1}^{N}\frac{\boldsymbol{p}_i}{m_i}\cdot\boldsymbol{f}_{i_{\text{ext}}}\vartheta_i, \tag{4.56}$$

The average of many such trajectories defined through Eqs. (4.54), (4.55) and (4.56) gives the mesoscopic expressions in Eqs. (4.10), (4.18) and (4.44), respectively. In the next subsection, the time integral of the single trajectory is considered.

4.3.2 Time integration of the microscopic CV equations

Integration of Eqs. (4.54), (4.55) and (4.56) over the time interval $[0,\tau]$ enables these equations to be usable in a molecular simulation. For the conservation of mass term,

$$\sum_{i=1}^{N} m_i\left[\vartheta_i(\tau) - \vartheta_i(0)\right] = -\int_0^{\tau}\sum_{i=1}^{N}\boldsymbol{p}_i\cdot d\mathbf{S}_i dt. \tag{4.57}$$

The surface crossing term, $d\mathbf{S}_i$, defined in Eq. (4.4), involves a Dirac δ function and therefore cannot be evaluated directly. Over the time interval $[0,\tau]$, molecule i passes through a given x position at times, $t_{xi,k}$, where $k = 1,2,...,N_{t_x}$ (Daivis *et al.*, 1996) . The positional Dirac δ can be expressed as,

$$\delta(x_i(t) - x) = \sum_{k=1}^{N_{t_x}}\frac{\delta(t - t_{xi,k})}{|\dot{x}_i(t_{xi,k})|}, \tag{4.58}$$

where $|\dot{x}_i(t_{xi,k})|$ is the magnitude of the velocity in the x direction at time $t_{xi,k}$. Equation (4.58) is used to rewrite $d\mathbf{S}_i$ in Eq. (4.57) in the form,

$$\begin{aligned} dS_{\alpha i,k} \equiv &\Big[sgn(t^+_{\alpha i,k} - \tau) - sgn(t^+_{\alpha i,k} - 0)\Big]\, S^+_{\alpha i,k}(t^+_{\alpha i,k}) \\ &-\Big[sgn(t^-_{\alpha i,k} - \tau) - sgn(t^-_{\alpha i,k} - 0)\Big]\, S^-_{\alpha i,k}(t^-_{\alpha i,k}), \end{aligned} \tag{4.59}$$

where $\alpha = \{x,y,z\}$, and the fluxes are evaluated at times, $t^+_{\alpha i,k}$ and $t^-_{\alpha i,k}$ for the right and left surfaces of the cube, respectively. Using the above expression, the time integral in Eq. (4.57) can be expressed as the sum of all molecule crossings, $N_t = N_{t_x} + N_{t_y} + N_{t_z}$ over the cube's

faces,

$$\overbrace{\sum_{i=1}^{N} m_i \left[\vartheta_i(\tau) - \vartheta_i(0)\right]}^{\text{Accumulation}} = \underbrace{-\sum_{i=1}^{N}\sum_{k=1}^{N_t} m_i \sum_{\alpha=1}^{3} \frac{p_{\alpha i}}{|p_{\alpha i}|} dS_{\alpha i,k}}_{\text{Advection}}. \tag{4.60}$$

In other words, the mass in a CV at time $t = \tau$ minus its initial value at $t = 0$ is the sum of all molecules that cross its surfaces during the time interval.

The momentum balance equation Eq. (4.55), can also be written in time-integrated form,

$$\sum_{i=1}^{N} \left[\boldsymbol{p}_i(\tau)\vartheta_i(\tau) - \boldsymbol{p}_i(0)\vartheta_i(0)\right] = -\int_0^\tau \left[\sum_{i=1}^{N} \frac{\boldsymbol{p}_i \boldsymbol{p}_i}{m_i} \cdot d\mathbf{S}_i - \frac{1}{2}\sum_{i,j}^{N} \boldsymbol{f}_{ij}\vartheta_{ij} - \sum_{i=1}^{N} \boldsymbol{f}_{i_{\text{ext}}}\vartheta_i\right] dt,$$

and using identity (4.59),

$$\overbrace{\sum_{i=1}^{N} \left[\boldsymbol{p}_i(\tau)\vartheta_i(\tau) - \boldsymbol{p}_i(0)\vartheta_i(0)\right]}^{\text{Accumulation}} + \overbrace{\sum_{i=1}^{N}\sum_{k=1}^{N_t} \boldsymbol{p}_i \sum_{\alpha=1}^{3} \frac{p_{\alpha i}}{|p_{\alpha i}|} dS_{\alpha i,k}}^{\text{Advection}} = \underbrace{\sum_{i,j}^{N} \int_0^\tau \boldsymbol{f}_{ij}(t)\vartheta_{ij}(t)dt + \sum_{i=1}^{N} \int_0^\tau \boldsymbol{f}_{i_{\text{ext}}}(t)\vartheta_i(t)dt}_{\text{Forcing}}. \tag{4.61}$$

The integral of the forcing term can be rewritten as the sum,

$$\int_0^\tau \boldsymbol{f}_{ij}(t)\vartheta_{ij}(t)dt \approx \Delta t \sum_{n=1}^{N_\tau} \boldsymbol{f}_{ij}\left(t_n\right)\vartheta_{ij}\left(t_n\right),$$

where N_τ is the number time steps. Equation (4.61) can be rearranged as follows,

$$\sum_{i=1}^{N} \frac{p_{\alpha i}(\tau)\vartheta_i(\tau) - p_{\alpha i}(0)\vartheta_i(0)}{\tau \Delta V} + \frac{\{\overline{\rho u_\alpha u_\beta}\}^+ - \{\overline{\rho u_\alpha u_\beta}\}^-}{\Delta r_\beta} = -\frac{\overline{K}^+_{\alpha\beta} - \overline{K}^-_{\alpha\beta}}{\Delta r_\beta} + \frac{\overline{T}^+_{\alpha\beta} - \overline{T}^-_{\alpha\beta}}{\Delta r_\beta} + \frac{1}{N_\tau \Delta V}\sum_{i=1}^{N}\sum_{n=1}^{N_\tau} f_{\alpha i_{\text{ext}}}(t_n)\vartheta_i(t_n), \tag{4.62}$$

where the overbar denotes a time average. The time-averaged traction in (4.62) is given by,

$$\overline{T}^{\pm}_{\alpha\beta} = -\frac{1}{N_\tau}\frac{1}{4\Delta A_\beta}\sum_{i,j}^{N}\sum_{n=1}^{N_\tau} \boldsymbol{f}_{\alpha ij}(t_n) dS^{\pm}_{\beta ij}(t_n),$$

The time-averaged kinetic component of the surface pressure in (4.62) is,

$$\overline{K}^{\pm}_{\alpha\beta} = \frac{1}{\tau}\frac{1}{2\Delta A_\beta}\sum_{i=1}^{N}\sum_{k=1}^{N_t} \frac{p_{\alpha i}(t_k)p_{\beta i}(t_k)}{|p_{\beta i}(t_k)|} dS^{\pm}_{\beta i,k}(t_k) - \{\overline{\rho u_\alpha u_\beta}\}^{\pm}.$$

Equation (4.62) demonstrates that the time average of the fluxes, stresses and body forces on a CV during the interval 0 to τ completely determines the change in momentum within the CV

for a single trajectory of the system through phase space (i.e. an MD simulation). The time evolution of the microscopic system, Eq. (4.62), can also be obtained directly by evaluating the derivatives of the mesoscopic expression (4.38) and invoking the ergodic hypothesis, hence replacing $\langle \alpha; f \rangle$ with $\frac{1}{\tau}\int_0^\tau \alpha dt$. The use of the ergodic hypothesis is justified provided that the time interval, τ, is sufficient to ensure phase space is adequately sampled.

Finally, there are no new techniques required to integrate the energy Eq. 4.56,

$$\sum_{i=1}^{N}\left[e_i(\tau)\vartheta_i(\tau) - e_i(0)\vartheta_i(0)\right] = -\int_0^\tau \left[\sum_{i=1}^{N} e_i \frac{\boldsymbol{p_i}}{m_i}\cdot d\mathbf{S}_i - \frac{1}{2}\sum_{i,j}^{N}\frac{\boldsymbol{p_i}}{m_i}\cdot \boldsymbol{f}_{ij}\vartheta_{ij}\right] dt \tag{4.63}$$

which gives the final form, written without external forcing,

$$\overbrace{\sum_{i=1}^{N}\left[e_i(\tau)\vartheta_i(\tau) - e_i(0)\vartheta_i(0)\right]}^{\text{Accumulation}} + \overbrace{\sum_{i=1}^{N}\sum_{k=1}^{N_t} e_i \sum_{\alpha=1}^{3}\frac{p_{\alpha i}}{|p_{\alpha i}|}dS_{\alpha i,k}}^{\text{Advection}} = \underbrace{\frac{1}{2}\sum_{i,j}^{N}\int_0^\tau \frac{\boldsymbol{p}_i(t)}{m_i}\cdot \boldsymbol{f}_{ij}(t)\vartheta_{ij}(t)dt}_{\text{Forcing}}. \tag{4.64}$$

As in the momentum balance equation, the integral of the Forcing term in Eq. (4.64) can be approximated by the sum,

$$\int_0^\tau \frac{\boldsymbol{p}_i(t)}{m_i}\cdot \boldsymbol{f}_{ij}(t)\vartheta_{ij}(t)dt \approx \Delta t \sum_{n=1}^{N_\tau}\frac{\boldsymbol{p}_i(t_n)}{m_i}\cdot \boldsymbol{f}_{ij}\left(t_n\right)\vartheta_{ij}\left(t_n\right),$$

where N_τ is the number time steps. In the next section, the elements, Accumulation, Advection and Forcing in the above equations are computed individually in an MD simulation to confirm Eqs. (4.60), (4.61) and (4.64) numerically.

4.4 Verifying the Control Volume Function

Molecular Dynamics (MD) simulations in 3D are used in this section to validate numerically, and explore the statistical convergence of, the CV formalism for three test cases. The first investigation was to confirm numerically the conservation properties of an arbitrary control volume. The second simulation compares the value of the scalar pressure obtained from the molecular CV formulation with that of the virial expression for an equilibrium system in a periodic domain. The final test is a Non Equilibrium Molecular Dynamics (NEMD) simulation of the start-up of Couette flow initiated by translating the top wall in a slit channel geometry. The NEMD system is analysed using the CV expressions Eqs. (4.60), (4.61) and (4.64), and the shear pressure was computed by the VA and CV routes. Newton's equations of motion were integrated using the half-step leap-frog Verlet algorithm, Allen & Tildesley (1987). The repulsive Lennard-Jones (LJ) or Weeks-Chandler-Andersen (WCA) potential (Rapaport, 2004),

$$\Phi(r_{ij}) = 4\epsilon\left[\left(\frac{\ell}{r_{ij}}\right)^{12} - \left(\frac{\ell}{r_{ij}}\right)^{6}\right] + \epsilon, \quad r_{ij} \le r_c,$$

was used for the molecular interactions, which is the Lennard-Jones potential shifted upwards by ϵ and truncated at the minimum in the potential, $r_{ij} = r_c \equiv 2^{1/6}\ell$. The potential is zero for

$r_{ij} > r_c$. The energy scale is set by ϵ, the length scale by ℓ and molecular mass by m. The results reported here are given in terms of ℓ, ϵ and m. A timestep of 0.005 was used for all simulations. The domain size in the first two simulations was 13.68, which contained $N = 2048$ molecules, the density was $\rho = 0.8$ and the reduced temperature was set to an initial value of $T = 1.0$. Test cases 1 and 2 described below are for equilibrium systems, and therefore did not require thermostatting. Case 3 is for a non-equilibrium system and required removal of generated heat, which was achieved by thermostatting the wall atoms only.

Case 1

In case 1, the periodic domain simulates a constant energy ensemble. The separate terms of the integrated mass, momentum and energy equations given in (4.60), (4.61) and (4.64) were evaluated numerically for several sizes of CV. The mass conservation can readily be shown to be satisfied as it simply requires tracking the number of molecules in the CV. The momentum and energy balance equations are conveniently checked for compliance at all times by evaluating the residual quantity,

$$\mathit{Residual} = \text{Accumulation} - \text{Forcing} + \text{Advection}, \tag{4.65}$$

which must be equal to zero at all times for the CV equations to be satisfied. This was demonstrated to be the case, as may be seen in Figs. 4.6a and 4.6b, for a cubic CV of side length 1.52 in the absence of body forces. The evolution of momentum inside the CV is shown numerically to be exactly equal to the integral of the surface forces until a molecule crosses the CV boundary. Such events give rise to a momentum flux contribution which appears as a spike in the Advection and Accumulation terms, as is evident in Fig. 4.6a. The residual nonetheless remains identically zero (to machine precision) at all times. The energy conservation is also displayed in Fig. 4.6b. The average error over the period of the simulation (100 LJ time units) was less than 1%, where the average error is defined as the ratio of the mean $|\mathit{Residual}|$ to the mean $|\mathit{Accumulation}|$ over the simulation. The error is attributed to the use of the leapfrog integration scheme, a conclusion supported by the linear decrease in error as timestep $\Delta t \to 0$.

Case 2

As in case 1, the same periodic domain is used in case 2 to simulate a constant energy ensemble. The objective of this exercise is to show that the average of the virial formula for the scalar pressure, Π_{vir}, applicable to an equilibrium periodic system,

$$\Pi_{vir} = \frac{1}{3V} \sum_{i=1}^{N} \left\langle \frac{\overline{\mathbf{p}}_i \cdot \overline{\mathbf{p}}_i}{m_i} + \frac{1}{2} \sum_{i \neq j}^{N} \mathbf{f}_{ij} \cdot \mathbf{r}_{ij}; f \right\rangle, \tag{4.66}$$

arises from the intermolecular interactions across the periodic boundaries (Tsai, 1978). The CV formula for the scalar pressure is,

$$\Pi_{CV} = \frac{1}{6} \left(P_{xx}^{+} + P_{xx}^{-} + P_{yy}^{+} + P_{yy}^{-} + P_{zz}^{+} + P_{zz}^{-} \right), \tag{4.67}$$

where the $P_{\alpha\alpha}^{\pm}$ normal pressure is defined in Eq. (4.34) and includes both the kinetic and configurational components on each surface. Both routes involve the pair forces, f_{ij}. However,

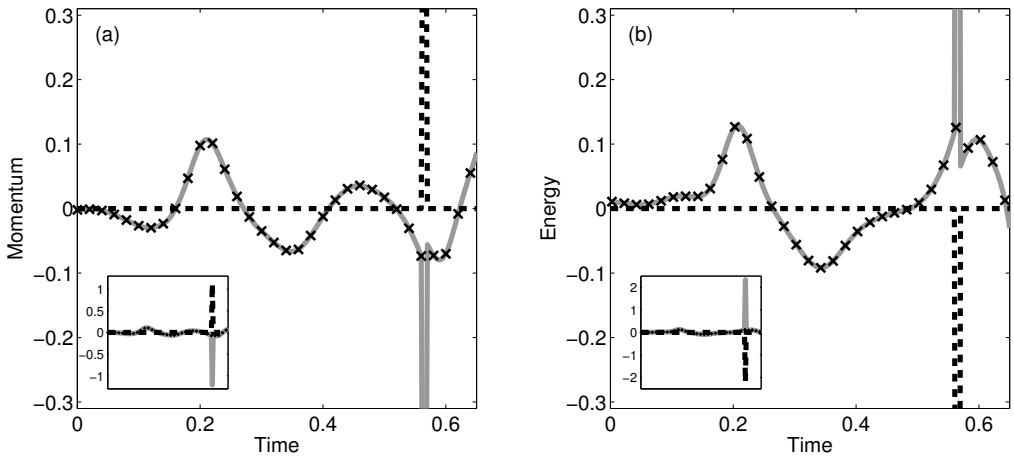

Figure 4.6: The various components in Eq. 4.65, 'Accumulation' (—), the time integral of the surface force, 'Forcing' (×), and momentum flux term, 'Advection' (- - -) are shown. 'Forcing' symbols are shown every 4th timestep for clarity and the insert shows the full ordinate scale over the same time interval on the abscissa. From top to bottom, (a) Momentum Control Volume, (b) Energy Control Volume.

the CV expression which uses MOP counts only those pair forces which cross a plane while VA (Virial) sums $f_{ij}r_{ij}$ over the whole volume. It is therefore expected that there would be differences between the two methods at short times, converging at long times. A control volume the same size as the periodic box was taken. The time averaged control volume, (Π_{CV}) and virial (Π_{vir}) pressure values are shown in Fig. 4.7a to converge towards the same value with increasing time. The simulation is started from an FCC lattice with a short range potential (WCA) so the initial configurational stress is zero. It is the evolution of the pressure from this initial state that is compared in Fig. 4.7a. The virial kinetic pressure makes use of the instantaneous values of the domain molecule's velocities at every time step. In contrast, the CV kinetic part of the pressure is due to molecular surface crossings only, which may explain its slower convergence to the limiting value than the kinetic part of the virial expression. To quantify this difference in convergence for the two measures of the pressure, the standard deviation, SD(x), is evaluated, ensuring decorrelation (Delgado-Buscalioni & Fabritiis, 2007) using block averaging (Rapaport, 2004). For the kinetic virial, SD(κ_{vir}) = 0.0056, and configurational, SD(σ_{vir}) = 0.0619. For the kinetic CV pressure SD(κ_{CV}) = 0.4549 and configurational SD(σ_{CV}) = 0.2901. The CV pressure, which makes use of the MOP formula, would therefore require more samples to converge to a steady state value (and is therefore more noisy in Fig. 4.7a). However, the MOP pressures are generally more efficient to calculate than the VA. This is especially true for large CV sizes, as only measurements at the surface of a volume are required instead of every molecule inside. In addition, a Heaviside function can be defined using assembly language to greatly optimise collecting MOP style statistics. More usefully, from an evaluation of only the interactions over the outer CV surface, the pressure in a volume of arbitrary size can be determined.

Figure 4.7b is a log-log plot of the Percentage Discrepancy (PD) between the two ($PD = [100 \times |\Pi_{CV} - \Pi_{vir}|/\Pi_{vir}]$). After 10 million timesteps or a reduced time of 5×10^4, the percentage discrepancy in the configurational part has decreased to 0.01%, and the kinetic part of the pressure matches the virial (and kinetic theory) to within 0.1%. The total pressure value agrees

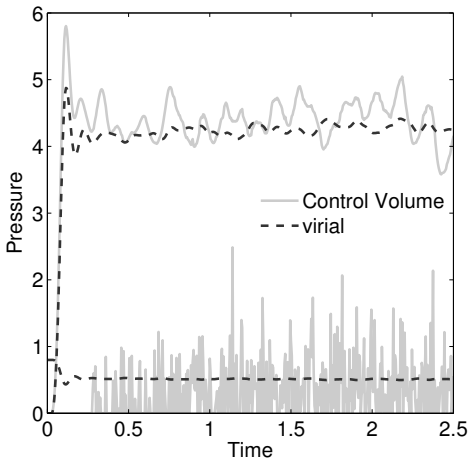

(a) The configurational and kinetic pressures are separated with configurational values typically having greater magnitudes (~ 4.0) than kinetic (~ 0.6). Continuous lines are control volume pressures and dotted lines are virial pressure.

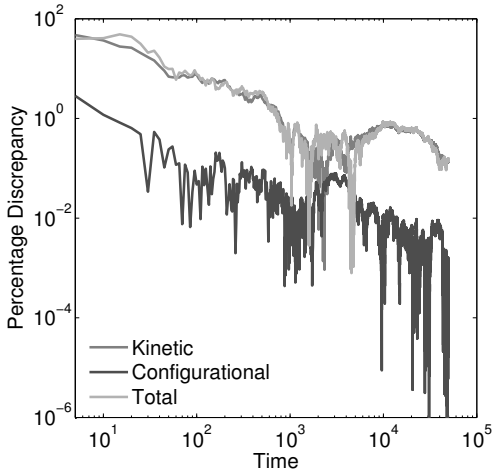

(b) The percentage relative difference between the virial and control volume time-accumulated scalar pressures (PD defined in the text). Values for the kinetic, configurational and total PD are shown.

Figure 4.7: Comparison of the pressures calculated using Π_{vir} and Π_{CV} from Eqs. (4.66) and (4.67) respectively as a function of time.

to within 0.1% at the end of this averaging period.

The simulation average temperature was 0.65, and the kinetic part of the CV pressure was statistically the same as the kinetic theory formula prediction, $\kappa_{CV} = \rho k_B T = 0.52$ (Rapaport, 2004). The VA formula for the pressure in a volume the size of the domain is by definition formally the same as that of the virial pressure. The next test case compares the CV and VA formulas for the shear stress in a system out of equilibrium.

Case 3

In this simulation study, Couette flow was simulated by entraining a model liquid between two solid walls. The top wall was set in translational motion parallel to the bottom (stationary) wall and the evolution of the velocity profile towards the steady-state Couette flow limit was followed. The velocity profile, and the derived CV and VA shear stresses are compared with the analytical solution of the unsteady diffusion equation. Four layers of tethered molecules were used to represent each wall, with the top wall given a sliding velocity of, $U_0 = 1.0$ at the start of the simulation, time $t = 0$. The temperature of both walls was controlled by applying the Nosé-Hoover (NH) thermostat to the wall atoms (Hoover, 1991). The two walls were thermostatted separately, and the equations of motion of the wall atoms were,

$$\dot{\mathbf{r}}_i = \frac{\overline{\mathbf{p}}_i}{m_i} + U_0 \mathbf{n}_x^+, \tag{4.68a}$$

$$\dot{\overline{\mathbf{p}}}_i = \mathbf{F}_i + \mathbf{f}_{i_{\text{ext}}} - \xi \overline{\mathbf{p}}_i, \tag{4.68b}$$

$$\mathbf{f}_{i_{\text{ext}}} = \mathbf{r}_{i_0} \left(4k_4 r_{i_0}^2 + 6k_6 r_{i_0}^4 \right), \tag{4.68c}$$

$$\dot{\xi} = \frac{1}{Q_\xi} \left[\sum_{n=1}^{N} \frac{\overline{\mathbf{p}}_n \cdot \overline{\mathbf{p}}_n}{m_n} - 3T_0 \right], \tag{4.68d}$$

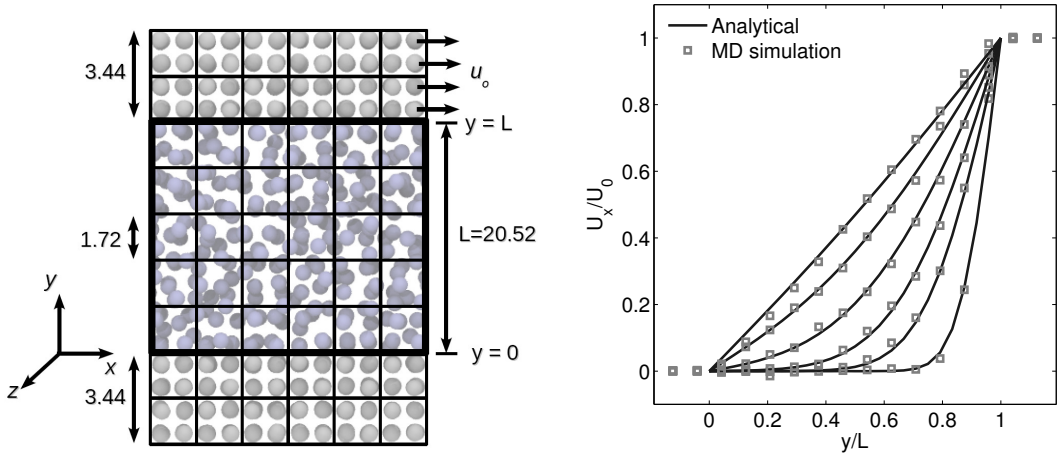

(a) Schematic diagram of the NEMD simulation geometry consisting of a sliding top wall and stationary bottom wall, both composed of tethered atoms. The simulation domain contained a lattice of contiguous CV used for pressure averaging (shown by the small boxes) while the thicker line denotes a single CV containing the entire liquid region.

(b) The $y-$ dependence of the streaming velocity profile at times $t = 2^n$ for $n = 0, 2, 3, 4, 5, 6$ from right to left. The squares are the NEMD CV data values and the analytical solution to the continuum equations of Eq. (4.71) is given at the same six times as continuous curves.

Figure 4.8: Couette flow domain schematic and velocity results

where $\mathbf{n}_x^+$ is a unit vector in the $x-$direction, $m_n \equiv m$, and $\mathbf{f}_{i_{\text{ext}}}$ is the tethered atom force, using the formula of Petravic & Harrowell (2006) ($k_4 = 5 \times 10^3$ and $k_6 = 5 \times 10^6$). The vector, $\mathbf{r}_{i_0} = \mathbf{r}_i - \mathbf{r}_0$, is the displacement of the tethered atom, i, from its lattice site coordinate, $\mathbf{r}_0$. The Nosé-Hoover thermostat dynamical variable is denoted by ξ, $T_0 = 1.0$ is the target temperature of the wall, and the effective time constant or damping coefficient, in Eq. (2.65c) was given the value, $Q_\xi = N\Delta t$. The simulation was carried out for a cubic domain of sidelength 27.40, of which the fluid region extent was 20.52 in the $y-$direction. Periodic boundaries were used in the streamwise (x) and spanwise (z) directions. The results presented are the average of eight simulation trajectories starting with a different set of initial atom velocities. The lattice contained 16384 molecules and was at a density of $\rho = 0.8$. The molecular simulation domain was sub-divided into 4096 (16^3) control volumes, and the average velocity and shear stress was determined in each of them. A larger single CV encompassing all of the liquid region of the domain, shown bounded by the thick line in Fig. 4.8a, was also considered.

The continuum solution for this configuration is considered now. Between two plates, there are no body forces and the flow eventually becomes fully developed, (Potter & Wiggert, 2002) so that Eq. (2.36) can be simplified and after applying the divergence theorem from Eq. (2.39) it becomes,

$$\frac{\partial}{\partial t}\int_V \rho \boldsymbol{u} dV = -\int_V \boldsymbol{\nabla}\cdot\boldsymbol{\Pi} dV,$$

which is valid for any arbitrary volume in the domain and must be valid at any point for a

continuum. The shear pressure in the fluid, $\Pi_{xy}(y)$, drives the time evolution,

$$\frac{\partial \rho u_x}{\partial t} = -\frac{\partial \Pi_{xy}}{\partial y}.$$

For a Newtonian liquid with viscosity, μ, (Potter & Wiggert, 2002),

$$\Pi_{xy} = -\mu \frac{\partial u_x}{\partial y}, \tag{4.69}$$

this gives the 1D diffusion equation,

$$\frac{\partial u_x}{\partial t} = \frac{\mu}{\rho} \frac{\partial^2 u_x}{\partial y^2}, \tag{4.70}$$

assuming the liquid to be incompressible. This can be solved for the boundary conditions,

$$u_x(0,t) = 0 \qquad u_x(L,t) = U_0 \qquad u_x(y,0) = 0,$$

where the bottom and top wall-liquid boundaries are at $y = 0$ and $y = L$, respectively. The Fourier series solution of these equations with inhomogeneous boundary conditions (Strauss, 1992) is,

$$u_x(y,t) = \begin{cases} U_0 & y = L \\ \sum_{n=1}^{\infty} u_n(t) sin\left(\frac{n\pi y}{L}\right) & 0 < y < L \\ 0 & y = 0 \end{cases} \tag{4.71}$$

where $\lambda_n = (n\pi/L)^2$ and $u_n(t)$ is given by,

$$u_n(t) = \frac{2U_0(-1)^n}{n\pi} \left[\exp\left(-\frac{\lambda_n \mu t}{\rho}\right) - 1\right].$$

The velocity profile resolved at the control volume level is compared with the continuum solution in Fig. 4.8b. There were 16 cubic NEMD CV of side length 1.72 spanning the system in the y direction, with each data point on the figure being derived from a local time average of 0.5 time units. The analytic continuum solution was evaluated numerically from Eq. (4.71) with $n = 1000$ and $\mu = 1.6$, the latter a literature value for the WCA fluid shear viscosity at $\rho = 0.8$ and $T = 1.0$, (Silva *et al.*, 2003). There is mostly very good agreement between the analytic and NEMD velocity profiles at all times, although some effect of the stacking of molecules near the two walls can be seen in a slight blunting of the fluid velocity profile very close to the tethered walls (located by the horizontal two squares on the far left and right of the figure) which is an aspect of the molecular system that the continuum treatment is not capable of reproducing.

The VA and CV shear pressure, given by Eqs. (4.32) and (4.34), are compared at time $t = 10$ in Fig. 4.9a. The comparison is for a single simulation trajectory resolved into 16 cubic volumes of size 1.72 in the $y-$direction, with averaging in the x and z directions and over 0.5 in reduced time.

The figure shows the shear pressure on the faces of the CV. Inside the CV, the pressure

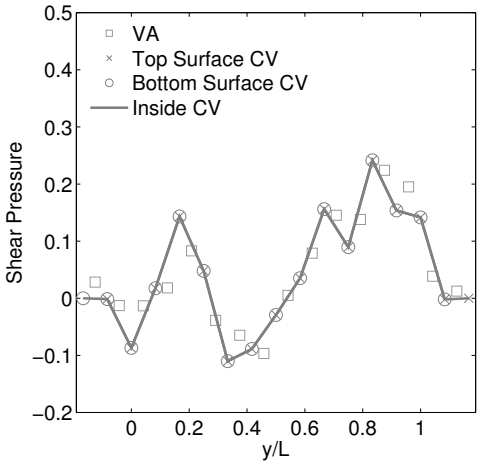

(a) The $y-$dependence of the shear pressure at $t = 10$, averaged over 100 timesteps and for a single simulation trajectory. The VA value from Eq. (4.32) are the squares. The CV surface traction from Eq. (4.34) is indicated by $\times$ and $\circ$ for the top and bottom surfaces, respectively. The solid gray line displays the resulting pressure field using Eq. (4.39) with linear shape functions.

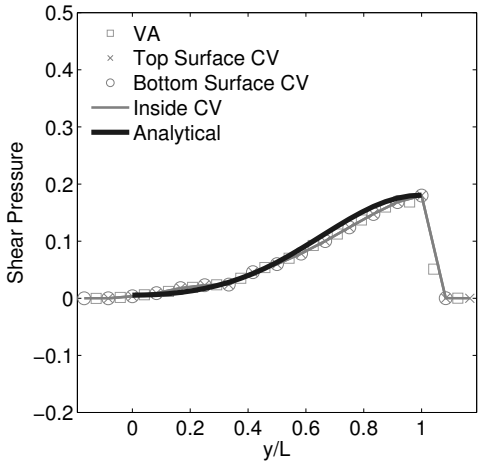

(b) As Fig. 4.9a, except that the NEMD results are averaged over a set of eight independent simulations of $1,000$ timesteps (5 reduced time units) each. The simulation-derived VA and CV shear pressures are compared with the continuum analytical solution given in Eq. (4.72) (solid black line). The jump in the profile on the right of the figure is due to the presence of the tethered wall.

Figure 4.9: Couette flow shear pressure results

was assumed to vary linearly, and the value at the midpoint is shown to be comparable to the VA-determined value. Figure 4.9a shows that there is good agreement between the VA and CV approaches. Note that the CV pressure is effectively the MOP formula applied to the faces of the cube, and hence this case study demonstrates a consistency between MOP and VA. We have shown previously that this is true for the special case of an infinitely thin bin or the limit of the pressure at a plane (Heyes *et al.*, 2011). Practically, the extent of agreement in this exercise is limited by the inherent assumptions and spatial resolution of the two methods; a single average over a volume is required for VA, but a linear pressure relationship is assumed for CV to obtain the pressure tensor value corresponding to the centre of the CV.

The continuum analytical xy pressure tensor component can be derived analytically using the same Fourier series approach for $\partial u_x/\partial y$,(Strauss, 1992),

$$\Pi_{xy}(y,t) = -\frac{\mu U_0}{L}\left[1 + 2\sum_{n=1}^{\infty}(-1)^n e^{-\frac{\lambda_n \mu t}{\rho}} cos\left(\frac{n\pi y}{L}\right)\right], \tag{4.72}$$

which is valid for the entire domain $0 \leq y \leq L$.

A statistically meaningful comparison between the CV, VA and continuum analytic shear pressure profiles requires more averaging of the simulation data than for the streaming velocity, (Hadjiconstantinou *et al.*, 2003), and eight independent simulation trajectories over 5 reduced time units were used. Figure 4.9b shows that the three methods exhibit good agreement within the simulation statistical uncertainty.

As a final demonstration of the use of the CV equations, the control volume is now chosen to encompass the entire liquid domain (see Fig. 4.8a), and therefore the external forces arise from interactions with the wall atoms only. The momentum equation, Eq. (4.55), is written as,

$$\frac{\partial}{\partial t}\sum_{i=1}^{N}\mathbf{p}_i\vartheta_i = -\sum_{i=1}^{N}\overbrace{\frac{\mathbf{p}_i\mathbf{p}_i}{m_i}\cdot d\mathbf{S}_i}^{①} + \sum_{i=1}^{N}\overbrace{\mathbf{f}_{i_{\text{ext}}}\vartheta_i}^{③} - \frac{1}{2}\sum_{i,j}^{N}\big[\underbrace{\mathbf{f}_{ij}dS_{xij}}_{②} + \underbrace{\mathbf{f}_{ij}}_{④}\,dS_{yij} + \underbrace{\mathbf{f}_{ij}dS_{zij}}_{②}\big],$$

which can be simplified as follows. For term, ① in the above equation, the fluxes across the CV boundaries in the streamwise and spanwise directions cancel due to the periodic boundary conditions. Fluxes across the xz boundary surface are zero as the tethered wall atoms prevent such crossings. The force term, ②, also vanishes because across the periodic boundary, $\mathbf{f}_{ij}dS^{+}_{xij} = -\mathbf{f}_{ij}dS^{-}_{xij}$, (similarly for z). The external force term, ③, is zero because all the forces in the system result from interatomic interactions. The sum of the f_{yij} force components across the horizontal boundaries will be equal and opposite, and by symmetry the two f_{zij} terms in ④ will be zero on average. The above equation therefore reduces to,

$$\frac{\partial}{\partial t}\sum_{i=1}^{N}\mathbf{p}_i\vartheta_i = -\frac{1}{2}\sum_{i,j}^{N}\left[f_{xij}dS^{+}_{yij} - f_{xij}dS^{-}_{yij}\right]. \tag{4.73}$$

As the simulation approaches steady state, the rate of change of momentum in the control volume tends to zero because the difference between the shear stresses acting across the top and bottom walls vanishes. The forces on the xz plane boundary and momentum inside the CV are plotted in Fig. 4.10 to confirm Eq. (4.73) numerically. The time evolution of these molecular momenta and surface stresses are compared to the analytical continuum solution for the CV,

$$\frac{\partial}{\partial t}\int_V \rho u_x dV = -\left[\int_{S_f^+}\Pi_{xy}dS_f^+ - \int_{S_f^-}\Pi_{xy}dS_f^-\right]. \tag{4.74}$$

The normal components of the pressure tensor are non-zero in the continuum, but exactly balance across opposite CV faces, i.e. $\Pi^{+}_{xx} = \Pi^{-}_{xx}$. By appropriate choice of the gauge pressure, Π_{xx} does not appear in the governing Eq. (4.74). The left hand side of the above equation is evaluated from the analytic expression for u_x,

$$\frac{\partial}{\partial t}\int_V \rho u_x dV = 2\Delta x\Delta z\frac{\mu U_0}{L}\sum_{n=1}^{\infty}\left[1-(-1)^n\right]e^{-\frac{\lambda_n\mu t}{\rho}}. \tag{4.75}$$

The right hand side is obtained from the analytic continuum expression for the shear stress, for the bottom surface at $y = 0$,

$$\int_{S_f^+}\Pi_{xy}dS_f^+ = -2\Delta x\Delta z\frac{\mu U_0}{L}\sum_{n=1}^{\infty}e^{-\frac{\lambda_n\mu t}{\rho}}, \tag{4.76}$$

and for the top $y = L$,

$$\int_{S_f^-}\Pi_{xy}dS_f^- = -2\Delta x\Delta z\frac{\mu U_0}{L}\sum_{n=1}^{\infty}(-1)^n e^{-\frac{\lambda_n\mu t}{\rho}}. \tag{4.77}$$

In Fig 4.10, the momentum evolution on the left hand side of Eq. (4.73) is compared to Eq. (4.75). Equations (4.76) and (4.77) are also given for the shear stresses acting across the top and bottom of the molecular control volume (right hand side of Eq. (4.73)).

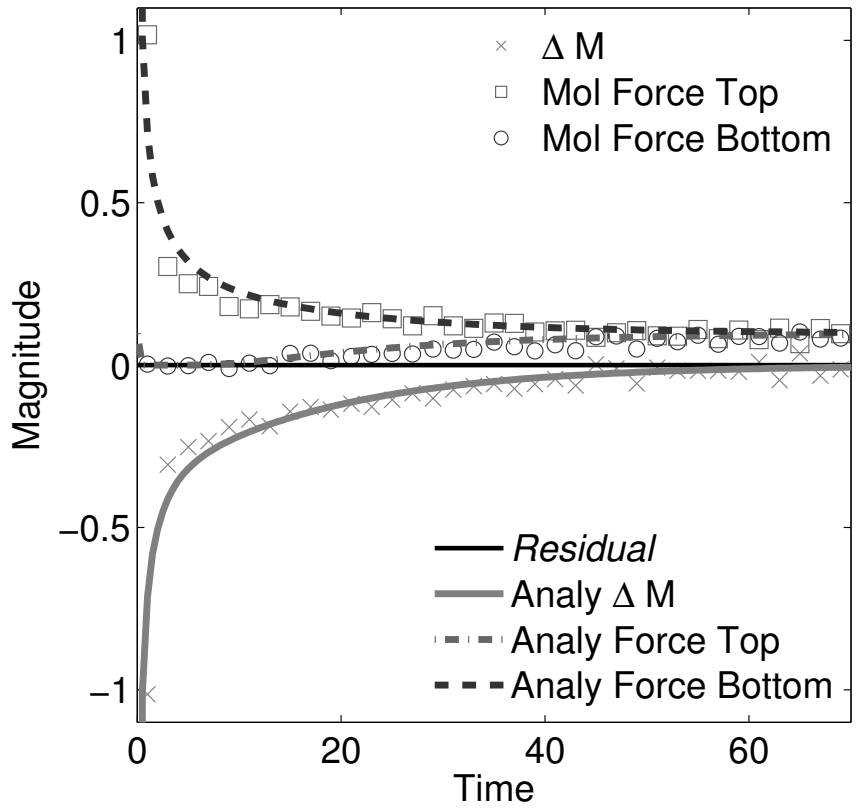

Figure 4.10: The evolution of surface forces and momentum change for a molecular CV from Eq. (4.73), (points) and analytical solution for the continuum (Eqs. (4.76), (4.77) and (4.75)), presented as lines on the figure. The *Residual*, defined in Eq. (4.65), is also given. Each point represents the average over an ensemble of eight independent systems and 40 timesteps.

The scatter seen in the MD data reflects the thermal fluctuations in the forces and molecular crossings of the CV boundaries. The average response nevertheless agrees well with the analytic solution, bearing in mind the element of uncertainty in the matching state parameter values. This example demonstrates the potential of the CV approach applied on the molecular scale, as it can be seen that computation of the forces across the CV boundaries determines completely the average molecular microhydrodynamic response of the system contained in the CV. In fact, the force on only one of the surfaces is all that was required, as the force terms for the opposite surface could have been obtained from Eq. (4.73).

4.5 Overview

In analogy to continuum fluid mechanics, the evolution equations for a molecular system have been expressed in a Control Volume (CV) form. A key ingredient is the definition and manipulation of a Lagrangian to Control Volume conversion function, ϑ, which identifies molecules within an arbitrary CV.

The key equations from this work are summarised here as they will form the basis for the next chapter. The Control Volume operator and its derivative are of the form,

$$\begin{aligned}\vartheta_i \equiv \quad & \left[H(x^+ - x_i) - H(x^- - x_i)\right] \\ & \times \left[H(y^+ - y_i) - H(y^- - y_i)\right] \\ & \times \left[H(z^+ - z_i) - H(z^- - z_i)\right],\end{aligned} \qquad \begin{aligned} dS_{xi} \equiv \frac{\partial \vartheta_i}{\partial x} = \quad & \left[\delta(x^+ - x_i) - \delta(x^- - x_i)\right] \\ & \times \left[H(y^+ - y_i) - H(y^- - y_i)\right] \\ & \times \left[H(z^+ - z_i) - H(z^- - z_i)\right]\end{aligned}$$

where $\vartheta_i = 1$ if molecule i is inside the CV and zero otherwise. Its derivative is only non-zero as i is crossing one of the surfaces of the CV. An analogous $\mathcal{LCV}$ function can be defined for the line of interaction $\boldsymbol{\iota} \equiv \boldsymbol{r}_i - s\boldsymbol{r}_{ij}$ between two molecules i and j,

$$\begin{aligned}\vartheta_s \equiv \quad & \left[H(x^+ - \iota_x) - H(x^- - \iota_x)\right] \\ & \times \left[H(y^+ - \iota_y) - H(y^- - \iota_y)\right] \\ & \times \left[H(z^+ - \iota_z) - H(z^- - \iota_z)\right],\end{aligned} \qquad \begin{aligned} dS_{xij} \equiv \quad & \left[\delta(x^+ - \iota_x) - \delta(x^- - \iota_x)\right] \\ & \times \left[H(y^+ - \iota_y) - H(y^- - \iota_y)\right] \\ & \times \left[H(z^+ - \iota_z) - H(z^- - \iota_z)\right]\end{aligned}$$

With derivative $d\mathbf{S}_{ij}$ selecting interactions crossing the x^+ and x^- surfaces of the control volume. Using these two forms of the $\mathcal{LCV}$ functions and their derivative, it is then possible to derive discrete analogues to the continuum control volumes equations. These include,

The time evolution of the mass,

$$\frac{d}{dt}\sum_{i=1}^{N} m_i \vartheta_i = -\sum_{i=1}^{N} \mathbf{p}_i \cdot d\mathbf{S}_i, \tag{4.78}$$

where m_i is molecular mass and $\mathbf{p}_i$ the momentum. The time evolution of momentum in the molecular control volume is,

$$\underbrace{\frac{d}{dt}\sum_{i=1}^{N} \mathbf{p}_i \vartheta_i}_{Accumulation} = \underbrace{-\sum_{i=1}^{N} \frac{\mathbf{p}_i \mathbf{p}_i}{m_i} \cdot d\mathbf{S}_i}_{Advection} + \underbrace{\frac{1}{2}\sum_{i,j}^{N} \boldsymbol{\varsigma_{ij}} \cdot d\mathbf{S}_{ij} + \sum_{i=1}^{N} \mathbf{f}_{i_{\text{ext}}} \vartheta_i}_{Forcing}, \tag{4.79}$$

where $\boldsymbol{\varsigma_{ij}}$ is a form of inter-molecular stress tensor and $\mathbf{f}_{i_{\text{ext}}}$ the external force term. The time evolution of energy, e_i, in a molecular control volume is,

$$\frac{d}{dt}\sum_{i=1}^{N} e_i \vartheta_i = -\sum_{i=1}^{N} e_i \frac{\mathbf{p}_i}{m_i} \cdot d\mathbf{S}_i + \frac{1}{2}\sum_{i,j}^{N} \frac{\mathbf{p}_i}{m_i} \cdot \boldsymbol{\varsigma_{ij}} \cdot d\mathbf{S}_{ij} + \sum_{i=1}^{N} \frac{\mathbf{p}_i}{m_i} \cdot \mathbf{f}_{i_{\text{ext}}} \vartheta_i, \tag{4.80}$$

The left hand sides of Eqs. (4.78), (4.79) and (4.80) are the time evolution of a volume in space and the resulting right hand side is written in terms of stresses and surface fluxes. The final appearance of the equations has the same form as Reynolds' Transport Theorem applied to a discrete system (see appendix A). The equations presented follow directly from Newton's

equation of motion for a system of discrete particles, requiring no additional assumptions and therefore sharing the same range of validity.

Using the $\mathcal{LCV}$ function, the relationship between Volume Average (VA) (Lutsko, 1988; Cormier *et al.*, 2001) and Method Of Planes (MOP) pressure (Todd *et al.*, 1995; Han & Lee, 2004) has been established, without Fourier transformation. These avoids the assumption of homogeneity in any coordinate direction and is therefore a three dimensional generalisation and localisation of the MOP form. The MOP and VA definitions of pressure are shown numerically to give equivalent results away from equilibrium and, for homogeneous systems, shown to equal the virial pressure.

A Navier–Stokes-like equation was derived for the evolution of momentum within the control volume, expressed in terms of surface fluxes and stresses. This provides an exact mathematical relationship between molecular fluxes/pressures and the evolution of momentum and energy in a CV. Numerical evaluations of the terms in the conservation of mass, momentum and energy equations demonstrated consistency with theoretical predictions.

The CV formulation is general, and can be applied to derive conservation equations for any fluid dynamical property localised to a region in space. It can also facilitate the derivation of conservative numerical schemes for MD, and the evaluation of the accuracy of numerical schemes. Finally, it allows for accurate evaluation of macroscopic flow properties, in a manner consistent with the continuum conservation laws. These properties will be exploited in the next chapter to derive coupling schemes localised to a region in space.

Chapter 5

Mathematical Development of a Coupling Scheme

5.1 Introduction

The $\mathcal{LCV}$ function formalism developed and verified in the previous chapter is used to devise a coupling scheme in this chapter.

This function is invoked in order to define the molecular equivalents to the continuum control volumes, *i.e.* for number of molecules, mass and momentum in a CV,

$$N_I = \sum_{i=1}^{N} \vartheta_i; \qquad \int_V \rho dV = \sum_{i=1}^{N} m_i \vartheta_i; \qquad \int_V \rho \boldsymbol{u} dV = \sum_{i=1}^{N} m_i \dot{\boldsymbol{r}}_i \vartheta_i.$$

The sums over all molecules N with a $\mathcal{LCV}$ function replaces the commonly used convention of summing over a limited subset in a given region N_I, *i.e.* for some arbitrary quantity $\mathcal{A}_i$,

$$\sum_{n=1}^{N} \mathcal{A}_i \vartheta_i \equiv \sum_{n=1}^{N_I} \mathcal{A}_i \equiv \sum_{n \in S} \mathcal{A}_i \;\text{ where }\; S = \{i | \boldsymbol{r}^- < \boldsymbol{r}_i < \boldsymbol{r}^+\}. \tag{5.1}$$

The advantage of these functional localisation, using ϑ_i, is in its mathematical utility. By using the $\mathcal{LCV}$ function, the limits of the sums in Eq. (5.1) are explicitly enforced by ϑ_i and the effects of integrals and derivatives are replaced by mathematical manipulation of the $\mathcal{LCV}$ function. This was demonstrated in the previous chapter where the time evolution of $\mathcal{LCV}$ localised regions was shown to yield the CV conservation Eq. (4.54), (4.55) and (4.56). The momentum equation, Eq. (4.55),

$$\frac{\partial}{\partial t} \sum_{i=1}^{N} m_i \dot{\boldsymbol{r}}_i \vartheta_i = -\sum_{i=1}^{N} m_i \dot{\boldsymbol{r}}_i \dot{\boldsymbol{r}}_i \cdot d\mathbf{S}_i + \frac{1}{2} \sum_{i,j}^{N} \boldsymbol{f}_{ij} \vartheta_{ij} + \sum_{i=1}^{N} \boldsymbol{f}_{i_{\text{ext}}} \vartheta_i,$$

and energy equation, Eq. (4.80), are relevant in this chapter,

$$\frac{d}{dt} \sum_{i=1}^{N} e_i \vartheta_i = -\sum_{i=1}^{N} e_i \dot{\boldsymbol{r}}_i \cdot d\mathbf{S}_i + \frac{1}{2} \sum_{i,j}^{N} \dot{\boldsymbol{r}}_i \cdot \boldsymbol{\varsigma_{ij}} \cdot d\mathbf{S}_{ij} + \sum_{i=1}^{N} \dot{\boldsymbol{r}}_i \cdot \mathbf{f}_{i_{\text{ext}}} \vartheta_i,$$

A change of notation is performed in this chapter, with $\boldsymbol{p}_i$ replaced by $m_i \dot{\boldsymbol{r}}_i$ as in this equation.

The symbol $\boldsymbol{p}_i$ is reserved for the canonical momentum conjugate in this chapter, therefore $\boldsymbol{p}_i \neq m_i\dot{\boldsymbol{r}}_i$ in general. The intermolecular forces can be expressed in terms of the stress over the CV surfaces,

$$\sum_{i,j}^{N} \boldsymbol{f}_{ij}\vartheta_{ij} = \sum_{i,j}^{N} \boldsymbol{\varsigma}_{ij} \cdot d\mathbf{S}_{ij},$$

where $d\mathbf{S}_i$ selects the molecules i currently crossing the CV surfaces and $d\mathbf{S}_{ij}$ select the interaction between i and j that are currently crossing the CV surface. As the overlap between the continuum and the MD may consist of a number of different CFD cells, the notation I, J and K is introduced to denote the cartesian location of the continuum cells. The CV function and its derivative include a superscript to denote the continuum volume which they correspond to, *e.g.* ϑ_i^{IJK} or its derivative $d\mathbf{S}_i^{IJK^{\pm}}$ for cell I, J, K with the $\pm$ denoting top and bottom surfaces.

The $\mathcal{LCV}$ function will be utilised in order to derive constrained dynamics algorithms which interlinks the evolution of the molecular system with its continuum counterpart. These algorithms will be derived from the principle of least action and Gauss' principle of least constraint. The key novelty here is the localisation of these constraints to a region in space, a requirement unique to coupling which is applied along an interface between two co-existent domains. It is here that the importance of the $\mathcal{LCV}$ function as a method to ensure the localisation of the constraint becomes clear. The resulting $\mathcal{LCV}$ coupling equation can be shown to be the most general form of coupling equation. Under certain assumptions, it can be shown to yield the coupling schemes discussed in the literature (see chapter 2) namely those of O'Connell & Thompson (1995), Nie *et al.* (2004*a*) and Flekkøy *et al.* (2000). The various assumptions inherent in the existing coupling schemes are thereby exposed. A study of the various terms in the $\mathcal{LCV}$ coupling equations, using MD simulation, provides insight into the importance of these terms and the nature of the coupling algorithm itself. The focus of this chapter is the derivation and anatomy of a new $\mathcal{LCV}$ coupling equation, not coupling in general. Coupled simulations are therefore presented to motivate this equation, before discussing the various terms in the context of controlling molecular systems only. A fully coupled case would introduce significant extra complexity and obscure the main contribution of the $\mathcal{LCV}$ coupling equations presented.

This chapter is organised as follows: section 5.2 contains the derivation of a $\mathcal{LCV}$ localised state coupling algorithm, first from the principle of least action and then from Gauss' principle. A general coupling equation is obtained and the relationship to the O'Connell & Thompson (1995) and Nie *et al.* (2004*a*) schemes is established. In the next section, 5.3, the various terms in the generalised constraint equations are tested numerically using coupled MD and CFD simulation of impulse-started Couette flow, Couette flow with wall roughness and a full MD simulation of a converging-diverging channel. Finally, the relationship to flux coupling is explored in section 5.4, followed by concluding remarks from this chapter in 5.5.

5.2 Control Volume State Coupling

In this section, the Control Volume methodology is applied to the field of MD-continuum coupling. The main challenge in coupling is to ensure that the molecular system matches the continuum. There is no unique solution as four averaged continuum parameters $(\boldsymbol{u}, P)$ must govern $6N$ molecular degrees of freedom. There are, however, guiding physical principles in the form of the

principle of least action or Gauss' principle of least constraint. These methods were introduced in chapter 2, section 2.2.2 and their application to coupling discussed in section 2.5.2. Using these methods, it is possible to develop equations of motion which evolve according to physical principles while ensuring the dynamics match, on average, those of the continuum system. The aim of this section is to develop a physically sound constraint localised to a consistent control volume in space.

This section starts by applying the principle of least action localised using the control volume function. The resulting equations are written in Hamiltonian form ($\dot{\boldsymbol{q}}, \dot{\boldsymbol{p}}$) to allow it to be related to the constrained form in the first paper on coupling by O'Connell & Thompson (1995). The assumptions required to obtain the form of O'Connell & Thompson (1995) are discussed. Through mathematical manipulation, the two Hamiltonian equations are written in a single equation in the form of Newton's law subject to a constraint force. The equation in terms of Newton's law can be shown to be consistent with the form obtained from Gauss' principle of least constraint localised to a control volume. The assumptions required to obtain the form of Nie *et al.* (2004*a*) are discussed. In the process, a number of additional terms not present in other coupling methodologies are identified and the importance of these are explained.

5.2.1 Control Volume Coupling Scheme from the Principle of Least Action

The principle of least action is employed in this section in order to constrain a CV in the molecular region. The governing equations will be expressed in Hamiltonian ($\boldsymbol{q}$,$\boldsymbol{p}$) form. This has a number of advantages and is commonly used in the NEMD literature (Evans & Morriss, 2007). It also allows the constraint to be compared to the coupling scheme of O'Connell & Thompson (1995). The constraint applied is the difference in momentum between a control volume in the continuum and molecular regions,

$$\boldsymbol{g}(\boldsymbol{q}, \dot{\boldsymbol{q}}, t) = \sum_{n=1}^{N} m_n \dot{\boldsymbol{q}}_n \vartheta_n - \int_V \rho \boldsymbol{u} dV = 0, \tag{5.2}$$

where V here is the volume of an equivalently size control volume in both regions. Notice that by expressing the constraint in terms of the CV function, the region of application is explicitly contained within the definition and the sum is over all possible molecules N in the system. In addition, the constraint is applied in the Eulerian reference frame in both MD and continuum regions. A constrained Lagrangian,

$$\mathcal{L}_c \equiv \mathcal{L} + \boldsymbol{\lambda} \cdot \boldsymbol{g}, \tag{5.3}$$

is to be minimised using the principle of least action, expressed in terms of the canonical momentum as in Eqs. (2.25a) and (2.25b). Recall from section 2.2.2 (see also Flannery (2005)) that the equations of motion for a non-holonomic constraint are obtained from,

$$\frac{d}{dt}\frac{\partial \mathcal{L}_c}{\partial \dot{q}_i} - \frac{\partial \mathcal{L}_c}{\partial q_i} = 0, \tag{5.4}$$

which is consistent with the non-holonomic form of the Euler Lagrange equation (Eq. (2.23)) and Gauss' Least constraint (Eq. (2.28)), provided the constraint satisfies Eq. (2.24) – *i.e.* Eq.

(5.2) is semi-holonomic. The CV constraint of Eq. (5.2) is substituted into Eq. (2.24) and gives,

$$\frac{d}{dt}\frac{\partial g_\alpha}{\partial \dot{q}_i} - \frac{\partial g_\alpha}{\partial q_i} = m_i \frac{d\vartheta_i}{dt} - m_i \dot{q}_i \frac{\partial \vartheta_i}{\partial q_i} = m_i \dot{q}_i dS_i - m_i \dot{q}_i dS_i = 0, \tag{5.5}$$

which demonstrates that the constraint of Eq. (5.2) is semi-holonomic. The Eq. (5.4) can therefore be used to derived equations of motion for this constrained system. It is the aim of this section to write the equations of motion in ($\boldsymbol{q}$,$\boldsymbol{p}$) form; therefore, the constrained conjugate momentum is obtained using the definition,

$$\boldsymbol{p}_i = \frac{\partial \mathcal{L}_c}{\partial \dot{\boldsymbol{q}}_{\boldsymbol{i}}} = m_i \dot{\boldsymbol{q}}_i + m_i \vartheta_i \boldsymbol{\lambda}. \tag{5.6}$$

The time evolution of the momentum in terms of $\dot{\boldsymbol{p}}_i$ is given by substituting Eq. (5.6) into the constrained Euler Lagrange equation 5.4,

$$\dot{\boldsymbol{p}}_i = \frac{\partial \mathcal{L}_c}{\partial \boldsymbol{q}_{\boldsymbol{i}}} = \boldsymbol{F}_i - \boldsymbol{\lambda} m_i \dot{\boldsymbol{q}}_i \cdot d\mathbf{S}_i. \tag{5.7}$$

Substituting Eq. (5.6) into the constraint Eq. (5.2), and solving for $\boldsymbol{\lambda}$ gives,

$$\boldsymbol{\lambda} = \frac{1}{\sum_{n=1}^{N} m_n \vartheta_n^2} \left[\sum_{n=1}^{N} \boldsymbol{p}_n \vartheta_n - \int_V \rho \boldsymbol{u} dV \right], \tag{5.8}$$

which is expressed in terms of the peculiar momenta $\boldsymbol{p}_i$. The Hamiltonian form of the equations of motion are therefore,

$$\dot{\boldsymbol{q}}_i = \frac{\boldsymbol{p}_i}{m_i} - \frac{\vartheta_i}{M_I} \left[\sum_{n=1}^{N} \boldsymbol{p}_n \vartheta_n - \int_V \rho \boldsymbol{u} dV \right], \tag{5.9a}$$

$$\dot{\boldsymbol{p}}_i = \boldsymbol{F}_i - \frac{m_i \dot{\boldsymbol{q}}_i \cdot d\mathbf{S}_i}{M_I} \left[\sum_{n=1}^{N} \boldsymbol{p}_n \vartheta_n - \int_V \rho \boldsymbol{u} dV \right], \tag{5.9b}$$

on introducing the definition $M_I \equiv \sum_{n=1}^{N} m_n \vartheta_n$ (note $M_I \equiv \int_V \rho dV$) and using the property of the Heaviside functions[1], $\vartheta_i^2 = \vartheta_i$. The constraints in Eqs. (5.9a) and (5.9b) are explicitly localised by the CV function, ϑ_i or $d\mathbf{S}_i$ and are therefore valid for the entire system. Outside of the constrained region, $\vartheta_i = 0$ or $d\mathbf{S}_i = 0$ and the dynamics are unconstrained. By deriving this equation using the principle of least action and a semi-holonomic constraint, the conservation of energy is ensured (Goldstein *et al.*, 2002).

The physical interpretation of Eq. (5.9a) is that the peculiar velocity of a given molecule i inside the constrained CV is adjusted in line with the difference between the molecular and the continuum momenta. This ensures the molecules move, on average, with a velocity consistent with the continuum. Equation (5.9b) applies a force to the molecules as soon as it enters or leaves a volume. This force acts to accelerate the entering molecule in line with the constraint currently applied to the molecules inside the volume.

Consider two adjacent MD cells with different constraints due to the difference in velocities in the overlapping continuum grid. These cells are denoted by I and $I+1$ and the CV function includes a superscript to identify which cell it corresponds to in a similar manner to the continuum

[1]The derivative of $d\vartheta_i^2/dr_i = 2\vartheta_i dS_i = dS_i$, because $\vartheta(r = r^{\pm}) = 1/2$ as $H(0) = 1/2$.

CV volume numbering,

$$\dot{\boldsymbol{p}}_i = \boldsymbol{F}_i \quad - \quad \frac{m_i\dot{q}_{xi}dS_{xi}^{I^+} - m_i\dot{q}_{xi}dS_{xi}^{I^-}}{M_I}\left[\sum_{n=1}^{N}\boldsymbol{p}_n\vartheta_n^I - \int_{V_I}\rho\boldsymbol{u}dV_I\right] \\ - \quad \frac{m_i\dot{q}_{xi}dS_{xi}^{[I+1]^+} - m_i\dot{q}_{xi}dS_{xi}^{[I+1]^-}}{M_{I+1}}\left[\sum_{n=1}^{N}\boldsymbol{p}_n\vartheta_n^{I+1} - \int_{V_{I+1}}\rho\boldsymbol{u}dV_{I+1}\right],$$

The top surface of CV I is the bottom of CV $[I+1]$ so that $\dot{q}_{xi}dS_{xi}^{I^+} = \dot{q}_{xi}dS_{xi}^{[I+1]^-}$. If the two adjacent volumes have the same momentum difference, $1/M_{I+1}\left[\sum_{n=1}^{N}\boldsymbol{p}_n\vartheta_n^{I+1} - \int_{V_{I+1}}\rho\boldsymbol{u}dV_{I+1}\right] = 1/M_I\left[\sum_{n=1}^{N}\boldsymbol{p}_n\vartheta_n^{I} - \int_{V_I}\rho\boldsymbol{u}dV_I\right]$, the connected surface flux terms will cancel and no forces are applied,

$$\dot{\boldsymbol{p}}_i = \boldsymbol{F}_i \quad - \quad \frac{m_i\dot{q}_{xi}dS_{xi}^{[I+1]^+} - m_i\dot{q}_{xi}dS_{xi}^{I^-}}{M_I}\left[\sum_{n=1}^{N}\boldsymbol{p}_n\vartheta_n^I - \int_{V_I}\rho\boldsymbol{u}dV_I\right] \tag{5.11a}$$

This equation therefore only applies a force to molecules which cross the top or bottom surface of the consolidated CV (size based on the combined I and $I+1$), which demonstrates that this equation remains valid for MD cells of an arbitrary size. As the MD cells volume tends to zero, the difference in constraint magnitude between cells will be less and the surface fluxes between adjacent cells become less significant.

Relationship to the method of O'Connell & Thompson (1995)

Once the formulation is expressed in the ($\dot{\boldsymbol{q}}$,$\dot{\boldsymbol{p}}$) form, it can be compared to those of O'Connell & Thompson (1995), (see Eqs. (2.72a) and (2.72b in chapter 2). In order to obtain the equations of O'Connell & Thompson (1995), a number of assumptions are required. The link between Eq. (5.9a) and Eq. (2.72a) is considered first. The mass of all molecules in the systems is assumed to be be the same ($\forall\, i : m_i = m$) so that $M_I = m\sum_i^N \vartheta = mN_I$. The momentum for the CV is approximated as a single value $\int_V \rho\boldsymbol{u}dV \approx M_I^{CFD}\boldsymbol{u}_I$ so that Eq. (5.9a) is,

$$\dot{\boldsymbol{q}}_i \quad = \quad \frac{\boldsymbol{p}_i}{m} + \vartheta_i\left[\frac{M_I^{CFD}}{mN_I}\boldsymbol{u}_I - \frac{1}{N_I}\sum_{n=1}^{N}\frac{\boldsymbol{p}_n}{m}\vartheta_n\right], \tag{5.12a}$$

which is identical in form to Eq. (2.72a) (*i.e.* equation 4a in the paper of O'Connell & Thompson (1995)). Note the $\mathcal{LCV}$ function replaces the limited sum notation as demonstrated by Eq. (5.1). The constraint ensures that the average of the molecular system follows the continuum values exactly. To prevent the constraint from being too rigid, O'Connell & Thompson (1995) introduce a scaling factor, ξ, in Eq. (5.12a) (*c.f.* Eq. (2.72a)) to relax the solutions over a number of timesteps.

Next, the link between Eqs. (5.9b) and (2.72b) is considered. Equation (5.9b) is equal to Eq. (2.72b) (*i.e.* equation 4b in O'Connell & Thompson (1995)) provided that the current molecule i is not crossing the surface ($m_i\dot{\boldsymbol{q}}_i \cdot d\mathbf{S}_i = 0$) or alternatively the constraint is satisfied and $\sum_{n=1}^{N}\boldsymbol{p}_n\vartheta_n = \int_V \rho\boldsymbol{u}dV$. The result is that Eq. (5.9b) simplifies to,

$$\dot{\boldsymbol{p}}_i \quad = \quad \boldsymbol{F}_i,$$

which is Eq. (2.72b). Discretising the equations in this form is non-trivial, as the constraint requires the molecular positions at the next time step. An iterative solution would be required in order to solve these equations effectively. Instead, implementation is deferred to the next section where this equation is written in the form of Newton's law and applied as a force. In this form, it can be verified by ensuring agreement with Gauss' principle of least constraint and compared to the coupling scheme derived by Nie *et al.* (2004*a*).

5.2.2 Reformulating in Terms of Newton's Law

In this section, the Hamiltonian equations (5.9a) and (5.9b), obtained in the previous section are combined to obtain a form of Newton's law with a constraint force. In this form, it can be verified against Gauss' principle of least constraint and compared to the coupling technique of Nie *et al.* (2004*a*). The starting point is Eqs. (5.9a) and (5.9b) simplified using $\boldsymbol{\lambda}$ from Eq. (5.8),

$$\dot{\boldsymbol{q}}_i = \frac{\boldsymbol{p}_i}{m_i} - \boldsymbol{\lambda}\vartheta_i, \tag{5.14a}$$

$$\dot{\boldsymbol{p}}_i = \boldsymbol{F}_i - \boldsymbol{\lambda} m_i \dot{\boldsymbol{q}}_i \cdot d\mathbf{S}_i. \tag{5.14b}$$

Differentiating Eq. (5.14a) and substituting the resulting expression in Eq. (5.14b) gives,

$$\ddot{\boldsymbol{q}}_i = \frac{\boldsymbol{F}_i}{m_i} - \dot{\boldsymbol{\lambda}}\vartheta_i. \tag{5.15}$$

The time derivative of the CV function $d\vartheta_i/dt = -\dot{\boldsymbol{q}}_i \cdot d\mathbf{S}_i$ cancels with the surface flux in Eq. (5.9b) (a consequence of the constraint satisfying the semi-holonomic condition Eq. (2.24)). The time derivative of $\boldsymbol{\lambda}$ from Eq. (5.8) is,

$$\dot{\boldsymbol{\lambda}} = \frac{1}{M_I}\Bigg[\underbrace{\frac{d}{dt}\sum_{n=1}^{N}\boldsymbol{p_n}\vartheta_n}_{\mathcal{A}} - \frac{d}{dt}\int_V \rho\boldsymbol{u}dV + \frac{\boldsymbol{\lambda}}{M_I}\sum_{n=1}^{N} m_n\dot{\boldsymbol{q}}_n \cdot d\mathbf{S}_n\Bigg]. \tag{5.16}$$

The $\mathcal{A}$ term can be re-written using Eqs. 5.14a and 5.14b,

$$\begin{aligned}\mathcal{A} = \frac{d}{dt}\sum_{n=1}^{N}\boldsymbol{p_n}\vartheta_n &= \sum_{n=1}^{N}\left[\dot{\boldsymbol{p}}_n\vartheta_n - \boldsymbol{p}_n\dot{\boldsymbol{q}}_n \cdot d\mathbf{S}_n\right] \\ &= \sum_{n=1}^{N}\left[\boldsymbol{F}_n\vartheta_n - m_n\dot{\boldsymbol{q}}_n\dot{\boldsymbol{q}}_n \cdot d\mathbf{S}_n\right] - \boldsymbol{\lambda}\sum_{n=1}^{N}\left[m_n\vartheta_n\dot{\boldsymbol{q}}_n \cdot d\mathbf{S}_n + m_n\vartheta_n\dot{\boldsymbol{q}}_n \cdot d\mathbf{S}_n\right],\end{aligned}$$

so that the time evolution of the Lagrangian multiplier becomes,

$$\begin{aligned}\dot{\boldsymbol{\lambda}} = \frac{1}{M_I}&\left[\sum_{n=1}^{N}\boldsymbol{F}_n\vartheta_n - \sum_{n=1}^{N}m_n\dot{\boldsymbol{q}}_n\dot{\boldsymbol{q}}_n \cdot d\mathbf{S}_n - \frac{d}{dt}\int_V \rho\boldsymbol{u}dV\right] \\ &+\frac{\boldsymbol{\lambda}}{M_I}\left[\sum_{n=1}^{N}m_n\dot{\boldsymbol{q}}_n \cdot d\mathbf{S}_n - 2\sum_{n=1}^{N}m_n\vartheta_n\dot{\boldsymbol{q}}_n \cdot d\mathbf{S}_n\right].\end{aligned} \tag{5.18}$$

using $\vartheta_n d\mathbf{S}_n = 1/2 d\mathbf{S}_n$ the second term in Eq. (5.18) is zero, inserting the remaining term into the equation of motion, Eq. (5.15) gives,

$$\ddot{\boldsymbol{q}}_i = \frac{\boldsymbol{F}_i}{m_i} - \frac{\vartheta_i}{M_I}\left[\sum_{n=1}^{N} \boldsymbol{F}_n \vartheta_n - \sum_{n=1}^{N} m_n \dot{\boldsymbol{q}}_n \dot{\boldsymbol{q}}_n \cdot d\mathbf{S}_n - \frac{d}{dt}\int_V \rho \boldsymbol{u} dV\right]. \tag{5.19}$$

It is important to verify Eq. (5.19) by comparing it to the one derived using the same CV constraint, Eq. (5.2), applied via Gauss' principle of least constraint Eq. (2.28) (or identically Eq. (2.23)). The notation is changed to represent the departure from the use of generalised coordinates, $\boldsymbol{q}_i \rightarrow \boldsymbol{r}_i$. The derivation is shown in appendix B.3 with the resulting equation,

$$\ddot{\mathbf{r}}_i = \frac{\mathbf{F}_i}{m_i} - \frac{\vartheta_i}{M_I}\left[\sum_{n=1}^{N} \mathbf{F}_n \vartheta_n - \sum_{n=1}^{N} m_n \dot{\mathbf{r}}_n \dot{\mathbf{r}}_n \cdot d\mathbf{S}_n - \frac{d}{dt}\int_V \rho \boldsymbol{u} dV\right]. \tag{5.20}$$

Equation (5.20) is identical to Eq. (5.19), confirming the equations obtained in the previous section are physically meaningful and correct. This is an important verification, as Gauss' principle is often considered to be more fundamental (Flannery, 2011) and capable of applying more general constraints (Evans & Morriss, 2007).

Relationship to the Nie *et al.* (2004*a*) method

The form of constraint Eq. (5.20) can be used to obtain the equations of Nie *et al.* (2004*a*), subject to three key assumptions: equivalent mass in both systems, convective flux is negligible and velocity in the molecular system tends to the continuum over the timestep Δt_{CFD}. The first two assumptions are required to obtain the equation of motion, the third to obtain the actual discretised equations implemented in the numerical algorithm proposed by the authors.

The first assumption means that the temporal change of mass inside the CV can be assumed to be negligible so that,

$$\frac{1}{M_I}\frac{d}{dt}\int_V \rho \boldsymbol{u} dV \approx \frac{\rho}{M_I}\frac{d}{dt}\int_V \boldsymbol{u} dV \approx \frac{\rho \Delta V}{M_I}\frac{D\boldsymbol{u}}{Dt}.$$

In addition, the mass in both systems is assumed to be the same $\rho \Delta V = M_I$ and the mass of all molecules is identical $\forall\, i : m_i = m$, so that $M_I = m\sum_i^N \vartheta = mN_I$. The equations of motion, Eq. (5.20), is then,

$$\ddot{\mathbf{r}}_i = \frac{\mathbf{F}_i}{m_i} - \frac{\vartheta_i}{mN_I}\sum_{n=1}^{N} \boldsymbol{F}_n \vartheta_n + \vartheta_i \frac{D\boldsymbol{u}}{Dt} + \frac{\vartheta_i}{mN_I}\sum_{n=1}^{N} m_n \dot{\mathbf{r}}_n \dot{\boldsymbol{r}}_n \cdot d\mathbf{S}_n. \tag{5.21}$$

The second assumption is that the surface momentum flux is negligible, $\sum_{n=1}^{N} m_n \dot{\boldsymbol{r}}_n \dot{\boldsymbol{r}}_n \cdot d\mathbf{S}_n = 0$. The equations of motion, Eq. (5.21), therefore reduce to,

$$\ddot{\boldsymbol{r}}_i = \frac{\boldsymbol{F}_i}{m} - \frac{\vartheta_i}{N_I m}\sum_{i=1}^{N} \boldsymbol{F}_i \vartheta_i + \vartheta_i \frac{D\boldsymbol{u}}{Dt}. \tag{5.22}$$

The above equation takes the form of Nie *et al.* (2004*a*) (*c.f.* Eq. (2.75) in section 2.5.2 or equation (2.6) in the paper by Nie *et al.* (2004*a*)) expressed in the formalism of the CV.

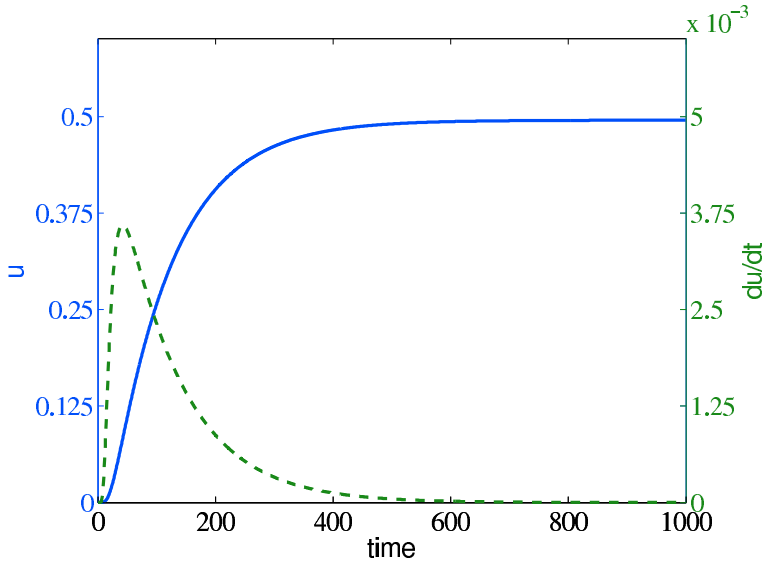

Figure 5.1: The time evolution of the unsteady Couette flow analytical solution, Eq. (A.11), velocity u and its temporal derivative du/dt. The velocity is evaluated at $y = H/2$ for a domain representative of a typical MD simulation with height $H = 52.1$, Reynolds number $Re = 0.372$ and wall velocity $u_0 = 1.0$.

In the work of Nie *et al.* (2004*a*), the Lagrangian time derivative $D\boldsymbol{u}/Dt$ is discretised:

$$\frac{D\boldsymbol{u}}{Dt} \approx \frac{\boldsymbol{u}(t + \Delta t_{MD}) - \boldsymbol{u}(t)}{\Delta t_{MD}} \tag{5.23}$$

which is simply the forward Euler discretisation (a first order approximation for the derivative). Substituting Eq. (5.23) into Eq. (5.22) results in an entirely differential constraint. This would apply a force only as the velocity changes, acting to maintain a velocity but not to enforce it. The result of applying Eq. (5.23) is demonstrated in Figure 5.1, using the analytical solution for Couette flow, Eq. (A.11) from appendix A, as a test case. Note the velocity change is very small so the force due to the velocity difference is two orders of magnitude less than the force due to the differences in velocity. The associated difficulties of applying the differential form of constraint resulting from Gauss' principle is well known in the NEMD literature. These difficulties occur for example in the implementation of the Gaussian thermostat (Evans & Morriss, 2007), where the algorithm is often supplemented with a rescaling or adjustment of the total temperature periodically to prevent drift. These techniques are typically applied to maintain a temperature, not to control it. For the case of coupling, the set-point of the constraint must change as a function of time (as in Figure 5.1).

In order to apply a time varying constraint, Nie *et al.* (2004*a*) implemented what they described as a 'special discretisation'. This is the third assumption required to obtain the Nie *et al.* (2004*a*) form of coupling. In order to apply the correct velocity, Nie *et al.* (2004*a*) introduce the definition of averaged macroscopic velocity, $\boldsymbol{u}(t) = 1/N_J \sum \langle \dot{\boldsymbol{r}}_i(t) \rangle_{MD}$ into the forward Euler

discretisation of Eq. (5.23),

$$\frac{D\boldsymbol{u}}{Dt} \approx \frac{1}{\Delta t_{MD}} \left[\boldsymbol{u}(t + \Delta t_{MD}) - \frac{1}{N_J} \sum_{i=1}^{N_I'} \left\langle \dot{\boldsymbol{r}}_{\boldsymbol{i}}(t) \right\rangle_{MD} \right], \tag{5.24}$$

which is the final equation (2.7) in the work of Nie *et al.* (2004*a*). Here N_I' is the some fixed number of molecules moving through space in the constrained Lagrangian 'parcel'. The 'special discretisation' of Eq. (5.24) changes the nature of the constraint from purely differential to a hybrid of proportional and differential. It is this step that makes Nie *et al.* (2004*a*) a state (velocity) based coupling. This subtle but important point results in the difference in the sum of the molecular and continuum velocity being applied as a constraint. The constrained equation Eq. (5.24) is inserted into Eq. (5.22) to yield,

$$\ddot{\boldsymbol{r}}_i = \frac{\boldsymbol{F}_i}{m} - \frac{\vartheta_i}{N_I m} \sum_{i=1}^{N} \boldsymbol{F}_i \vartheta_i + \frac{\vartheta_i}{\Delta t_{MD}} \left[\boldsymbol{u}(t + \Delta t_{MD}) - \frac{1}{N_J} \sum_{i=1}^{N_I'} \left\langle \dot{\boldsymbol{r}}_{\boldsymbol{i}}(t) \right\rangle_{MD} \right]. \tag{5.25}$$

The Nie *et al.* (2004*a*) style of discretisation in Eq. (5.24) applies proportional control to a moving volume in space. This proportional control ensures the difference in velocity between the Lagrangian collection of N_I' molecules (at time t) and the velocity of the coupled continuum Lagrangian parcel (at time $t+\Delta t_{MD}$) is applied as a force. In practice both constrained region and continuum are in the Eulerian reference frame. Provided the continuum convection is negligible, as in Couette flow, this detail is unimportant (*i.e.* $Du/Dt \approx \partial u/\partial t$). However, a generalised coupling scheme is presented in the next section which considers the convection term explicitly using Reynolds' transport theorem and avoids the three assumptions introduced in this section.

5.2.3 General Constraint Equation

In practice, the continuum is expressed as a fixed Eulerian control volume. As a result, it is more convenient to express the time evolution of the continuum volume in Eq. (5.20), using Reynolds' transport theorem,

$$\frac{d}{dt} \int_V \rho \boldsymbol{u} dV = \int_V \frac{\partial (\rho \boldsymbol{u})}{\partial t} dV + \oint_S (\rho \boldsymbol{u} \boldsymbol{u}) \cdot d\mathbf{S}. \tag{5.26}$$

The constraint in Eq. (5.20) therefore becomes,

$$\ddot{\mathbf{r}}_i = \frac{\mathbf{F}_i}{m_i} - \frac{\vartheta_i}{M_I} \left[\sum_{n=1}^{N} \boldsymbol{F}_n \vartheta_n - \int_V \frac{\partial (\rho \boldsymbol{u})}{\partial t} dV - \oint_S (\rho \boldsymbol{u} \boldsymbol{u}) \cdot d\mathbf{S} - \sum_{n=1}^{N} m_n \dot{\mathbf{r}}_n \dot{\mathbf{r}}_n \cdot d\mathbf{S}_n \right]. \tag{5.27}$$

This is the most general form of constrained equation, owing to is explicit localisation using the $\mathcal{LCV}$ function. The localised constraint was applied using Gauss' principle which is the most fundamental form of constrained dynamics algorithm. It has also been shown that it is also derivable from the general Hamiltonian equations of constraint, Eqs. (5.9a) and (5.9b), which can be shown to simplify to the equations of O'Connell & Thompson (1995). Equation (5.27) can also be simplified to obtain the Nie *et al.* (2004*a*) form of coupling as already demonstrated in the previous subsection. The importance of the various terms in this equation, and the link to the existing works in the literature, will be explored through numerical simulation in the next

section, 5.3. Finally, in section 5.4 of this chapter, it will be shown that the general constraint Eq. (5.27) is a form of flux coupling and can be simplified to obtain the flux coupling scheme of Flekkøy *et al.* (2000).

5.3 Implementation

The aim of this section is to test the importance of the various terms in the general constraint equation form, Eq. (5.27),

$$\ddot{\boldsymbol{r}}_i = \frac{\boldsymbol{F}_i}{m_i} - \overbrace{\frac{\vartheta_i}{M_I}\left[\underbrace{\sum_{n=1}^{N}\boldsymbol{F}_n\vartheta_n}_{\text{MD Forcing}} - \underbrace{\int_V \frac{\partial(\rho\boldsymbol{u})}{\partial t}dV}_{\text{CFD Accumulation}}\right]}^{\text{Nie } et\ al.\ (2004a)\text{ terms}} - \overbrace{\frac{\vartheta_i}{M_I}\left[\underbrace{\oint_S(\rho\boldsymbol{u}\boldsymbol{u})\cdot d\mathbf{S}}_{\text{CFD Advection}} - \underbrace{\sum_{n=1}^{N} m_n\dot{\boldsymbol{r}}_n\dot{\boldsymbol{r}}_n\cdot d\mathbf{S}_n}_{\text{MD Advection}}\right]}^{\text{New to current work}}, \quad (5.27\text{L})$$

This equation includes all the necessary terms for coupling between the continuum and the MD descriptions. As discussed in the previous section, simplifications of this constraint are successful because of carefully designed control strategies (constraints) for the specific problem of interest. The key change was to discretise the temporal evolution term, changing it from a differential constraint to a proportional constraint,

$$\int_V \frac{\partial(\rho\boldsymbol{u})}{\partial t}dV \approx \frac{1}{\Delta t_{MD}}\left[\int_V \rho\boldsymbol{u}(\boldsymbol{r},t+\Delta t_{MD})dV - \int_V \rho\boldsymbol{u}(\boldsymbol{r},t)dV\right] \quad (5.28)$$

$$\approx \frac{1}{\Delta t_{MD}}\left[\int_V \rho\boldsymbol{u}(\boldsymbol{r},t+\Delta t_{MD})dV - \sum_{i=1}^{N} m_i\dot{\boldsymbol{r}}_i(t)\vartheta_i(\boldsymbol{r},t)\right]. \quad (5.29)$$

It is demonstrated in this section that the 'CFD Accumulation' term alone, written as a momentum difference in Eq. (5.29), is sufficient to ensure the success of the coupling scheme in the cases tested by Nie *et al.* (2004*a*). These include starting Couette in subsection 5.3.1 and Couette with wall roughness in subsection 5.3.2. In both cases, the 'New to current work' terms of Eq. (5.27L) are shown to be inappreciable, as are the 'MD Forcing' terms. In subsection 5.3.3, the case of a converging-diverging channel is investigated, being one of the simplest geometry which includes a permanent and significant 'MD Advection' term. The importance of this term relative to the 'MD Forcing' term is explored. The 'MD Advection'/'MD Forcing' terms are shown to govern the time evolution of molecules in a CV. They can be reformulated in terms of stress, convection and pressure. This leads on to the need for flux coupling in scenarios where advection is present and this is discussed in section 5.4.

5.3.1 Starting Couette

The coupled simulation setup in this section is identical to the verification case used in section 3.4.3. The reader is referred to section 3.4.3 and the original work of (Nie *et al.*, 2004*a*) for full details of the setup. The simulation is a coupled simulation of impulse started Couette flow with the top wall in the CFD domain moved at a velocity of $u_w(t) = 1$ with the MD bottom wall stationary. The constraint of Eq. (5.27L) will be investigated in three parts;

The first case, ***a***), will address the 'CFD Accumulation' term in Eq. (5.27L) using the discretisation Eq. (5.28) and assuming equivalent mass in both systems,

$$\ddot{\boldsymbol{r}}_i = \frac{\boldsymbol{F}_i}{m} + \vartheta_i \frac{\boldsymbol{u}(t + \Delta t_{_{CFD}}) - \boldsymbol{u}(t)}{\Delta t_{_{CFD}}}. \qquad (5.30\ \boldsymbol{a})$$

Next, in case ***b***) the 'CFD Accumulation' term of the previous equation will be expressed as a proportional constraint using Eq. (5.29) with equivalent mass in both systems,

$$\ddot{\boldsymbol{r}}_i = \frac{\boldsymbol{F}_i}{m} + \frac{\vartheta_i}{\Delta t_{_{MD}}} \left[\boldsymbol{u}(t + \Delta t_{_{MD}}) - \frac{1}{N_J} \sum_{i=1}^{N_J} \left\langle \dot{\boldsymbol{r}}_{\boldsymbol{i}}(t) \right\rangle_{_{MD}} \right], \qquad (5.30\ \boldsymbol{b})$$

where the time step has been changed due to requirement that velocities be averaged and compared at every timestep. The CFD velocity can be interpolated between t and $t + \Delta t_{_{CFD}}$. The constraint is in the form of the proportional velocity control of Borg *et al.* (2010). This simplified approach is based on control theory with a proportional velocity control chosen to correctly match the dynamics between the two systems.

Finally, in case ***c***) the full 'Nie *et al.* (2004*a*) terms' of Eq. (5.27L) are applied, again with the discretisation of Eq. (5.29) and assuming equivalent mass in both systems,

$$\ddot{\boldsymbol{r}}_i = \frac{\boldsymbol{F}_i}{m} - \frac{\vartheta_i}{N_I m} \sum_{i=1}^{N} \boldsymbol{F}_i \vartheta_i + \frac{\vartheta_i}{\Delta t_{_{MD}}} \left[\boldsymbol{u}(t + \Delta t_{_{MD}}) - \frac{1}{N_J} \sum_{i=1}^{N_J} \left\langle \dot{\boldsymbol{r}}_{\boldsymbol{i}}(t) \right\rangle_{_{CFD}} \right]. \qquad (5.30\ \boldsymbol{c})$$

is identical to Eq. (5.25).

These three test cases do not consider the 'New to Current Work' terms. The results of implementing these three constraints for the identical coupled simulation of impulse started Couette are displayed in Figure 5.2. Case ***a)*** is close to zero throughout the evolution of the system and is shown by triangles which appear below the other results (negative) as a result of fluctuations. Case ***a***) is applied as a differential constraint and, as expected, only applies a force when the system is evolving in time. The result is no evolution beyond the initial unsteady period. Good agreement to the analytical solution is observed for cases to ***b)*** and ***c)***.

It is clear that the constraint of Borg *et al.* (2010), case ***b***), offers similarly good agreement to Nie *et al.* (2004*a*), case ***c***), for unsteady Couette flow. The misalignment in symbols observed in Figure 5.2 is an artefact of the plotting process. The analytical solution is matched to the location where the molecular fluid no longer has zero velocity. The different constraints have an effect on the apparent location of zero velocity in the molecular system. The extra term in the full Nie *et al.* (2004*a*) formulation (case ***c***) above) acts to compress the system, resulting in greater stick near the wall and, therefore, the location of zero velocity moving further into the liquid part of the channel.

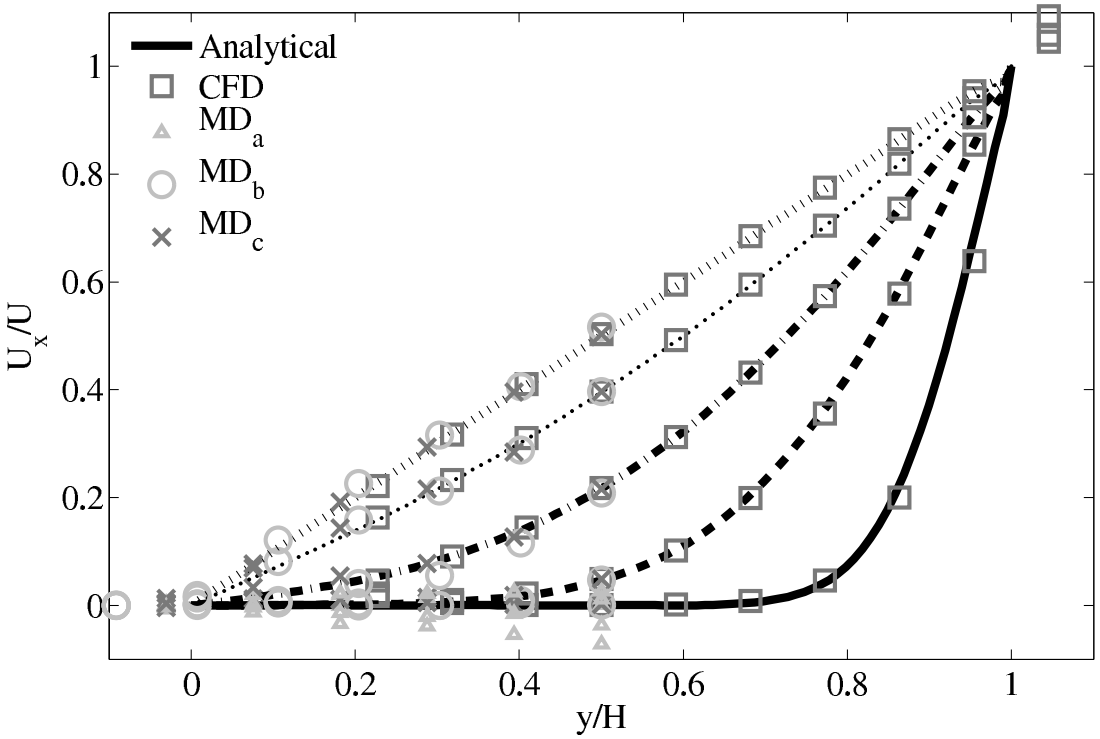

Figure 5.2: Coupled cases Eq. (5.30a) differential velocity constraint (△), Eq. (5.30b) proportional velocity constraint (Borg *et al.*, 2010) and Eq. (5.30c) Nie *et al.* (2004*a*) constraint. (×)

There are three main conclusions drawn from the results of this coupled simulation of impulse started Couette flow.

The first and most important conclusion is that without the 'special discretisation' of Nie *et al.* (2004*a*), given in Eq. (5.29), the constraint does not work. This is supported by the failure of case ***a***) in enforcing any agreement between the CFD and MD systems. The assumption from Eq. (5.28) to Eq. (5.29) is key to the success of the coupling methodology of Nie *et al.* (2004*a*). It changes the constraint from differential to proportional, making it a form of state coupling which enforces the correct velocity difference between systems.

The second conclusion is that the 'Nie *et al.* (2004*a*) terms' in Eq. (5.27L) are sufficient to correctly couple the temporal evolution of both systems. The 'MD Advected' and 'CFD Advected' terms have not been included and the coupling performs correctly. This is consistent with the derivation of the analytical solution of time evolving Couette flow (appendix A), in which the 'CFD Advection' term is assumed to be negligible. It is clear that a more complicated case is required to fully evaluate the general coupling Eq. (5.27L).

The third conclusion is that the 'MD Forcing' term of Eq. (5.27L) is also not essential to apply successful coupling in this case. The agreement between cases ***b***) and ***c***) in Figure 5.2 suggests that the feedback algorithm of Borg *et al.* (2010) performs as well as the less straightforward algorithm proposed by Nie *et al.* (2004*a*) for the case of Couette flow. Again, a more complicated case is required to fully evaluate the importance of the 'MD Forcing'.

In the next subsection, the more complicated case of a post on the wall is recreated from the work of Nie *et al.* (2004*a*) to further test the various constraints.

5.3.2 Couette with Wall Roughness

In line with the second verification case of Nie *et al.* (2004*a*), the simulation of Couette flow with a single post is recreated in this subsection. The coupling scheme of Nie *et al.* (2004*a*) (case ***c***) above) is applied and the results are verified against the original paper. Having verified the coupling is correct, the importance of the 'MD Advected' and 'MD Forcing' in Eq. (5.27L) is investigated for this case.

The bottom wall includes a square post of dimension $5.12 \times 5.12 \times 41.0$, with all dimensions in this section given in MD units. The MD region is $41.0 \times 41.0 \times 41.0$ with a density of $\rho = 0.8$ giving $N = 51,840$ molecules. The molecular domain is simulated on 4 processes with topology $2 \times 2 \times 1$. The MD code was coupled to the full 3D DNS code $\mathcal{T}ransFlow$ (run on a single processor). The CFD solver uses a viscosity of $\mu = 2.14$ (or equivalent Reynolds number). This viscosity is matched using prior simulations. Without this matching, the coupling scheme would fail. This point is revisited in subsection 3.4.4, where the importance of flux coupling is investigated.

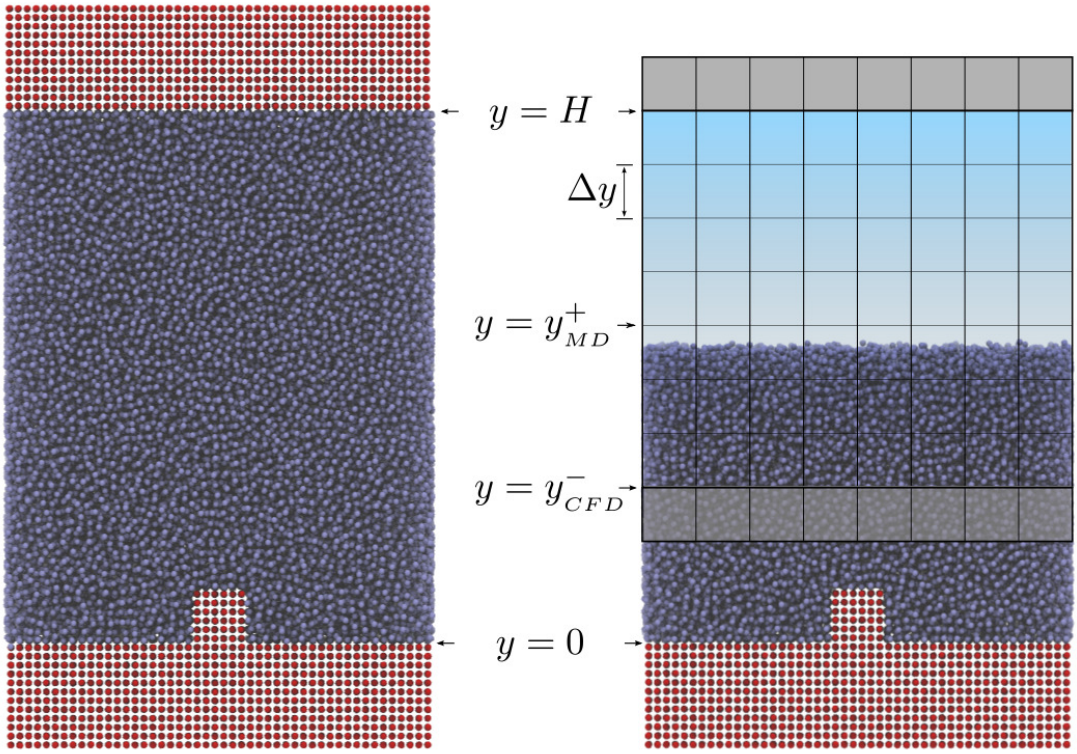

Figure 5.3: Full reference MD solution (left) compared to coupled case (right). In the MD domain, red atoms are tethered and blue are liquid. In the CFD domain, Grey cells are boundary conditions and blue are domain cell. The labels define the key dimension in the coupled layout, defined in the text.

A VMD (Humphrey *et al.*, 1996) snapshot of the coupled case is shown in Figure 5.3 compared to an equivalent MD domain of size $41.0 \times 71.8 \times 41.0$ with $N = 96,768$ simulated using $2 \times 2 \times 2$ processors. The same case simulated using MD to model the entire domain allows verification of the coupled algorithm as well as collection of detailed CV statistics at the location where

coupling is applied.

The setup of the coupled case (see Figure 5.3) was specified by molecular domain top, $y^+_{MD} = 31.3$, CFD domain bottom $y^-_{CFD} = 15.6$, total coupled fluid domain height $H = 52.1$ with cell size of $\Delta y = 5.12$. The overlap was of size 15.6 and was split into three overlap cells. Molecules in the top MD cell were subjected to the boundary forces (Eq. (2.81)) to prevent molecules escaping. A number of molecules were removed heuristically during initialisation in order to maintain the same density in the presence of this boundary force. In addition, the top cell, together with the cell below, experienced the constrained force (Eq. (5.25)) to ensure they were matched to the continuum. The halo for the CFD was obtained by averaging the pure MD region below the overlap region. The ratio of timesteps between the MD and CFD simulations was 50.

A bottom (and top) wall of thickness 10.24 were kept in place using the Petravic & Harrowell (2006) tethering potential introduced in the NEMD section 3.2.5. Both solid walls and fluid regions were initialised at the same density of 0.8. The fluid-fluid and solid-fluid interaction potential were both $\epsilon = 1.0$, which represents a departure from Nie *et al.* (2004*a*) who used 0.6 for the solid-fluid interactions. The cutoff length was $r_c = 2.2$ and the temperature $T = 1.0$. A Nosè-Hoover thermostat was applied instead of the Langevin with application to the z component of momentum only.

The contour plots of velocity are presented in Figure 5.4 for the full MD and coupled case. The velocity profiles are shown for the steady state averaged over the z direction and $20,000$ MD samples each separated by 15 timesteps. The velocity field is consistent for both the all MD reference and the coupled simulation. More detailed comparison is provided by the two verification plots from the work of Nie *et al.* (2004*a*), reproduced in Figure 5.5. The full comparison of the streamlines in Figure 5.5a shows good agreement between both cases. The vertical component of velocity is shown as a function of y for each x location in Figure 5.5b. Note a mechanism for particle insertion is not applied and the mass flux is not included in this model. Despite this, the agreement between the all-MD case and the coupled simulation appears to be fairly good.

The shear stress in both the full MD and coupled cases are in good agreement, as shown in Figure 5.6. In the MD region, the stress was obtained using the CV stress discussed in the last Chapter 4, section 4.2.7. In the CFD region, the stress can be calculated using the hydrodynamic pressure, the gradient of velocity and shear viscosity via Eq. (2.48). The highest shear was next to the post on the walls (magnitudes of $\sigma_{xy} = -0.55/0.24$ for minimum/maximum respectively). The remaining domain has a finite stress with a domain average of $\sigma_{xy} = 0.04$ in Figure 5.6. This is consistent with the steady state analytical solution for Couette flow, $\sigma_{xy} = \mu \partial u_x \partial y = 2.14[1-0]/51.2 = 0.04$. The post is relatively small and the effect on the stress field is minimal and localised to the region adjacent to the post. The effect of this post at the coupling interface would therefore be expected to be negligible.

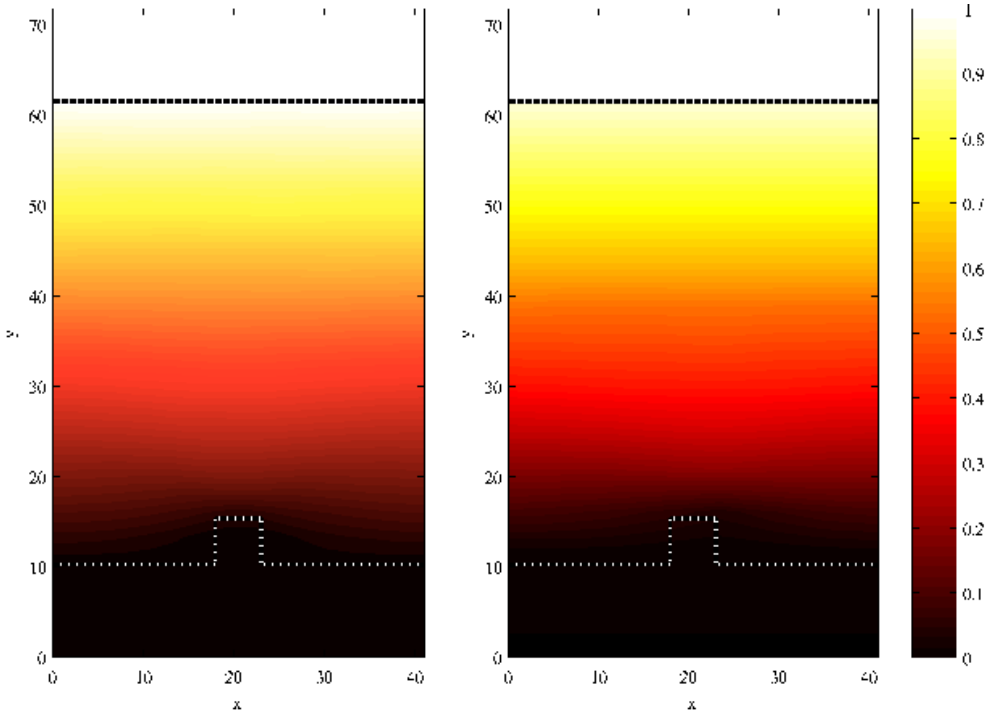

(a) All MD **(b)** Coupled

Figure 5.4: Velocity contour plots for all MD case (left) and coupled simulation (right) at steady state. Dotted lines indicate the limits of the tethered regions.

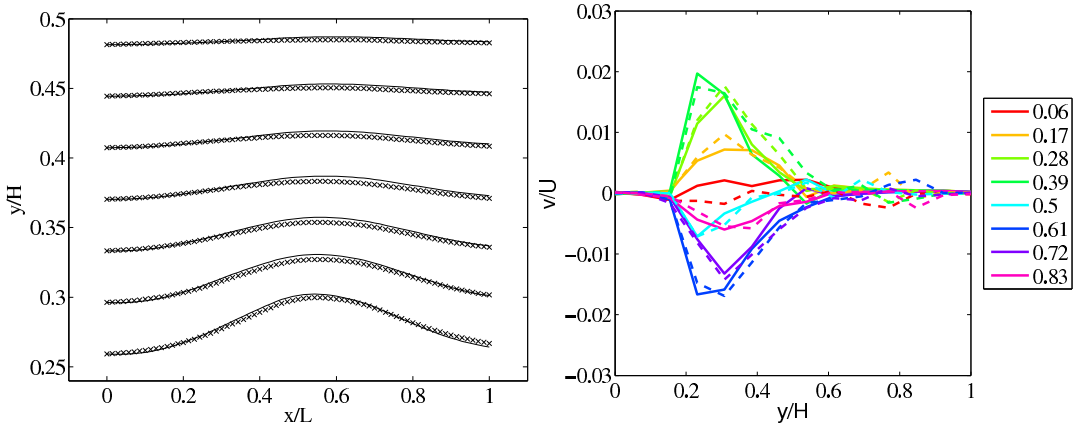

(a) Streamlines: CPL (×) vs all MD (—) **(b)** Velocity v : CPL (—) vs all MD (- -)

Figure 5.5: Recreation of the verification plots from Nie *et al.* (2004*a*) showing matching between all MD and the coupled simulations.

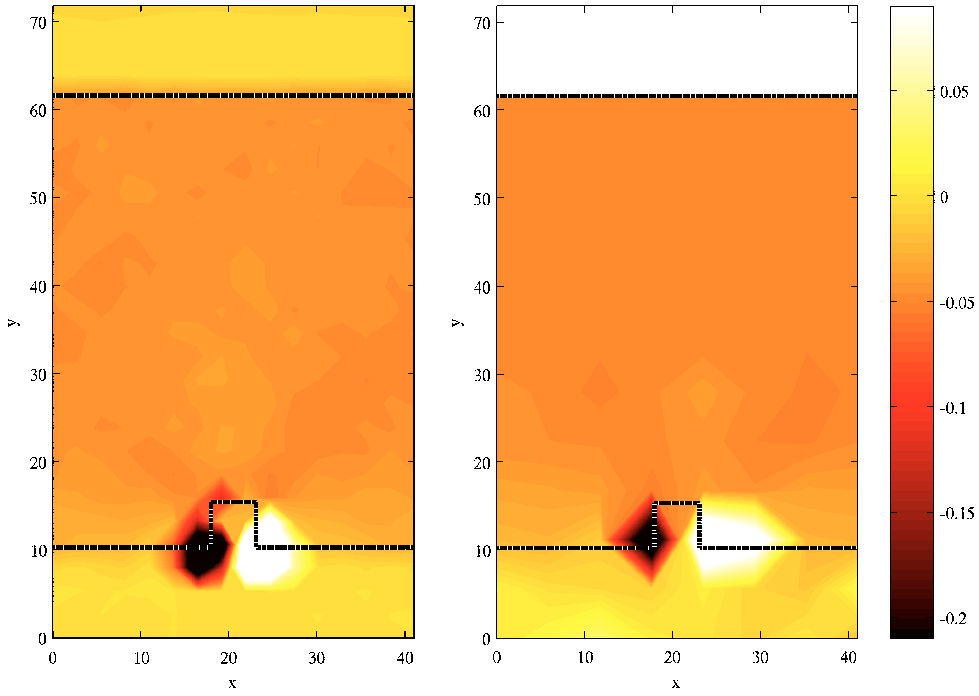

(a) All MD **(b)** Coupled

Figure 5.6: Stress contour plots for all MD case and coupled simulation

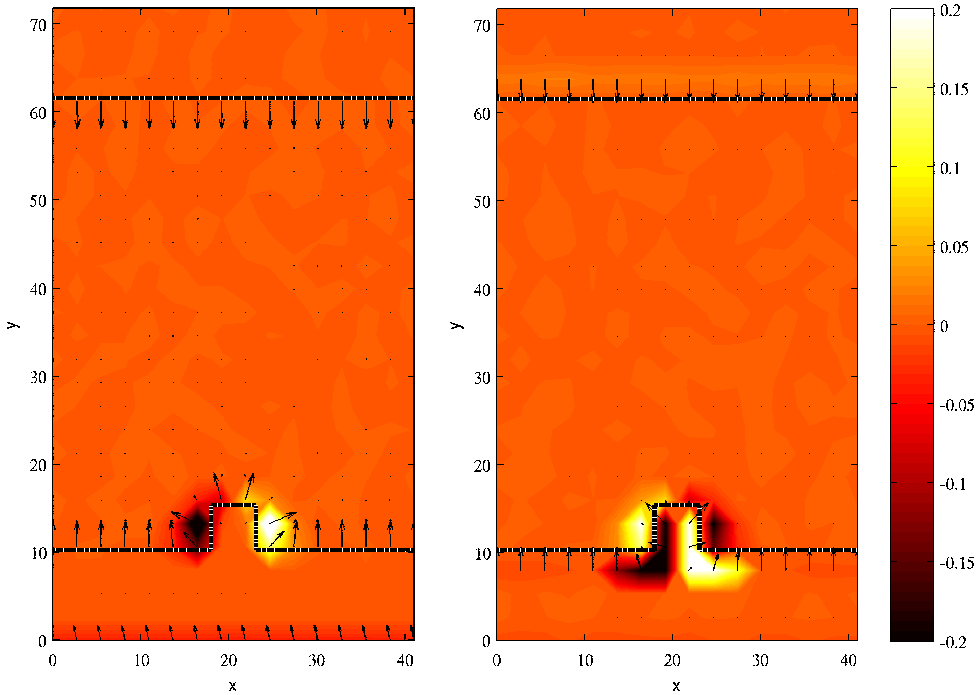

(a) 'MD Advection' **(b)** 'MD Forcing'

Figure 5.7: The x magnitude contours with x and y components vector plots of the 'MD Advection' and 'MD Forcing' terms from Eq. (5.27L) in an all MD system.

Having verified the results of the coupled simulation are consistent with the full MD, the reason the coupling works without the 'MD advection' term is explored. Figure 5.7b shows a contour of the x component of 'MD advection' (5.7a) and 'MD Forcing' (5.7b) for the full MD reference case. The vector of x and y components of advection and forcing are overlaid to show the relative magnitude of the y component. These averages are taken at steady state, counting every force and flux on a CV for $300,000$ MD time units. It is clear that both the 'MD advection' and 'MD Forcing' are, on average, zero even a small distance away from the post. At the location of the constrained region ($y = 31.3$), these terms would be zero on average and not contribute to the constrained dynamics of Eq. (5.27L). However, these terms are not zero instantaneously and fluctuate considerably. The importance of these fluctuations will become clear in the next section on flux coupling 5.4, where these terms are shown to be the forces and fluxes which govern the evolution of the CV each timestep.

The conclusion from simulating steady state coupled flow over a post in this subsection is that the 'MD Advection' and 'MD Forcing' terms in 5.27L are not essential for correct simulation of this case. In the above simulation, the 'MD Advection' and 'MD Forcing' terms were inappreciable away from the post, and hence the state coupling of Nie *et al.* (2004*a*) was sufficient. This is, in part, a result of using a small post which has minimal impact on the flow field. Taking a bigger post would result in greater disturbance of the stress field which would in turn introduce significant 'MD Advection' and 'MD Forcing' terms. In the next subsection 5.3.3, the logical extreme of this case is taken with an all MD simulation of a converging-diverging channel.

5.3.3 Converging-Diverging Channel

In this section, an all MD simulation of a converging-diverging channel is performed in order to explore the relationship between the 'MD Forcing' and 'MD Advection' terms of Eq. (5.27L),

$$\ddot{\boldsymbol{r}}_i = \frac{\boldsymbol{F}_i}{m_i} - \frac{\vartheta_i}{M_I}\Bigg[\underbrace{\sum_{n=1}^{N}\boldsymbol{F}_n\vartheta_n}_{\text{MD Forcing}} - \underbrace{\int_V \frac{\partial\left(\rho\boldsymbol{u}\right)}{\partial t}dV}_{\text{CFD Accumulation}}\Bigg] - \frac{\vartheta_i}{M_I}\Bigg[\underbrace{\oint_S\left(\rho\boldsymbol{u}\boldsymbol{u}\right)\cdot d\mathbf{S}}_{\text{CFD Advection}} - \underbrace{\sum_{n=1}^{N} m_n\dot{\boldsymbol{r}}_n\dot{\boldsymbol{r}}_n\cdot d\mathbf{S}_n}_{\text{MD Advection}}\Bigg], \quad \text{(5.27L)}$$

The details of the setup and extended analysis of the converging-diverging channel is included in the appendix D with only the main results for forcing and advection considered here.

The channel was formed by molecules tethered using a cosinusoidally varying curve. The channel maximum height was $L_y = 47.0\ell$, the minimum (centre) height was $l_y = 18.5\ell$ (defined as the channel throat) and the channel length was $L_x = 285\ell$. The total simulation domain dimensions were $285 \times 56.9 \times 11.4\ell$ with $200 \times 40 \times 1$ control volumes each of size $1.4227 \times 1.4227 \times 11.4\ell$. The walls had a minimum thickness of half a binsize (0.711ℓ) above a Nosé-Hoover thermostatted region. The thermostatted region has a width of three binsizes (4.268ℓ). The domain is homogeneous in z with periodic boundaries in the x and z direction. A force is applied to the molecules between $x = 0$ and $x = 10$ to drive the flow by enforcing a difference in inlet pressure and outlet (or reservoir) pressure. The simulation is run for $500,000$ timestep with a timestep of $\Delta t_{MD} = 0.005$.

Figure 5.8 shows a plot of the x component of 'MD Advection' (top) and 'MD Forcing' (bottom) for the converging-diverging channel, both are displayed on the same colour scale. The system is run for $120,000$ timesteps to steady state before records are taken. The results are then obtained by recording every molecular crossing and force over every surface of the 8000 CV

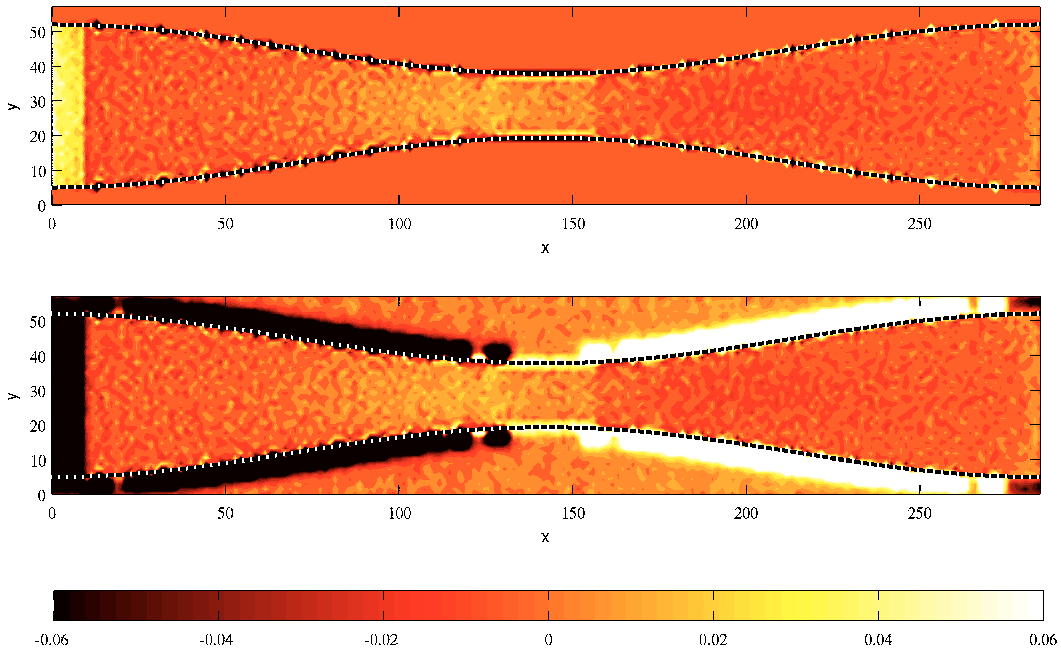

Figure 5.8: x component of 'MD Advection' (top) and 'MD Forcing' (bottom) contours on the same colour scale.

for $380,000$ timesteps. It can be seen in Figure (5.8 top) that the 'MD Advection' term is zero in the tethered region. This is a consequence of no molecules crossing the CV surfaces and so no additions to the 'MD Advection' term. There is a maximum in the forced region near the inlet due to the application of the localised external force. The magnitude of the 'MD Advection' terms increases from the inlet reaching a maximum at the throat of the channel. The key observation is the 'MD Advection' term in Figure (5.8 top) remains non-zero on average. It would therefore be an important and sustained contribution to the general constraint Eq. (5.27L). This is a key change from the Couette post case in which the 'MD Advection' term was zero for the steady state.

Similarly, the 'MD Forcing' also remains non-zero in the steady state and will therefore contribute to Eq. (5.27L). The largest difference in the 'MD Forcing' of Figure (5.8 bottom) is next to the wall. The dense tethered molecules are stationary, resulting in a large interactive force with the moving fluid. Ignoring the wall regions and the inlet-forced region, the contour in the fluid region is seen to be identical to the 'MD Advection'.

The identical 'MD Forcing' and 'MD Advection' profiles can be understood by considering the time evolution of a representative control volume. The CV of interest is located just before the nozzle, where the 'MD Forcing'/'MD Advection' contribution is greatest. The CV is chosen to include only the fluid part of the converging-diverging channel between $x = 104$ and $x = 118$, up to but not including the walls located at $y = 18.5$ and 38.4, and for all z. The results are shown in Figure 5.9, with each light grey point the result of the sum of every force and flux over the CV surface for a period of $3,000$ timesteps (15 MD time units). The magnitudes in Figure 5.9 are equivalent to those of Figure 5.8 divided by the timestep $\Delta t_{MD} = 0.005$. The results fluctuate significantly (light grey results), however, the general trend is displayed using the thick lines/red crosses, obtained using polynomially smoothed fits. The details of the smoothing

are unimportant. These plots are comparable to the ones used to demonstrate conservation of momentum in a CV Figure 4.6a, displayed in the previous chapter. The sum of the 'MD Forcing' and 'MD Advection' terms over a CV surface can be seen to be exactly equal to the time evolution within that CV, from Eq. (4.61),

$$\underbrace{\frac{d}{dt}\sum_{i=1}^{N} m_i\dot{\boldsymbol{r}}_i\vartheta_i}_{\text{MD Accumulation}} = \underbrace{-\sum_{i=1}^{N} m_i\dot{\boldsymbol{r}}_i\dot{\boldsymbol{r}}_i\cdot d\mathbf{S}_i}_{\text{MD Advection}} + \underbrace{\frac{1}{2}\sum_{i,j}^{N}\boldsymbol{\varsigma_{ij}}\cdot d\mathbf{S}_{ij}\vartheta_i}_{\text{MD Forcing}}, \tag{5.31}$$

The control volume conservation is observed to machine precision. The time evolution of momentum is shown in Figure 5.9 and is exactly equal to the difference in the 'MD Forcing' and 'MD Advection' terms. The 'MD Forcing' and 'MD Advection' are different during the initial unsteady part of the simulation, but tend to the same value over time. When both forcing and advection terms are equal, the system is at steady state and there is no further change in momentum over time. Notice however that both terms remain non-zero at steady state. This is an important point, only if both 'MD Forcing' and 'MD Advection' are included would no force be applied at steady state. Including only 'MD Forcing' in a constraint equation would introduce a spurious and continuous force at steady state that should have been cancelled by the corresponding fluxes. Another key observation is that these terms continue to fluctuate significantly even when the overall system is no longer evolving in time. To not include these fluctuating terms in Eq. (5.31) would mean a significant and meaningful contribution would be omitted from the constrained equation. The impact of this can be observed by substituting Eq. (5.31) into the constraint Eq. (5.27L),

$$\ddot{\boldsymbol{r}}_i = \frac{\boldsymbol{F}_i}{m_i} - \frac{\vartheta_i}{M_I}\underbrace{\frac{d}{dt}\sum_{i=1}^{N} m_i\dot{\boldsymbol{r}}_i\vartheta_i}_{\text{MD Accumulation}} + \frac{\vartheta_i}{M_I}\Bigg[\underbrace{\int_V \frac{\partial\left(\rho\boldsymbol{u}\right)}{\partial t}dV}_{\text{CFD Accumulation}} + \underbrace{\oint_S \left(\rho\boldsymbol{u}\boldsymbol{u}\right)\cdot d\mathbf{S}}_{\text{CFD Advection}}\Bigg], \tag{5.32}$$

The general constraint Eq. (5.27L) in this guise can be interpreted as removing any change in the time evolution of the molecular CV and replacing it with the continuum values.

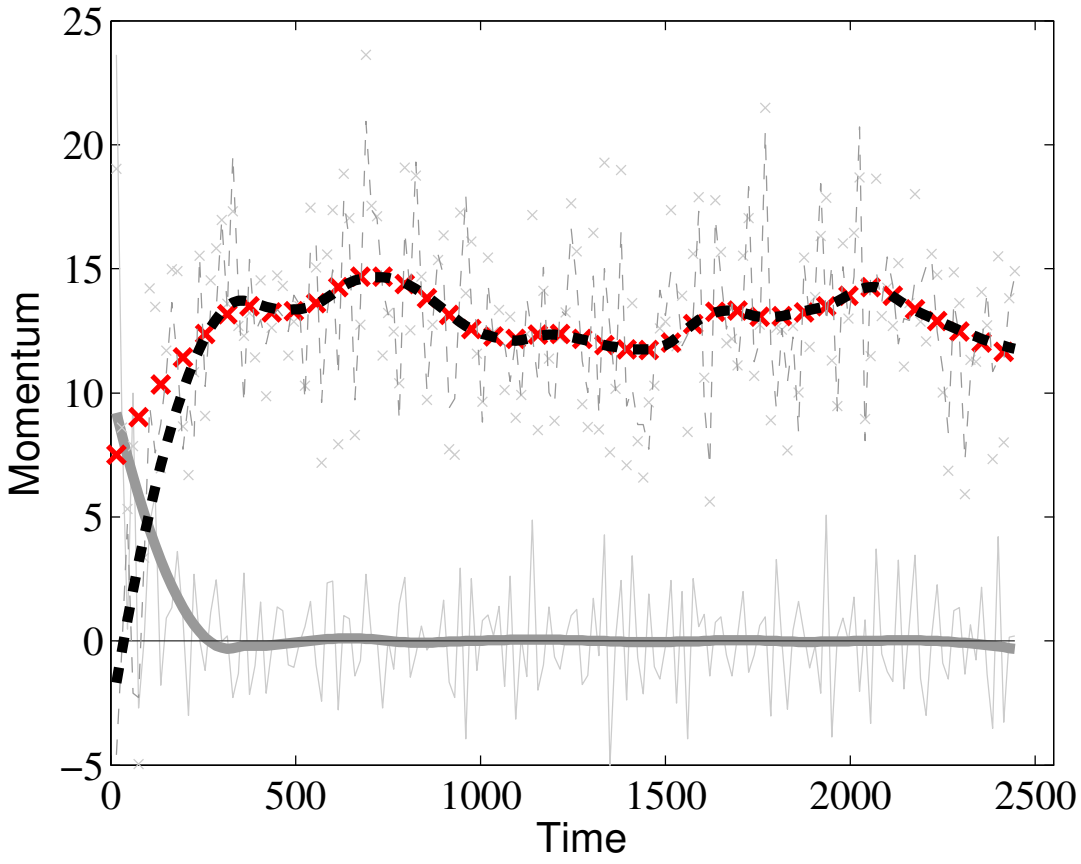

Figure 5.9: The time evolution (in reduced units) of terms in a CV located near the channel throat (fluid between $x = 104$ and $x = 118$). The faint grey values are the sum of counting every molecular crossing (- -), intermolecular force (×) or external force (—) over an interval of 15 MD time units. The continuous line is the change in velocity between the start and finish of the same time interval (—). The thick lines are smoothed (using MATLAB second order polynomial smoothing) to highlight the conservation of momentum from Eq. (5.31). The 'Accumulation' (▬), 'MD Forcing' (×), and 'MD Advection' (▪ ▪) sum to zero. Smoothed 'Forcing' symbols are shown every 4th averaging time for clarity

In order to gain further insight into the nature of the 'MD Forcing' and 'MD Advection' terms, they can be split into their constitutive parts. The 'MD Forcing' terms can be written in terms of configurational stress. The 'MD Advection' expressed in terms of kinetic pressure and convection.

The 'MD Forcing' term can be written in terms of the forces acting over each of the MD CV surfaces,

$$\sum_{i=1}^{N} \boldsymbol{F}_i \vartheta_i = \sum_{i,j}^{N} \boldsymbol{f}_{ij} \vartheta_{ij} = \sum_{i,j}^{N} \boldsymbol{\varsigma}_{ij} \cdot d\mathbf{S}_{ij}.$$

Each of the surface terms is a form of traction, given by the definition from Eq. (4.35) in the previous chapter, for example the CV top surface in the x direction has the following component

of surface stress,

$$\int_{S_x^+} \boldsymbol{\sigma} \cdot d\mathbf{S}_{S_x^+} = \sum_{i,j}^{N} \boldsymbol{\varsigma}_{xij} dS_{xij} = -\frac{1}{4} \sum_{i,j}^{N} \boldsymbol{f}_{ij} dS_{xij}^{+}.$$

where $\boldsymbol{\varsigma}_{ij}$ on the x surface is simply $\boldsymbol{\varsigma}_{xij} = \boldsymbol{f}_{ij}\tilde{n}_x = \boldsymbol{f}_{ij}$ and dS_{xij}^{+} selects only the interactions crossing the top x surface. The average stress for a given surface $\int_{S_x^+} \boldsymbol{\sigma} \cdot d\mathbf{S}_{S_x^+} \approx \mathbf{T}_x^+ \Delta A_x^+$ (as $\boldsymbol{\sigma} \cdot \mathbf{n}_x^+ = \mathbf{T}_x^+$, the traction),

$$\mathbf{T}_x^+ = -\frac{1}{4\Delta A_x^+} \sum_{i,j}^{N} \boldsymbol{f}_{ij} dS_{xij}^{+}. \tag{5.33}$$

which are approximations for the direct and shear stresses, σ_{xx}, σ_{yx} and σ_{zx}, localised to the x^+ surface of the CV. The shear stresses are statistically similar to the forces on a different surface, for example σ_{yx} the y component of force acting over the x^+ surface is similar to σ_{yx} defined by the x component of force acting over the y^+ surface,

$$\mathrm{T}_{yx}^+ = -\frac{1}{4\Delta A_x^+} \sum_{i,j}^{N} f_{yij} dS_{xij}^{+}; \qquad \mathrm{T}_{xy}^+ = -\frac{1}{4\Delta A_y^+} \sum_{i,j}^{N} f_{xij} dS_{yij}^{+}.$$

The use of a finite volume means the stress components are defined at different location and are not exactly symmetric.

The 'MD Advection' term can be split into a convective (streaming) and kinetic pressure contribution,

$$\sum_{n=1}^{N} m_n \dot{\boldsymbol{r}}_n \dot{\boldsymbol{r}}_n \cdot d\mathbf{S}_n = \oint_S \{\rho \boldsymbol{u}\boldsymbol{u}\}_{MD} \cdot dS + \sum_{n=1}^{N} m_n \overline{\dot{\boldsymbol{r}}}_i \overline{\dot{\boldsymbol{r}}}_i \cdot d\mathbf{S}_n \tag{5.34}$$

using the breakdown of Irving & Kirkwood (1950) for interactions localised to the CV surfaces where $\overline{\dot{\boldsymbol{r}}}_i \equiv (\dot{\boldsymbol{r}}_n - \boldsymbol{u})$. Each of the peculiar parts of the surface fluxes are a form of kinetic pressure. For example, the kinetic pressure on the x^+ CV surface is,

$$\int_{S_x^+} \boldsymbol{\kappa} \cdot d\mathbf{S}_{S_x^+} = \sum_{i=1}^{N} \frac{\overline{\dot{\boldsymbol{r}}}_i \overline{\dot{r}}_{ix}}{m_i} dS_{xi}^{+}. \tag{5.35}$$

The average kinetic pressure for a given surface $\int_{S_x^+} \boldsymbol{\kappa} \cdot d\mathbf{S}_{S_x^+} \approx \mathbf{K}_x^+ \Delta A_x^+$ (as $\boldsymbol{\kappa} \cdot \mathbf{n}_x^+ = \mathbf{K}_x^+$, the kinetic pressure analogue to traction) is,

$$\mathbf{K}_x^+ = \frac{1}{\Delta A_x^+} \sum_{i=1}^{N} m_i \overline{\dot{\boldsymbol{r}}}_i \overline{\dot{r}}_{ix} dS_{xi}^{+}. \tag{5.36}$$

which are approximations for the direct and shear kinetic pressures, κ_{xx}, κ_{yx} and κ_{zx} localised to the x^+ surface of the CV. Therefore, the total pressure on the x surface $\boldsymbol{p}_x^+ = \mathbf{K}_x^+ - \mathbf{T}_x^+$ is the combination of kinetic and configurational terms,

$$\boldsymbol{p}_x^+ = \frac{1}{\Delta A_x^+} \sum_{i=1}^{N} m_i \overline{\dot{\boldsymbol{r}}}_i \overline{\dot{r}}_{ix} dS_{xi}^{+} + \frac{1}{4\Delta A_x^+} \sum_{i,j}^{N} \boldsymbol{f}_{ij} dS_{xij}^{+}, \tag{5.37}$$

which corresponds to Π_{xx}, Π_{xy} and Π_{xz} components of pressure localised to the x^+ surface of the CV. This is identical in form to the method of planes stress (Todd *et al.*, 1995) but localised to a region in space (Han & Lee, 2004).

The 'MD Forcing' term can be expressed in terms of configurational stresses using the definition Eq. (5.33). The 'MD Advection' terms can be written in terms of kinetic pressure and convection using Eq. (5.34) together with the definition Eq. (5.36). Therefore, both the 'MD Forcing' and 'MD Advection' terms together are,

$$\sum_{n=1}^{N} F_{\alpha n}\vartheta_n - \sum_{n=1}^{N} m_n \dot{r}_{\alpha n}\dot{r}_{\beta n} \cdot dS_{\beta n} = -\frac{\{\rho u_\alpha u_\beta\}^+_{MD} - \{\rho u_\alpha u_\beta\}^-_{MD}}{\Delta r_\beta} - \frac{K^+_{\alpha\beta} - K^-_{\alpha\beta}}{\Delta r_\beta} + \frac{T^+_{\alpha\beta} - T^-_{\alpha\beta}}{\Delta r_\beta},$$

where the right hand side is a sum over 18 terms for each coordinate direction. There are 9 components of configurational stress, 9 components of convection and 9 components of kinetic pressure defined for both top and bottom CV surface. For flow in a converging-diverging nozzle, only the x convection $\{\rho u_x u_x\}_{MD}$, the three direct configurational stress $\sigma_{\alpha\alpha}$, three direct kinetic pressures $\kappa_{\alpha\alpha}$ and the Π_{xy}/Π_{yx} shear pressures components for each surface are significant (> 0.01). It is the magnitudes of these convection, pressure and stress terms that will be considered in this subsection.

The contour plot of the molecular convective terms $\{\rho u_x u_x\}_{MD}$ is displayed in Figure 5.10, where the maximum is observed in the centre. The direct kinetic pressure and configurational stresses are plotted as contours in Figures 5.11 and 5.12 respectively. All three directions are statistically equal, therefore the average of the three direct components over the x, y and z faces are shown in Figures 5.11 ($\kappa_{CV} \equiv \mathrm{K}^+_{xx} + \mathrm{K}^-_{xx} + \mathrm{K}^+_{yy} + \mathrm{K}^-_{yy} + \mathrm{K}^+_{zz} + \mathrm{K}^-_{zz}$) and 5.12 ($\sigma_{CV} \equiv \mathrm{T}^+_{xx} + \mathrm{T}^-_{xx} + \mathrm{T}^+_{yy} + \mathrm{T}^-_{yy} + \mathrm{T}^+_{zz} + \mathrm{T}^-_{zz}$). Figure 5.13 shows a contour of the total Π_{yx} shear component including both kinetic and configurational contributions. This is statistically identical to the Π_{xy} component obtained from the y components of force and flux on the x CV surfaces.

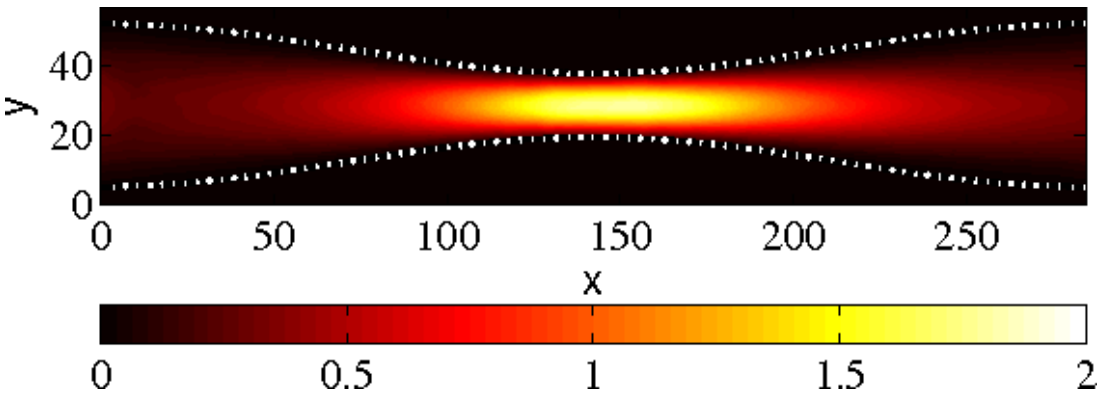

Figure 5.10: Convection in the x direction $\{\rho u_x u_x\}_{MD}$ for the MD converging diverging channel

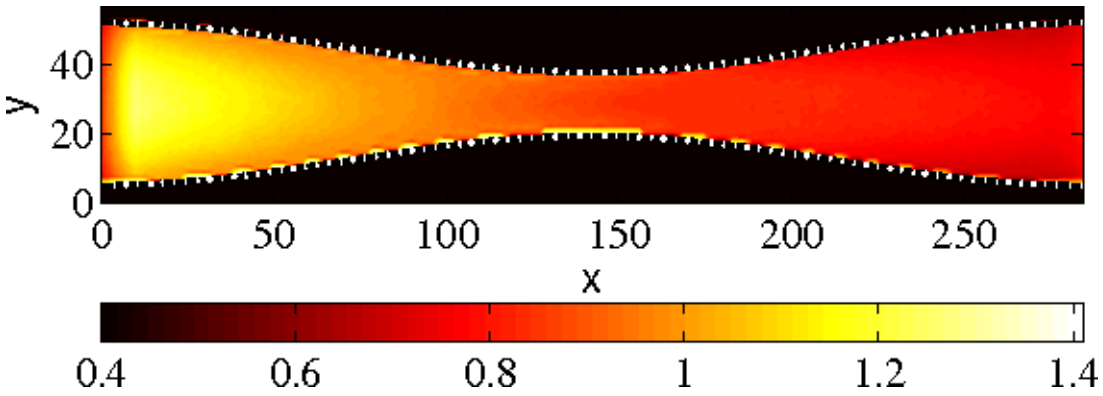

Figure 5.11: Kinetic pressure contour κ_{CV} in the MD converging diverging channel

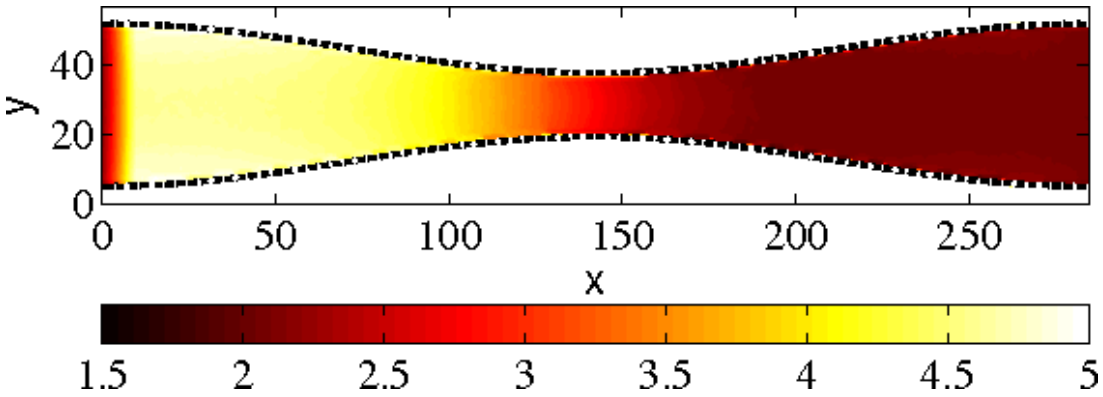

Figure 5.12: Configurational stress contour σ_{CV} in the MD converging diverging channel

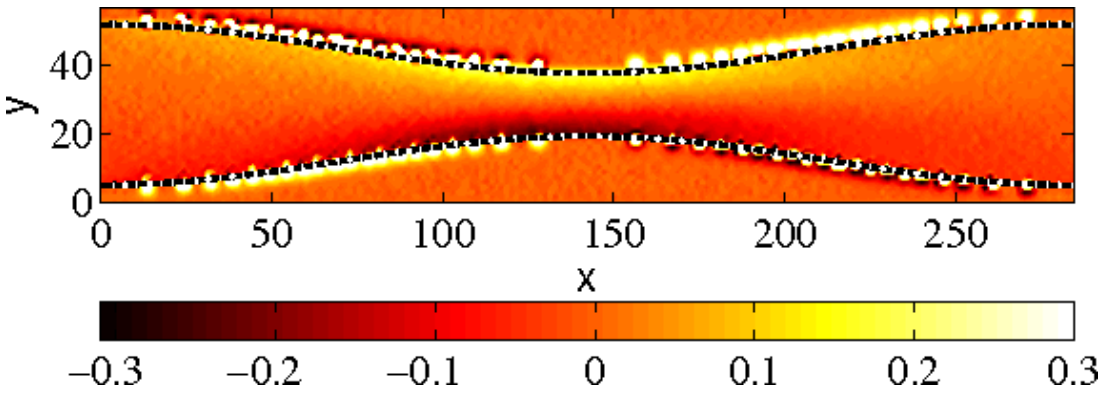

Figure 5.13: Shear stress Π_{xy}/Π_{yx} (kinetic and configurational contour in the MD converging diverging channel).

The centreline profiles as a function of x for the convective term, the kinetic pressure and the configurational stress are plotted in Figure 5.14. The kinetic pressure in Figure 5.11 is a maximum after the pumping region and drops to a minimum at the outlet. Similar behaviour is observed for the configurational stresses in Figure 5.12. However, comparison of the centreline

profiles in Figure 5.14 reveals a difference in the spatial behaviour of the two. The kinetic pressure drops continuously throughout the channel while the configurational drops most noticeably in the narrowest part of the channel, before reaching a minimum value at around $x = 200$.

The maximum configurational stress is of order 5 while the kinetic pressure account for 1.4 of the total pressure. The convective term has a magnitude of about 1.8 while the shear stress is relatively small at a maximum of about ± 0.3 near the wall. In the wall, configurational stress values are as high as 65 because molecules are held artificially close by the tethered potential. The large configurational stresses are balanced by the tethered forces which are accounted for as external body forces in the CV balance.

The 'MD Forcing' and 'MD Advection' terms are a result of the differences in the convection, stress and pressure as a function of spatial position. Therefore, the relative magnitudes of the various components are not relevant, only the changes as a function of spatial position are. It is clear from the four contour plots above, 5.10,5.11,5.12 and 5.13 that spatial gradients are present throughout the domain. These are most significantly in the x direction for kinetic pressure (Figure 5.11) and configurational stress (Figure 5.12). The x dependence is clearly seen in Figure 5.14. The shear stress has strongest gradients in the y direction in Figure 5.13, although it has a weak gradient in x following the nozzle geometry. The convective term contour of Figure 5.10 appears elliptic and varies continuously in both x and y. Consideration of the various convective and stress components in this section provides insight into the magnitudes of the 'MD Forcing' and 'MD Advection' terms. The key observation is that the terms present in the generalised coupling equation Eq. (5.27L) are related to the spatial variation in stresses, convections and pressures throughout the molecular system. The importance of these terms as fluxes and stresses is the subject of the next section where the generalised Eq. (5.27L) is shown to be a form of flux coupling.

There are three key conclusions from the study of the converging-diverging nozzle.

The first conclusion is that the 'MD Forcing' and 'MD Advection' terms are not zero for this geometry, unlike the previous case of Couette flow with a post. They have an average value which does not disappear. It is reasonable to expect that many coupled simulations of interest will also contain persistent advection and forcing components at steady state. As a result, these terms will not disappear and correct coupling will require them to be enforced.

The second conclusion is that the sum of the 'MD Forcing' and 'MD Advection' terms is zero for a steady state system. In fact, these two terms are the right hand side of the molecular CV equation Eq. (5.31) and entirely govern the evolution of that CV in time. To include only one of the terms would introduce spurious oscillations into a steady state solution. If both are included, these fluctuations are balanced and cancel on average. However, even for a steady state system, the instantaneous 'MD Forcing' and 'MD Advection' terms will not be zero, possibly taking very large values. By interpreting these terms as the right hand side of Eq. (5.31), they can be seen to govern entirely the time evolution inside the CV as a result of interaction with molecules outside the CV. In the generalised constraint Eq. (5.27L), the 'MD Forcing' and 'MD Advection' are negative and so are removed from the system by the constraint. The effect of removing these terms can therefore be seen to prevent the time evolution of the molecular CV as a result of interacting with the surrounding system.

The third conclusion of this section is that the 'MD Forcing' and 'MD Advection' terms in Eq. (5.27L) can be re-written in terms of the convection, pressures and stresses (fluxes) for the constrained CV. The various fields for these flux terms were examined and the effect on the 'MD

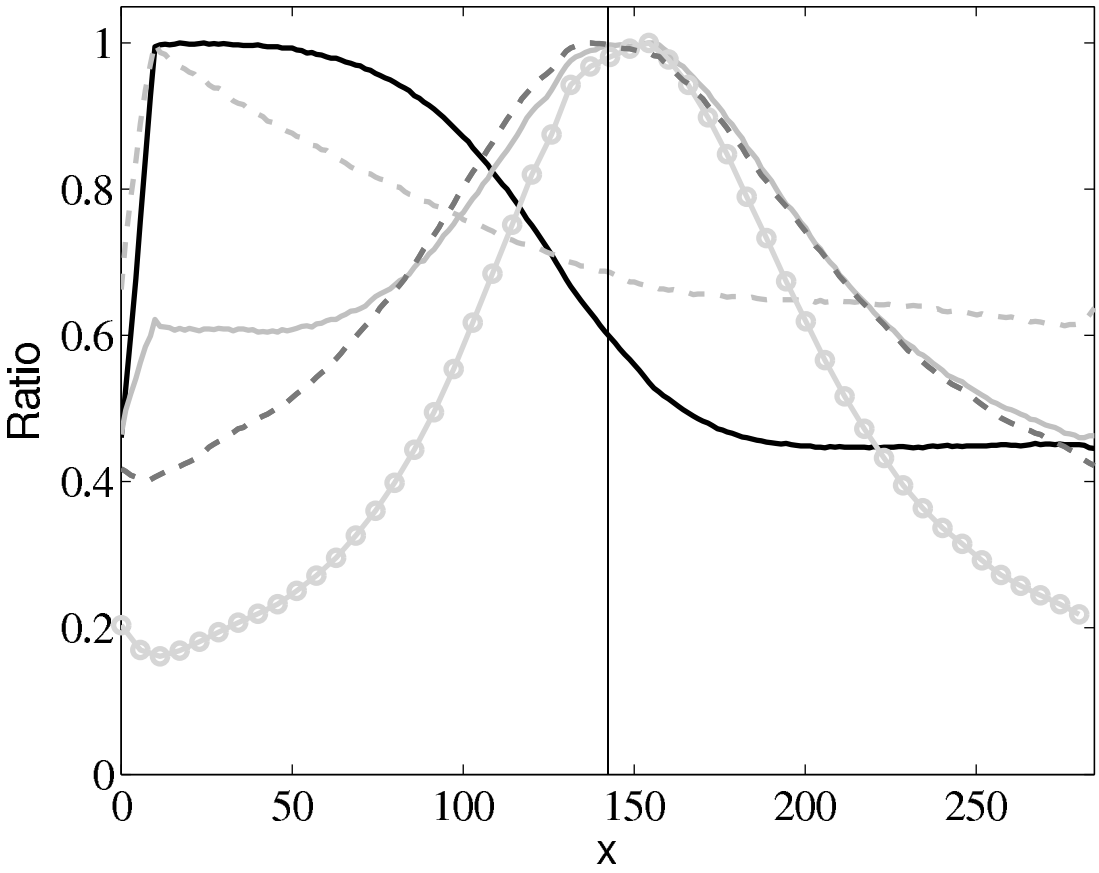

Figure 5.14: The change in x of various flux/stress quantities along the centre line in the converging-diverging channel. The configurational pressure σ_{CV}/σ_{0CV} (—), the left hand side of Eq. (5.34) normalised to one (—), broken down into kinetic pressure κ_{CV}/κ_{0CV} (- -) and the convective term $\rho\boldsymbol{uu}/\rho_0\boldsymbol{u}_0\boldsymbol{u}_0$ (–o–). The mass flux ratio (- -) obtained from flow of molecules (Eq. (4.60) Advection) is also plotted which, on average, matches $\rho u/\rho_0 u_0$ in figure D.8. Subscript 0 denotes channel maximum, $\sigma_{0CV} = 4.6$, $\kappa_{0CV} = 1.3$ and $\rho_0\boldsymbol{u}_0\boldsymbol{u}_0 = 1.8$.

Forcing' and 'MD Advection' terms in Eq. (5.27L) were discussed. With the terms interpreted in this manner, subtracting them as part of the constraint applied in Eq. (5.27L) can be interpreted as removing the fluxes in the molecular system. This will be shown explicitly in the next section 5.4, where Eq. (5.27L) is shown to be a form of flux coupling.

5.4 Control Volume Flux Coupling

This section discusses the extension of the general equation, Eq. (5.27), to the coupling of fluxes. Flux coupling is used by several authors and has a number of advantages including; higher-order agreement between the MD and CFD (Shan *et al.*, 2006), allowance for viscosity mismatch as well as positive entropy generation (Delgado-Buscalioni & Coveney, 2004). However, it should be noted that the work of Hadjiconstantinou *et al.* (2003) suggests that flux coupling is prohibitively expensive. In appendix E, this claim is shown to be true only for certain points on the phase diagram.

The general form of constraint, Eq. (5.27), is expressed in terms of the divergence of flux discussed in the previous section. This form of equation is shown to control an arbitrary molecular CV in a manner which exactly matches a continuum CV. Next, the assumptions required to obtain the flux coupling schemes of Flekkøy *et al.* (2000) and Delgado-Buscalioni & Coveney (2003a) are discussed. This exposes the underlying relationship between the Nie *et al.* (2004a) form and flux coupling schemes of Flekkøy *et al.* (2000) and Delgado-Buscalioni & Coveney (2003a). The momentum equation and stresses derived in chapter 4 are essential for this process. The result is a rigorous derivation of a flux coupling scheme from the variational principles of mechanics.

5.4.1 The General Equation as the Divergence of Flux

As a starting point, consider the most general form of constraint equation, Eq. (5.27), with the terms reordered,

$$\ddot{\boldsymbol{r}}_i = \frac{\boldsymbol{F}_i}{m_i} - \frac{\vartheta_i}{M_I}\left[- \oint_S (\rho \boldsymbol{u}\boldsymbol{u}) \cdot d\mathbf{S} - \int_V \frac{\partial (\rho \boldsymbol{u})}{\partial t} dV - \sum_{n=1}^{N} m_n \dot{\mathbf{r}}_n \dot{\boldsymbol{r}}_n \cdot d\mathbf{S}_n + \sum_{n=1}^{N} \boldsymbol{F}_n \vartheta_n \right]. \quad (5.27\mathrm{R})$$

In this section, the discretisation of $\partial(\rho \boldsymbol{u})/\partial t$ used by Nie *et al.* (2004a) is avoided, instead the time evolution of the continuum element is rewritten as the forces acting over the surface of an element (neglecting body forces in the continuum),

$$\int_V \frac{\partial (\rho \boldsymbol{u})}{\partial t} dV = F_{surface} = \oint_S \mathbf{\Pi} \cdot d\mathbf{S}.$$

which includes both kinetic pressure κ and the stress σ. The force in the MD can be expressed in terms of surface tractions,

$$\sum_{n=1}^{N} \boldsymbol{F}_n \vartheta_n = \sum_{n,m}^{N} \boldsymbol{f}_{nm} \vartheta_{nm} = \sum_{n,m}^{N} \boldsymbol{\varsigma}_{nm} \cdot d\mathbf{S}_{nm}.$$

The time evolutions of both continuum and molecular CV can then be rewritten in terms of fluxes and stresses using the continuum momentum balance equation (Eq. (2.36)) and the molecular

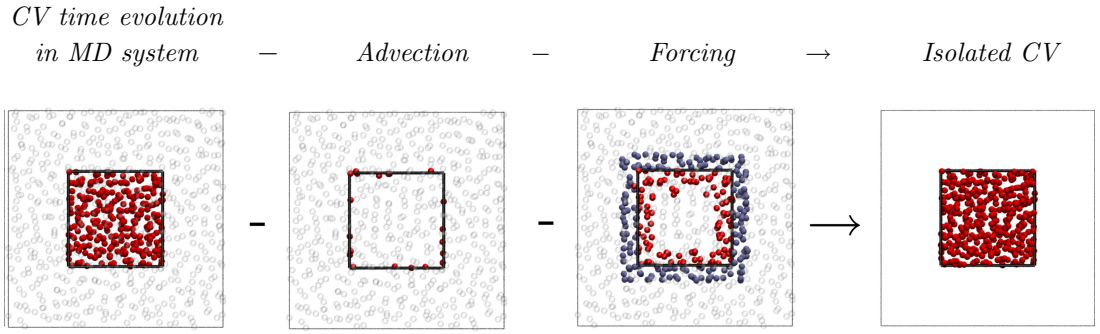

Figure 5.15: Schematic of the effect of removing the 'MD advection' and 'MD Forcing' terms from Eq. (5.38) leaving an effectively isolated CV of molecules.

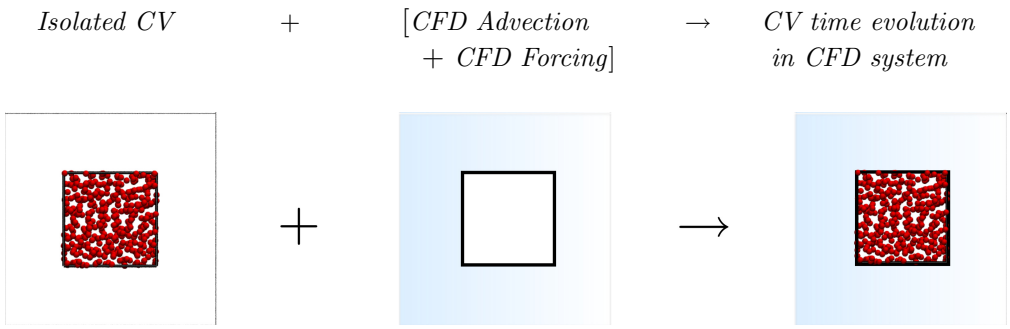

Figure 5.16: Schematic of the effect of adding the 'CFD advection' and 'CFD Forcing' terms from Eq. (5.38). The isolated CV of molecules from figure 5.15 therefore evolves as if directly surrounded by the continuum fluid.

equivalent Eq. (4.55),

$$\ddot{\boldsymbol{r}}_i = \frac{\boldsymbol{F}_i}{m_i} - \frac{\vartheta_i}{M_I}\Bigg[\underbrace{\oint_S \rho \boldsymbol{u}\boldsymbol{u}\cdot d\mathbf{S}}_{\text{CFD Advection}} - \underbrace{\oint_S \boldsymbol{\Pi}\cdot d\mathbf{S}}_{\text{CFD Forcing}} - \underbrace{\sum_{n=1}^{N} m_n \dot{\boldsymbol{r}}_{\boldsymbol{n}}\dot{\boldsymbol{r}}_{\boldsymbol{n}}\cdot d\mathbf{S}_n}_{\text{MD Advection}} + \underbrace{\frac{1}{2}\sum_{n,m}^{N} \boldsymbol{\varsigma}_{nm}\cdot d\boldsymbol{S}_{nm}}_{\text{MD Forcing}}\Bigg]. \quad (5.38)$$

A schematic view of the effect of applying the constraint of Eq. (5.38) is shown in Figures 5.15 and 5.16. First, in Figure 5.15 the 'MD advection' and 'MD Forcing' terms are removed. These terms describe the sum of all fluxes and external forces acting over the CV surface. Removing them has the effect of ensuring that the CV of molecules is isolated from the rest of the MD system in an average sense (as shown on the far left of Figure 5.15). Note that fluctuations due to the surrounding system and local interaction are retained, only the average forces and fluxes are removed. The isolated CV then has the 'CFD Advection' and 'CFD Forcing' added to it. These terms define the continuum field which acts over the surface of a continuum CV. This has the effect, as shown in Figure 5.16, of ensuring that the molecules in the CV evolve as if they are surrounded by the continuum fluid. This will be shown rigorously in the next subsection by combining the constraint Eq. (5.38) with the CV momentum Eq. (5.39).

Effect on the Momentum Equation

As the constraint in Eq. (5.38) is an external force applied to the system, it can be shown to apply the correct momentum flux equation by substituting it as an external force into the molecular momentum CV Eq. (4.55),

$$\frac{\partial}{\partial t}\sum_{i=1}^{N} m_i \dot{\boldsymbol{r}}_i \vartheta_i = -\sum_{i=1}^{N} m_i \dot{\boldsymbol{r}}_{\boldsymbol{i}} \dot{\boldsymbol{r}}_{\boldsymbol{i}} \cdot d\mathbf{S}_i + \frac{1}{2}\sum_{i,j}^{N} \boldsymbol{\varsigma}_{ij} \cdot d\mathbf{S}_{ij} + \sum_{i=1}^{N} \boldsymbol{f}_{i_{\text{ext}}} \vartheta_i. \tag{5.39}$$

This equation, introduced in the previous chapter, governs the time evolution of a molecular control volume. The time evolution is due to molecular flux, molecular forces and the external force $\boldsymbol{f}_{i_{\text{ext}}}$, typically neglected in the previous section. The constraint force of Eq. (5.38) can be considered as a form of external force of the form,

$$\boldsymbol{f}_{i_{\text{ext}}} = -\frac{m_i}{M_I}\left[\oint_S \rho \boldsymbol{u}\boldsymbol{u} \cdot d\mathbf{S} - \oint_S \boldsymbol{\Pi} \cdot d\mathbf{S} - \sum_{n=1}^{N} m_n \dot{\boldsymbol{r}}_{\boldsymbol{n}} \dot{\boldsymbol{r}}_{\boldsymbol{n}} \cdot d\mathbf{S}_n + \frac{1}{2}\sum_{n,m}^{N} \boldsymbol{\varsigma}_{nm} \cdot d\boldsymbol{S}_{nm}\right]. \tag{5.40}$$

Therefore, Eq. (5.38) can be written as Newton's law with an additional external force, $m_i \ddot{\boldsymbol{r}}_i = \boldsymbol{F}_i + \boldsymbol{f}_{i_{\text{ext}}} \vartheta_i$. Substituting Eq. (5.40) into Eq. (5.39) and noting that $\sum_i^N m_i \vartheta_i / M_I = 1$, the molecular terms cancel and the momentum conservation equation becomes,

$$\frac{\partial}{\partial t}\sum_{i=1}^{N} m_i \dot{\boldsymbol{r}}_i \vartheta_i = -\oint_S \rho \boldsymbol{u}\boldsymbol{u} \cdot d\mathbf{S} + \oint_S \boldsymbol{\Pi} \cdot d\mathbf{S}, \tag{5.41}$$

which shows that the molecular momentum evolution is exactly equal to the continuum surface fluxes and forces in the constrained control volume. This has the corollary that,

$$\frac{\partial}{\partial t}\sum_{i=1}^{N} m_i \dot{\boldsymbol{r}}_i \vartheta_i = \frac{\partial}{\partial t}\int_V \rho \boldsymbol{u} dV, \tag{5.42}$$

the MD CV evolves in time in exactly the same way as the coupled continuum CV. The importance of removing the molecular momentum terms before adding the continuum values is clear. If the continuum values are simply applied as a force to the molecular system they will introduce additional momentum, rather than ensuring that the momentum evolution reaches the required value. This would also result in an addition of energy as discussed next.

Effect on the Energy Equation

The derivation of the effect on the momentum equation is exact. No assumption was required in the derivation and the constraint of momentum ensures that the MD system matches the continuum evolution exactly at all times. The energy applied to the system by the constraint of Eq. (5.38) can also be explored by considering the external term in the energy equation, Eq. (4.56). The energy equation for a CV is,

$$\frac{\partial}{\partial t}\sum_{i=1}^{N} e_i \vartheta_i = -\sum_{i=1}^{N} e_i \dot{\boldsymbol{r}}_i \cdot d\mathbf{S}_i + \frac{1}{2}\sum_{i,j}^{N} \dot{\boldsymbol{r}}_i \cdot \boldsymbol{\varsigma}_{ij} \cdot d\mathbf{S}_{ij} + \sum_{i=1}^{N} \dot{\boldsymbol{r}}_i \cdot \boldsymbol{f}_{i_{\text{ext}}} \vartheta_i, \tag{5.43}$$

The energy added to the molecular system by the external body force from Eq. (5.40) is,

$$\sum_{i=1}^{N} \dot{\boldsymbol{r}}_i \cdot \boldsymbol{f}_{i_{\text{ext}}} \vartheta_i = \frac{1}{M_I} \sum_{i=1}^{N} m_i \dot{\boldsymbol{r}}_i \cdot \Bigg[\oint_S \rho \boldsymbol{u}\boldsymbol{u} \cdot d\mathbf{S} - \oint_S \boldsymbol{\Pi} \cdot d\mathbf{S} - \sum_{n=1}^{N} m_n \dot{\boldsymbol{r}}_{\boldsymbol{n}} \dot{\boldsymbol{r}}_{\boldsymbol{n}} \cdot d\mathbf{S}_n + \frac{1}{2} \sum_{n,m}^{N} \boldsymbol{\varsigma}_{nm} \cdot d\boldsymbol{S}_{nm} \Bigg] \vartheta_i. \tag{5.44}$$

The energy applied can be understood by expressing the fluxes in terms of time evolution using Eq. (4.61) for the molecular terms and Eq. (2.36) for the continuum,

$$\sum_{i=1}^{N} \dot{\boldsymbol{r}}_i \cdot \boldsymbol{f}_{i_{\text{ext}}} \vartheta_i = \frac{1}{M_I} \sum_{i=1}^{N} m_i \dot{\boldsymbol{r}}_i \vartheta_i \cdot \left[\frac{\partial}{\partial t} \int_V \rho \boldsymbol{u} dV - \frac{\partial}{\partial t} \sum_{i=1}^{N} m_i \dot{\boldsymbol{r}}_i \vartheta_i \right]. \tag{5.45}$$

From the insertion of the constraint force into the momentum equation in the previous subsection, it was shown that the time evolution of the molecular CV is exactly matched to the continuum CV Eq. (5.42). Therefore, the energy applied by the external constraint force is zero,

$$\sum_{i=1}^{N} \dot{\boldsymbol{r}}_i \cdot \boldsymbol{f}_{i_{\text{ext}}} \vartheta_i = 0. \tag{5.46}$$

The general constraint equation of Eq. (5.27L) or equivalently Eq. (5.38) are therefore seen to add exactly no energy to the molecular system in the process of constraining the momentum. This is consistent with the derivation of Eq. (5.27L) from the principle of least action applying non-holonomic constraints, which is known to conserve energy (Goldstein *et al.*, 2002). Note, the insertion of molecules into the molecular system is not considered in this energy equation.

In the next section, the requirement of exact matching of the divergence in both systems of Eq. (5.38) is relaxed to instead ensure the agreement of individual fluxes between both systems. Although this constraint should still satisfy Eq. (5.38), the agreement of the time evolution of both systems may no longer be exact. The process in the next section weakens the formulation in a way which is analogous to weakening a continuum description using the finite element method (FEA). The continuum FEA formulation is derived in a manner which ensures energy conservation, therefore it should be possible to construct a flux scheme which exactly maintains the energy conservation demonstrated here.

5.4.2 Flux Coupling from the General Equation

The flux form of the general constraint Eq. (5.38) is the starting point for the work in this section. The requirement of this constraint, Eq. (5.38), is that the difference in stress over all CV surfaces is the same in both systems. If each surface is instead matched independently, the original constraint requirement would still be satisfied. Using a similar concept to the finite element method (Zienkiewicz, 2005), the constraint force can be re-written in a manner which allows stress at every point inside the molecular CV to be linked using a weighting function. The requirement is that Eq. (5.38) is satisfied by the choice of weighting function.

Noting that the stress acting over the surface is by definition the traction which can be related to the internal stresses using a shape function N_a (see Eq. (4.39) and associated discussion in

section 4.2.7). The constraint Eq. (5.38) can therefore be written as,

$$\ddot{\boldsymbol{r}}_i = \frac{\boldsymbol{F}_i}{m} - \frac{N_a\vartheta_i}{M_I}\left(\oint_{S^+}\rho\boldsymbol{u}\boldsymbol{u}\cdot d\mathbf{S}^+ - \oint_{S^+}\boldsymbol{\Pi}\cdot d\mathbf{S}^+ - \sum_{i=1}^{N} m\dot{\boldsymbol{r}}_{\boldsymbol{n}}\dot{\boldsymbol{r}}_{\boldsymbol{n}}\cdot d\mathbf{S}_n^+ + \frac{1}{2}\sum_{n,m}^{N}\boldsymbol{\varsigma}_{nm}\cdot d\boldsymbol{S}_{nm}^+\right) - \frac{(1-N_a)\,\vartheta_i}{M_I}\left(\oint_{S^-}\rho\boldsymbol{u}\boldsymbol{u}\cdot d\mathbf{S}^- - \oint_{S^-}\boldsymbol{\Pi}\cdot d\mathbf{S}^- - \sum_{i=1}^{N} m\dot{\boldsymbol{r}}_{\boldsymbol{n}}\dot{\boldsymbol{r}}_{\boldsymbol{n}}\cdot d\mathbf{S}_n^- + \frac{1}{2}\sum_{n,m}^{N}\boldsymbol{\varsigma}_{nm}\cdot d\boldsymbol{S}_{nm}^-\right). \tag{5.47}$$

The choice of weighting function is entirely arbitrary provided the surface stresses and fluxes are satisfied. The simplest choice in order to satisfy the boundaries is a linear shape function, $N_a = (r_{i\beta} - r_\beta^-)/\Delta r_\beta$, where $r_\beta^- = r_\beta - \Delta r_\beta/2$. The CV function is only non-zero where $r_\beta - \Delta r_\beta/2 < r_{i\beta} < r_\beta + \Delta r_\beta/2$, so that $0 < N_a < 1$. It is also possible to use more complicated functions for N_a, for example an RDF based shape function of the type given in Eq. (2.81) and derived from the representation used by Werder *et al.* (2005). The RDF weighting function could be used to apply forces in a manner as close as possible to inter-molecular forces,

$$N_a = -2\pi\int_{z=r_w}^{r_c}\int_{x=0}^{(r_c^2-z^2)^{\frac{1}{2}}} g(r)\frac{xz}{r}dxdz \tag{5.48}$$

where $g(r)$ is the radial distribution function in radial coordinates. The choice of shape function could also be different for the molecular system and continuum system, for example,

$$\ddot{\boldsymbol{r}}_i = \frac{\boldsymbol{F}_i}{m} - \sum_{i=1}^{N} m\dot{\boldsymbol{r}}_{\boldsymbol{n}}\dot{\boldsymbol{r}}_{\boldsymbol{n}}\cdot d\mathbf{S}_n + \frac{1}{2}\sum_{n,m}^{N}\boldsymbol{\varsigma}_{nm}\cdot d\boldsymbol{S}_{nm} - \frac{N_a\vartheta_i}{M_I}\left(\oint_{S^+}\rho\boldsymbol{u}\boldsymbol{u}\cdot d\mathbf{S}^+ - \oint_{S^+}\boldsymbol{\Pi}\cdot d\mathbf{S}^+\right) - \frac{(1-N_a)\,\vartheta_i}{M_I}\left(\oint_{S^-}\rho\boldsymbol{u}\boldsymbol{u}\cdot d\mathbf{S}^- - \oint_{S^-}\boldsymbol{\Pi}\cdot d\mathbf{S}^-\right),$$

where all the CV molecular interactions are entirely removed and the continuum forces are applied based on a weighting function. This ensures that the fluxes and forces of the molecular system are exactly removed as in Eq. (5.41), and that the continuum forces can be applied using any choice of weighting function. The appropriate choice of weighting function is implementation specific and can result in the various forms of flux coupling from the literature, as shown in the next subsection.

The constraint Eq. (5.47) can be interpreted as removing molecular fluxes/forces and replacing them with the continuum fluxes/forces, as shown schematically in Figures 5.15 and 5.16. The key change in this section is that Eq. (5.47) no longer simply constrains the sum of all the fluxes/forces. Instead, the flux and force are constrained on a surface by surface basis for the six CV surfaces. The constraint force therefore varies throughout the control volume and enforces a higher order of agreement. In the previous section, using Eq. (5.38), a single force was applied to each volume and only the sum of all the surfaces fluxes/forces was enforced.

Relationship to the methods of Flekkøy *et al.* (2000) and Delgado-Buscalioni & Coveney (2003*a*)

The pioneering flux coupling methodology of Flekkøy *et al.* (2000) can be seen as a special case of Eq. (5.47), given by appropriate choice of weighting function. The flux constraint of Flekkøy *et al.* (2000) does not include removal of the 'MD advection' and pressures at each timestep so Eq. (5.47) simplifies to,

$$\ddot{\boldsymbol{r}}_i = \frac{\boldsymbol{F}_i}{m} - \frac{N_a \vartheta_i}{M_I}\left(\oint_{S^+} \rho \boldsymbol{u}\boldsymbol{u}\cdot d\mathbf{S}^+ - \oint_{S^+} \boldsymbol{\Pi}\cdot d\mathbf{S}^+\right) - \frac{(1-N_a)\,\vartheta_i}{M_I}\left(\oint_{S^-} \rho \boldsymbol{u}\boldsymbol{u}\cdot d\mathbf{S}^- - \oint_{S^-} \boldsymbol{\Pi}\cdot d\mathbf{S}^-\right), \tag{5.49}$$

The importance of removing the molecular terms was demonstrated in the previous subsection 5.4.1 using the momentum and energy equation. By simply adding the continuum flux, the constraint of Flekkøy *et al.* (2000) add energy to the system without any corresponding removal of molecular energy. Later work by the same group removed the added energy by velocity rescaling (Wagner *et al.*, 2002) when considering the coupled energy exchange.

The work of Flekkøy *et al.* (2000) apply the pressure $\int_{S_y^+} \boldsymbol{\Pi}\cdot d\mathbf{S}_y^+$ and convection $\int_{S_y^+} \rho\boldsymbol{u}\boldsymbol{u}\cdot d\mathbf{S}_y^+$ at the top of the molecular region only *i.e.* $\int_{S^-} \boldsymbol{\Pi}\cdot d\mathbf{S}^- = 0$ and $\int_{S^-} \rho\boldsymbol{u}\boldsymbol{u}\cdot d\mathbf{S}^- = 0$ so,

$$\ddot{\boldsymbol{r}}_i = \frac{\boldsymbol{F}_i}{m} - \quad \frac{N_{a_y}\vartheta_i}{M_I} \quad \left(\int_{S_y^+} \rho \boldsymbol{u}\boldsymbol{u}\cdot d\mathbf{S}_y^+ - \int_{S_y^+} \boldsymbol{\Pi}\cdot d\mathbf{S}_y^+\right). \tag{5.50}$$

This constraint enforces the three components of continuum convection and pressure acting over the top surface. The convection terms are adjusted to be consistent with the insertion of molecules and the applied force is corrected to take this into account. The weighting function chosen by Flekkøy *et al.* (2000) is said to be arbitrary. A diverging function, Eq. (2.92), is chosen which provides a lower density region in which to insert molecules.

The work of Delgado-Buscalioni & Coveney (2003*a*) extends the coupling of Flekkøy *et al.* (2000). As with Flekkøy *et al.* (2000), the molecular fluxes/stresses of Eq. (5.47) are not removed before adding the continuum forces so the reduced form of Eq. (5.49) is used. Delgado-Buscalioni (2012) asserts that the applied force must have a constant value to prevent heat being produced in an uncontrolled manner. This constant force can be implemented in the framework of Eq. (5.49) by setting $N_a = 1/2$ in Eq. (5.49), so that the average value between the top and bottom surfaces is applied,

$$\ddot{\boldsymbol{r}}_i = \frac{\boldsymbol{F}_i}{m} - \frac{1}{2}\frac{\vartheta_i}{M_I}\left(\oint_{S^+} \rho \boldsymbol{u}\boldsymbol{u}\cdot d\mathbf{S}^+ - \oint_{S^+} \boldsymbol{\Pi}\cdot d\mathbf{S}^+ + \oint_{S^-} \rho \boldsymbol{u}\boldsymbol{u}\cdot d\mathbf{S}^- - \oint_{S^-} \boldsymbol{\Pi}\cdot d\mathbf{S}^-\right). \tag{5.51}$$

Setting N_a to a constant value would not satisfy the original constraint Eq. (5.38) exactly, as a constant weighting cannot simultaneously satisfy the different top and bottom surface fluxes. Delgado-Buscalioni & Coveney (2004) observe that the flux values at the surfaces and not cell centres are required to accurately enforce a coupling scheme. Therefore, the coupling scheme in this form would be offset by half a cell in practice, in order to ensure the centre is a surface flux of the cell of interest. As the 'MD Forcing' and 'MD Advection' are not removed, energy is

added to the system. The correct energy exchange between the systems is ensured by removing this energy through a combination of localised thermostats and particle insertions with appropriate kinetic and potential energies (Delgado-Buscalioni & Coveney, 2003*a*). However, the more elegant scheme introduced in later work by Flekkøy, Delgado-Buscalioni and Coveney (Flekkøy *et al.*, 2005) ensures the constraint does no work on the molecular system. This is derived using thermodynamics arguments and results in a number of the molecular terms ('MD Forcing' and 'MD Advection' split into streaming and fluctuating parts) being added into the constraint. As a result, it is closer to the more general coupling of Eq. (5.47) which includes removal of the molecular contribution and does not result in any addition of energy to the molecular system.

5.5 Overview

This chapter has discussed the application of the control volume (CV) formulation derived in chapter 4 to the field of coupling. By using the localising properties of the CV operator, together with variational principles of mechanics, a rigorous and general constraint equation, Eq. (5.27), was obtained,

$$\ddot{\boldsymbol{r}}_i = \frac{\boldsymbol{F}_i}{m_i} - \frac{\vartheta_i}{M_I}\Bigg[\overbrace{\underbrace{\sum_{n=1}^{N}\boldsymbol{F}_n\vartheta_n}_{\text{MD Forcing}} - \underbrace{\int_V \frac{\partial\left(\rho\boldsymbol{u}\right)}{\partial t}dV}_{\approx \boldsymbol{u}_{CFD}-\boldsymbol{u}_{MD}}}^{\approx \boldsymbol{\sigma}_{MD}-\boldsymbol{\Pi}_{CFD}} - \underbrace{\oint_S\left(\rho\boldsymbol{u}\boldsymbol{u}\right)\cdot d\mathbf{S} + \sum_{n=1}^{N} m_n\dot{\boldsymbol{r}}_n\dot{\boldsymbol{r}}_n\cdot d\mathbf{S}_n}_{\text{Advection (New to current work)}}\Bigg]. \qquad (5.27\text{O})$$

where the underbrace and overbrace denote the interpretation of the various terms discussed in this section. As Eq. (5.27O) is directly derived using variational principles of mechanics, it provides the molecular system with a trajectory as close as possible to the true trajectory, but subject to the required constraint for coupling.

Equation (5.27O) is the key contribution of this chapter and the interpretations of its various terms have been demonstrated through numerical experiments and comparison to the literature. The manner in which it can simplified to obtain the various form of existing coupling has also been shown, demonstrating the link between the existing literature (O'Connell & Thompson, 1995; Borg *et al.*, 2010; Nie *et al.*, 2004*a*; Flekkøy *et al.*, 2000; Delgado-Buscalioni & Coveney, 2003*a*). Finally, the advection terms in Eq. (5.27O) are new to this work and their importance has been demonstrated.

The summary of the various forms of constraints is shown in Figure 5.17 with the generalised equation, Eq. (5.27O), highlighted in light grey.

The starting point of Figure 5.17 is to enforce the 'CV momentum constraint' which ensures the momentum of a localised CV agrees between both systems,

$$\boldsymbol{g}(\boldsymbol{q},\dot{\boldsymbol{q}},t) = \sum_{n=1}^{N} m_n\dot{\boldsymbol{q}}_n\vartheta_n - \int_V \rho\boldsymbol{u}dV = 0. \qquad (5.52)$$

The use of the $\mathcal{LCV}$ function is key to ensure the constraint is applied correctly, localised to a volume in space. The result from applying this constraint, using the principle of least action, is the Hamiltonian form of the equations of motion Eq. (5.9a) and Eq. (5.9b). These can be simplified to yield the (O'Connell & Thompson, 1995) form of coupling, as shown in Figure 5.17.

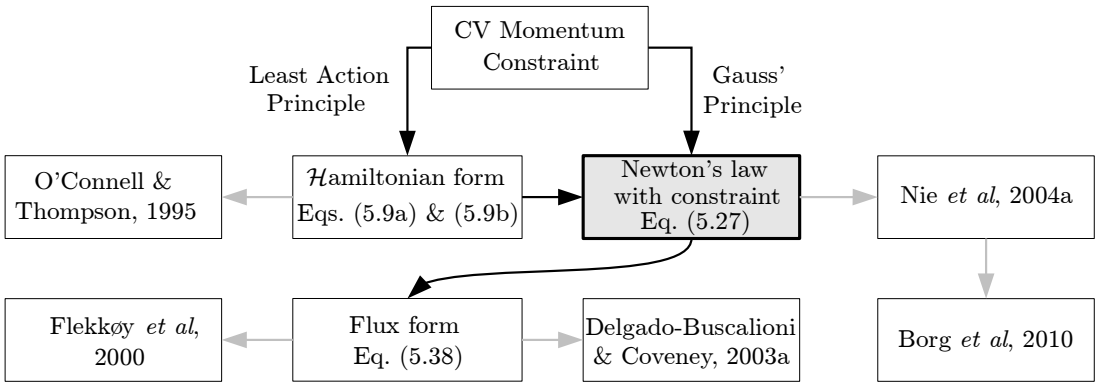

Figure 5.17: Schematic summary of the constraint derivation in this chapter. The dark arrows represent formal mathematical manipulations while the grey arrows indicate steps which require neglecting terms or assumptions. The light grey box is the generalised equation Eq. (5.27O).

The Hamiltonian equations can also be combined to give Newton's law with constraint, Eq. (5.27O). The Newtonian form can also be obtained directly from Gauss' principle, as shown in Figure 5.17, demonstrating that the least action and Gauss' principles are consistent for this case.

Newton's law with the constraint can be shown to yield the Nie *et al.* (2004*a*) form (see Figure 5.17) using a 'special discretisation' to replace the velocity differential with a velocity difference, $D\boldsymbol{u}/Dt \approx \boldsymbol{u}_{_{CFD}} - \boldsymbol{u}_{_{MD}}/\Delta t$ and neglecting 'Advection'. This assumption is of key importance to the success of the Nie *et al.* (2004*a*) coupling, as demonstrated in section 5.3.1. The 'special discretisation' converts the constraint to a form of state coupling, where the 'MD Forcing' terms is unimportant. The more complicated case of Couette flow with a post in section 5.3.2, also demonstrates the relative unimportance of 'MD Forcing' and the new 'Advection' terms to the steady state solution.

The reason for the unimportance of the 'MD Forcing' and 'Advection' terms was attributed to the small post. These terms will be expected to be increasingly more important as the post becomes larger. The logical limit of this assertion was taken using an all MD simulation of a converging diverging nozzle in section 5.3.3. The importance of the 'MD Forcing' and 'Advection' terms is then demonstrated as they are seen to be non-zero at steady state. Furthermore, the 'MD Forcing' and 'Advection' terms together are shown to entirely govern the time evolution of momentum in a control volume (from Eq. (4.79)). This demonstrates that they are not only required in general, but that the new 'Advection' component in Eq. (5.27O) is as important as the 'MD Forcing', having equal magnitude at steady state. Without both terms, spurious forces would be introduced into the steady state solution by the coupling constraint of Nie *et al.* (2004*a*). Finally, the 'MD Forcing' and 'Advection' terms are shown to be the result of variations in the convection and pressure (flux) field in the MD converging-diverging channel. The importance of these terms was therefore demonstrated as a form of flux based constraint.

This leads on to the final section 5.4, where the constraint is weakened in order to obtain a form of flux coupling. On Figure 5.17, this is shown by the link from the Newtonian form of the equation of motion to the flux form. The flux form of the general equation, Eq. (5.27O), was then linked to the flux constraints of Flekkøy *et al.* (2000) and Delgado-Buscalioni & Coveney (2003*a*).

This achieves the goal of providing a rigorous derivation of flux coupling from the variational

principles. The advantage is that the evolution due to the flux constraint is consistent with the variational principles. In addition, the energy conservation is automatically satisfied due to the derivation of the constraint from the principle of least action (Goldstein *et al.*, 2002). In addition, the CV framework provides a way of validating the choice of constraint in section 5.4.1. This is performed by evaluating the effect of the constraint on the molecular momentum and energy equations.

Chapter 6

Conclusions and Future Work

6.1 Motivation and challenges

This work has presented the development of coupling methodologies between continuum computational fluid mechanics (CFD) and molecular dynamics (MD). This emerging subject is of vital importance to the future of micro and nano scale engineering.

The field of continuum based fluid mechanics has a long history, however there remain very few analytical solutions. Only since the development of computers and the field of CFD have real solutions of the fluid flow equations been possible. The development of stable numerical methods and techniques occurred hand in hand with the growth of computing power. Understanding and modelling of turbulence has also developed, with large eddy simulation and Reynolds averaged Navier-Stokes equations being essential for most engineering applications. CFD is now widely used in many fields of engineering prediction, for example aerodynamics, automotive, nuclear reactors, gas turbines, weather modelling and biological flows. However, at smaller scales and in limiting cases, even direct numerical simulation (DNS) of the Navier-Stokes equations can be insufficient to capture the full extent of the physics.

The discrete modelling techniques of molecular dynamics provide many advantages. Cases where the continuum assumption is no longer valid can be explored, including detailed capturing of shockwaves, the contact line between fluids and insight into the non-slip boundaries even for apparent discontinuities of impulse started or corner flow. The effect of realistic molecular walls or surface textures can be easily explored. The molecular model naturally captures many physical effects, which would require complex extensions to the Navier-Stokes equations. Examples include bubble formation, shear thinning, viscosity change due to temperature, solidification and heat flow. The modelling of complicated fluids and solids is greatly simplified by MD, as the actual molecular structure of polymers, complicated lubricants or carbon nano-tube structures can be explicitly built into the model. Even the modelling of the surface chemistry is within the remit of molecular dynamics. The engineering importance of simulating these effects is clear in many fields, for example the nano-tribology of microelectromechanical (MEMS) and nano-electromechanical (NEMS) devices, the aerodynamics of space shuttle re-entry and the design of computing hardware from cooling transistors to the nano-scale gap problems in hard drive design. Beyond the purely practical engineering advantages of MD, lies the theoretical possibilities of improved insight into concepts such as viscosity, pressure, heat flows and the microscale origins of turbulence.

The field of non-equilibrium molecular dynamics, as with CFD, originated with the birth

of computers. In moving away from equilibrium, very little theoretical guidance is available (Rapaport, 2004). The theoretical framework and techniques for simulation have been developed recently (Thermostats (Hoover, 1991; Evans & Morris, 1984; Morriss & Dettman, 1998), Green-Kubo (Green, 1954; Kubo, 1957), SLLOD (Hoover, 1991; Todd & Daivis, 2005), constrained dynamics (Evans & Morriss, 2007; Flannery, 2005; Saletan & Cromer, 1970; Goldstein *et al.*, 2002), polymers (Rapaport, 2004), wall tethering (Petravic & Harrowell, 2006; Liem *et al.*, 1992)) and, despite rapid advances, are still developing. Many of these techniques remain the subject of some controversy and debate (*e.g.* SLLOD vs p-SLLOD, Velocity rescaling, Langevin, Gaussian or Nosè Hoover thermostats).

Molecular dynamic simulation is prohibitively expensive at all but sub-micrometer scales and very short times. By combining molecular scale models with the widely used larger scale simulation techniques of continuum CFD, the range of problems which can be addressed is expanded far beyond either simulation technique alone. However, the linking of these models is a hard problem. The coupling between them must surmount both CFD and MD difficulties, before addressing a consistent way to link the two. Attempts to link the continuum and discrete systems extends well beyond the conception of calculus, however, the type of computational coupling discussed in this document is a very modern field (since 1995). The mathematical link is most attributable to Irving & Kirkwood (1950) and this has formed the basis for much of the work in chapter 4. Developing these mathematical models and converting them into algorithms to couple the continuum and molecular description has been the aim of this work.

6.2 Overview of this Work

6.2.1 Summary

In this work, the problem of coupling has been attacked on three fronts: the development of robust and efficient computing tools, the development of a rigorous theoretical framework to link the two systems and a method to apply a coupling constraint to the MD system in a physically meaningful way.

6.2.2 Software Developments

As a result of this project, software has been developed to enable the simulation of coupled MD-CFD schemes on a large scale. The MD, CFD and CPL-library have all been designed to work efficiently on high performance computing (HPC) architecture.

A major part of the work during this project has been on the development of a new molecular dynamics (MD) solver. The MD solver has been optimised so as to have similar performance to the MD code LAMMPS but designed especially for non equilibrium fluid dynamics (NEMD) and fluid mechanics style simulations. It is written in parallel, using the message passing interface (MPI). The code has been fully verified, implements a range of NEMD techniques such as thermostats, tethered molecules and constraints, additionally it contains a range of statistical collection techniques and post processing routines.

The CFD code employed in this project, $\mathcal{T}ransFlow$, is fully optimised and has been used in high performance calculations. Further to this, a simple CFD solver was written as part of the development and testing of the coupled framework.

The CPL library computational framework is designed to link any CFD and MD codes on a HPC platform. The philosophy is similar to MPI, where a number of initialised calls are used to setup the topology of the grid. The user then simply specifies which cells to exchange and the send and receive commands handle all the appropriate communication. This software has been made open source (Smith & Trevelyan, 2013) and it is hoped it will be beneficial to the coupling community.

The CPL-library has been employed to link the CFD and MD codes and a number of cases from the literature have been recreated to verify its functionality. The largest case tested, although relatively small (32 MD cores and 8 CFD cores), includes all the possible communicational complexity of simulation using any number of processes. In addition, the profiling test pushed the coupled MD system to over 3 million molecules and 1024 cores. The coupled $\mathcal{T}rans\mathcal{F}low$-MD solver has been validated for an exhaustive range of cases and is ready to simulate coupled cases of arbitrary size.

6.2.3 CV Formulation to Link Descriptions

The work in chapter 4 developed a novel mathematical framework to extend the concept of a control volume (CV) to the molecular system. The derivation builds on the rigorous approach of Irving & Kirkwood (1950). The motivation for this is to express both the continuum and molecular systems in a consistent manner. As both continuum and molecular system exist together in a coupling simulation, a one-to-one correspondence is required between points in both domains. By using the CV form, the requirement of an exact description at a point is relaxed so that only the changes and fluxes over a CV are required. The advantage of writing both descriptions in terms of an averaged CV is that they can be directly related. Continuum CFD is often solved using the finite volume (FV) method so this is naturally amenable to connecting the different regions in this form.

A key advantage of the CV formulation is a re-interpretation of the descriptions of stress. In this form, the volume average (VA (Lutsko, 1988; Cormier *et al.*, 2001)) and method of planes (MOP (Todd *et al.*, 1995)) forms of stress are seen as simply the result of different assumption in the derivation of the CV formulation. The MOP description is also localised and generalised to three dimensions. The stress tensor is known to be non-unique (Schofield & Henderson, 1982), however, a direct and exact link is given between the CV surface stresses (MOP over six surface of a CV) and the change of momentum inside the CV. The surface stresses are formally the starting point for the Cauchy definition of stress, and by taking the limit as the volume tends to zero, it was demonstrated that the Irving & Kirkwood (1950) expression is formally equivalent to the Cauchy stress. Therefore, it is shown that any practical implementation of the MD stress cannot correspond to the Cauchy definition but must always relax the requirement using an averaged volume. The advantage of the CV methodology is the choice of average volume is very explicit in the formulation. The choice of CV can be made entirely consistent with the continuum as part of a coupling scheme. Therefore, the resulting stresses on the coupling interface are also exactly consistent and can be directly linked to the time evolution of the coupled system.

The new mathematical operator defined in chapter 4 is useful as it mathematically localises MD properties to a region in space (CV). The time evolution of this localised description can then be explored mathematically in order to obtain conservation equations for that CV. This leads to equations for mass, momentum and energy that have been demonstrated to be exactly

conservative using MD simulation, with agreement to machine precision. The $\mathcal{LCV}$ operator also has the advantage that mathematical operations can be localised – the starting point for the derivation of localised constraint equations in chapter 5.

6.2.4 Variational Formulation Localised with CV Function

In the final chapter of this work 5, the localisation properties of the CV are employed, together with variational principles, in order to derive physically meaningful equations. The molecular system has 6N degrees of freedom compared to the 4 degrees of freedom in the continuum. The manner in which a constraint is applied to force the MD system to match the continuum is therefore non-unique. The use of constrained dynamics is essential as it provides a system evolution which is as close as possible to the true dynamics, while still satisfying the constraint. The resulting equation from this process is shown to be the most general form of coupling equation. Through simplification, it is shown that the various existing state and flux coupling schemes present in the literature can be recovered (O'Connell & Thompson, 1995; Borg *et al.*, 2010; Nie *et al.*, 2004*a*; Flekkøy *et al.*, 2000; Delgado-Buscalioni & Coveney, 2003*a*). In addition, the general equation has extra advection terms which are shown to be essential to the correct evolution of the system. The constrained algorithm is shown to add no energy to the molecular system as a result of the constraint.

The aim of this work was to develop the methodology for linking a local molecular description to a large region simulated using a continuum description. This included both computational and theoretical developments. The computational development focused on a general purpose, modern and robust computational tools to simulate a wide range of problems. The theoretical emphasis was on the development of a rigorous mathematical framework based on sound physical principles. This framework was then employed in order to derived constrained dynamics algorithms based on fundamental physical principles. The end result is a constraint applied to a local region in space which evolves according to the continuum values. The coupled algorithm is shown to yield extra terms, previously not considered in the coupling literature. These extra terms are shown to be essential in order to give the correct dynamics and ensure the constraint applies no energy to the system. The analysis of this coupled system is possible using the CV formulation. Finally, these theoretical developments are supplemented with the development of a range of computational tools to facilitate coupling. The end result of this computational development is a coupled MD-CFD code which is verified for use on multi-core architecture. The next step is to bring together the general coupling equation with the coupled computer code to simulate coupled problems of interest. This is discussed in the next section on future work.

6.3 Future work

6.3.1 Short Term

Development and Maintenance of Existing Software

The software developed and used during this project is hosted on a subversion server in order to allow collaborative developments. A number of bash and python scripts are periodically employed to compare serial/parallel codes, verify correct and consistent output of statistics and run simple test cases. In addition, the CPL-library includes a dummy test suite used to 'soak

test' all possible inputs. As part of the ongoing collaborative software development of both the the MD solver and the CPL-library, a more formal method of verification and error detection is required. This may employ a FORTRAN based unit test (*e.g.* FORTRAN Unit Test Framework `Fruit`) or possibly the python unit testing framework interfaced with FORTRAN. In addition, this testing process should recreate the range of verification tests detailed in section 3.2.5.

In addition, batch runs, input consistency checks, ensemble averages of many runs and post processing are currently handled using a combination of bash, python and MATLAB scripting. The development of a single python framework is currently underway owing to its flexibility and open-source licence.

Port the CPL library to link OpenFoam to LAMMPS

The coupling framework developed as part of this project is available as open source code (Smith & Trevelyan, 2013). This includes extensive documentation but no example applications with established open source or commercial software. As part of the development of the coupling code, the CPL library will be used to link LAMMPS and OpenFoam. This requires writing interfaces to allow the code to work with C++. This interoperability is provided by the latest FORTRAN standard so should be relatively straight forward to implement.

Explore the Energy Conservation of the Weakened Form of Equations

The energy conservation presented in section 5.4 is only for the total flux on a CV. By careful construction of the weakened form using principles from the FEA literature it should be possible to demonstrate energy conservation of the weakened flux based coupling. This should then provide a link to fluctuation added in later work by Flekkøy *et al.* (2005).

Exactly Conservative Coupling

The Finite Volume method used in the continuum is, by construction, exactly conservative for every volume. A number of smaller volumes can be combined and the large volume is also conservative. The CV formulation for the MD system also allows the same conservation to be checked in the MD system. Therefore, by defining a CV surrounding the coupling interface, the conservation of the coupling scheme can be evaluated, see Figure 6.1.

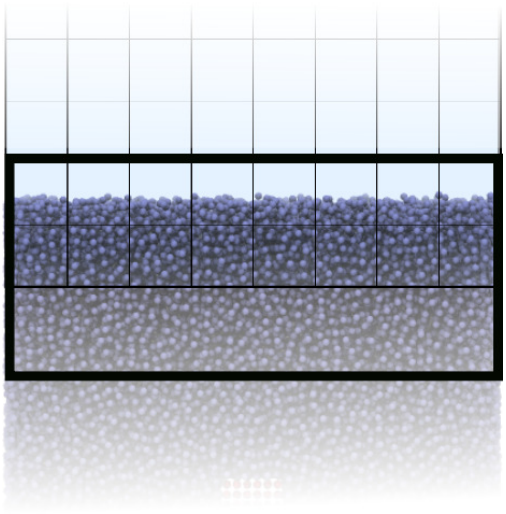

Figure 6.1: Schematic showing CV (thick line) which could be used to verify coupling is exactly conservative.

This will provide a rigorous platform in order to evaluate the various existing coupling schemes and explore the performance of the one proposed in this work. More importantly, the combined effect of the averaged MD properties applied as a boundary condition to the CFD code, together with the applied constraint can be evaluated. The effect of flux-flux or velocity-flux can be examined and a coupling scheme derived which *exactly* ensures the mass, momentum and energy flux of the coupling between the domains.

Implement the General Coupled Equations

Having developed a conservative coupling, the implementation of the general coupling equation to a problem of interest is the next step in the development of the coupling schemes. This involves accounting for all flux and pressure terms in the coupled region for a problem where the inclusion of these terms is essential. This model can then be applied to the simulation of a microscale problem of engineering interest.

6.3.2 Longer Term

Development and Maintenance of Existing Software

The long term aims of the development is to combine unit testing, batch runs, pre-processing and post-processing into a single python based framework. The entire process of running a coupled simulation can therefore be initiated by a single command. This would provide the possibility for a GUI, where inputs are chosen and evolving graphical results are displayed to allow the user to ensure the simulation is progressing correctly.

The implementation of GPGPU acceleration using the latest CUDA libraries will also be reviewed, together with OpenCL which allows implementation of other GPUs than NVIDIA. Since the previous attempt to employ CUDA, hardware and software have greatly improved (especially double precision support). In addition, OpenCL has been applied to MD problems

with superior results in some cases (Mulla *et al.*, 2013). In addition, the recent introduction of compiler directives may prove a simple way to obtain speed-up. However, it is possible that transfer of data will still be a bottle-neck, as discussed in section 3.2.4. Therefore, it is more likely that speed-up will be obtained by delegating an internal subsection of the domain to a bank of GPUs. The current MD code can therefore simulate the boundaries with complicated tethering, coupling forces and thermostatting routines, while a simple and optimised GPU code solves a large number of the internal molecules entirely on the GPU. In this way, data exchange will be limited to the connecting boundaries between the CUDA MD block and the rest of the simulation. This has the advantage that the CPL-library can, in principle, be employed to facilitate this exchange of data between the CUDA MD block and the MD solution of the remaining domain.

Add Mass Conservation in a Rigorous Manner

Mass conservation and insertion of molecules has not been explored in this work. The insertion of mass can be included in the variational principles using a constraint of the form,

$$\boldsymbol{g}(\boldsymbol{q},t) = \sum_{n=1}^{N} m_n \vartheta_n - \int_V \rho dV = 0. \tag{6.1}$$

This would provide a rigorous mechanism for the insertion of molecules that satisfies the correct dynamics and should add no energy to the system.

Simulation of turbulent flow using Couette flow minimal channel

Based on the work of Jimenez & Moin (1991), the minimum channel size required to support turbulent flow is expected to be $(6000\pi \times 12000 \times 1800\pi)$ MD units with $64 \times 256 \times 32$ cells in x, y and z respectively. This is based on the scaling from $Re = 3,000$ using the CFD length scale to $Re = 0.5$ using MD length scales. This results in a cellsize of $\Delta x = 295$ and $\Delta z = 177$. For a coupling scheme where the MD domain occupies the near wall region with a height of ~ 20 MD units, each cell requires around 1 million molecules at a density of $\rho = 0.8$. This domain could be computed on a single processor and the MD domain could be simulated on 2048 processes in order to explore the near wall effect of turbulence on an MD system. Although reasonably large, this scale of simulation is easily possible with modern HPC facilities. Alternatively, a subset of the near wall region in x and z could be solved using MD and the remainder using CFD.

Explore Surface Roughness, Textures and Polymer Coating.

Building on the coupled simulation of the minimal channel, the effect of using different wall textures on the overall flow could be explored. The use of real molecularly rough wall could be used to gain insight into the no-slip assumption. The effect of nano-posts and wall textures could also be explored. Inclusion of polymers and other complex fluids near the wall could be used to explore the effect of surface coating on drag reduction. More complicated solid structures such as graphene could also be employed to investigate the reduction in slip length and low drag properties.

6.4 Concluding Remarks

Coupling is an extremely complicated problem and the work presented here represents a contribution towards greater rigour and understanding. It is hoped that the computational, theoretical and algorithmic tools developed herein may be of use to the future development and ongoing research in this field. There remain many challenges in the field of continuum to molecular coupling, however as computing power grows and engineering moves to smaller and smaller scales, it is anticipated that the rewards of the research will continue to grow too.

Appendix A

Analytical solution for unsteady couette flow

The Navier-Stokes equation is simplified to,

$$\cancel{\frac{\partial \boldsymbol{u}}{\partial t}} + (\boldsymbol{u}\cdot\boldsymbol{\nabla})\cancel{\boldsymbol{u}} = -\boldsymbol{\nabla}\cancel{P} + \frac{1}{Re}\left[\cancel{\frac{\partial u}{\partial x}} + \frac{\partial u}{\partial y} + \cancel{\frac{\partial u}{\partial z}}\right]. \tag{A.1}$$

The aim is to find the analytical solution of the diffusion equation in dimensionless form,

$$\frac{\partial u}{\partial t} = \frac{1}{Re}\frac{\partial^2 u}{\partial y^2}, \tag{A.2}$$

with boundary conditions in domain $0 < y < H$ and $t > 0$,

$$u(y=0,t) = 0 \tag{A.3a}$$
$$u(y=H,t) = u_0 \tag{A.3b}$$
$$u(y,t=0) = 0. \tag{A.3c}$$

Try the following solution based on a Fourier series for non-Homogeneous boundary conditions in Strauss (1992),

$$u(y,t) = \sum_{n=1}^{N} u_n(t) sin\frac{n\pi y}{H}, \tag{A.4}$$

where $u_n(t)$ for the boundary conditions $u(0,t) = h(t)$, $u(H,t) = j(t)$,

$$u_n(t) = Ce^{-\lambda_n kt} - 2n\pi H^{-2}k\int_0^H e^{-\lambda_n k(t-s)}\left[(-1)^n j(s) - h(s)\right] ds. \tag{A.5}$$

Note that the definition $k = 1/Re$ is used for simplicity and C is a constant of integration to be evaluated by choice of initial condition. Now, for the impulse started plate case, we set the boundary conditions as follows $h(t) = U_0$ and $j(t) = 0$, which results in

$$u_n(t) = Ce^{-\lambda_n kt} - 2n\pi H^{-2}k\int_0^t U_0 e^{-\lambda_n k(t-s)} ds, \tag{A.6}$$

This can be integrated exactly to give,

$$\int_0^H e^{-\lambda_n k(t-s)} ds = \left[\frac{e^{-\lambda_n k(t-s)}}{\lambda_n k} \right]_0^t . \tag{A.7}$$

Applying limits in Eq. (A.7) gives,

$$\left[\frac{e^{-\lambda_n k(t-s)}}{\lambda_n k} \right]_0^t = \frac{e^{-\lambda_n k(t-t)}}{\lambda_n k} - \frac{e^{-\lambda_n k(t-0)}}{\lambda_n k} = \frac{1}{\lambda_n k} \left[1 - e^{-\lambda_n kt} \right], \tag{A.8}$$

the quantity u_n can be simplified using $\lambda_n = (n\pi/l)^2$ to,

$$u_n(t) = Ce^{-\lambda_n kt} - \frac{2U_0}{n\pi} \left[1 - e^{-\lambda_n kt} \right]. \tag{A.9}$$

Evaluating C using $u_n(0) = 0$ gives the final form of the solution to the equation for unsteady diffusive flow,

$$u(y,t) = \sum_{n=1}^{N} -\frac{2U_0}{n\pi} \left(1 - e^{-\lambda_n kt} \right) sin \frac{n\pi y}{H}. \tag{A.10}$$

Notice that the solution in Eq. (A.10) does not accurately reproduce the wall velocity U_0 as $sin(H/H) = 0$. An extra functional is introduced to give the expected form of the analytical solution,

$$u(y,t) = \sum_{n=1}^{N} -\frac{2U_0}{n\pi} \left(1 - e^{-\lambda_n kt} \right) sin \frac{n\pi y}{H} + U_0 \varphi \left(\frac{y}{H} \right). \tag{A.11}$$

Here $\varphi(x)$ is defined as

$$\varphi(x) \equiv \begin{cases} 1 & \text{if } x = 0 \\ 0 & \text{else} \end{cases}$$

.

The continuum analytical xy pressure tensor component can be derived analytically using the same Fourier series approach for $\partial u_x/\partial y$,(Strauss, 1992),

$$\Pi_{xy}(y,t) = -\frac{\mu U_0}{L} \left[1 + 2 \sum_{n=1}^{\infty} (-1)^n e^{-\frac{\lambda_n \mu t}{\rho}} cos \left(\frac{n\pi y}{H} \right) \right], \tag{A.12}$$

which is valid for the entire domain $0 \leq y \leq H$.

Appendix B

Constrained Dynamics

B.1 From O'Connell & Thompson (1995) Coupling to Nie *et al.* (2004*a*)

The following section combines the constraint equations of O'Connell & Thompson (1995) 2.72a and 2.72b to give the equation of Nie *et al.* (2004*a*). Starting from Eqs. (2.72a) and (2.72b), repeated here for convenience,

$$\dot{r}_{\alpha i} = \frac{p_{\alpha i}}{m} + \xi \left[\frac{M_I}{mN_I} u_{\alpha I} - \frac{1}{N_I} \sum_{n=1}^{N_I} \frac{p_{\alpha n}}{m} \right] \tag{B.1a}$$

$$\dot{p}_{\alpha i} = -\frac{\partial \phi}{\partial \boldsymbol{r_{\alpha i}}} = F_{\alpha i}. \tag{B.1b}$$

Differentiating B.1b with respect to time and combining with the equation B.1b,

$$\ddot{q}_i = \frac{\dot{p}_i}{m} + \xi \frac{d}{dt} \left[\frac{1}{N_I} \left(\frac{M_I U_I}{m} - \sum_{i=1}^{N_I} \frac{p_i}{m} \right) \right], \tag{B.2}$$

expanding out the derivative,

$$\ddot{x}_i = \frac{\dot{p}_i}{m} + \frac{dN_I}{dt} \frac{\xi}{N_I^2} \left[\frac{M_I U_I}{m} - \sum_{i=1}^{N_I} \frac{p_i}{m} \right] + \frac{\xi}{mN_I} \left[\left(\frac{dM_I}{dt} U_I + M_I \frac{dU_I}{dt} \right) - \sum_{i=1}^{N_I} \dot{p}_i \right]. \tag{B.3}$$

Assuming the number of molecular in the cell is constant, dN_I/dt and the mass of the continuum is constant dM_I/dt (incompressibility),

$$\ddot{x}_i = \frac{\dot{p}_i}{m} + \frac{\xi}{mN_I} \left[M_I \frac{dU_I}{dt} - \sum_{n=1}^{N_I} F_n \right], \tag{B.4}$$

where equation B.1b has been used. As the two regions overlap in a region where both descriptions apply, the molecular mass is assumed to be equal to the sum of all the molecules' individual masses so that $M_I = mN_I$,

$$\ddot{x}_i = \frac{F_i}{m} + \left[\frac{dU_I}{dt} - \frac{1}{N_I} \sum_{n=1}^{N_I} \frac{F_n}{m} \right], \tag{B.5}$$

where for $\xi = 1$ the equations of Nie *et al.* (2004*a*) are recovered.

B.2 Nie *et al.* (2004*a*) Constraint Equations from Gauss' Principle

Using Gauss' principle of least constraint which can incorporate non-holonomic constraints for a constrain equation of the form,

$$g(x, \dot{x}, t) = \frac{1}{N_I} \sum_{i=1}^{N_I} \dot{x_i} - U_I = 0, \tag{B.6}$$

Nie *et al.* (2004*a*) take the 'Lagrangian derivative' D/Dt.

$$\dot{g}(x, \dot{x}, t) = \frac{1}{N_I} \sum_{i=1}^{N_I} \ddot{x_i} - \frac{DU_I}{Dt} = 0. \tag{B.7}$$

In this form (accelerations) the constraint Eq. (B.6) can be introduced into Eq. (2.28).

$$\frac{\partial}{\partial \ddot{r_j}} \left[\frac{1}{2} \sum_{i=1}^{N} m_i \left(\ddot{r_i} - \frac{F_i}{m_i} \right)^2 - \lambda \left(\frac{1}{N_I} \sum_{i=1}^{N_I} \ddot{x_i} - \frac{DU_I}{Dt} \right) \right]. \tag{B.8}$$

Multiplying out the brackets and differentiating the equation gives the constrained equation of motion.

$$\ddot{x_j} = \frac{F_{xj}}{m} + \frac{\lambda}{mN_I}. \tag{B.9}$$

Note that $\partial \ddot{x_i}/\partial \ddot{x_j} = 0$ as all degrees of freedom of the system are independent. This results in the equation of a particle j with all other terms of the sums being zero. This equation B.9 is solved with B.7 to obtain the value of λ.

$$\lambda = mN_I \frac{DU_I}{Dt} - \sum_{i=1}^{N_I} F_{xi}. \tag{B.10}$$

So the equation of motion for the constrained system obtained using Gauss' least constrain is the form stated by Nie *et al.* (2004*a*)

$$\ddot{x} = \frac{F_{xi}}{m} + \left[\frac{DU_I}{Dt} - \frac{1}{mN_I} \sum_{i=1}^{N_I} F_{xi} \right]. \tag{B.11}$$

B.3 Derivation of the Control Volume Constraint Equations from Gauss' Principle

The control volume form of non-holonomic constraint Eq. 5.2 is,

$$\boldsymbol{g}(\boldsymbol{r}, \dot{\boldsymbol{r}}, t) = \sum_{n=1}^{N} m_n \dot{\boldsymbol{r}}_n \vartheta_n - \int_V \rho \boldsymbol{u} dV = 0. \tag{B.12}$$

differentiating with respect to time,

$$\dot{\boldsymbol{g}}(\boldsymbol{r}_i, \dot{\boldsymbol{r}}_i) = -\sum_{n=1}^{N} m_n \dot{\boldsymbol{r}}_n \dot{\boldsymbol{r}}_n \cdot d\mathbf{S}_n + \sum_{n=1}^{N} m_n \ddot{\boldsymbol{r}}_n \vartheta_n - \frac{d}{dt}\int_V \rho \boldsymbol{u} dV = 0, \tag{B.13}$$

which is introduced into Gauss' principle of least constraint,

$$\frac{\partial}{\partial \ddot{\boldsymbol{r}}_i}\left[\frac{1}{2}\sum_{n=1}^{N} m_n \left(\ddot{\boldsymbol{r}}_n - \frac{\boldsymbol{F}_n}{m_n}\right)^2 + \boldsymbol{\lambda}\cdot\left(\sum_{n=1}^{N} m_n \dot{\boldsymbol{r}}_n \dot{\boldsymbol{r}}_n \cdot d\mathbf{S}_n - \sum_{n=1}^{N} m_n \ddot{\boldsymbol{r}}_n \vartheta_n + \frac{d}{dt}\int_V \rho \boldsymbol{u} dV\right)\right] \tag{B.14}$$

Multiplying out the brackets and differentiating the equation gives the constrained equation of motion.

$$m_i \ddot{\boldsymbol{r}}_i = \boldsymbol{F}_i - \boldsymbol{\lambda} m_i \vartheta_i \tag{B.15}$$

Note that $\partial \ddot{\boldsymbol{r}}_n / \partial \ddot{\boldsymbol{r}}_i = 0$ as all degrees of freedom of the system are independent. This equation B.15 is substituted into Eq. B.13 to obtain the value of $\boldsymbol{\lambda}$,

$$\boldsymbol{\lambda} = \frac{1}{M_I}\left[-\sum_{n=1}^{N} m_n \dot{\boldsymbol{r}}_n \dot{\boldsymbol{r}}_n \cdot d\mathbf{S}_n + \sum_{i=1}^{N} \boldsymbol{F}_n \vartheta_i - \frac{d}{dt}\int_V \rho \boldsymbol{u} dV\right] \tag{B.16}$$

So the CV equation of motion for the constrained system obtained using Gauss' least constrain is,

$$\ddot{\boldsymbol{r}}_i = \frac{\boldsymbol{F}_i}{m_i} - \frac{\vartheta_i}{M_I}\left[\sum_{n=1}^{N} \boldsymbol{F}_n \vartheta_n - \sum_{n=1}^{N} m_n \dot{\boldsymbol{r}}_n \dot{\boldsymbol{r}}_n \cdot d\mathbf{S}_n + \frac{d}{dt}\int_V \rho \boldsymbol{u} dV\right] \tag{B.17}$$

Appendix C

The Control Volume Operator

C.1 Discrete form of Reynolds' Transport Theorem and the Divergence Theorem

In this Appendix, both Reynolds' Transport Theorem and the Divergence Theorem for a discrete system are derived. The relationship between an advecting and fixed control volume is shown using the concept of peculiar momentum.

The microscopic form of the continuous Reynolds' Transport Theorem (Reynolds, 1903) is derived for a property $\boldsymbol{\chi} = \boldsymbol{\chi}(\boldsymbol{r}_i, \boldsymbol{p}_i, t)$ which could be mass, momentum or the pressure tensor. The $\mathcal{LCV}$ function, ϑ_i, is dependent on the molecule's coordinate; the location of the cube centre, $\boldsymbol{r}$, and side length, $\Delta\boldsymbol{r}$, which are all a function of time. The time evolution of the CV is therefore,

$$\frac{d}{dt}\sum_{i=1}^{N}\boldsymbol{\chi}(t)\vartheta_i(\boldsymbol{r}_i(t),\boldsymbol{r}(t),\Delta\boldsymbol{r}(t)) = \sum_{i=1}^{N}\left[\frac{d\boldsymbol{\chi}}{dt}\vartheta_i + \boldsymbol{\chi}\frac{d\boldsymbol{r}_i}{dt}\cdot\frac{\partial\vartheta_i}{\partial\boldsymbol{r}_i} \qquad + \boldsymbol{\chi}\frac{d\boldsymbol{r}}{dt}\cdot\frac{\partial\vartheta_i}{\partial\boldsymbol{r}} + \boldsymbol{\chi}\frac{d\Delta\boldsymbol{r}}{dt}\cdot\frac{\partial\vartheta_i}{\partial\Delta\boldsymbol{r}}\right].$$

The velocity of the moving volume is defined as $\tilde{\boldsymbol{u}} = d\boldsymbol{r}/dt$, which can be different to the macroscopic velocity $\boldsymbol{u}$. Surface translation or deformation of the cube, $\partial\vartheta_i/\partial\Delta\boldsymbol{r}$, can be included in the expression for velocity $\tilde{\boldsymbol{u}}$. The above analysis is for a microscopic system, although a similar process for a mesoscopic system can be applied and includes terms for CV movement in Eq. (2.33).

Hence Reynolds treatment of a continuous medium (Reynolds, 1903) is extended here to a discrete molecular system,

$$\frac{d}{dt}\sum_{i=1}^{N}\boldsymbol{\chi}(t)\vartheta_i(\boldsymbol{r}_i(t),\boldsymbol{r}(t),\Delta\boldsymbol{r}(t)) = \sum_{i=1}^{N}\left[\frac{d\boldsymbol{\chi}}{dt}\vartheta_i + \boldsymbol{\chi}\left(\tilde{\boldsymbol{u}} - \frac{\boldsymbol{p}_i}{m_i}\right)\cdot d\mathbf{S}_i\right]. \tag{C.1}$$

The conservation equation for the mass, $\boldsymbol{\chi} = m_i$, in a moving reference frame is,

$$\frac{d}{dt}\sum_{i=1}^{N}m_i\vartheta_i = \sum_{i=1}^{N}\left[m_i\left(\tilde{\boldsymbol{u}} - \frac{\boldsymbol{p}_i}{m_i}\right)\cdot d\mathbf{S}_i\right]. \tag{C.2}$$

In a Lagrangian reference frame, the translational velocity of CV surface must be equal to the

molecular streaming velocity, *i.e.*, $\tilde{\boldsymbol{u}}(\boldsymbol{r}^{\pm}) = \boldsymbol{u}(\boldsymbol{r}_i)$, so that,

$$\sum_{i=1}^{N}\left[m_i\left(\boldsymbol{u}-\frac{\boldsymbol{p}_i}{m_i}\right)\cdot d\mathbf{S}_i\right] = -\sum_{i=1}^{N}\overline{\boldsymbol{p}}_i\cdot d\mathbf{S}_i.$$

The evolution of the peculiar momentum, $\boldsymbol{\chi}=\overline{\boldsymbol{p}}_i$, in a moving reference frame is,

$$\frac{d}{dt}\sum_{i=1}^{N}\overline{\boldsymbol{p}}_i\vartheta_i = \sum_{i=1}^{N}\left[\boldsymbol{F}_i\vartheta_i+\overline{\boldsymbol{p}}_i\left(\boldsymbol{u}-\frac{\boldsymbol{p}_i}{m_i}\right)\cdot d\mathbf{S}_i\right] = \sum_{i=1}^{N}\left[\boldsymbol{F}_i\vartheta_i-\frac{\overline{\boldsymbol{p}}_i\overline{\boldsymbol{p}}_i}{m_i}\cdot d\mathbf{S}_i\right].$$

Here an inertial reference frame has been assumed so that $d\overline{\boldsymbol{p}}_i/dt = d\boldsymbol{p}_i/dt = \boldsymbol{F}_i$. For a simple case (e.g. one dimensional flow) it is possible to utilise a Lagrangian description by ensuring, $\tilde{\boldsymbol{u}}(\boldsymbol{r}^{\pm}) = \boldsymbol{u}(\boldsymbol{r}_i)$, throughout the time evolution. In more complicated cases, this is not always possible and the Eulerian description is generally adopted.

Next, a microscopic analogue to the macroscopic divergence theorem is derived for the generalised function, $\boldsymbol{\chi}$,

$$\int_V\sum_{i=1}^{N}\frac{\partial}{\partial\boldsymbol{r}}\cdot\Big[\boldsymbol{\chi}(\boldsymbol{r}_i,\boldsymbol{p}_i,t)\delta(\boldsymbol{r}_i-\boldsymbol{r})\Big]dV = \int_V\sum_{i=1}^{N}\boldsymbol{\chi}(\boldsymbol{r}_i,\boldsymbol{p}_i,t)\cdot\frac{\partial}{\partial\boldsymbol{r}}\delta(\boldsymbol{r}_i-\boldsymbol{r})dV.$$

The vector derivative of the Dirac δ followed by the integral over volume results in,

$$\begin{aligned}\int_V\frac{\partial}{\partial\boldsymbol{r}}\delta(x_i-x)\delta(y_i-y)\delta(z_i-z)dV &= \begin{pmatrix}[\delta(x_i-x)H(y_i-y)H(z_i-z)]_V\\ [H(x_i-x)\delta(y_i-y)H(z_i-z)]_V\\ [H(x_i-x)H(y_i-y)\delta(z_i-z)]_V\end{pmatrix}\\ &= \begin{pmatrix}[\delta(x_i-x^+)-\delta(x_i-x^-)]\,S_{xi}\\ [\delta(y_i-y^+)-\delta(y_i-y^-)]\,S_{yi}\\ [\delta(z_i-z^+)-\delta(z_i-z^-)]\,S_{zi}\end{pmatrix} = d\mathbf{S}_i,\end{aligned}$$

where the limits of the cuboidal volume are, $\boldsymbol{r}^+ = \boldsymbol{r}+\frac{\Delta\boldsymbol{r}}{2}$ and $\boldsymbol{r}^- = \boldsymbol{r}-\frac{\Delta\boldsymbol{r}}{2}$. The mesoscopic equivalent of the continuum divergence theorem (Eq. (2.39)) is therefore,

$$\int_V\frac{\partial}{\partial\boldsymbol{r}}\cdot\sum_{i=1}^{N}\boldsymbol{\chi}\delta(\boldsymbol{r}_i-\boldsymbol{r})dV = \sum_{i=1}^{N}\boldsymbol{\chi}\cdot d\mathbf{S}_i.$$

C.2 Relation between Control Volume and Description at a Point

This Appendix proves that the Irving & Kirkwood (1950) expression for the flux at a point is the zero volume limit of the CV formulation. As in the continuum, the control volume equations at a point are obtained using the gradient operator in Eq. (2.40). the flux at a point can be shown by taking the zero volume limit of the gradient operator of Eq. (2.40). Assuming the three side lengths of the control volume, $\Delta x, \Delta y$ and Δz, tend to zero and hence the volume, ΔV, tends to

zero,

$$\boldsymbol{\nabla}\cdot\rho\boldsymbol{u} = \lim_{\Delta x\to 0}\lim_{\Delta y\to 0}\lim_{\Delta z\to 0}\frac{1}{\Delta x\Delta y\Delta z}\times\sum_{i=1}^{N}\left\langle p_{ix}\frac{\partial\vartheta_i}{\partial x}+p_{iy}\frac{\partial\vartheta_i}{\partial y}+p_{iz}\frac{\partial\vartheta_i}{\partial z};f\right\rangle. \tag{C.3}$$

from Eq. (4.9). For illustration, consider the x component above, where

$$\frac{\partial\vartheta_i}{\partial x} = \overbrace{\left[\delta(x^+-x_i)-\delta(x^--x_i)\right]}^{x_{face}}S_{xi}. \tag{C.4}$$

Using the definition of the Dirac δ function as the limit of two slightly displaced Heaviside functions,

$$\delta(\xi) = \lim_{\Delta\xi\to 0}\frac{H\left(\xi+\frac{\Delta\xi}{2}\right)-H\left(\xi-\frac{\Delta\xi}{2}\right)}{\Delta\xi},$$

the limit of the S_{xi} term is,

$$\lim_{\Delta y\to 0}\lim_{\Delta z\to 0}S_{xi} = \delta(y_i-y)\delta(z_i-z)$$

The $\Delta x\to 0$ limit for x_{face} (defined in Eq. (C.4)) can be evaluated using L'Hôpital's rule, combined with the property of the δ function,

$$\frac{\partial}{\partial(\Delta\xi)}\delta\left(\xi-\frac{\Delta\xi}{2}\right) = -\frac{1}{2}\frac{\partial}{\partial\xi}\delta\left(\xi-\frac{\Delta\xi}{2}\right),$$

so that,

$$\lim_{\Delta x\to 0}x_{face} = \frac{\partial}{\partial x}\delta\left(x-x_i\right).$$

Therefore, the limit of $\partial\vartheta_i/\partial x$ as the volume approaches zero is,

$$\lim_{\Delta x\to 0}\lim_{\Delta y\to 0}\lim_{\Delta z\to 0}\frac{\partial\vartheta_i}{\partial x} = \frac{\partial}{\partial x}\delta\left(\boldsymbol{r}_i-\boldsymbol{r}\right),$$

Taking the limits for the x, y and z terms in Eq. (C.3) yields the expected Irving & Kirkwood (1950) definition of the divergence at a point,

$$\boldsymbol{\nabla}\cdot\rho\boldsymbol{u} = \sum_{i=1}^{N}\left\langle\frac{\partial}{\partial\boldsymbol{r}}\cdot\boldsymbol{p}_i\delta(\boldsymbol{r_i}-\boldsymbol{r});f\right\rangle.$$

This zero volume limit of the CV surface fluxes shows that the divergence of a Dirac δ function represents the flow of molecules over a point in space. The advection and kinetic pressure at a point is, from Eq. (4.13),

$$\boldsymbol{\nabla}\cdot[\rho\boldsymbol{u}\boldsymbol{u}+\boldsymbol{\kappa}] = \sum_{i=1}^{N}\left\langle\frac{\partial}{\partial\boldsymbol{r}}\cdot\frac{\boldsymbol{p}_i\boldsymbol{p}_i}{m_i}\delta(\boldsymbol{r_i}-\boldsymbol{r});f\right\rangle.$$

The same limit of zero volume for the surface tractions defines the Cauchy stress. Using Eq. (2.40) and taking the limit of Eq. (4.35), written in terms of tractions,

$$\boldsymbol{\nabla}\cdot\boldsymbol{\sigma}=\lim_{\Delta V\to 0}\frac{1}{\Delta V}\sum_{faces}^{6}\int_{S_f}\boldsymbol{\sigma}\cdot d\mathbf{S}_f=\lim_{\Delta r_x\to 0}\lim_{\Delta r_y\to 0}\lim_{\Delta r_z\to 0}\times\left[\frac{\mathbf{T}_x^+-\mathbf{T}_x^-}{\Delta r_x}+\frac{\mathbf{T}_y^+-\mathbf{T}_y^-}{\Delta r_y}+\frac{\mathbf{T}_z^+-\mathbf{T}_z^-}{\Delta r_z}\right].$$

For the r_x^+ surface, and taking the limits of Δr_y and Δr_z using L'Hôpital's rule,

$$\lim_{\Delta V\to 0}\frac{\mathbf{T}_x^+}{\Delta r_x}=-\lim_{\Delta r_x\to 0}\frac{1}{2\Delta r_x}\sum_{i,j}^{N}\left\langle f_{\alpha ij}\varpi_{xyz}^+;f\right\rangle.$$

where ϖ is

$$\begin{aligned}\varpi_{\beta\kappa\gamma}^{\dagger}\equiv&\left[H(r_\beta^\dagger-r_{\beta j})-H(r_\beta^\dagger-r_{\beta i})\right]\\&\times\delta\left(r_\kappa-r_{\kappa i}-\frac{r_{\kappa ij}}{r_{\beta ij}}\left(r_\beta^\dagger-r_{\beta i}\right)\right)\\&\times\delta\left(r_\gamma-r_{\gamma i}-\frac{r_{\gamma ij}}{r_{\beta ij}}\left(r_\beta^\dagger-r_{\beta i}\right)\right).\end{aligned}\tag{C.5}$$

The indices β,κ and γ can be x,y or z and $\dagger$ denotes the top surface (+ superscript), bottom surface (− superscript) or CV centre (no superscript). The ϖ selecting function includes only the contribution to the stress when the line of interaction between i and j passes through the point $\boldsymbol{r}^\dagger$ in space. The difference between $\mathbf{T}_x^+$ and $\mathbf{T}_x^-$ tends to zero on taking the limit $\Delta r_x\to 0$, so that L'Hôpital's rule can be applied. Using the property,

$$\frac{\partial}{\partial(\Delta\xi)}\delta\left(\xi-\frac{1}{2}\Delta\xi\right)H\left(\xi-\frac{1}{2}\Delta\xi\right)=-\frac{1}{2}\frac{\partial}{\partial\xi}\delta\left(\xi-\frac{1}{2}\Delta\xi\right)H\left(\xi-\frac{1}{2}\Delta\xi\right),$$

then,

$$\lim_{\Delta V\to 0}\frac{\mathbf{T}_x^+-\mathbf{T}_x^-}{\Delta r_x}=-\frac{1}{2}\sum_{i,j}^{N}\left\langle f_{\alpha ij}\frac{\partial\varpi_{xyz}}{\partial r_x};f\right\rangle.$$

where $r^+\to r$ and $r^-\to r$. The $\varpi_{\beta\kappa\gamma}$ function is the integral between two molecules introduced in Eq. (4.25),

$$\begin{aligned}\int_0^1\delta(\boldsymbol{r}-\boldsymbol{r}_i+s\boldsymbol{r}_{ij})ds=&\,sgn\left(\frac{1}{r_{xij}}\right)\frac{1}{|r_{xij}|}\\&\times\left[H(r_x-r_{xj})-H(r_x-r_{xi})\right]\\&\times\delta\left(r_y-r_{yi}-\frac{r_{yij}}{r_{xij}}\left(r_x-r_{xi}\right)\right)\\&\times\delta\left(r_z-r_{zi}-\frac{r_{zij}}{r_{xij}}\left(r_x-r_{xi}\right)\right).\end{aligned}$$

where the sifting property of the Dirac δ function in the r_x direction has been used to express the integral between two molecules in terms of the ϖ_{xyz} function. Hence,

$$\int_0^1 \delta(\boldsymbol{r} - \boldsymbol{r}_i + s\boldsymbol{r}_{ij})ds = \frac{\varpi_{xyz}}{r_{xij}}.$$

As the choice of shifting direction is arbitrary, use of r_y or r_z in the above treatment would result in ϖ_{yzx} and ϖ_{zxy}, respectively. Therefore, Eq. (4.27), without the volume integral, can be expressed as,

$$\frac{1}{2}\sum_{i,j}^{N}\left\langle f_{\alpha ij} r_{\beta ij}\frac{\partial}{\partial r_\beta}\int_0^1 \delta(\boldsymbol{r} - \boldsymbol{r}_i + s\boldsymbol{r}_{ij})ds; f\right\rangle = \frac{1}{2}\sum_{i,j}^{N}\left\langle f_{ij\alpha}\left[\frac{\partial \varpi_{xyz}}{\partial r_x} + \frac{\partial \varpi_{yxz}}{\partial r_y} + \frac{\partial \varpi_{zxy}}{\partial r_z}\right]; f\right\rangle.$$

As Eq. (4.27) is equivalent to the Irving & Kirkwood (1950) stress of Eq. (4.24), the Irving Kirkwood stress is recovered in the limit that the CV tends to zero volume.
This Appendix has proved therefore that in the limit of zero control volume, the molecular CV Eqs. (4.10) and (4.38) recover the description at a point in the same limit that the continuum CV Eqs. (2.35) and (2.36) tend to the differential continuum equations. This demonstrates that the molecular CV equations presented here are the molecular scale equivalent of the continuum CV equations.

C.3 Relationship Between Volume Average and Method Of Planes Stress

This Appendix gives further details of the derivation of the Method Of Planes form of stress from the Volume Average form. Starting from Eq. (4.27) written in terms of the CV function for an integrated volume,

$$-\sum_{faces}^{6}\int_{S_f}\boldsymbol{\sigma}\cdot d\mathbf{S}_f = \frac{1}{2}\sum_{i,j}^{N}\left\langle \boldsymbol{f}_{ij}\boldsymbol{r}_{ij}\cdot\int_0^1\frac{\partial \vartheta_s}{\partial \boldsymbol{r}}ds; f\right\rangle = \frac{1}{2}\sum_{i,j}^{N}\left\langle \boldsymbol{f}_{ij}\int_0^1\left[x_{ij}\frac{\partial \vartheta_s}{\partial x} + y_{ij}\frac{\partial \vartheta_s}{\partial y} + z_{ij}\frac{\partial \vartheta_s}{\partial z}\right]ds; f\right\rangle. \tag{C.6}$$

Taking only the x derivative above,

$$x_{ij}\frac{\partial \vartheta_s}{\partial x} = x_{ij}\big[\overbrace{\delta(x^+ - x_i + sx_{ij})}^{x^+_{face}} \qquad -\delta(x^- - x_i + sx_{ij})\big]G(s) \tag{C.7}$$

where $G(s)$ is,

$$G(s) \equiv \big[H(y^+ - y_i + sy_{ij}) - H(y^- - y_i + sy_{ij})\big] \times \big[H(z^+ - z_i + sz_{ij}) - H(z^- - z_i + sz_{ij})\big].$$

As $\delta(ax) = \frac{1}{|a|}\delta(x)$ the $x_{ij}x^+_{face}G(s)$ term in Eq. (C.7) can be expressed as,

$$x_{ij}x^+_{face}G(s) = \frac{x_{ij}}{|x_{ij}|}\delta\left(\frac{x^+ - x_i}{x_{ij}} + s\right)G(s). \tag{C.8}$$

The integral can be evaluated using the sifting property of the Dirac δ function (Thankoppan, 1985) as follows,

$$\int_0^1 x_{ij}x^+_{face}G(s)ds = \frac{x_{ij}}{|x_{ij}|}\int_0^1 \delta\left(\frac{x^+ - x_i}{x_{ij}} + s\right)G(s)ds = sgn(x_{ij})\left[H\left(\frac{x^+ - x_j}{x_{ij}}\right) - H\left(\frac{x^+ - x_i}{x_{ij}}\right)\right]S^+_{xij}.$$

where the signum function, $sgn(x_{ij}) \equiv x_{ij}/|x_{ij}|$. The S^+_{xij} term is the value of s on the cube surface,
$S^+_{xij} = G\left(s = -\frac{x^+ - x_i}{x_{ij}}\right)$ which is,

$$\begin{aligned} S^+_{xij} \equiv &\left[H\left(y^+ - y_i - \frac{y_{ij}}{x_{ij}}\left(x^+ - x_i\right)\right) - H\left(y^- - y_i - \frac{y_{ij}}{x_{ij}}\left(x^+ - x_i\right)\right)\right] \\ &\times \left[H\left(z^+ - z_i - \frac{z_{ij}}{x_{ij}}\left(x^+ - x_i\right)\right) - H\left(z^- - z_i - \frac{z_{ij}}{x_{ij}}\left(x^+ - x_i\right)\right)\right]. \end{aligned} \tag{C.9}$$

The definition S^+_{xij} (analogous to S_{xi} in Eq. (4.3)) has been introduced as it filters out those ij terms where the point of intersection of line r_{ij} and plane x^+ has y and z components between the limits of the cube surfaces. The corresponding terms, $S^{\pm}_{ij\alpha}$, are defined for $\alpha = \{y, z\}$. Taking $H(0) = \frac{1}{2}$, the Heaviside function can be rewritten as $H(ax) = \frac{1}{2}\left(sgn(a)sgn(x) - 1\right)$, and,

$$H\left(\frac{x^+ - x_j}{x_{ij}}\right) - H\left(\frac{x^+ - x_i}{x_{ij}}\right) = \frac{1}{2}sgn\left(\frac{1}{x_{ij}}\right)\left[sgn(x^+ - x_j) - sgn(x^+ - x_i)\right],$$

so the expression, $x_{ij}x^+_{face}G(s)$ in Eq. (C.7) becomes,

$$x_{ij}\int_0^1 x^+_{face}G(s)ds = \frac{1}{2}sgn(x_{ij})sgn\left(\frac{1}{x_{ij}}\right) \times \left[sgn(x^+ - x_j) - sgn(x^+ - x_i)\right]S^+_{xij}.$$

The signum function, $sgn\left(\frac{1}{x_{ij}}\right)$, cancels the one obtained from integration along s, $sgn(x_{ij})$. The expression for the x^+ face is therefore,

$$-\int_{S^+_x} \boldsymbol{\sigma}\cdot d\mathbf{S}_{S^+_x} = \frac{1}{2}\sum_{i,j}^{N}\left\langle \boldsymbol{f}_{ij}x_{ij}\int_0^1 x^+_{face}G(s)ds; f\right\rangle = \frac{1}{4}\sum_{i,j}^{N}\left\langle \boldsymbol{f}_{ij}\left[sgn(x^+ - x_j) - sgn(x^+ - x_i)\right]S^+_{xij}; f\right\rangle$$

Repeating the same process for the other faces allows Eq. (C.6) to be expressed as,

$$\sum_{faces}^{6}\int_{S_f}\boldsymbol{\sigma}\cdot d\mathbf{S}_f = -\frac{1}{2}\sum_{i,j}^{N}\left\langle \boldsymbol{f}_{ij}\boldsymbol{r}_{ij}\cdot\int_0^1\frac{\partial\vartheta_s}{\partial\boldsymbol{r}}ds; f\right\rangle = -\frac{1}{4}\sum_{i,j}^{N}\left\langle \boldsymbol{f}_{ij}\sum_{\alpha=1}^{3}\tilde{n}_\alpha\left[dS^+_{\alpha ij} - dS^-_{\alpha ij}\right]; f\right\rangle,$$

where $dS^{\pm}_{\alpha ij} \equiv \frac{1}{2}\left[sgn(r^{\pm}_{\alpha} - r_{\alpha j}) - sgn(r^{\pm}_{\alpha} - r_{\alpha i})\right] S^{\pm}_{\alpha ij}$ and $\tilde{n}_{\alpha} \equiv sgn(r_{\alpha ij}) sgn\left(\frac{1}{r_{\alpha ij}}\right) = [1\ \ 1\ \ 1]$. This is the force over the CV surfaces, Eq. (4.35), in section 4.2.3.

To verify the interpretation of S^{+}_{xij} used in this work, consider the vector equation for the point of intersection of a line and a plane in space. The equation for a vector $\boldsymbol{a}$ between $\boldsymbol{r}_i$ and $\boldsymbol{r}_j$ is defined as $\boldsymbol{a} = \boldsymbol{r}_i - s\frac{\boldsymbol{r}_{ij}}{|\boldsymbol{r}_{ij}|}$. The plane containing the positive face of a cube is defined by $(\boldsymbol{r}^{+} - \boldsymbol{p}) \cdot \mathbf{n}$ where $\boldsymbol{p}$ is any point on the plane and $\mathbf{n}$ is normal to that plane. By setting $\boldsymbol{a} = \boldsymbol{p}$ and upon rearrangement of $\left(\boldsymbol{r}^{+} - \boldsymbol{r}_i + s\frac{\boldsymbol{r}_{ij}}{|\boldsymbol{r}_{ij}|}\right) \cdot \mathbf{n}$, the value of s at the point of intersection with the plane is,

$$s = -\frac{(\boldsymbol{r}^{+} - \boldsymbol{r}_i) \cdot \mathbf{n}}{\frac{\boldsymbol{r}_{ij}}{|\boldsymbol{r}_{ij}|} \cdot \mathbf{n}},$$

The point on line $\boldsymbol{a}$ located on the plane is,

$$\boldsymbol{a}^{+}_{p} \equiv \boldsymbol{r}_i + \boldsymbol{r}_{ij}\left[\frac{(\boldsymbol{r}^{+} - \boldsymbol{r}_i) \cdot \mathbf{n}}{\boldsymbol{r}_{ij} \cdot \mathbf{n}}\right].$$

Taking $\mathbf{n}$ as the normal to the x surface, i.e.
$\mathbf{n} \rightarrow \mathbf{n}_x = [1, 0, 0]$, then,

$$x^{+}_{\alpha p} = \begin{pmatrix} x^{+}_{xp} \\ x^{+}_{yp} \\ x^{+}_{zp} \end{pmatrix} = \begin{pmatrix} x^{+} \\ y_i + \frac{y_{ij}}{x_{ij}}(x^{+} - x_i) \\ z_i + \frac{z_{ij}}{x_{ij}}(x^{+} - x_i) \end{pmatrix}$$

written using index notation with $\alpha = \{x, y, z\}$. The vector $\boldsymbol{x}^{+}_{p}$ is the point of intersection of line $\boldsymbol{a}$ with the x^{+} plane. A function to check if the point $\boldsymbol{x}^{+}_{p}$ on the plane is located on the region between $y^{\pm}$ and $z^{\pm}$, would use Heaviside functions and is similar to the form of Eq. (4.3),

$$\begin{aligned} S^{+}_{xij} = &\left[H\left(y^{+} - \boldsymbol{x}^{+}_{yp}\right) - H\left(y^{-} - \boldsymbol{x}^{+}_{yp}\right)\right] \\ &\times \left[H\left(z^{+} - \boldsymbol{x}^{+}_{zp}\right) - H\left(z^{-} - \boldsymbol{x}^{+}_{zp}\right)\right], \end{aligned}$$

which is the form obtained in the text by direct integration of the expression for stress, *i.e.* Eq. (C.9).

Appendix D

Simulation of a Converging Diverging Channel

This appendix contains full setup details and detailed results for the converging-diverging channel discussed in section 5.3.3.

D.1 Setup

The walls consisted of tethered molecules using the Petravic & Harrowell (2006) potential with $k_4 = 5,000$ and $k_6 = 5,000,000$. Two strips of molecules away from the fluid were thermostatted as shown in red in Figure D.1. This allows the walls to develop a temperature profile and prevents the thermostatted region from interfering strongly with the simulation. The Nosè-Hoover thermostat was used with a target temperature of $T = 1.0$ (the same as the initial temperature of the simulation) and temperature is seen to be controlled adequately reaching an average value of $T \approx 1.3$ at steady state.

The WCA potential was employed for both fluid and wall atoms. The wall needed to be sufficiently dense to ensure it conducted heat from the liquid to the thermostatted region. It was found that FCC crystals with $\rho < 0.8$ do not interact for the WCA potential. The wall density was $\rho = 1.389$ and molecules were removed from the non-tethered liquid region to give a lower fluid density ($\rho = 0.6$) giving $172,476$ molecules in total. This was simulated using 20 processors with topology $20 \times 1 \times 1$. The process of control volume averaging requires calculation of forces for each CV, essentially an averaging bin. For computational efficiency and simplicity these were chosen to be the same size as the computational cells. The solid density was chosen to ensure the FCC crystal unit cells were equivalent in size to the averaging bins/computational cells.

The top and bottom walls formed a smoothly varying surface whose y-coordinate is given by the equation,

$$y_w^{\pm} = \pm\alpha \left[1 - cos\left(\frac{2\pi x}{L_x}\right)\right] \tag{D.1}$$

where $\alpha = (L_y - l_y)/2$ with the maximum channel height $L_y = 47.0\ell$, the minimum (centre) height $l_y = 18.5\ell$ (defined as the channel throat) and the channel length $L_x = 285\ell$. The total simulation domain dimensions are $285 \times 56.9 \times 11.4\ell$ with $200 \times 40 \times 8$ averaging bins of size $1.4227 \times 1.4227 \times 1.4227\ell$. The wall have a minimum thickness of half a binsize (0.711ℓ) above the thermostatted region. The thermostatted region has a width of three binsizes (4.268ℓ). The domain is homogeneous in z with periodic boundaries in the z direction.

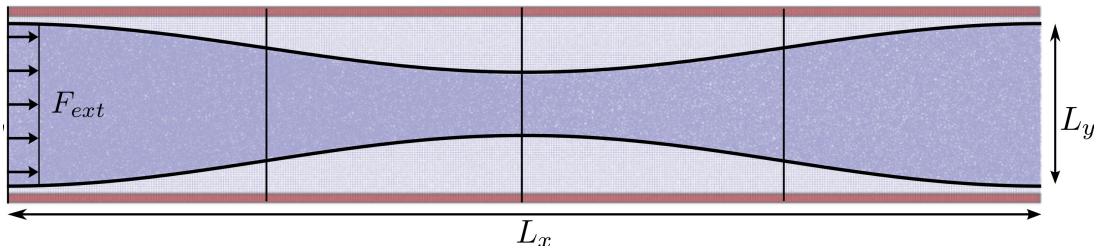

Figure D.1: Channel VMD (Humphrey *et al.*, 1996) snapshot with blue liquid molecules and grey wall molecules. The overlayed annotations show the forced region, the key channel dimensions and the thermostatted regions (red overlay). The four vertical lines denote the location where planer slices are taken in figures D.4 and D.7.

The molecules were driven through the channel using an external force $F_{ext} = 0.5$ applied in a local region of width 10ℓ near the inlet of the domain, and periodic boundaries are applied in x so molecules are fed in from the domain outlet. This force works as a type of molecular pump resulting in a pressure (and density) gradient along the length of the channel. This is the preferred method of force application for non-uniform geometries (Liang & Tsai, 2012; Borg *et al.*, 2013*a*) where the pressure gradient cannot be approximated by a constant force.

After an initial transient period (600 time units), the system reached a steady state and time averages of the quantities of interest were collected. These included number of molecules N_I, density Eq. (4.6), velocity Eq. (4.11) and the CV integration of temperature Eq. (2.57) for each control volume,

$$N_I = \sum_{i=1}^{N} \langle \vartheta_i \rangle; \quad \int_V \rho dV = \sum_{i=1}^{N} \langle m_i \vartheta_i \rangle; \quad \int_V \rho \boldsymbol{u} dV = \sum_{i=1}^{N} \langle m_i \dot{\boldsymbol{r}}_i \vartheta_i \rangle;$$
$$\frac{3}{2} \int_V \rho k_B T dV = \frac{1}{2} \sum_{i=1}^{N} \langle m_i \left(\dot{\boldsymbol{r}}_i - \boldsymbol{u} \right) \cdot \left(\dot{\boldsymbol{r}}_i - \boldsymbol{u} \right) \vartheta_i \rangle,$$

Here the advantage of the CV notation is apparent in the concise and explicit definition of localised bin averaged quantities. The angular brackets denote the temporal average of the steady state system. Assuming an average in each bin $\int_V A dV \approx AV$, $k_B = 1$ and $\rho = N_I/V$ yields the familiar expressions for density, velocity and temperature (Rapaport, 2004) localised to a spatial bin,

$$\rho = \frac{1}{N} \sum_{i=1}^{N} \langle m_i \vartheta_i \rangle; \quad \boldsymbol{u} = \frac{1}{N_I} \sum_{i=1}^{N} \langle m_i \dot{\boldsymbol{r}}_i \vartheta_i \rangle; \quad T = \frac{1}{3N_I} \sum_{i=1}^{N} \langle m_i \left(\dot{\boldsymbol{r}}_i - \boldsymbol{u} \right) \cdot \left(\dot{\boldsymbol{r}}_i - \boldsymbol{u} \right) \vartheta_i \rangle, \quad \text{(D.2)}$$

D.2 Results

The flow fields generated using Eq. (D.2) for volumes $V = 1.4227^3 = 2.8795$ are shown in contour form in Figures D.2, D.3 and D.5 for density, velocity and temperature respectively. The results are averaged over $20,000$ snapshots separated by 25 timesteps and 10 bins in the spanwise z direction. All axis quantities are in MD units. The density and velocity profile as a function of y at the inlet ($x = 0$), at a quarter of the way down the domain ($x = 71.1$), at half way ($y = 142.3$) and at three quarters ($x = 213.4$) are plotted in Figure D.4. The centreline density, velocity,

momentum and temperature values are plotted as a function of x in Figure D.7.

This density contour of Figure D.2 shows a variation throughout the system. The pumping region increases the density from $\rho \approx 0.55$ to $\rho \approx 0.7$ and the velocity, induced by this pumping, causes the molecules to move into the converging part of the channel. This increases the density to give a maximum at around $x = 75$ (1/4 of the domain), shown by the largest y profile in D.4a. The centreline density profile as a function of x shown in Figure D.4a drops to a minimum around $x = 200$ (3/4 of the domain) shown by the smallest y profile in D.4a. The density drops smoothly throughout both the converging and diverging parts of the channel between this maximum and minimum, appearing almost perfectly anti-symmetric about the channel centreline in Figure D.4a.

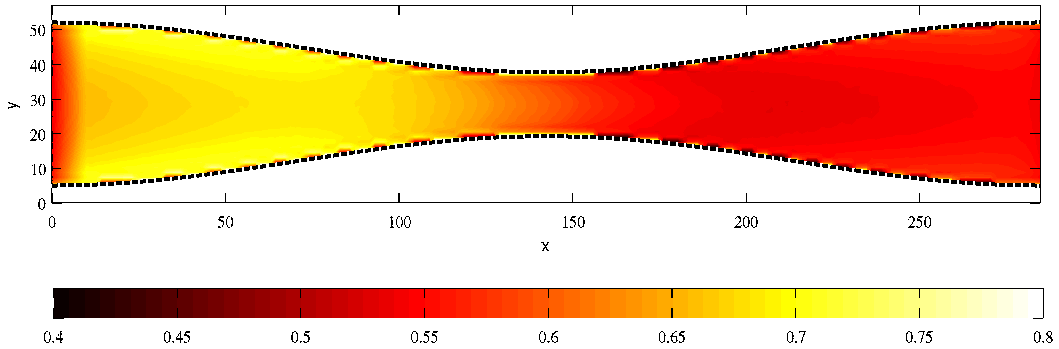

Figure D.2: Density contour in the MD converging diverging channel

This velocity contour shown in Figure D.3 indicates acceleration through the converging section to a maximum velocity at the throat followed by slowing in the diverging part. The velocity maximum is off centre, attributed in part to the use of a pumping region which introduces asymmetry in the channel. However, the density drop is the main reason for this asymmetry as highlighted in Figure D.8. The x profile to the momentum drop $\rho u/\rho_0 u_0$ is seen to be almost symmetric about the centreline $x = 142.3$ while the velocity is clearly off-centre. The velocity profiles are parabolic, as in Poiseuille flow, with an increasing magnitude at the narrower locations D.4b.

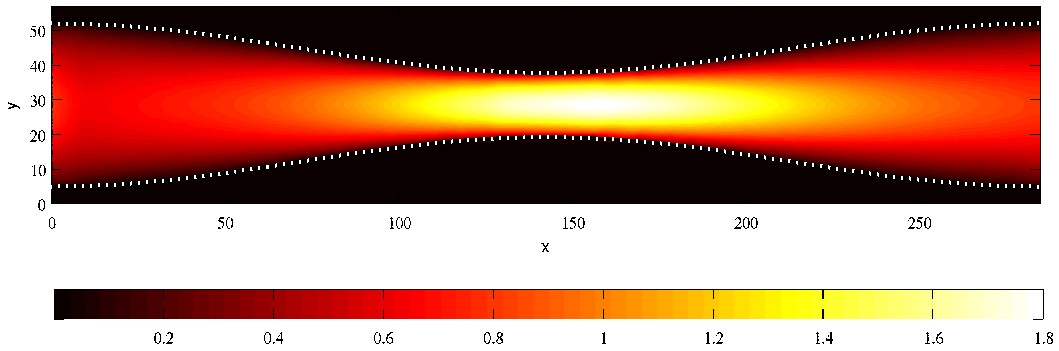

Figure D.3: Velocity contour in the MD converging diverging channel

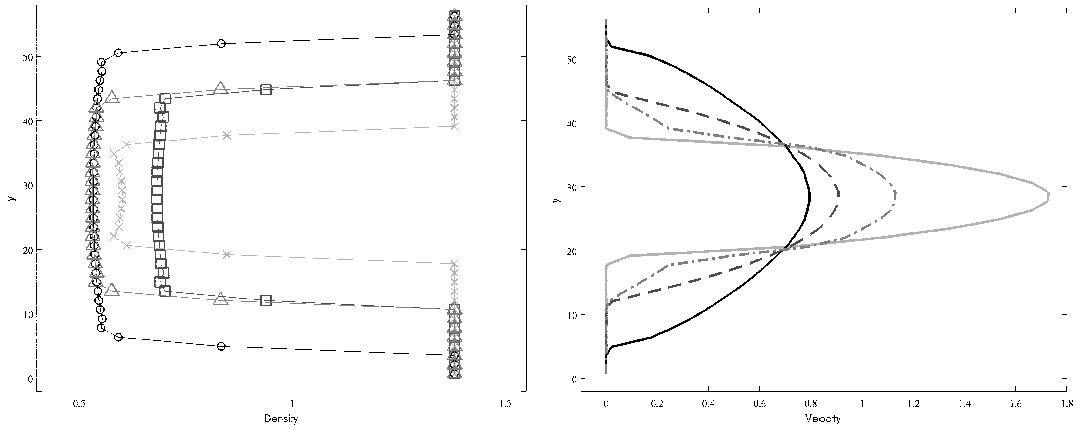

Figure D.4: Profiles at four locations alone the converging diverging channel – the entry ($x = 0$), at one quarter along the domain ($x = 71.1$) at the throat ($x = 142.3$) and at three quarters ($x = 213.4$)

.

This localised values of temperature are displayed in Figure D.5. Instead of using the definition of temperature in terms of the peculiar momentum of equation Eq. (D.2), the expression is reformulated by expanding out the terms in brackets,

$$T = \underbrace{\frac{1}{3N_I}\sum_{i=1}^{N}\left\langle m_i \dot{r}_i^2 \vartheta_i \right\rangle}_{\overline{T}} - \frac{2\boldsymbol{u}}{3}\cdot\underbrace{\frac{1}{N_I}\sum_{i=1}^{N}\left\langle m_i \dot{\boldsymbol{r}}_i \vartheta_i \right\rangle}_{\boldsymbol{u}} + \frac{u^2}{3N_I}\underbrace{\sum_{i=1}^{N}\left\langle \vartheta_i \right\rangle}_{N_I} = \overline{T} - \frac{1}{3}\rho u^2.$$

The form, $\overline{T}$, is advantageous as it is simply the square of the laboratory frame velocity for the molecules in a given bin. The square of velocity can then be removed as part of post processing. The resulting temperature contour in the domain shows the highest temperatures near the 'pumping region' which include all the liquid region from 0 to 10. This generation of heat is consistent with the physical act of pumping. The force attempts to generate coherent velocity u_x in the x direction, however, the molecules move directly into the slower molecules in the adjacent unforced region and much of this directional velocity will become thermal.

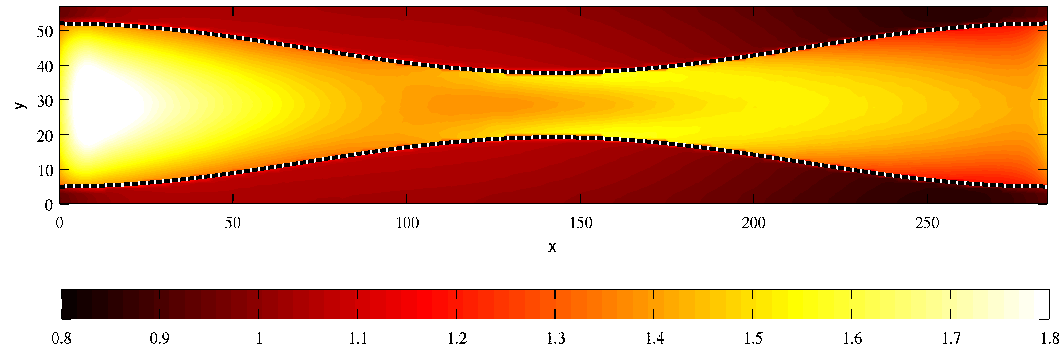

Figure D.5: Temperature contour in the MD converging diverging channel

The wall in the converging regions in Figure D.5 act as a heat sink, being kept cooler by the attached Nosé Hoover thermostat region. As a result, the walls show a temperature contour with highest temperatures at the interface with the fluid and decreases moving towards the thermostatted regions. However, for fluid in the throat of the channel, the generation of heat by the interaction (shear) with the walls becomes evident. The high flowrate through the centre coupled with the highest shear rates at the wall results in an unusual temperature profile with a lower value in the centre. The shear stress contour are shown in Figure D.6 which supports this showing highest shear rates in the nozzle throat adjacent to the walls.

The temperature and shear stress profile as a function of y at the inlet ($x = 0$), at a quarter of the way down the domain ($x = 71.1$), at half way ($y = 142.3$) and at three quarters ($x = 213.4$) are plotted in Figure D.7.

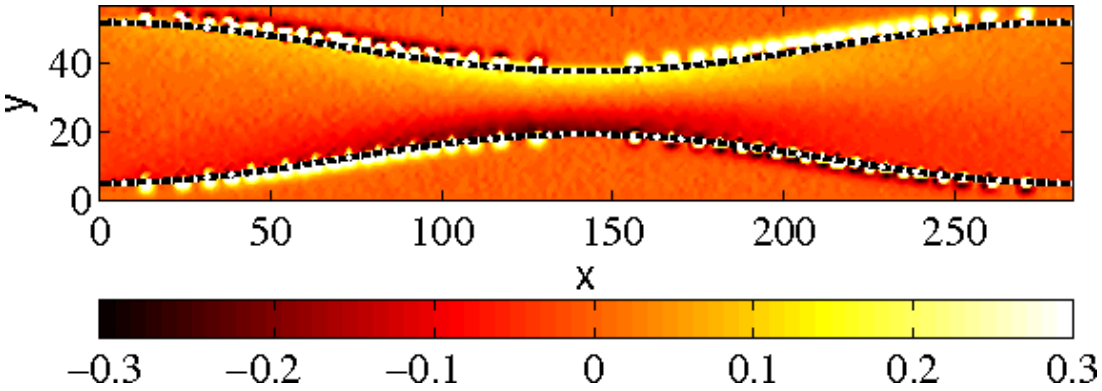

Figure D.6: Shear stress Π_{xy} (kinetic and configurational, see Eq. (5.37)) contour in the MD converging diverging channel.

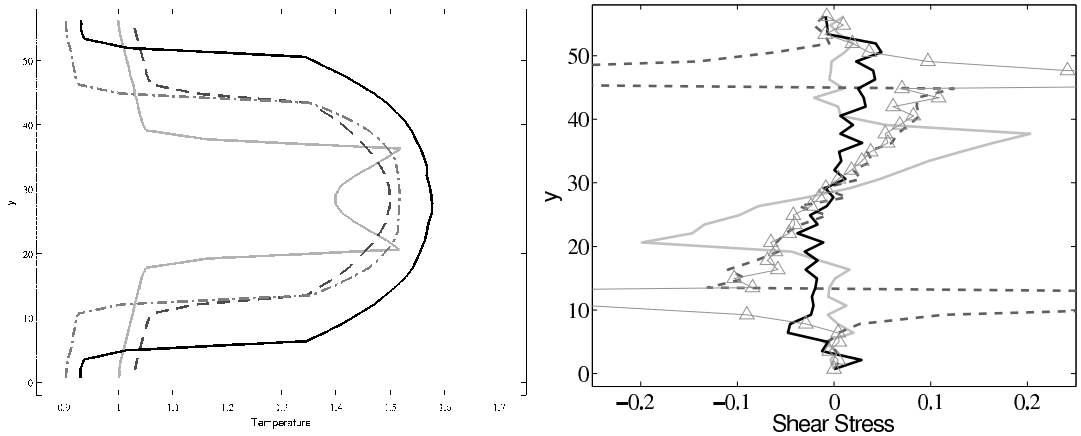

Temperature Shear Stress

Figure D.7: Profiles at four locations alone the converging diverging channel – the entry ($x = 0$), at one quarter along the domain ($x = 71.1$) at the throat ($x = 142.3$) and at three quarters ($x = 213.4$)

.

In order to obtain fine-grained statistics, a number of smaller cubic CV are used throughout the domain. As conservation is ensured locally, these can be upscaled to obtain larger control

volumes which are also conserved.

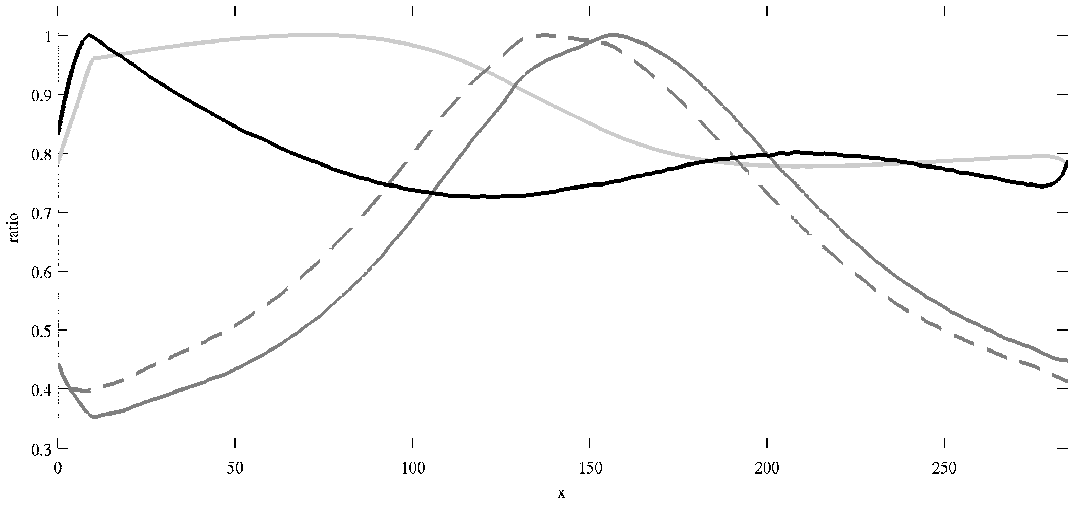

Figure D.8: The change in x of various quantities state quantities along the centre line in the converging-diverging channel. The density ratio ρ/ρ_0 (——), the velocity ratio u/u_0 (- -) and the temperature ratio T/T_0 (▬). The momentum ratio $\rho u/\rho_0 u_0$ (——) is also plotted. Subscript 0 denotes channel maximum where $\rho_0 = 0.7$, $u_0 = 1.8$ and $T_0 = 1.9$.

The simulation setup and results presented in this appendix support the discussion in section 5.3.3.

Appendix E

Error analysis of flux coupling

The error analysis of Hadjiconstantinou *et al.* (2003) is extended to density, velocity and pressure/stress calculation of dense fluids. The error in the pressure results are obtained from a molecular simulation. Using the standard deviation s and mean μ of the MD pressure, the required samples M_P for an error E_P is calculated in Hadjiconstantinou *et al.* (2003) from the relative standard error, Eq. (2.83),

$$M_P = \left(\frac{s}{\mu E_P} \right)^2. \tag{E.1}$$

The molecular system used a cutoff of $r_c = 3.0$, the standard long range corrections were included and a Nosè-Hoover Thermostat was applied to control the temperature. The required samples for 5% error ($E_P = 0.05$) at three temperatures values across a range of densities are plotted as points in Figure E.1.

The samples estimated obtained from MD simulation using, Eq. (E.1), can be compared to the Hadjiconstantinou *et al.* (2003) estimates which are derived from Eq. (E.1) and should be equivalent,

$$M_\rho = \frac{\kappa_T k_B T_0}{V E_\rho^2} \quad M_u = \frac{k_B T}{u^2} \frac{1}{\rho V E_u^2} \quad M_P = \frac{\gamma k_B T}{P^2 \kappa_T} \frac{1}{V E_P^2}, \tag{E.2}$$

In order to evaluate Eq. (E.2), accurate values of the density (ρ), velocity (u), pressure (P), isothermal compressibility (κ_T) and ratio of specific heats (γ) at each state point are required. To obtain these parameters, the pressure, temperature and density are matched to empirical expressions for the Lennard-Jones phase diagrams (Johnson *et al.*, 1993). The Johnson *et al.* (1993) empirical values for isothermal compressibility and ratio of specific heats are used in Eq. (E.2) to generate the full range of averaging requirements at all densities. These are shown as lines in Figure E.1. Typically, the analytical Lennard-Jones phase diagram of Johnson *et al.* (1993) is valid for temperatures greater than $T = 1$ (a real temperature of $120K$).

The MD results from Eq. (E.1) and results using analytical Lennard-Jones values from Eq. (E.2) show similar trends. The largest value, given by the peak in Figure E.1a is at the same location from both methods. Typically the MD results are larger than the analytical, although at higher density this is no longer true. Only the general trends are important for the conclusions in this section.

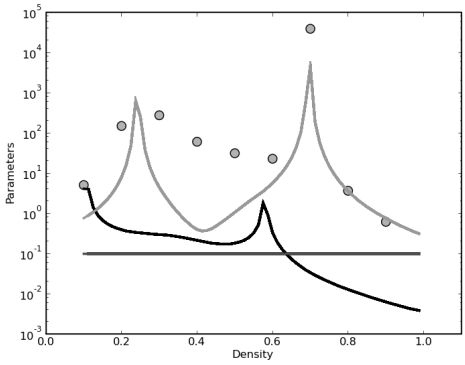

(a) Required samples at temperature $T = 1.0$

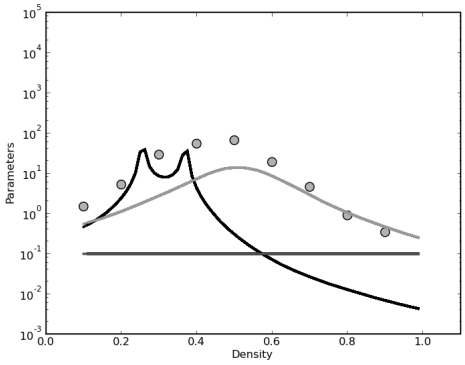

(b) Required samples at temperature $T = 1.3$

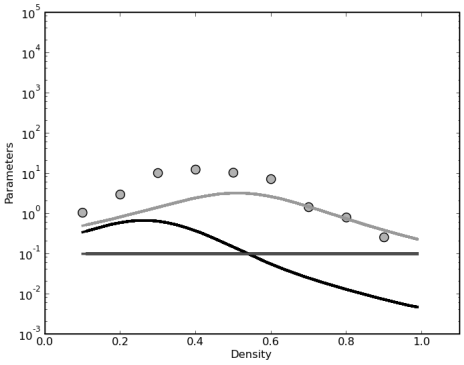

(c) Required samples at temperature$T = 1.5$

Figure E.1: Estimate of the required samples for a 5% error from Eq. 2.86 shown by M_ρ $(-)$, M_u $(-)$ and M_P $(-)$ with MD estimates for M_P $(\circ)$ calculated from equation E.1

The number of required samples becomes prohibitively large, $\tilde{O}(10^4)$ on Figure E.1a, a conclusion supported by both MD and analytical results. This is a result of the mean pressure approaching a value of zero (μ in the denominator of Eq. (E.1)), while fluctuations (standard deviation s) remains non-zero. This is a numerical artefact of the definition of relative standard error, Eq. (E.1), and not representative of the quality of averaged variables in a coupling scheme. This suggests that the standard error, s/M_P, may be a better measure of signal to noise ratio for coupling. For common molecular temperatures and densities, the requires samples for a 5% error in pressure are of order 10^2 or lower. In addition, the velocity or density can sometimes be more expensive than flux averages. The velocity used in the above parameter curve for M_u is calculated from average molecular speed using Maxwell Boltzmann statistics $u = \sqrt{2k_BT/m}$. In practice, with no driving forces, the average velocity of a cell tends to zero as the averaging region increases and the sample estimate for velocity would also tend to infinity.

The conclusion of this parameter study is that flux coupling is not prohibitively expensive as stated in Hadjiconstantinou (2005). Typicall pressure sample requirements are $\tilde{O}(10^2)$ or less for a unit volume. This does not diminish the importance of removing noise in molecular to continuum coupling, but it does suggest that for dense fluid the errors in fluxes are not prohibitive. In addition, a different measure of errors may be more appropriate to evaluate the feasibility of coupling schemes.

Bibliography

Admal, N. C. & Tadmor, E. B. 2010 A unied interpretation of stress in molecular systems. *J. Elast.* **100**, 63.

Alder, B. J. & Wainwright, T. E. 1957 Phase transition for a hard sphere system. *J. Chem. Phys.* **27** (1208).

Alder, B. J. & Wainwright, T. E. 1959 Studies in molecular dynamics. i. general method. *J. Chem. Phys.* **31** (2).

Allen, M. P. & Tildesley, D. J. 1987 *Computer Simulation of Liquids*, 1st edn. Clarendon Press, Oxford.

Anderson, J. A., Lorenz, C. D. & Travesset, A. 2008 General purpose molecular dynamics simulation fully implemented on graphical processing units. *J. of Comp. Phys.* **227**, 5342.

Anton, L. & Smith, E. 2012 Scalable coupling of molecular dynamics (md) and direct numerical simulation (dns) of multi-scale flows. *Tech. Rep.*.

Baidakov, V., Protsenko, S. & Kozlova, Z. 2008 Thermal and caloric equations of state for stable and metastable lennard-jones fluids: I. molecular-dynamics simulations. *Fluid Phase Equilibria* **263** (1), 55 – 63.

Borg, M. K., Lockerby, D. A. & Reese, J. M. 2013*a* A hybrid molecular-continuum simulation method for incompressible flows in micro/nanofluidic networks. *Microfluidics and Nanofluidics* pp. 1–17.

Borg, M. K., Lockerby, D. A. & Reese, J. M. 2013*b* A multiscale method for micro/nano flows of high aspect ratio. *J. of Comp. Phys.* **233** (0), 400 – 413.

Borg, M. K., Macpherson, G. B. & Reese, J. M. 2010 Controllers for imposing continuum-to-molecular boundary conditions in arbitrary fluid flow geometries. *Molec. Sims.* **36**, 745.

Borisenko, A. I. & Tarapov, I. E. 1979 *Vector and Tensor Analysis with applications*, 2nd edn. Dover Publications Inc, New York.

Boyle, R. 1666 *The Origin of forms and Qualities (according to the corpuscular philosophy) Illustrated by Considerations and Experiments*.

Brown, W. M., Wang, P., Plimpton, S. J. & Tharrington, A. N. 2011 Implementing molecular dynamics on hybrid high performance computers-short range forces. *Comp. Phys. Comms.* **182**, 898.

Chapman, S. & Cowling, T. G. 1970 *The Mathematical Theory of Non-Uniform Gases*, 3rd edn. Cambridge University press, Cambridge.

Chorin, A. J. 1967 A numerical method for solving incompressible viscous flow problems. *J. of Comp. Phys.* **2**, 12.

Cormier, J., Rickman, J. M. & Delph, T. J. 2001 Stress calculation in atomistic simulations of perfect and imperfect solids. *J. Appl. Phys* **89**, 99.

Coveney, P. & Highfield, R. 1991 *The Arrow of Time*, 1st edn. HarperCollins, London.

Curtin, W. A. & Miller, R. E. 2003 Atomistic/continuum coupling in computational material science. *Modelling Simul. Mater. Sci. Eng.* **11**, 33.

Daivis, P. J., Travis, K. P. & Todd, B. D. 1996 A technique for the calculation of mass, energy and momentum densities at planes in molecular dynamics simulations. *J. Chem. Phys* **104**, 9651.

Dalton, J., Wollaston, W. H. & Thomson, T. 1808 *Foundations of the atomic theory*.

Delgado-Buscalioni, R. 2012 Tools for multiscale simulation of liquids using open molecular dynamics. *Lecture Notes in Computational Science and Engineering* **82**, 145.

Delgado-Buscalioni, R. & Coveney, P. 2003*a* Continuum-particle hybrid coupling for mass, momentum, and energy transfers in unsteady fluid flow. *Phys. Rev. E* **67**, 046704.

Delgado-Buscalioni, R. & Coveney, P. 2003*b* Usher: an algorithm for particle insertion in dense fluids. *J. of Chem. Phys.* **119**, 978.

Delgado-Buscalioni, R. & Coveney, P. 2004 Hybrid molecular-continuum fluid dynamics. *Phil. Trans. R. Soc. Lond.* **362**, 1639.

Delgado-Buscalioni, R. & Fabritiis, G. D. 2007 Embedding molecular dynamics within fluctuating hydrodynamics in multiscale simulation of liquids. *Phys. Rev. E* **76**, 036709.

Evans, D. J. & Morris, G. P. 1984 Non-newtonian molecular dynamics. *Comp. Phys. Rep. 1* **1-6**, 297.

Evans, D. J. & Morriss, G. P. 2007 *Statistical Mechanics of Non-Equilibrium Liquids*, 2nd edn. Australian National University Press, Canberra.

Fabritiis, G. D., Delgado-Buscalioni, R. & Coveney, P. 2006 Multiscale modeling of liquids with molecular specificity. *Phys. Rev. Lett.* **97**, 134501.

Fabritiis, G. D., Serrano, M., Delgado-Buscalioni, R. & Coveney, P. 2007 Fluctuating hydrodynamic modeling of fluids at the nanoscale. *Phys. Rev. E* **75**, 026307.

Flannery, M. R. 2005 The enigma of nonholonomic constraints. *American Journal of Physics* **73** (3), 265–272.

Flannery, M. R. 2011 d'alembert–lagrange analytical dynamics for nonholonomic systems. *J. Math. Phys.* **52** (3), 032705.

Flekkøy, E. G., Delgado-Buscalioni, R. & Coveney, P. V. 2005 Flux boundary conditions in particle simulations. *Phys. Rev. E* **72**, 026703.

Flekkøy, E. G., Wagner, G. & Feder, J. 2000 Hybrid model for combined particle and continuum dynamics. *Europhys. Lett.* **52**, 271.

Germann, T. C. & Kadau, K. 2008 Trillion-atom molecular dynamics becomes a reality. *International Journal of Modern Physics C* **19** (09), 1315–1319.

Goldstein, H., Poole, C. & Safko, J. 2002 *Classical Mechanics*, 3rd edn. Addison Wesley, Boston.

Green, M. S. 1954 Markoff random processes and the statistical mechanics of time-dependent phenomena. ii. irreversible processes in fluids. *The Journal of Chemical Physics* **22** (3), 398–413.

Gropp, W. D., Lusk, E. L. & Skjellum, A. 1999*a* *Using MPI: Portable Parallel Programming With the Message-Passing Interface, Volume 1*, 1st edn. MIT Press.

Gropp, W. D., Lusk, E. L. & Thakur, R. 1999*b* *Using MPI-2:Advanced Features of the Message-Passing Interface, Volume 2*, 1st edn. Falcon.

Hadjiconstantinou, N. G. 1998 Hybrid atomisticcontinuum formulations and the moving contact-line problem. PhD thesis, MIT(U.S.).

Hadjiconstantinou, N. G. 1999 Hybrid atomisticcontinuum formulations and the moving contact-line problem. *J. Comp. Phys.* **154**, 245.

Hadjiconstantinou, N. G. 2005 Discussion of recent developments in hybrid atomistic-continuum methods for multiscale hydrodynamics. *Bulletin of the Polish Academy of Science* **53**, 335.

Hadjiconstantinou, N. G., Garcia, A. L., Bazant, M. Z. & He, G. 2003 Statistical error in particle simulations of hydrodynamic phenomena. *J. Comp. Phys.* **187**, 274.

Gad-el Hak, M. 1995 Questions in fluid mechanics. *Journal of Fluids Engineering* **117**, 3.

Gad-el Hak, M. 2006 Gas and liquid transport at the microscale. *Heat Transfer Eng.* **27(4)**, 13.

Han, M. & Lee, J. S. 2004 Method for calculating the heat and momentum fluxes of inhomogeneous fluids. *Phys. Rev. E* **70**, 061205.

Hardy, R. J. 1982 Formulas for determining local properties in molecular dynamics simulations: Shock waves. *J. Chem. Phys* **76**, 622.

Heyes, D. M., Smith, E. R., Dini, D., Spikes, H. A. & Zaki, T. A. 2012 Pressure dependence of confined liquid behavior subjected to boundary-driven shear. *J. Chem. Phys* **136**, 134705.

Heyes, D. M., Smith, E. R., Dini, D. & Zaki, T. A. 2011 The equivalence between volume averaging and method of planes denitions of the pressure tensor at a plane. *J. Chem. Phys* **135**, 024512.

Hirsch, C. 2007 *Numerical Computation of Internal and External Flows*, 2nd edn. Elsevier, Oxford.

Hoover, W. G. 1991 *Computational Statistical Mechanics*, 1st edn. Elsevier Science, Oxford.

Hoover, W. G., Hoover, C. & Lutsko, J. 2009 Microscopic and macroscopic stress with gravitational and rotational forces. *Phys. Rev. E* **79**, 036709.

Humphrey, W., Dalke, A. & Schulten, K. 1996 Vmd - visual molecular dynamics. *J. Molec. Grap.* **14.1**, 33.

Irving, J. H. & Kirkwood, J. G. 1950 The statistical mechanics theory of transport processes. iv. the equations of hydrodynamics. *J. Chem. Phys.* **18**, 817.

Itterbeek, V. & Verbeke, O. 1960 Density of liquid nitrogen and argon as a function of pressure and temperature. *Physica* **931** (26).

Jimenez, J. & Moin, P. 1991 The minimal flow unit in near-wall turbulence. *J. Fluid Mech.* **225**, 213.

Johnson, J. K., Zollweg, J. A. & Gubbins, K. E. 1993 The lennard-jones equation of state revisited. *Molecular Physics* **78** (3), 591–618.

K. Kadau, a. J. L. B., Germann, T. C., Holian, B. L. & Alder, B. J. 2010 Atomistic methods in fluid simulation. *Phil. Trans. R. Soc. A* **368** (1916), 1547–1560.

Kim, J., Moin, P. & Moser, R. 1987 Turbulence statistics in fully developed channel flow at low reynolds number. *J. Fluid Mech.* **177** (1), 133–166.

Kotsalis, E. M., Walther, J. H. & Koumoutsakos, P. 2007 Control of density fluctuations in atomistic-continuum simulations of dense liquids. *Phys. Rev. E* **76**, 016709.

Kubo, R. 1957 Statistical-mechanical theory of irreversible processes. i. general theory and simple applications to magnetic and conduction problems. *Journal of the Physical Society of Japan* **12** (6), 570–586.

Landau, L. D. & Lifshitz, E. M. 1969 *Fluid Mechanics*, 1st edn. Pergamon Press.

Landau, L. D. & Lifshitz, E. M. 1980 *Statistical Physics*, 2nd edn. Butterworth-Heinemann.

Li, J., Liao, D. & Yip, S. 1997 Coupling continuum to molecular-dynamics simulation: Reflecting particle method and the field estimator. *Phys. Rev. E* **57**, 7259.

Liang, Z. & Tsai, H. 2012 A method to generate pressure gradients for molecular simulation of pressure-driven flows in nanochannels. *Microfluidics and Nanofluidics* **13**, 289.

Liem, S. Y., Brown, D. & Clarke, J. H. R. 1992 Investigation of the homogeneous-shear nonequilibrium-molecular-dynamics method. *Phys. Rev. A* **45**, 3706–3713.

Liu, J., Chen, S., Nie, X. & Robbins, M. O. 2007 A continuumatomistic simulation of heat transfer in micro- and nano-flows. *Journal of Computational Physics* **227** (1), 279.

Liu, J., Chen, S. Y., Nie, X. B. & Robbins, M. O. 2008 A continuum-atomistic multi-timescale algorithm for micro/nano flow. *Comms. in Comp. Phys.* **4**, 1279.

Lockerby, D. A., Reese, J. M. & Struchtrup, H. 2009 Switching criteria for hybrid rarefied gas flow solvers. *Proc. R. Soc. A* **465** (2105), 1581.

Lutsko, J. F. 1988 Stress and elastic constants in anisotropic solids: Molecular dynamics techniques. *J. Appl. Phys* **64**, 1152.

Mohamed, K. M. & Mohamad, A. A. 2009 A review of the development of hybrid atomistic-continuum methods for dense fluids. *Microfluidics and Nanofluidics* **8**, 283.

Morriss, G. P. & Dettman, C. P. 1998 Thermostats: Analysis and application. *Chaos* **8,2**, 321.

Motte, A. 1729 *The Mathematical Principles of Natural Philosophy*, 1st edn.

Mulla, S., Ivekovic, S. & Reese, J. M. 2013 Molecular dynamics simulation of multi-scale flows on gpus. *Tech. Rep.*.

Murdoch, A. I. 2007 A critique of atomistic definitions of the stress tensor. *J. Elast.* **88**, 113.

Murdoch, A. I. 2010 On molecular modelling and continuum concepts. *J. Elast* **100**, 33.

Nemat-Nasser, S. 2004 *Plasticity: A Treatise on the Finite Deformation of Heterogeneous Inelastic Materials*, 1st edn. Cambridge University Press, Cambridge.

Nethercote, N. 2004 Dynamic binary analysis and instrumentation. PhD thesis, University of Cambridge.

Neuenschwander, D. E. 2011 *Emmy Noether's Wonderful Theorem*, 1st edn. John Hopkins University Press.

Newton, I. 1726 *Philosophiæ Naturalis Principia Mathematica*, 3rd edn.

Nie, X. B., Chen, S., E, W. N. & Robbins, M. 2004*a* A continuum and molecular dynamics hybrid method for micro- and nano-fluid flow. *J. of Fluid Mech.* **500**, 55.

Nie, X. B., Chen, S. & Robbins, M. 2004*b* Hybrid continuumatomistic simulation of singular corner flow. *Phys. of Fluids* **16**, 3579.

Nie, X. B., Robbins, M. & Chen, S. 2006 Resolving singular forces in cavity flow: Multiscale modeling from atomic to millimeter scales. *Phys. Rev. Lett.* **96**, 134501.

NIST 2013 Benchmark results for the lennard-jones fluid.

Noll, W. 1955 Die herleitung der grundgleichungen der thermomechanik der kontinua aus der statistischen mechanik. *Indiana Univ. Math. J.* **4**, 627.

NVIDIA 2010 *NVIDIA CUDA C Programming Guide*, 3rd edn. NVIDIA Corporation, 2701 San Tomas Expressway, Santa Clara, CA 95050.

O'Connell, S. 1995 The development of a molecular dynamics - continuum hybrid computation for modeling fluid flows. PhD thesis, Duke University (U.S.).

O'Connell, S. T. & Thompson, P. A. 1995 Molecular dynamics-continuum hybrid computations: A tool for studying complex fluid flow. *Phys. Rev.* **E 52**, R5792.

Parker, E. N. 1954 Tensor virial equations. *Phys. Rev.* **96**, 1686.

Petravic, J. & Harrowell, P. 2006 The boundary fluctuation theory of transport coefficients in the linear-response limit. *J. Chem. Phys.* **124**, 014103.

Plimpton, S. 1995 Fast parallel algorithms for short range molecular dynamics. *J. of Comp. Phys.* **117**, 1.

Plimpton, S., Crozier, P. & Thompson, A. 2003 *LAMMPS Users Manual - Largescale Atomic/Molecular Massively Parallel Simulator*, 7th edn. http://lammps.sandia.gov.

Potter, M. C. & Wiggert, D. C. 2002 *Mechanics of Fluids*, 3rd edn. Brooks/Cole, California.

Rahman, A. 1964 Correlations in the motion of atoms in liquid argon. *Phys. Rev.* **A136** (405).

Rapaport, D. C. 2004 *The Art of Molecular Dynamics Simulation*, 2nd edn. Cambridge University Press, Cambridge.

Ren, W. 2007 Analytical and numerical study of coupled atomistic-continuum methods for fluids. *J. of Comp. Phys.* **227**, 1353.

Reynolds, O. 1903 *Papers on Mechanical and Physical Subjects - Volume 3*, 1st edn. Cambridge University Press, Cambridge.

Rosenfeld, M., Kwak, D. & Vinokur, M. 1991 A fractional step solution method for the unsteady incompressible navierstokes equations in generalized coordinate systems. *J. Comput. Phys* **94**, 102.

Saletan, E. J. & Cromer, A. H. 1970 A variational principle for nonholonomic systems. *American Journal of Physics* **38** (7), 892–897.

Sandler, S. I. & Woodcock, L. V. 2010 Historical observations on laws of thermodynamics. *J. Chem. & Eng. Data* **55** (10), 4485.

Schofield, P. & Henderson, J. R. 1982 Statistical mechanics of inhomogeneous fluids. *Proc. R. Soc. Lond. A* **379**, 231.

Serrano, M. & Español, P. 2001 Thermodynamically consistent mesoscopic fluid particle model. *Phys. Rev. E* **64**, 046115.

Shan, X., Yuan, X. & Chen, H. 2006 Kinetic theory representation of hydrodynamics: a way beyond the navier-stokes equation. *J. of Fluid Mech.* **550**, 413.

Shende, S. & Malony, A. D. 2006 The tau parallel performance system. *Int. J. High Perf. Comp. Apps.* **20**, 287.

Silva, F. D. C., Coelho, L. A. F., Tavares, F. W. & Cardoso, M. J. E. M. 2003 Shear viscosity calculated by perturbation theory and molecular dynamics for dense fluids. *Int. J. Quantum Chem.* **95**, 79.

Smith, E., Trevelyan, D. & Zaki, T. A. 2013 Scalable coupling of molecular dynamics (md) and direct numerical simulation (dns) of multi-scale flowspart 2. *Tech. Rep.*.

Smith, E. R., Heyes, D. M., Dini, D. & Zaki, T. A. 2012 Control-volume representation of molecular dynamics. *Phys. Rev. E.* **85**, 056705.

Smith, E. R. & Trevelyan, D. 2013 Cpl-library.

Soutas-Little, R. & Merodio, J. 2007 *Continuum Mechanics, chapter 2 – History of Continuum mechanics*. Encyclopedia of Life Support Systems (EOLSS),, developed under the Auspices of the UNESCO, Eolss Publishers, Oxford ,UK, [http://www.eolss.net].

Spoel, D. V. D., Lindahl, E., Hess, B., Groenhoff, G., Mark, A. E. & Berendsen, H. J. C. 2005 Gromacs: Fast, flexible, and free. *J. of Comp. Chem.* **26**, 1701.

Strauss, W. A. 1992 *Partial Differential Equations*, 1st edn. John Wiley and Sons, New Jersey.

Subramaniyan, A. K. & Sun, C. T. 2007 A critique of atomistic definitions of the stress tensor. *J. Elast.* **88**, 113.

Succi, S. 2001 *The Lattice Boltzmann Equation for Fluid Dynamics and Beyond*, 1st edn. Oxford University Press, Oxford.

Sun, J., He, Y. & Tao, W. 2010 Scale effect on flow and thermal boundaries in micro-/nano-channel flow using molecular dynamicscontinuum hybrid simulation method. *Int. J. Numer. Meth. Engng* **81**, 207.

Sun, J., He, Y., Tao, W., Yin, X. & Wang, H. 2012 Roughness effect on flow and thermal boundaries in microchannel/nanochannel flow using molecular dynamics-continuum hybrid simulation. *Int. J. Numer. Meth. Engng* **89**, 2.

Thankoppan, V. 1985 *Quantum Mechanics*, 1st edn. New Age pub, New Delhi.

Todd, B. D. & Daivis, P. J. 2005 A simple, direct derivation and proof of the validity of the sllod equations of motion for generalised homogeneous flow. *J. Chem. Phys* **124**, 194103–1.

Todd, B. D., Evans, D. J. & Daivis, P. J. 1995 Pressure tensor for inhomogeneous fluids. *Phys. Rev. E* **52**, 1627.

Tsai, D. H. 1978 The virial theorem and stress calculation in molecular dynamics. *J. Chem. Phys.* **70**, 1375.

Wagner, G., Flekky, E., Feder, J. & Jossang, T. 2002 Coupling molecular dynamics and continuum dynamics. *Comp. Phys. Comms.* **147**, 670.

Wang, Y. & He, G. 2007 A dynamic coupling model for hybrid atomisticcontinuum computations. *Chem. Eng. Sci.* **62**, 3574.

Werder, T. 2005 Multiscale simulations of carbon nanotubes in aqueous environments. PhD thesis, Swiss Federal Institute Of Technology, Zurich.

Werder, T., Walther, J. H. & Koumoutsakos, P. 2005 Hybrid atomistic continuum method for the simulation of dense fluid flows. *J. of Comp. Phys.* **205**, 373.

Wu, X. & Durbin, P. A. 2001 Evidence of longitudinal vortices evolved from distorted wakes in a turbine passage. *Journal of Fluid Mechanics* **446**, 199–228.

Yamell, J. L., Katz, M. J., Wenzel, R. G. & Koenig, S. H. 1973 Structure factor and radial distribution function for liquid argon at 85k. *Phys. Rev. A* **7**, 2130.

Yen, T. H., Soong, C. Y. & Tzeng, P. 2007 Hybrid molecular dynamics-continuum simulation for nano/mesoscale channel flows. *Microfluid Nanofluid* **3**, 665.

Zaki, T. A. & Durbin, P. A. 2005 Mode interaction and the bypass route to transition. *J. Fluid Mech.* **531**, 85.

Zaki, T. A. & Durbin, P. A. 2006 Continuous mode transition and the effects of pressure gradient. *J. Fluid Mech.* **563**, 357.

Zaki, T. A., Wissink, J. G., Rodi, W. & Durbin, P. A. 2010 Direct numerical simulations of transition in a compressor cascade: the influence of free-stream turbulence. *J. Fluid Mech.* **665**, 57.

Zhou, M. 2003 A new look at the atomic level virial stress: on continuum-molecular system equivalence. *Proc. R. Soc. Lond.* **459**, 2347.

Zienkiewicz, O. 2005 *The Finite Element Method: Its Basis and Fundamentals*, 6th edn. Elsevier Butterworth-Heinemann, Oxford.